OBJECTIVE-PRISM SPECTROPHOTOMETRY OF QUASARS

Roger G. Clowes

Doctor of Philosophy
University of Edinburgh
1980

This thesis is my own composition; the work is my own except for the contributions from others that are indicated in the text.

3rd October, 1980

Abstract

A procedure is derived for obtaining low-resolution spectrophotometry of quasars directly from the objective-prism plates on which they were discovered. Measurements with a PDS microdensitometer of ~ 130 quasar candidates in approximately the central 19 square degrees of the UK Schmidt prism plate UJ3682P were used in the application of the procedure (practical details of the searches for quasars and of the objective-prism spectrophotometry are given). The success of the objective-prism spectrophotometry is demonstrated in a comparison with 12 slit spectra. Redshifts and equivalent widths can be determined with typical discrepancies of 1% and 40% respectively.

This work on objective-prism spectrophotometry leads to a quantification of the selection effects that operate in the searches for emission-line objects on objective-prism plates. The quantification successfully explains an apparent discrepancy in the detection efficiencies of the CTIO-4m and Curtis Schmidt surveys for quasars.

Spectra of quasars that were observed with the Image Photon Counting System on the Anglo-Australian Telescope are presented. The observations of quasars with broad absorption troughs indicate the ejection of matter with velocities up to ~ 22000kms^{-1} and with velocity dispersions up to ~ 11000kms^{-1}.

Data on the wavelength dependences of the contrast γ and the grain response function g of the Kodak emulsion IIIaJ are presented.

Contents

1. Introduction

This thesis is mainly concerned with the objective-prism spectrophotometry of quasars directly from the objective-prism plates on which they were discovered (Chapters 3 and 4) and with the quantification of the selection effects that operate in the searches for quasars (strictly emission-line objects) on objective-prism plates (Chapter 6). Details of the searches for quasars on objective-prism plates (Chapter 2), the wavelength dependences of the Kodak emulsion IIIaJ (Chapter 5) and the AAT observations of particular quasars (Chapter 7) are included.

This chapter continues with a review of the surveys for quasars and an explanation of the usefulness of the objective-prism spectrophotometry and the quantification of the selection effects.

1.1 Quasar Samples

Quasars must, of course, be discovered by the properties that distinguish them observationally from the other objects on the sky. They may, for example, be discovered by radio emission, ultraviolet excess, emission lines, variability, infrared excess, polarisation and x-ray emission.

A subset of quasars may be discovered by spectroscopic examination of the optical counterparts of radio sources. A second subset, which may overlap the first, may be discovered by spectroscopic examination of objects with ultraviolet excesses. A third subset, which may overlap the previous two subsets, may be discovered by searching for emission-line objects on objective-prism or grism plates (the remaining discovery techniques are not widely used at present).

Despite the overlaps of these subsets, surveys with different search techniques detect, in general, quasars with different properties. The ultraviolet-excess quasars are biased towards low redshifts (Braccesi et al (1980)) while the quasars detected by emission lines are biased towards high redshifts (Osmer (1980), Osmer and Smith (1980)). The "emission-line" quasars are typically (~ 90%) not detectable as radio sources (Smith and Wright (1980); also Savage

(1978) and Savage and Bolton (1979) for quasars that were discovered by one or both of ultraviolet excess and emission lines).

There are samples of "radio" quasars that are claimed to be essentially complete above particular observed radio and optical flux limits (Wills and Lynds 1978)). However, no such claims are presently made for emission-line quasars because of the obvious selection effects that cause incompleteness.

The emission-line quasars that are detected on, for example, objective-prism plates from the UK Schmidt Telescope are selected by the detection of emission lines on continua (a few quasars are selected by their ultraviolet continua rather than by emission lines; such quasars certainly require slit spectroscopy for their confirmation and they should be regarded as excluded from the class of "emission-line" quasars). Consequently the quasars are selected to have emission lines with equivalent widths above a particular limit at a particular continuum flux; the limit in equivalent width depends on the continuum flux, the seeing, the sky background, the photographic emulsion, the plate noise, the plate scale and the prism dispersion. The limit in equivalent width as a function of continuum flux will generally be different for different objective-prism plates.

If the selection effects - the dependence of the limit in equivalent width on the above variables - are not quantified the emission-line quasars can be used correctly as a source of interesting objects only and then their potential is not being fully exploited. In order to obtain complete and defined samples of emission-line quasars from several plates or from different surveys (with different dispersions, plate scales, emulsions, ...) both spectrophotometry of the quasars and a quantification of the selection effects are required. For example, for two plates (or surveys) that have spectrophotometry and quantified selection effects a complete and defined sample may be obtained by extracting a subset of quasars with continuum magnitude $m_V \leq m_{lim}$ and equivalent width, of the line causing the detection, $w \geq w_{lim}$ (w_{lim} may be a function of m_V) such that those quasars would not be missed on either plate (or survey). Such a re-selection is necessary before (for example) the surface densities of the quasars on the two plates (or surveys) can be correctly compared.

The work of this thesis, then, is concerned with (i) obtaining, directly from the discovery plates, low-resolution, objective-prism spectrophotometry of quasars, and (ii) quantifying the selection effects so that complete samples may be obtained and different plates (or surveys) compared. The theoretical aspects of objective-prism spectrophotometry are given in Chapter 3. The application of the technique is described in Chapter 4 and the results are compared with slit spectroscopy. Chapter 6 shows that the objective-prism spectrophotometry leads to a quantification of the selection effects that operate in the searches for emission-line quasars on objective-prism (or grism) plates. The quantification should lead to the automated selection of large, complete samples of emission-line quasars from objective-prism plates that have been scanned by, for example, COSMOS at the Royal Observatory, Edinburgh or the APM at the Institute of Astronomy, Cambridge.

1.2 Catalogues of Quasars

There are many lists, individual identifications and observations of quasars scattered throughout the literature. Hewitt and Burbidge (1980) have collected these in a data catalogue of 1549 quasars and BL Lac objects, which, they say, is complete (in the sense of publications) to September 1979. A large part of the increase in numbers from the 637 objects in the earlier edition of the catalogue by Burbidge et al (1977) is due to the identification from ultra-violet-excess and emission-line surveys. The catalogue, being an assimilation of the data from many surveys and techniques, is inhomogeneous and it should not be used naively for statistical studies - it is, nevertheless, a very valuable compilation.

Complete samples of radio quasars are given by Wills and Lynds (1978). Following the work of this thesis large, complete samples of emission-line quasars are possible.

Osmer and Smith (1980) have produced a spectrophotometric catalogue of the quasars that were discovered in the Curtis Schmidt survey and Osmer (1980) has produced a similar catalogue for the CTIO-4m survey. Both catalogues are used in Chapter 6 to demonstrate the selection effects. The Curtis Schmidt survey is described by

Smith (1975) and the CTIO-4m survey is described by Hoag and Smith (1977). The Curtis Schmidt survey is now being extended by a group from the University of Michigan who have so far produced five lists of emission-line objects: MacAlpine et al (1977a, b), MacAlpine et al (1977), MacAlpine and Lewis (1978), and MacAlpine and Williams (1980). Spectrophotometry of the University of Michigan quasars is in progress (Lewis et al (1979)).

The CTIO-4m survey (Osmer (1980)) used Kodak emulsion IIIaF (formerly 127-04). A smaller CTIO-4m survey on emulsion IIIaJ is described by Bohuski and Weedman (1979) and a KPNO-4m survey on IIIaJ is described by Sramek and Weedman (1978). References in this thesis to the CTIO-4m survey mean the CTIO-4m survey on IIIaF.

Savage and Bolton (1979) list the quasars that they have discovered in combined ultraviolet-excess and emission-line surveys using plates from the UK Schmidt Telescope.

Two new lists of probable quasars are given in Chapter 2. The quasars were detected by, in general, emission lines in their spectra on objective-prism plates from the UK Schmidt Telescope.

1.3 Applications of the Emission Line Quasars

The work in this thesis on the low-resolution, objective-prism spectrophotometry of quasars and the quantification of the selection effects, when combined with automated search methods, should result in the emission-line quasars being well suited to studies of, for example, (i) their surface density as a function of magnitude and equivalent width, (ii) their surface distribution and its relation to the galaxy distribution, (iii) their luminosity function and its evolution, and (iv) their spectral properties. Such studies can now profit from the advantages of the emission-line quasars of immediate positive identifications and of their relatively large surface density compared with that of the radio quasars.

The surface density of emission-line quasars is indeed much greater than that of radio quasars, but the apparently extreme difference in radio properties of the two classes is not reflected in the optical spectra, which Osmer (1977) reports are very similar at

similar redshifts. Smith and Wright (1980) observed 122 emission-line quasars with the Parkes radio telescope at 5.0 and 14.5 GHz and detected only ~ 10% above 20mJy, but, apparently, with a higher detection rate (~ 35%) for quasars with intrinsically high optical luminosities. Similar overall detection rates (~ 10%) have been obtained by Savage and Bolton (1979) and by Sramek and Weedman (1978, 1980). At present the largest detection rate is that of Condon et al (1980) who observed intrinsically bright quasars and detected ~ 50% above 0.6mJy. They too suggest that the detection rate increases with intrinsic optical luminosity.

The surface densities of quasars are usually quoted in the form x quasars per square degree brighter than magnitude m. Unless there is further qualification such surface densities will be misleading for the emission-line quasars because the limiting equivalent widths are less at bright magnitudes than at faint magnitudes: the simple surface densities then reflect the different levels of incompleteness at different magnitudes, and those levels are, in general, different for different emission-line surveys. The dependence of the limiting equivalent width on magnitude is derived in Chapter 6 and it is subsequently used to investigate the apparent discrepancy between the surface densities from the CTIO-4m and Curtis Schmidt surveys.

Studies of the surface density and distribution of quasars require samples that represent the whole sky. There is no reason to assume that the 340 square degrees of the high galactic latitude zone of the Curtis Schmidt survey (Osmer and Smith (1980)) represent the whole sky, but even if that assumption is made the zone is covered by 15 plates and the selection effects must be quantified for each one before they may be correctly compared and combined.

On a small scale, each of the two 25 square degree fields that were searched for ultraviolet excess and emission line quasars by Savage and Bolton (1979) gives a simple - that is, considering positions only -, local surface distribution of quasars that is consistent with randomness (Savage (1978)). This simple approach is not really adequate because (i) the tedium of eyeball searches for quasars could lead to artificial holes in the surface distribution: automated and objective searches are required, and (ii) the plates could have spatial variations in their properties: Ellery (1980) has

found field effects of up to $0^{m}.5$ in 2° with some IIaO and IIaD plates although the relative contributions of emulsion response, image structure and influences from COSMOS have not been determined. The possible existence of field effects with IIIaJ plates means that the calibration objects for the objective-prism spectrophotometry should be well distributed over the plates.

Savage (1978) and Savage and Bolton (1979) find apparent discrepancies (e.g. proportion with ultraviolet excess; redshift and magnitude distributions) between the samples of quasars from their two fields. The work of Chapter 6 is intended to describe the selection effects that operate in emission-line surveys rather than in their surveys, which combine the emission-line and ultraviolet excess methods. Consequently, to investigate the reality of their discrepancies either the selection effects for the combined search methods should be quantified or the samples should be restricted to those quasars that were detected by emission lines. In the latter case objective-prism spectrophotometry and the quantification of selection effects would be required in order to determine the reality of discrepancies.

Wills (1978) has reviewed the evidence for the clustering, pairing, and anisotropic surface and redshift distributions of quasars, and also for the association of galaxies with quasars. He concludes that there is no convincing evidence to contradict the views that quasars are distributed uniformly on the sky (but for some evidence see Wills and Lynds (1978) and Murdoch (1978)) and that quasars are unassociated with other quasars or with bright galaxies.

The large, complete samples of emission-line quasars, covering large areas of sky, that can now be obtained from (automated) searches for quasars on objective-prism plates and from using the work of this thesis should help to settle the issue of the reality of anisotropic surface distributions.

In a review of the associations of quasars with galaxies Burbidge (1979) concludes that there are probably both real associations of quasars with galaxies at similar redshifts and real associations at different redshifts -but see the criticism by Browne (1980). Weedman (1980) has found that the associations of quasars with galaxies and of

quasars with quasars for the Curtis Schmidt sample (Osmer and Smith (1980)) and three of the University of Michigan samples are consistent with randomly distributed quasars. Arp (1980) claims associations of Cutis Schmidt quasars with bright, nearby galaxies. Seldner and Peebles (1979) have found, using 382 quasars from the catalogue by Burbidge et al (1977), an average excess of 1.45 ± 0.39 galaxies within 17.5 arcmin of quasars. Again, complete samples of emission-line quasars, together with automated star-galaxy separation, should provide a source of data for a new, objective approach to the study of associations of quasars with galaxies.

The apparent association of some quasars with other quasars must now be regarded as established following the discovery of double and triple quasars (Walsh et al (1979), Weymann et al (1980)) that are believed to be multiple images, produced by intervening gravitational lenses, of single quasars.

The study of the luminosity function of quasars at a given redshift and its evolution with redshift ideally requires large, complete samples at several redshifts. Such samples can now be obtained from surveys using objective-prism plates or plates taken through narrow-band filters. At present the samples that are claimed to be complete (e.g. Wills and Lynds (1978)) are of small numbers of radio quasars and they cover wide redshift ranges. The unknown selection effects in inhomogeneous samples diminish the value of the results obtained from them. Present determinations of the luminosity function require assumptions about its evolution that could be avoided by using large, complete samples that cover narrow redshift ranges.

Note that "luminosity function" refers here to the differential absolute luminosity function $N(P,z)$ - the number per unit volume per unit interval of absolute power at absolute power P and redshift z - so that "luminosity and density evolution" are both implied by "evolution of the luminosity function". Setti and Zamorani (1978) have considered an inhomogeneous sample of optically-selected quasars and they find $N \sim P^{-2.2}$, or $N \sim P^{-2.5}$ after an attempt to allow for incompleteness. They assume throughout that the functional forms of the luminosity functions do not vary with redshift. For radio quasars with steep radio spectra they find that the optical luminosity

function is $N \sim P^{-2.27}$ for a single power law or, in a better fit, $N \sim P^{-1.78}$ for faint quasars and $N \sim P^{-2.87}$ for bright quasars. They find that the optical luminosity function of radio quasars with flat radio spectra can be adequately represented by $N \sim P^{-2.06}$. For radio quasars without regard to their radio spectra the power laws are $N \sim P^{-1.65}$ for faint quasars and $N \sim P^{-2.5}$ for bright quasars. The luminosity function is flatter for quasars with flat radio spectra and it extends to at least one magnitude brighter than the luminosity function for quasars with steep radio spectra.

Sramek and Weedman (1978) include class 1 Seyferts in their tabulation of the local ($z < 0.5$) luminosity function of quasars (which they give in terms of the H_β line power).

The work in Chapter 6 suggests that the luminosity function of strong-lined quasars is flatter ($N \sim P^{-1}$) than the functions obtained by Setti and Zamorani.

The evolution of the luminosity function is best indicated by the radio quasars, which can imply density evolution in comoving space of the forms $\rho \sim (1 + z)^6$ or $\rho \sim \exp\left(\frac{10z}{1 + z}\right)$ - see the review by Schmidt (1978), and also Schmidt (1972). Braccesi et al (1980) claim even faster evolution for ultraviolet-excess quasars while Stewart and Hawkins (1978) claim that a sample from the catalogue by Burbidge et al (1977) is consistent with slow or zero evolution (but see the criticism by Wills (1979)).

Schmidt (1976) has found that the radio quasars with steep radio spectra show evolution while those with flat radio spectra do not. Bentley et al (1976) have shown that Parkes 2700MHz quasars with steep radio spectra tend to be extended radio sources while those with flat radio spectra tend to be compact sources, coincident with the optical sources. This result raises the possibility that there is a selection effect associated with the radio morphology that either mimics or disguises evolution. Because the proportion of flat and steep spectrum sources depends on the radio frequency at which selection occurs (Wall (1975)) the evolutionary properties of radio quasars will be a function of frequency.

There is evidence from optically-selected samples (e.g. Sramek and Weedman (1978), Green and Schmidt (1978)) that suggests strong density evolution but at present such results must be regarded

cautiously because of the selection effects and the possibility that the survey areas are unrepresentative.

There is no clear indication of a cut-off in the quasar redshifts (Carswell and Smith (1978)) but strong evolution cannot continue indefinitely. Constraints on the surface density of quasars at faint magnitudes may be obtained from the X-ray background (Setti and Woltjer (1979)) and, with colour restrictions, from star counts (Bahcall and Soneira (1980), Gilmore (1980)). The constraints are one or two orders of magnitude smaller than the predictions of extrapolated number-magnitude diagrams (Bahcall and Soneira (1980)).

The spectral properties of the emission-line quasars can be determined only internally at present (see Osmer (1980) and Osmer and Smith (1980)) because of the wavelength-dependent selection effects, which are formulated in Chapter 6 but which cannot yet be reliably applied because of the lack of photographic data at short wavelengths. Richstone and Schmidt (1980) present a detailed study of the radio and optical properties of 85 radio quasars. General reviews of the optical spectra of quasars are given by Osterbrock (1979) and Baldwin (1979).

When new photographic data become available the work of this thesis, combined with automated and objective search methods, should permit work on the spectral properties of the emission-line quasars.

2. The Searches For Quasars

Two fields, each of 25 square degrees, were searched for quasars using objective-prism plates that were taken with the UK Schmidt Telescope. The searches and some general results are described in this chapter. The first two sections are introductory and are concerned with the telescope and the photography.

2.1 The UK Schmidt Telescope

The telescope is a classical Schmidt which is situated near Coonabarabran in New South Wales, Australia at an altitude of 1130m and on the same mountain as the 3.9m Anglo-Australian Telescope. A UKST Handbook has been distributed and it comprehensively describes the telescope, complementary equipment, and observing and photographic procedures.

The mirror diameter, the aperture diameter and the focal length are 1.83m, 1.24m and 3.07m respectively. Each photographic plate covers 6.4 x 6.4 degrees of sky and the plate scale is 67.12 arcsec mm^{-1}.

The corrector plate of the telescope is an achromatic doublet of Schott UBK7 and LLF6 glass. The variation of the relative transmission with wavelength (which is needed for objective-prism spectrophotometry) of the achromat was obtained from manufacturers data and it is given in Table 4.3.2. The achromat has two corrected wavelengths whereas the earlier BK7 singlet corrector has one. UK Schmidt plates with identification numbers greater than 3148 were taken through the achromat.

The image spread of the achromat is approximately constant with wavelength except for wavelengths shorter than ~ 3300Å and it is superior to that of the earlier singlet corrector which descends steeply to a minimum at the corrected wavelength of 4200Å. The image spread of the achromat is greater than that of the earlier corrector only for wavelengths close to 4200Å. The half-maximum intensity image diameters, including emulsion spread, are ~ 20μm or ~ 1.3 arcsec for the achromat. At short wavelengths the image diameters for the earlier corrector exceed 60μm.

A full-aperture objective prism may be mounted on the telescope. The prism has an apex angle of 44 arcmin and a reciprocal dispersion, on the plate, of approximately 2400Åmm^{-1} at 4300Å. The dispersion curve is given in Nandy et al (1977) and formulated in Cooke (1980). The prism may be rotated to change the direction of dispersion on the sky but generally the dispersion is north-south with shorter wavelengths at the northern end. The glass of the prism is BK7 and the variation of relative transmission with wavelength, obtained from manufacturers data, is given in Table 4.3.2. The BK7 transmission values also apply to the earlier corrector.

A new prism with a reciprocal dispersion of 800Åmm^{-1} at 4300Å should soon be in use with the UK Schmidt and when combined with the existing prism the additional reciprocal dispersions of 600 and 1200Å mm^{-1} should be possible. The higher dispersions will permit work with the emulsions IIIaF and IV-N.

Step wedges are presently exposed on the northern and eastern wedges of each Schmidt plate and they lead to values of the contrast, γ, for broadband exposures. The step wedges have the advantage of being on the plate. The wavelength dependence of γ can presently be found only from small calibration spectrograms that have been exposed in the calibration grating spectrograph at the Schmidt Unit in Australia. A new, on-the-plate calibration system for finding the wavelength dependence is proposed. The new system should extend below the present limit of ~ 3950Å with the calibration spectrograph.

2.2 Photographic Plates and Hypersensitisation

The objective-prism plates that were used for the quasar searches were taken on the fine-grained, high contrast Kodak emulsion IIIaJ. The IIIaJ plates are 1mm thick and 356mm square. They have an anti-halation backing.

Millikan reported (in the discussion following the paper by Lewis et al (1971)) that the average grain size of IIIaJ is 0.55μm and that most of the grains lie within 15% of that value.

The plates were hypersensitised using the technique that is outlined in the UKST Handbook and given in more detail by Sim (1978). Briefly, the hypersensitisation consists of many days soaking in dry nitrogen followed by a few hours soaking in hydrogen. The soaking

occurs at 20°C and at atmospheric pressure. Plates might be kept in a nitrogen atmosphere in cold storage for a few days before use.

Hypersensitisation reduces the exposure time for IIIaJ by a factor ~ 20. Some evidence is given in Chapter 5 that hypersensitisation also changes the shape of the curve for the variation of the contrast, γ, with wavelength.

The useful wavelength range of IIIaJ extends from the atmospheric cut-off at ~ 3200Å to the sharp emulsion cut-off at ~ 5400Å. Data from calibration spectrograms for the spectral responses of several IIIaJ emulsion batches are given in Chapter 5.

2.3 The Searches For Quasars

The fields SGP (for south galactic pole) on plate number UJ3682P and 345 on plate number UJ2461P were searched for quasars by the author and Dr Ann Savage. The SGP plate contains the south galactic pole but it is actually centred on (1950) $00^h\ 53^m$ -28° 03', which is about 1° from the pole. The 345 plate is centred on (1950) $22^h\ 32^m$ -40° 00', which is about 31° from the pole. Details of the plates are listed in Table 2.3.1. Notice that the SGP plate was taken through the achromat while the 345 plate was taken through the earlier corrector. For this reason and also because no calibration spectrogram was available for the emulsion batch of the 345 plate the SGP plate only was used for the work on the objective-prism spectrophotometry of quasars that is described in Chapters 3 and 4. The number of quasars found in field 345 cannot be compared easily with the number found in the SGP field because the image spread of the earlier corrector is generally greater than that of the achromat and it varies with wavelength. See Chapter 6 on the selection effects in quasar searches for the influence of the seeing disc (which includes the image spread from the optics) on the quasar samples.

The two fields were chosen from existing objective-prism plates because they were at high galactic latitudes and because they were also being used for other, possibly complementary purposes by several astronomers in Edinburgh. There is now a new prism plate of field 345, taken through the achromat and in good seeing, so a new search would be worthwhile.

Plate Number	UJ3682P	UJ2461P
Field	SGP	345
Field Centre (1950)	$00^h\ 53^m$ -28° 03'	$22^h\ 32^m$ -40° 00'
IIIaJ Batch Number	2C7	1I5
Spectrogram?	Yes	No
Hypersensitisation	27N + 6H +4*	50N + 7¾ H*
Exposure Time	70m	60m
Date	17/18 October 1977	21/22 July 1976
Angular Distance Of Field Centre From SGP	1°	31°
Dispersion Direction	North-South	North-South
Trailed?	No	No
Corrector	Achromat	Singlet Corrector
Seeing	2"	~3"

TABLE 2.3.1 Details of the plates used in the quasar searches

*Symbols defined in Chapter 5

Both searchers simultaneously searched each plate using the "Zeiss" (the modified Zeiss blink comparator) at the Royal Observatory, Edinburgh in an attempt to achieve good completeness in a short time (~ one month per plate).

The Zeiss uses TV cameras to view two Schmidt plates, which for this work, were the objective-prism plate and the corresponding direct plate. A high-contrast camera was used for the prism plates. There is a control console that may be used to drive to a particular area, to scan, and to relatively rotate and shift the two plates until they are aligned. The images of the two plates may be switched, mixed, or displayed side by side; these facilities are ideal for distinguishing quasar spectra from overlapped spectra. A third camera may be used to display a digital readout of the X-Y position coordinates and a graticule. The stepping unit of the Zeiss is 12.5μm.

The Zeiss has a facility that permits a tracing of a prism spectrum, in the form of a line from the television raster, to be displayed on an oscilloscope. This facility was not available when the plates were searched so that selection was based entirely on visual examination of the prism spectra.

A disadvantage of using the Zeiss for quasar searches is that when the contrast of the television is optimised for the quasars at $B \sim 19$ the relatively few quasars at $B \lesssim 17$ might be missed because their prism spectra will appear totally black. Of course bright quasars may be seen if they have strong ultraviolet continua or if their emission lines cause a perceptible widening of the spectra.

The detection of quasars using objective-prism plates generally depends on the appearance of highly-redshifted Ly-α + NV λλ1216, 1240 and CIV λ1549 in the wavelength range, for emulsion IIIaJ, from ~ 3200Å to ~ 5400Å, although quasars are occasionally detected by MgII λ2798 and CIII] λ1909. A few low redshift ($z \lesssim 1$) quasars may be detected by their ultraviolet continua alone.

When searching for quasars on IIIaJ objective-prism plates there could be some confusion caused by late M stars, including Mira variables at minimum light (see, for example, Savage (1978) and Tapia and Catchpole (1980)), and Wolf-Rayet stars. The Wolf-Rayet stars are more concentrated in the galactic plane than the M stars and are consequently not likely to be seen at the typical magnitudes of the quasars at high galactic latitudes. The absorption bands in late M

stars cause the surviving continua to resemble Ly-α and CIV or CIV and CIII]. Such stars may be distinguished because the "emission line" at longer wavelengths appears to be the stronger, and this is not generally so in quasars. The Wolf-Rayet stars have real emission lines that are broad but still narrower than the permitted lines of typical quasars in their rest frames. Because of this and also the zero redshift, the emission lines of Wolf-Rayet stars appear circular on prism plates and so they may be distinguished from quasar lines, which are, in general, extended in the direction of dispersion.

A method for quantifying the wavelength-dependent selection effects for detection by emission lines is given in Chapter 6. It requires (for example) knowledge of the wavelength dependences of the emulsion IIIaJ and these are not yet known adequately. However, a simplified form of the quantification neglects the wavelength dependences, considers typical objective-prism quasars to have Ly-α + NV at a redshift of 2.2, and apparently works well (see Chapter 6).

For both plates, UJ3682P and UJ2461P, the 25 square degree search areas were central squares. The outside (vignetted) regions were searched for very obvious, strong-lined quasars only. Tables 2.3.2 and 2.3.3 give the (1950) right ascensions and declinations and the approximate X-Y positions for the "probable" quasars that were found on UJ3682P and UJ2461P respectively. The X-Y positions on the plates are in millimetres and are with respect to the field centres with X increasing to the west and Y increasing to the north.

The work described in Chapter 4 and, in particular, the results in Table 4.6.1 demonstrate that in approximately the central 19 square degrees of UJ3682P ~ 75% of the probable quasars have emission lines with signal-to-noise ratios greater than two. Because of the processing of the density spectra (explained in Chapter 4) the proportion of unprocessed spectra with signal-to-noise ratios greater than two will be greater than 75%. Consequently, if a ratio greater than two denotes a certain quasar then the expected minimum success rate for the probable quasars of Tables 2.3.2 and 2.3.3 is ~ 75%.

161 of the 210 probable quasars listed in Table 2.3.2 and 87 of the 107 in Table 2.3.3 are within their respective central squares of 25 square degrees.

The right ascensions and declinations of the quasars were calculated from the X-Y positions of the quasars and the X-Y positions and the known right ascensions and declinations of neighbouring SAO stars, using a program that was supplied by John Barrow. All X-Y positions were measured on direct plates using the Zeiss with the graticule mixed with the plate display. A comparison of the calculated positions with AAT positions of some of the quasars showed that the typical discrepancies were within 3 arcsecs but that they could be ~ 10 arcsecs when the quasars were in regions of few SAO stars. Most of the AAT positions were obtained from the (unpublished) observations by Cannon, Smith and Boksenberg that followed Cannon's earlier, quick (unpublished) searches of the fields.

TABLE 2.3.2 SGP PROBABLE QUASARS

RA 1950			DEC			X MM	Y
00	40	33.1	-28	22	14	170.4	-19.7
00	40	41.3	-29	17	24	167.4	-69.0
00	40	41.6	-29	37	44	166.8	-87.2
00	40	53.8	-25	37	01	170.6	128.1
00	40	58.6	-30	25	41	162.2	-129.9
00	41	06.7	-30	06	22	161.1	-112.6
00	41	07.8	-30	45	30	159.9	-147.6
00	41	16.9	-26	08	27	165.2	100.1
00	41	19.5	-26	22	45	164.3	87.3
00	41	38.2	-26	58	27	159.7	55.5
00	41	40.7	-28	59	36	156.2	-52.7
00	41	55.4	-30	38	38	150.9	-141.2
00	42	12.9	-30	02	38	148.4	-108.9
00	42	36.0	-30	53	29	142.8	-154.3
00	42	41.8	-29	30	55	143.5	-80.4
00	42	44.2	-27	14	57	146.1	41.1
00	42	48.5	-28	51	59	143.1	-45.6
00	42	52.5	-26	57	15	144.9	57.0

00	43	02.1	-29	37	01	139.4	-85.7
00	43	03.6	-27	28	20	142.0	29.2
00	43	15.3	-30	30	48	135.7	-133.8
00	43	32.6	-28	45	34	134.6	-39.6
00	43	50.0	-30	06	35	129.5	-111.9
00	43	50.2	-30	46	11	128.7	-147.4
00	43	58.0	-28	01	41	130.5	-0.3
00	44	00.7	-27	01	09	131.2	53.8
00	44	07.3	-31	08	54	124.9	-167.6
00	44	07.9	-26	59	15	129.8	55.5
00	44	14.5	-26	28	44	129.1	82.8
00	44	20.9	-28	07	54	125.9	-5.8
00	45	04.8	-30	02	51	115.1	-108.3
00	45	18.0	-26	14	02	116.6	96.2
00	45	20.1	-29	14	48	113.0	-65.3
00	45	25.3	-28	29	24	112.8	-24.7
00	45	40.9	-25	51	28	112.4	116.5
00	45	41.4	-28	50	27	109.3	-43.4
00	45	49.9	-26	04	06	110.4	105.2
00	45	55.2	-28	00	53	107.4	0.9
00	46	01.7	-28	12	39	105.9	-9.6
00	46	13.3	-25	07	54	106.6	155.6
00	46	21.0	-26	16	41	104.0	94.1

00	46	41.5	-28	21	01	98.0	-16.9
00	46	44.9	-29	22	34	96.4	-71.9
00	46	51.9	-26	45	53	97.3	68.1
00	46	51.9	-30	40	17	93.8	-141.3
00	47	00.3	-29	11	06	93.5	-61.6
00	47	03.3	-26	21	25	95.4	90.0
00	47	06.1	-29	22	48	92.2	-72.0
00	47	12.8	-30	56	15	89.6	-155.6
00	47	15.0	-29	21	33	90.5	-70.9
00	47	45.6	-26	33	48	86.8	79.0
00	47	49.7	-27	59	36	84.8	2.4
00	48	02.3	-30	56	32	80.1	-155.7
00	48	16.3	-29	52	37	78.2	-98.4
00	48	21.8	-26	05	39	79.9	104.3
00	48	22.5	-27	59	40	78.4	2.4
00	48	25.0	-30	54	19	75.8	-153.6
00	48	26.4	-27	34	26	77.9	25.0
00	48	28.5	-27	52	04	77.3	9.2
00	48	31.6	-26	45	34	77.4	68.6
00	48	34.9	-25	45	04	77.5	122.7
00	48	35.2	-29	49	46	74.6	-95.8
00	48	35.6	-25	05	09	77.8	158.4
00	48	42.5	-26	08	34	75.7	101.7

00	48	46.9	-28	04	17	73.5	-1.6
00	48	48.5	-26	59	17	73.9	56.4
00	48	48.6	-30	44	46	71.3	-145.0
00	48	50.7	-29	57	41	71.5	-102.9
00	48	51.9	-26	56	26	73.3	59.0
00	48	52.0	-29	07	20	71.8	-57.9
00	48	52.3	-27	09	05	73.1	47.7
00	48	55.1	-29	44	46	70.8	-91.3
00	49	01.4	-28	20	54	70.5	-16.4
00	49	03.1	-30	52	50	68.5	-152.2
00	49	29.4	-27	14	01	65.6	43.4
00	49	29.8	-29	00	43	64.5	-51.9
00	49	30.1	-26	06	48	66.2	103.4
00	49	32.8	-26	53	44	65.2	61.5
00	49	44.5	-27	36	11	62.4	23.6
00	50	05.9	-28	04	27	57.9	-1.6
00	50	10.3	-28	07	11	57.0	-4.0
00	50	13.2	-31	02	09	54.9	-160.3
00	50	18.0	-25	23	08	56.9	142.5
00	50	19.1	-26	40	40	56.0	73.2
00	50	27.9	-26	34	48	54.3	78.5
00	50	35.2	-30	37	43	50.9	-138.4
00	50	37.6	-28	25	30	51.5	-20.3

00	50	49.6	-28	06	30	49.3	-3.3
00	50	55.2	-28	43	14	47.9	-36.1
00	51	02.7	-30	01	57	45.9	-106.4
00	51	10.8	-26	47	39	45.7	67.1
00	51	12.9	-27	15	38	45.1	42.1
00	51	14.4	-27	33	45	44.6	25.9
00	51	17.6	-28	55	10	43.5	-46.7
00	51	21.5	-28	39	57	42.8	-33.1
00	51	25.8	-26	30	00	42.8	82.9
00	51	26.5	-30	51	46	41.0	-150.9
00	51	27.2	-26	49	12	42.4	65.7
00	51	36.2	-30	13	55	39.3	-117.1
00	51	40.1	-28	46	47	39.1	-39.2
00	51	40.6	-26	37	32	39.8	76.2
00	51	43.2	-28	01	20	38.8	1.4
00	51	47.2	-28	11	54	37.9	-8.1
00	51	51.1	-27	24	54	37.4	33.9
00	51	52.6	-26	35	34	37.4	77.9
00	51	54.0	-26	39	50	37.1	74.1
00	52	14.5	-29	24	14	32.2	-72.6
00	52	16.6	-28	32	32	32.0	-26.5
00	52	21.2	-27	34	12	31.4	25.6
00	52	31.6	-26	37	27	29.6	76.3

00	52	39.0	-28	23	45	27.7	-18.6
00	52	57.9	-29	42	06	23.7	-88.5
00	53	06.1	-28	21	14	22.4	-16.3
00	53	20.0	-29	21	53	19.5	-70.5
00	53	20.3	-28	13	50	19.6	-9.7
00	53	38.5	-27	09	14	16.2	48.0
00	54	06.5	-27	33	34	10.6	26.3
00	54	18.1	-30	57	44	8.0	-156.1
00	54	18.7	-26	50	00	8.2	65.2
00	54	22.5	-28	10	27	7.4	-6.7
00	54	27.7	-31	00	59	6.2	-159.0
00	54	33.1	-29	34	04	5.2	-81.3
00	54	55.4	-26	01	52	0.9	108.2
00	55	07.1	-27	54	29	-1.4	7.6
00	55	09.1	-27	06	22	-1.8	50.6
00	55	42.6	-28	50	11	-8.3	-42.1
00	56	03.2	-27	16	17	-12.5	41.7
00	56	21.7	-29	15	35	-15.9	-64.8
00	56	22.6	-29	11	23	-16.1	-61.1
00	56	35.2	-29	05	31	-18.6	-55.8
00	56	43.5	-31	01	55	-19.8	-159.9
00	57	04.7	-27	59	49	-24.6	2.8
00	57	12.2	-29	21	17	-25.7	-69.9

00	57	18.9	-27	54	40	-27.4	7.4
00	57	37.4	-28	20	02	-30.9	-15.3
00	57	38.1	-30	31	10	-30.4	-132.4
00	57	41.3	-29	08	17	-31.5	-58.4
00	57	44.1	-27	08	06	-32.6	48.9
00	57	44.5	-27	58	29	-32.4	3.9
00	57	45.6	-25	29	26	-33.4	137.1
00	57	50.7	-28	51	33	-33.4	-43.4
00	57	51.4	-28	21	02	-33.7	-16.2
00	58	04.6	-29	03	51	-36.0	-54.4
00	58	07.2	-30	38	18	-36.0	-138.8
00	58	15.7	-25	08	29	-39.6	155.8
00	58	28.8	-29	56	23	-40.4	-101.4
00	58	33.1	-28	40	46	-41.7	-33.9
00	58	39.7	-26	55	12	-43.7	60.4
00	58	42.9	-29	24	09	-43.4	-72.6
00	58	43.4	-26	43	27	-44.6	70.9
00	58	57.6	-27	05	41	-47.2	51.0
00	59	01.6	-30	07	55	-46.7	-111.8
00	59	06.8	-30	25	53	-47.5	-127.8
00	59	12.3	-28	48	46	-49.4	-41.1
00	59	14.3	-26	55	09	-50.6	60.4
00	59	15.6	-29	43	52	-49.6	-90.3

00	59	26.1	-29	09	20	-51.9	-59.5
00	59	27.6	-26	25	07	-53.5	87.2
00	59	52.0	-25	18	52	-59.0	146.3
00	59	57.4	-26	57	52	-59.2	57.9
01	00	02.3	-28	04	12	-59.5	-1.4
01	00	02.5	-30	32	00	-58.2	-133.4
01	00	16.2	-29	10	21	-61.6	-60.5
01	00	32.6	-29	09	20	-64.9	-59.6
01	00	33.0	-28	09	45	-65.5	-6.4
01	00	35.2	-27	39	46	-66.3	20.4
01	00	57.9	-28	06	10	-70.5	-3.3
01	01	00.4	-29	17	54	-70.2	-67.3
01	01	02.0	-27	08	49	-71.9	47.9
01	01	03.3	-28	01	31	-71.6	0.9
01	01	03.7	-26	35	31	-72.6	77.7
01	01	08.1	-25	06	35	-74.5	157.2
01	01	14.5	-29	32	04	-72.8	-80.0
01	01	18.3	-29	15	44	-73.7	-65.4
01	01	32.0	-30	25	56	-75.5	-128.2
01	01	40.1	-29	59	58	-77.4	-105.0
01	01	43.0	-30	48	25	-77.4	-148.3
01	02	25.9	-28	18	23	-87.7	-14.4
01	02	39.1	-28	42	29	-89.9	-36.0

01	02	47.6	-25	59	05	-93.9	110.0
01	02	56.7	-26	34	16	-95.2	78.5
01	02	57.6	-29	41	04	-92.7	-88.4
01	03	02.7	-29	05	53	-94.2	-56.9
01	03	03.5	-27	38	38	-95.6	21.0
01	03	05.5	-30	36	36	-93.4	-138.0
01	03	08.0	-27	07	36	-97.0	48.7
01	03	11.8	-29	25	19	-95.7	-74.3
01	03	15.3	-29	27	12	-96.3	-76.0
01	03	26.9	-26	40	23	-101.2	72.9
01	03	34.8	-27	08	44	-102.3	47.6
01	03	51.7	-26	34	29	-106.2	78.1
01	03	51.9	-30	32	36	-102.4	-134.6
01	03	54.6	-29	13	07	-104.2	-63.6
01	03	57.2	-27	49	52	-106.1	10.8
01	03	57.4	-28	38	05	-105.3	-32.3
01	04	01.9	-27	34	14	-107.3	24.7
01	04	12.5	-26	49	00	-110.1	65.1
01	04	13.1	-27	28	59	-109.6	29.3
01	04	15.4	-28	10	00	-109.3	-7.3
01	04	21.3	-27	08	29	-111.5	47.6
01	04	22.7	-26	35	02	-112.4	77.5
01	04	26.5	-27	17	14	-112.4	39.8

01	04	29.6	-24	59	30	-115.4	162.9
01	04	39.7	-26	59	59	-115.4	55.2
01	04	43.1	-28	30	38	-114.4	-25.8
01	04	50.1	-29	11	20	-115.1	-62.2
01	04	55.6	-29	35	18	-115.7	-83.6
01	05	29.1	-26	50	01	-125.4	63.9
01	05	46.7	-26	23	53	-129.4	87.1
01	06	37.2	-27	21	12	-138.3	35.7

TABLE 2.3.3 345 PROBABLE QUASARS

RA 1950			DEC			X MM	Y
22	17	08.1	-40	16	22	152.0	-17.8
22	17	14.4	-40	39	04	150.1	-38.0
22	17	43.1	-38	30	34	149.8	76.9
22	18	04.3	-41	58	17	138.8	-108.4
22	18	09.7	-42	22	02	137.1	-129.6
22	18	10.1	-37	09	53	147.8	149.3
22	19	19.5	-39	44	58	130.5	11.1
22	22	25.4	-41	14	00	96.5	-67.4
22	22	30.6	-39	45	52	97.7	11.3
22	22	44.3	-39	39	50	95.5	16.8
22	23	16.3	-40	20	10	89.1	-19.1
22	24	13.1	-40	52	09	78.8	-47.4
22	24	14.1	-41	18	34	78.1	-71.0
22	24	32.5	-40	49	03	75.6	-44.6
22	24	55.6	-40	20	52	72.2	-19.3
22	25	03.9	-39	34	33	71.6	22.0
22	25	24.6	-40	08	12	67.5	-7.9
22	25	28.1	-41	27	24	65.6	-78.6

22	25	30.6	-40	25	16	66.1	-23.2
22	25	33.3	-38	20	42	67.7	88.1
22	25	45.8	-38	31	46	65.3	78.2
22	26	05.9	-42	09	22	58.6	-116.0
22	26	12.1	-40	18	06	59.2	-16.6
22	26	23.3	-41	12	35	56.5	-65.3
22	26	43.3	-40	09	27	54.0	-8.8
22	27	19.3	-37	49	21	49.5	116.4
22	27	37.3	-39	37	41	45.1	19.6
22	27	44.8	-39	58	14	43.6	1.3
22	28	24.8	-40	18	13	36.6	-16.4
22	28	29.9	-39	39	19	36.0	18.3
22	28	39.9	-39	54	18	34.2	4.9
22	28	44.7	-41	20	10	32.7	-71.7
22	29	00.1	-39	42	10	30.9	15.8
22	29	00.7	-40	04	53	30.6	-4.5
22	29	06.9	-39	26	59	29.8	29.4
22	29	09.4	-42	05	37	28.2	-112.3
22	29	16.8	-42	25	24	26.9	-130.0
22	29	24.4	-40	12	12	26.5	-11.0
22	29	50.6	-39	21	04	22.3	34.7
22	30	00.1	-39	01	49	20.8	51.9
22	30	02.1	-41	00	51	19.8	-54.4

22	30	27.4	-38	58	45	16.1	54.6
22	30	27.4	-41	05	25	15.6	-58.4
22	30	27.4	-40	10	34	15.8	-9.5
22	31	09.6	-41	18	14	8.4	-69.9
22	31	27.9	-41	24	26	5.4	-75.4
22	31	34.8	-42	03	51	4.1	-110.6
22	31	47.9	-41	54	52	2.0	-102.6
22	31	50.4	-39	57	27	1.6	2.3
22	32	00.9	-39	58	16	-0.2	1.5
22	32	03.6	-40	06	47	-0.6	-6.1
22	32	08.4	-42	27	10	-1.4	-131.4
22	32	29.9	-39	03	51	-5.2	50.1
22	32	34.8	-38	36	08	-6.1	74.9
22	32	43.8	-40	10	02	-7.5	-9.0
22	33	21.9	-38	33	58	-14.3	76.8
22	33	37.1	-38	56	59	-16.9	56.2
22	33	48.7	-39	57	46	-18.6	1.9
22	34	53.1	-43	06	34	-28.3	-166.8
22	35	15.4	-39	46	25	-33.6	12.0
22	35	46.3	-41	09	00	-38.1	-61.8
22	35	52.8	-42	30	38	-38.4	-134.8
22	36	32.6	-42	05	21	-45.2	-112.2
22	37	03.8	-38	08	46	-53.4	99.0

22	37	36.9	-39	18	14	-58.2	36.8
22	37	49.7	-40	49	12	-59.1	-44.4
22	38	01.6	-42	59	53	-59.1	-161.2
22	38	04.8	-36	57	47	-65.2	162.3
22	38	23.7	-41	23	36	-64.3	-75.2
22	38	41.1	-42	18	59	-66.3	-124.8
22	38	54.3	-41	15	04	-69.6	-67.7
22	39	04.3	-41	43	50	-70.7	-93.4
22	39	14.8	-39	17	42	-75.2	37.0
22	39	24.3	-42	46	42	-72.9	-149.7
22	39	24.5	-38	16	58	-77.9	91.2
22	39	29.3	-42	31	06	-74.0	-135.8
22	39	46.4	-39	44	36	-80.1	12.9
22	40	00.4	-41	57	28	-79.8	-105.8
22	40	33.0	-42	00	16	-85.2	-108.5
22	40	37.1	-39	20	21	-89.3	34.3
22	40	37.8	-39	08	57	-89.7	44.5
22	40	42.0	-39	24	06	-90.1	31.0
22	40	48.8	-41	54	34	-87.9	-103.4
22	40	51.9	-42	35	14	-87.6	-139.8
22	40	55.4	-37	02	50	-95.6	157.2
22	40	57.8	-42	21	48	-88.8	-127.8
22	41	14.9	-37	46	45	-98.0	117.8

22	41	20.4	-41	25	13	-93.9	-77.3
22	41	20.8	-42	08	44	-92.9	-116.2
22	41	27.2	-42	33	15	-93.4	-138.2
22	41	29.1	-42	25	35	-93.9	-131.3
22	42	28.6	-41	58	04	-104.5	-107.0
22	42	35.4	-39	58	28	-108.8	-0.2
22	42	40.9	-41	02	48	-107.9	-57.7
22	42	48.2	-41	15	30	-108.8	-69.1
22	43	10.4	-40	48	55	-113.3	-45.5
22	43	53.8	-38	42	32	-124.4	67.1
22	44	13.8	-37	13	37	-130.6	146.5
22	44	19.3	-40	52	49	-124.9	-49.3
22	44	31.8	-41	56	41	-125.0	-106.5
22	44	33.6	-41	21	10	-126.4	-74.8
22	44	41.1	-41	13	07	-127.9	-67.6
22	44	51.6	-42	17	03	-127.6	-124.8
22	45	12.1	-37	59	28	-139.5	105.2
22	46	56.6	-38	55	56	-155.8	54.0
22	47	05.6	-42	43	50	-148.8	-149.7
22	47	56.1	-39	40	28	-164.4	13.8

3. Theoretical Aspects of the Prism Spectra

This chapter discusses the theory of extracting the intrinsic spectrum of an object after its processing by the atmosphere, the telescope, and the photographic plate.

3.1 The light at the photographic plate

Suppose that the spectrum of a quasar is $I_*(\lambda)$ at the top of the atmosphere. This spectrum is modified by the transmission $A(\lambda)$ of the atmosphere, by the transmission $T(\lambda)$ of the glass of the telescope, and by the seeing disc and the image spread due to the optics. The objective prism disperses the light from the quasar into a small spectrum of maximum length ~ 1mm on the plate when the low-dispersion prism is used. The prism changes the variable from wavelength λ to a distance on the plate, x, with respect to a reference point such as that corresponding to the emulsion cut-off. Then,

$$A(\lambda),\ T(\lambda) \rightarrow A(x),\ T(x) \qquad [3.1.1]$$

and

$$\text{"}E(\lambda)\ \frac{d\lambda}{dx} = E(x)\text{"} \qquad [3.1.2]$$

where $\frac{d\lambda}{dx}$ is the reciprocal dispersion.

The light that is finally recorded by the photographic plate is the convolution of $A(x')\ I_*(x')$ with the seeing disc, followed by transmission through the telescope:

$$E_*(x) = T(x) \int A(x')\ I_*(x')\ \psi\ (x-x')\ dx' \qquad [3.1.3]$$

Equation 3.1.3 assumes that the seeing disc convolution occurs after the light has been transmitted through most of the atmosphere. ψ expresses the form of the seeing disc and it may also be taken to include the image spread of the optics, provided that the variation of this spread with λ or x is negligible. The variation for the achromatic doublet corrector is indeed negligible, but if this were not so the convolutions would need to be two-dimensional.

So at a point x the photographic plate responds to the monochromatic exposure $E_*(x)$ and the broadband sky exposure, and it

introduces noise of its own.

Suppose that these combined exposures produce a density $D_*'(x')$ at x'. If this density spectrum is scanned by a densitometer that responds to light intensity then the density it attributes to the point x is

$$D_*(x) = -\log \int 10^{-D_*'(x')} \phi(x-x')dx' \qquad [3.1.4]$$

where ϕ describes the scanning aperture and the intensity profile of the light source. The densitometer may, of course, superimpose more noise.

In what follows $D_*(x)$ is the measured quantity and is used without deconvolution as an approximation to $D_*'(x)$ to obtain $E_*(x)$. This $E_*(x)$ is used without deconvolution as an approximation to $A(x)\,T(x)\,I_*(x)$ to obtain $I_*(\lambda)$. These approximations are equivalent to regarding ψ in 3.1.3 and ϕ in 3.1.4 as delta functions.

3.2 Extraction of $E_*(x)$ from $D_*(x)$: the Van Kreveld law

At a point x of the density spectrum the density that results from the combined monochromatic object and broadband sky exposures is $D_*(x)$. The sky radiation alone ideally produces a locally uniform density D_B. $D_*(x)$ and D_B are densities above fog, and they are the observables from which the spectrum $E_*(x)$ must be obtained.

The problem of separating the monochromatic exposure $E_*(x)$ may be solved by using the Van Kreveld law for the simultaneous application of radiation of different wavelengths.

In its general form the Van Kreveld law states that if exposures E_1 centred on a small wavelength band at λ_1, E_2 at λ_2 ... E_n at λ_n separately produce density D then the mixture

$$\alpha_1 E_1(\lambda_1) + \alpha_2 E_2(\lambda_2) + \ldots + \alpha_n E_n(\lambda_n) \qquad [3.2.1]$$

will also produce the same density D provided only that

$$\alpha_1 + \alpha_2 + \ldots + \alpha_n = 1 \qquad [3.2.2]$$

Van Kreveld (1934) and Webb (1936) have given restricted forms of the law and Altman (1977) has given the generalised law.

Suppose that a mixture of radiation has exposure $E(\lambda)$ at wavelength λ and that this mixture produces density D. That is,

$$\Sigma\ E(\lambda) \rightarrow D \qquad [3.2.3]$$

Imagine that the exposure at λ is increased by a factor $\beta(\lambda)$ so that it individually produces density D. Then by Van Kreveld's law any mixed exposure of the form

$$\Sigma\ \alpha(\lambda)\ \beta(\lambda)\ E(\lambda) \rightarrow D \text{ if } \Sigma\ \alpha(\lambda) = 1 \qquad [3.2.4]$$

Comparison of 3.2.4 with 3.2.3 requires that

$$\alpha(\lambda)\ \beta(\lambda) = 1 \qquad [3.2.5]$$

The monochromatic speeds are defined by

$$S_D(\lambda) = \frac{1}{\beta(\lambda)\ E(\lambda)} \qquad [3.2.6]$$

while the mixture speed is

$$S_D(\text{mixture}) = \frac{1}{\Sigma\ \alpha(\lambda)\ \beta(\lambda)\ E(\lambda)} = \frac{1}{\Sigma\ E(\lambda)} \qquad [3.2.7]$$

Van Kreveld's law has $\Sigma\ \alpha(\lambda) = 1$ so,

$$S_D(\text{mixture}) = \frac{\Sigma\ \alpha(\lambda)}{\Sigma\ E(\lambda)} = \frac{\Sigma\ {}^{1}/_{\beta(\lambda)}}{\Sigma\ E(\lambda)} = \frac{\Sigma\ E(\lambda)\ S_D(\lambda)}{\Sigma\ E(\lambda)} \qquad [3.2.8]$$

Finally, writing the fractional exposure at λ as $f(\lambda) = {}^{E(\lambda)}/_{\Sigma\ E(\lambda)}$ the equation 3.2.8 becomes

$$S_D(\text{mixture}) = \Sigma\ f(\lambda)\ S_D(\lambda) \qquad [3.2.9]$$

Equation 3.2.9 is a useful expression of the Van Kreveld law and it permits the extraction of $E_*(x)$ from the densities $D_*(x)$ and D_B:

At a point x along the density spectrum that corresponds to the wavelength λ the total exposure from sky and object is

$$E_{tot}(x) = E_B + E_*(x) = \sum_r f_B(\lambda_r)\, E_B + E_*(x) \qquad [3.2.10]$$

where E_B is the total sky exposure and $f_B(\lambda_r)$ is the fraction of it that occurs in the small band centred at λ_r.

The sky exposure at λ_r is the fraction

$$\frac{f_B(\lambda_r)\, E_B}{E_{tot}(x)} = \frac{f_B(\lambda_r)\, E_B}{E_B + E_*(x)} \qquad [3.2.11]$$

of the total exposure at x. Similarly the object exposure at x is the fraction

$$\frac{E_*(x)}{E_{tot}(x)} = \frac{E_*(x)}{E_B + E_*(x)} \qquad [3.2.12]$$

of the total exposure at x.

The Van Kreveld equation 3.2.9 with 3.2.11 and 3.2.12 then gives

$$\frac{1}{E_{tot}(x)} = \frac{E_*(x)}{E_B + E_*(x)} \cdot S_{D_*}(x) + \sum_r \frac{f_B(\lambda_r) E_B}{E_B + E_*(x)} \cdot S_{D_*}(\lambda_r) \qquad [3.2.13]$$

That is,

$$1 = E_*(x)\, S_{D_*}(x) + E_B \sum_r f_B(\lambda_r)\, S_{D_*}(\lambda_r) \qquad [3.2.14]$$

Since the sky alone produces a density D_B, 3.2.9 gives

$$\frac{1}{E_B} = \sum_r f_B(\lambda_r)\, S_{D_B}(\lambda_r) \qquad [3.2.15]$$

Substituting for E_B in 3.2.14 leads to the expression for $E_*(x)$,

$$E_*(x) = \left\{ 1 - \frac{\sum_r f_B(\lambda_r)\, S_{D_*}(\lambda_r)}{\sum_r f_B(\lambda_r)\, S_{D_B}(\lambda_r)} \right\} \cdot \frac{1}{S_{D_*}(x)} \qquad [3.2.16]$$

If the equation of the linear characteristic of the emulsion is written as

$$"D(\lambda) = \gamma(\lambda) \log g(\lambda) E(\lambda)" \qquad [3.2.17]$$

then the speed is

$$"S_D(\lambda) = \frac{1}{E_D(\lambda)} = g(\lambda)\ 10^{-D/\gamma(\lambda)}" \qquad [3.2.18]$$

and 3.2.18 consequently becomes

$$E_*(x) = \left\{ 1 - \frac{\sum_r f_B(\lambda_r)\ g(\lambda_r)\ 10^{-D_*(x)/\gamma(\lambda_r)}}{\sum_r f_B(\lambda_r)\ g(\lambda_r)\ 10^{-D_B/\gamma(\lambda_r)}} \right\} \cdot \frac{10^{D_*(x)/\gamma(x)}}{g(x)} \qquad [3.2.19]$$

Equation 3.2.19 is the relation for the extraction of $E_*(x)$ from the densities $D_*(x)$ and D_B, but it has the disadvantage of being unwieldy. An approximation follows from writing

$$10^{(D_B - D_*(x))/\gamma_s} = \frac{\sum_r f_B(\lambda_r)\ g(\lambda_r)\ 10^{-D_*(x)/\gamma(\lambda_r)}}{\sum_r f_B(\lambda_r)\ g(\lambda_r)\ 10^{-D_B/\gamma(\lambda_r)}} \qquad [3.2.20]$$

or

$$10^{(D_B - D_*(x))/\gamma_s} = \frac{\sum_r \{f_B(\lambda_r)\ g(\lambda_r)\ 10^{-D_B/\gamma(\lambda_r)}\}}{\sum_r \{f_B(\lambda_r)\ g(\lambda_r)\ 10^{-D_B/\gamma(\lambda_r)}\}}\ 10^{\frac{D_B - D_*(x)}{\gamma(\lambda_r)}} \qquad [3.2.21]$$

and taking γ_s to be a constant rather than a function of $D_*(x)$. Experiments with plausible numbers indicate that the errors introduced into $E_*(x)$ by the use of a constant γ_s are less than 2%. With this approximation 3.2.19 becomes

$$E_{*}(x) = \{1 - 10^{(D_B - D_{*}(x))/\gamma_s}\} \quad \frac{10^{D_{*}(x)/\gamma(x)}}{g(x)} \qquad [3.2.22]$$

This is the equation to use in the reduction of the prism spectra. It is essential, of course, that the spectra have not saturated the emulsion and that the sky density D_B and the sky and object density $D_{*}(x)$ are on the linear section of the characteristic curve. In the approximation mentioned in section 3.1 $E_{*}(x)$ can be corrected for the transmission of the telescope and the atmosphere and subsequently used to obtain $I_{*}(\lambda)$, the intrinsic spectrum.

3.3 $\gamma(\lambda)$ and $g(\lambda)$

The relation between density above fog and exposure has been given in 3.2.17 as

$$D(\lambda) = \gamma(\lambda) \log g(\lambda) E(\lambda)$$

$$= \gamma(\lambda) \log E(\lambda) - \gamma(\lambda) \log {}^{1}/_{g(\lambda)} \qquad [3.1.1]$$

on the linear characteristic, where $\gamma(\lambda)$ is the gamma or contrast and $\log {}^{1}/_{g(\lambda)}$ is the intercept on the log E axis. The exposure ${}^{1}/_{g(\lambda)}$ is sometimes referred to as the inertia. Fig 3.3.1 shows that $g(\lambda)$ may be regarded as a sensitivity or grain response function. For light at two wavelengths λ_1 and λ_2 suppose that $\gamma(\lambda_1)$ and $\gamma(\lambda_2)$ are identical. The greater response for λ_1 is indicated by the values of the sensitivity function $g(\lambda)$ at points A and B: $g(\lambda_1) > g(\lambda_2)$.

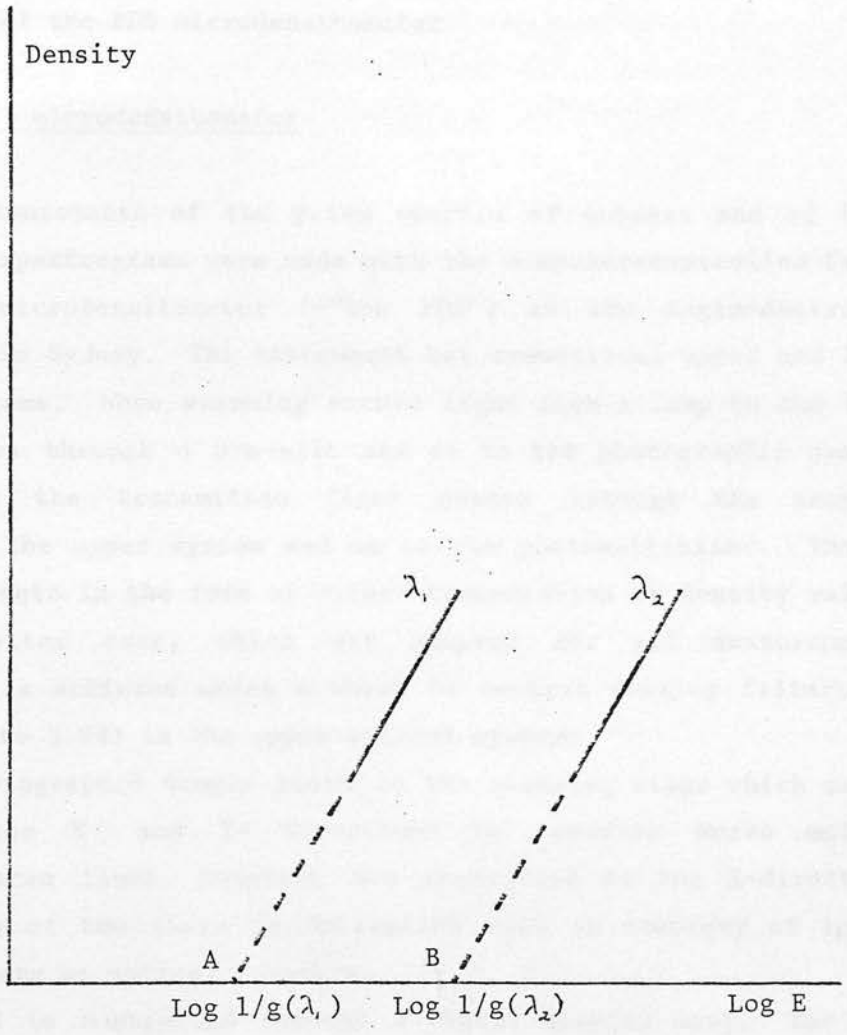

Fig.3.3.1 The use of g(λ) as a sensitivity function

4. Measurements with the PDS microdensitometer and presentation of results

This chapter is concerned with the measurements of the prism spectra of quasars in the SGP field, the subsequent data reduction and the presentation of results. The F_λ spectra from the prism are compared with IPCS observations. The chapter begins with a description of the PDS microdensitometer.

4.1 The PDS microdensitometer

The measurements of the prism spectra of quasars and of UKSTU calibration spectrograms were made with the computer-controlled Perkin Elmer PDS microdensitometer (-"the PDS") at the Anglo-Australian Observatory in Sydney. The instrument has symmetrical upper and lower optical systems. When scanning occurs light from a lamp in the lower system passes through a pre-slit and on to the photographic sample. Subsequently the transmitted light passes through the scanning aperture in the upper system and on to the photomultiplier. The PDS will output data in the form of either transmission or density values; for the latter case, which was adopted for all measurements, calibration is achieved using a wheel of neutral density filters (in the range 0 to 3.93) in the upper optical system.

The photographic sample rests on the scanning stage which may be moved in the X- and Y- directions by separate servo motors. Individual scan lines, however, are restricted to the X-direction. The position of the stage is determined with an accuracy of 1μm in each coordinate by optical encoders.

The PDS is controlled through a visual display unit. The scan pattern is entered in terms of the type of scan (edge or raster), the starting point, the scanning speed, the length, number and separation of scan lines, and the spacing of data samples. Data are recorded on magnetic tape. For all measurements the preslit and scanning aperture were squares with projected sides of 30μm and 20μm respectively.

Before use the photomultiplier needs a considerable period to become stable: five hours are reasonable and twenty-four are not excessive.

At AAO the PDS is kept in an air-conditioned room within the computer room so that a constant temperature may be maintained. Typical changes in the position readout of a stationary stage were found to be only ~ 1μm per five hours.

4.2 Scanning the quasars; the wavelength reference point

The PDS was used to scan ~ 130 quasar candidates in the UKSTU field SGP, which is centred at 00^h53^m - 28°03'. The area of the SGP prism plate UJ3682P that encloses these quasars extends from the plate centre to 2°.09 north, 2°.07 south, 2°.20 east, and 2°.33 west. The enclosed area is approximately 18.8 square degrees and goes from -25°57' to -30°07' in declination and, at the declination of the plate centre, from $00^h42^m12^s$ to $01^h03^m12^s$ in right ascension (1950 coordinates).

At the maximum angular distance of 3°.13 from the plate centre the vignetting is estimated at less than $0^m.1$ (UKST Handbook) and can safely be neglected.

The conversion of the prism spectra to conventional intensity spectra requires (i) a sky subtraction technique, (ii) knowledge of the emulsion characteristics, and (iii) knowledge of the dispersion curve and a point on each spectrum that can be identified with a definite wavelength. Items (i) and (ii) are the particular concerns of chapter 3 and 5 while (iii) will be discussed now.

The dispersion curve for the low-dispersion objective prism is given by Nandy et al (1977) and it has been expressed in functional form by Cooke (1980). The only object-independent point in a prism spectrum that can be identified with a wavelength is the sharp cut-off - "the green head" - of Kodak IIIaJ emulsion. The sharpness of this cut-off is ~ 200Å: that is, the functional $g(\lambda)$ declines over this range. In fitting the dispersion curve the cut-off wavelength was taken as 5380Å (Nandy et al (1977)).

The green heads of the prism spectra of quasars are not necessarily easy to identify: if a quasar has, for example, a strong emission line at ~ 5000Å but a weak continuum, then the green head might be misidentified as the long wavelength edge of the emission line. In the scanning of the quasars the green head or wavelength

reference point for each object was found in the following way. Twenty-five faint, late-type stars were selected and the positions of their images and the quasars' images were measured on a direct plate of the field. The stars were evenly distributed in the 18.8 square degrees. Immediately before scanning, with the prism plate on the PDS, the green heads of the stars were measured. Because these faint stars had prism spectra that increased in density with increasing wavelength and that had widths determined by the seeing rather than by the scattering of light in the emulsion, the green heads could be measured without difficulty. The relation between the positions of the direct images of the stars and their green heads resulted in a transformation which was used to calculate the green heads of the quasars from the positions of their direct images. Scanning was caused to commence at a fixed distance from the green head of each quasar. The program to compute the transformation and modifications of the PDS operating software were written by the AAO software group.

The prism was mounted on the telescope so that objects in the centre of the field had minimum deviation; elsewhere the deviations in the dispersion direction were found to depend quadratically on both coordinates. Consequently the following transformation equations were used to relate the coordinates of a fixed wavelength point X_p, Y_p (the green head) on the prism plate to the coordinates X, Y of the direct image

$$X_p = a + bX + cY + dX^2 + eXY + fY^2$$

$$Y_p = g + hX + iY \qquad [4.2.1]$$

where X is the direction of dispersion. Strictly, the term eXY is superfluous but it was retained to generalise the quadratic. The r.m.s. errors between the predicted and measured green heads of the 25 stars were 5.3μm and 2.5μm in X and Y respectively.

Incidentally, a further advantage of the transformation procedure is that if repeated scans are required later then the green heads of only 25 stars rather than 130 quasars need to be re-measured.

Each quasar was scanned with a square aperture of side 20μm in a scan pattern of 20 lines along the direction of dispersion. Each line

had a length of 1023μm and the separation between lines was 5μm. Data were sampled at 1μm intervals along each line so that each line had 1024 data channels and was consequently compatible with the powerful set of data reduction programs, the Scanner Data Reduction System (SDRSYS), at AAO. Channel number increased with increasing wavelength. The scan speed along each line was ~ $1mms^{-1}$ and a scan pattern took ~ 30s to complete. With a spectrum width ~ 30μm the scan pattern included substantial areas of sky background at the sides. The scan pattern was displaced relative to the quasar spectrum so that the cut-off at 5380Å was assigned to channel number 1001. Using Cooke's prototype formula for the dispersion curve the relation between the channel number of the density data (channel number is equivalent to distance in μm along the spectrum) and the wavelength in Å is

$$X = 1834 - \frac{3188357}{\lambda - 1552.38} \qquad [4.2.2]$$

(Cooke (1980) gives a slightly improved fit to the dispersion curve).

The importance of the machine noise relative to the plate noise with the 20μm aperture was determined by scanning each of the northern and eastern wedges on the plate UJ3682P twice along the same lines. The duplication of features in the repeated scans over a density range from 0 to 4 with respect to fog indicated that the machine noise was negligible compared with the plate noise.

4.3 Processing the density data

The reduction of the density data requires the relation 3.2.22, which is,

$$E_*(x) = \{1 - 10^{(D_B - D_*(x))/\gamma_s}\} \; \frac{10^{D_*(x)/\gamma(x)}}{g(x)} \qquad [4.3.1]$$

where γ_s is defined by equation 3.2.21. D_B is the local background density with respect to chemical fog and $D_*(x)$ is the density with respect to fog that corresponds to the simultaneous sky and object

exposures at x. The term $D_B - D_*(x)$ must be determined using the local background density: the use of a mean D_B will lead to serious errors, particularly for the fainter objects.

The term in brackets uses a wavelength - averaged γ with weighting according to $g(\lambda)$ and the distribution with wavelength of the sky radiation. This constant γ_s implies that the sky radiation may be represented by an effective wavelength. The wavelength dependences occur in the important multiplicative term.

Apart from three quasars that had problems with overlapped spectra the data reduction was automatic and proceeded in the following way. First of all the PDS density data were converted to the SDRSYS format using a program that was written by John Straede of the AAO software group. The zero point of density (ZP) was a central point of the sky background of UJ3682P. Because the errors in the calculated scanning positions were small the scan patterns were symmetrical and the "object + sky" density-with-respect-to-ZP as a function of x for each quasar was consequently taken as the unsmoothed average of the central two scan lines. The local sky background (LSB) density-with-respect-to-ZP was taken to be the smoothed average of the outermost two scan lines, and the smoothing was a 50-channel running average. For use in equation 4.3.1, $(D_*(x)-D_B)$ was obtained as "object + sky" minus LSB; consideration of the bracketed term in 4.3.1 shows that if D_B is taken as the mean background density then there will be serious errors for $D_*(x) \sim D_B$ - the local sky background must be used. $D_*(x)$ with respect to chemical fog was obtained by adding the density of ZP with respect to chemical fog, taken as the mean sky background, to the local $D_*(x)-D_B$. Notice that by this procedure chemical fog was simply subtracted. The sky background on UJ3682P varied by ~ 0.1 in PDS density over the whole plate so that the inclusion of the mean background into $D_*(x)$ will have introduced only small errors into $E_*(x)$.

Equation 3.2.21 was used to calculate $\gamma_s = 3.84$ for data in the wavelength range 3950 to 5300Å inclusive. Chapter 5 will describe in detail how $\gamma(\lambda)$ and $g(\lambda)$ were obtained. Briefly, the UK Schmidt Telescope Unit supplied a hypersensitised calibration spectrogram of the IIIaJ emulsion batch 2C7, which corresponds to UJ3682P, and it was

scanned by the PDS under the same operating conditions. $\gamma(\lambda)$ and $g(\lambda)$ could be determined only at those wavelengths for which the densities had reached the linear characteristic - that is, from 3950Å to 5300Å and possibly at 5450Å. Relative values of $g(\lambda)$, again from 3950Å to 5300Å, were found from $\gamma(\lambda)$ and the intersection of the linear characteristic with the log (relative exposure) axis after assuming firstly that the light source of the spectrograph was a blackbody radiator at 3100K and secondly that the transmission of the spectrograph was constant with wavelength. The distribution of the sky radiation with wavelength, SKY(λ), was also needed for the calculation of γ_s. Relative SKY(λ) was obtained as a by-product of a ten-hour integration in dark time by Elliott and Malin, using the IPCS on the AAT. The spectrum was very noisy and so the values of relative SKY(λ) in Table 4.3.1 should not be taken too seriously.

A sequence of SDRSYS programs was used to generate $E_*(x)$ from $D_*(x)$, D_B, $\gamma(x)$, γ_s, and $g(x)$. For this data reduction the slightly dubious values of $\gamma(\lambda)$ and $g(\lambda)$ at 5450Å were used. Below 3950Å, in the absence of any real data, $\gamma(\lambda)$ and $g(\lambda)$ retained their respective values at 3950Å; these constructed functions (Table 4.3.1) were found to give good agreement with IPCS data but were not unique: in the small usable magnitude range many other compatible pairs of functions could have been constructed. For future work two spectrograms of each emulsion batch should be made: one should be exposed normally to give $\gamma(\lambda)$ and $g(\lambda)$ for $\lambda \gtrsim 3950$Å and the other should be overexposed for $\lambda \gtrsim 3950$Å to give $\gamma(\lambda)$ and $g(\lambda)$ for $\lambda \lesssim 3950$Å.

Each spectrum $E_*(x)$ was corrected for the transmission of the telescope and the prism. Manufacturers data for the transmission of the achromatic doublet corrector (use for plates of number greater than 3148) and the prism are given in Table 4.3.2. The prism and the earlier corrector are made of the same type of glass (note that with the earlier corrector the variation of image spread with wavelength must be included).

Subsequently each spectrum was "scrunched" - that is, the wavelength scale was assigned using the relation 4.2.2 for the dispersion curve, and the data were rebinned so that wavelength was linearly related to channel number. Following Cooke (1980) any variations in the dispersion relation across the plate were taken to

λ(Å)	γ(λ)	g(λ)	SKY(λ)
3200	3.10	1.42	
3350	3.10	1.42	
3500	3.10	1.42	
3650	3.10	1.42	
3800	3.10	1.42	
3950	3.10	1.42	1.22
4100	3.70	1.21	1.18
4250	3.83	1.05	1.01
4400	3.95	1.00	1.03
4550	3.84	1.00	1.00
4700	3.95	1.00	0.97
4850	3.86	1.00	0.94
5000	4.19	1.00	0.91
5150	4.15	1.00	0.94
5300	4.62	0.74	0.96
5450	3.43	0.21	1.03

TABLE 4.3.1

Values of γ(λ), relative g(λ) and relative SKY(λ). γ(λ) and g(λ) at 5450Å are unreliable. Values of γ(λ) and g(λ) below 3950Å are invented. The emulsion is hypersensitised IIIaJ, batch 2C7.

λ(Å)	ACHROMAT TRANSMISSION	PRISM TRANSMISSION	λ(Å)	ATMOSPHERIC TRANSMISSION (SDRSYS)
3100	0.09	0.10	3200	0.37
3200	0.40	0.34	3400	0.50
3300	0.57	0.62	3571	0.57
3400	0.76	0.80	3862	0.65
3500	0.84	0.88	4167	0.72
3700	0.92	0.97	4464	0.77
3900	0.96	0.99	4785	0.81
4200	1.00	1.00	5000	0.83
4500	1.00	1.00	5263	0.84

TABLE 4.3.2

Achromat and prism relative transmissions; (SDRSYS) atmospheric transmission at the zenith

be negligible.

Each scrunched spectrum $E_*(\lambda)$ was corrected for the transmission of the atmosphere using the standard function in SDRSYS, appropriate to the mean hour angle of UJ3682P of 01^h58^m. A standard function may be expected to give errors, particularly at the shorter wavelengths. Table 4.3.2 gives values of the SDRSYS function for atmospheric transmission at the zenith.

Finally the spectrum was divided by the relative $g(\lambda)$ to give, in arbitrary units, the $I_*(\lambda)$ of the approximation that was described in Chapter 3.

Ideally, the product $g(\lambda)A(\lambda)$ of the grain response function and the atmospheric transmission should be determined in absolute units from spectrophotometry of faint stars because each quasar spectrum could then be calibrated and the unreliable relative $g(\lambda)$ from the calibration spectrogram would not be required. Unfortunately, attempts to do this spectrophotometry in 1978 and 1979 were frustrated by poor weather at the AAT.

The three overlapped quasars were reduced separately.

The raw density data and the steps in the reduction process are illustrated in Figs 4.3.1 and 4.3.2 for the quasar Q00 47 49.7 - 27 59 36, which is relatively bright ($\sim 18^m$) and which has a strong Ly-α emission line at a redshift of $z = 2.14$. An IPCS spectrum of the quasar was obtained at the AAT in September 1977 by Cannon, Smith and Boksenberg but is published for the first time in Clowes et al (1980), as are three other quasars that were observed then (these quasars were first found in Cannon's quick search and were re-discovered by Clowes and Savage in their detailed search of UJ3682P). Fig 4.3.1 is a hidden-line plot of the complete scan pattern of Q00 47 49.7 - 27 59 36 and has a separation on the plate of 5μm between the tracings. CIV λ1549 is to the left and Ly-α λ1216 is the emission line at the centre. Notice (as far as possible) the symmetry of the scan pattern, and also the coherence of the plate noise over many scan lines. The average of the central two scan lines, after subtraction of the smoothed local sky background and biasing by the mean sky background density of 1.63, is shown in Fig 4.3.2(a). Fig 4.3.2(a) is reversed relative to Fig 4.3.1 so that CIV λ1549 is to the right. The wavelength of 5380Å corresponds to channel number 1001. Figs 4.3.2(a)

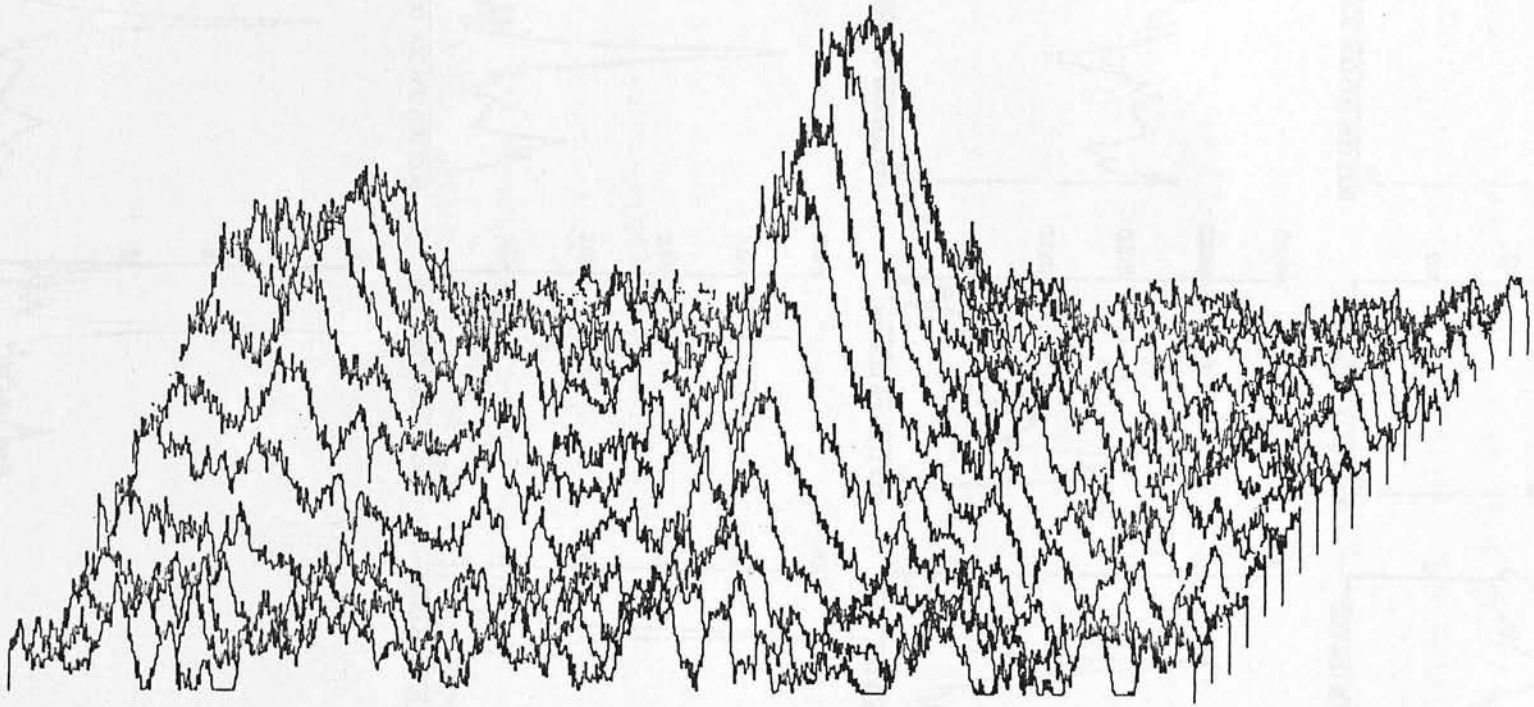

Fig.4.3.1 PDS density data for the quasar Q00 47 49.7-27 59 36 showing CIV λ1549 (left) and Ly-α λ1216 (centre). The on-plate separation of the tracings is 5μm.

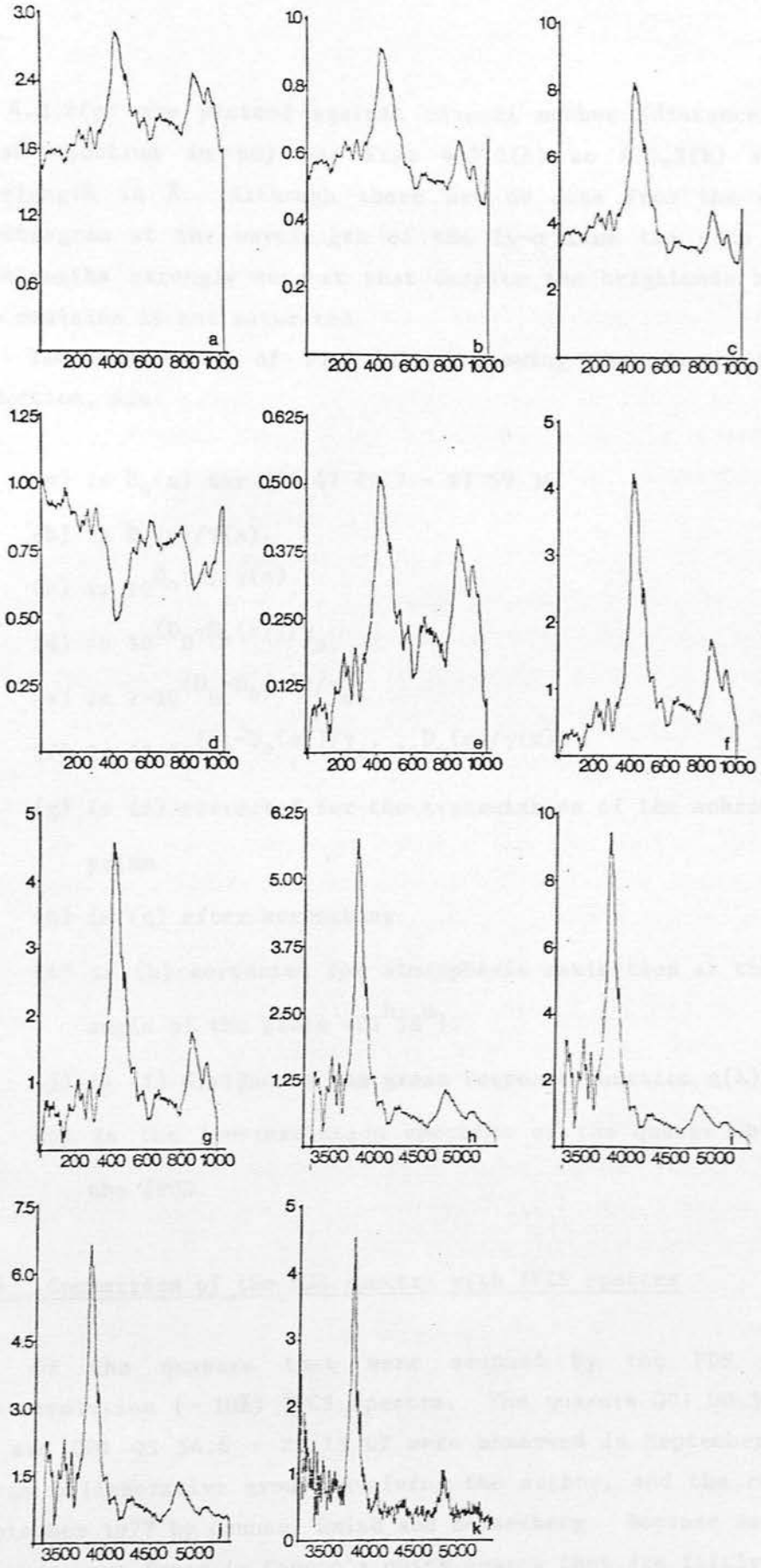

Fig.4.3.2 Stages in the reduction of 000 47 49.7-27 59 36.Details are given in the text.Fluxes,where appropriate,are per unit wavelength with an arbitrary scale.

to 4.3.2(g) are plotted against channel number (distance along the prism spectrum in μm) and Figs 4.3.2(h) to 4.3.2(k) are against wavelength in Å. Although there are no data from the calibration spectrogram at the wavelength of the Ly-α line the data for longer wavelengths strongly suggest that despite the brightness of the line the emulsion is not saturated.

The components of Fig 4.3.2, showing the steps in the data reduction, are:

(a) is $D_*(x)$ for Q00 47 49.7 - 27 59 36.

(b) is $D_*(x)/\gamma(x)$.

(c) is $10^{D_*(x)/\gamma(x)}$.

(d) is $10^{(D_B-D_*(x))/\gamma_s}$.

(e) is $1-10^{(D_B-D_*(x))/\gamma_s}$.

(f) is $\{1-10^{(D_B-D_*(x))/\gamma_s}\}\ 10^{D_*(x)/\gamma(x)}$.

(g) is (f) corrected for the transmission of the achromat and the prism.

(h) is (g) after scrunching.

(i) is (h) corrected for atmospheric extinction at the mean hour angle of the plate (01^h58^m).

(j) is (i) divided by the grain response function $g(\lambda)$.

(k) is the low-resolution spectrum of the quasar obtained with the IPCS.

4.4 Comparison of the PDS spectra with IPCS spectra

Of the quasars that were scanned by the PDS twelve had low-resolution (~ 10Å) IPCS spectra. The quasars Q01 00 33.0 - 28 09 45 and Q01 03 54.6 - 29 13 07 were observed in September 1978 by a large collaborative group involving the author, and the remainder in September 1977 by Cannon, Smith and Boksenberg. Because most of these quasars were found in Cannon's quick search they are fairly bright and frequently have strong Ly-α emission.

These quasars were used to test the reliability of the wavelengths and equivalent widths that were obtained from the PDS spectra. SDRSYS procedures were used to measure equivalent widths and centroid wavelengths for the emission lines of the IPCS and the PDS spectra. Table 4.4.1 gives the PDS and IPCS wavelengths and equivalent widths for the emission lines of each quasar and lists the percentage discrepancies of the PDS measurements over those of the IPCS. A question mark that follows an IPCS entry in Table 4.4.1 indicates greater uncertainty than usual in the measurement; a question mark after a PDS entry is to cast doubt on the identification of the feature as an emission line.

Of the twelve quasars in Table 4.4.1, Q00 47 49.7 -27 59 36 is shown in Figs 4.3.1 and 4.3.2, and the PDS reduced spectra, density data $D_*(x)$ and IPCS spectra of Q00 48 35.2 - 29 49 46, Q00 48 55.1 - 29 44 46, Q01 00 35.2 - 27 39 46 and Q01 03 54.6 - 29 13 07 are shown in Fig 4.4.1. These quasars are chosen to be representative of the twelve. Note that in Fig 4.4.1 the PDS spectra have not been divided by the rather uncertain relative $g(\lambda)$.

The wavelength agreement between the PDS and the IPCS spectra is generally very good: typically 1% for emission lines at ~ 4000Å. Some deterioration of the wavelength agreement would be expected near the emulsion cut-off at wavelengths greater than ~ 5000Å, partly because of the steepness of $d\lambda/dx$ but mostly because of the tendency of the cut-off to effectively move emission lines to shorter wavelengths. This last effect could explain part of the large (4%) wavelength discrepancy for the CIV line of Q00 48 35.2 - 29 49 46 (Table 4.4.1) since the Ly-α line occurs at the correct wavelength; however the apparently spurious nature of the feature at ~ 4550Å suggests that the CIV line might not be entirely real, but is perhaps enhanced by a speck of dirt on the plate. Similarly the "broad absorption" at ~ 4600Å in Q00 48 55.1 - 29 44 46 is presumably a plate flaw. But as Fig 4.4.1 shows, the general agreement between the PDS and the IPCS spectra of these brighter quasars is really quite good (of course when the quasars are so faint that their continua barely appear above the sky background their prism spectra are not impressive).

The discrepancies for the equivalent widths (Table 4.4.1) range

QUASAR	B	IPCS λ, W_λ	PDS λ, W_λ	% λ DISCREPANCY	% W_λ DISCREPANCY
00 45 41.4		Ly-α 3969 187	3960 176	0.2	6
-28 50 27	18.9	CIV 5033 57	NOT DETECTED	-	-
00 46 01.7		Ly-α 3270 166?	NOT DETECTED	-	-
-28 12 39	18.1	CIV 4163 110	4216? 89?	-1?	19?
00 47 15.0		Ly-α 3826 284	3800 317	1	-12
-29 21 33	19.5	CIV 4871 98	4783? 60?	2?	39?
00 47 49.7		Ly-α 3823 530	3829 686	-0.2	-29
-27 59 36	18.2	CIV 4846 122	4837 121	0.2	1
00 48 16.3		Ly-α 3667 224	3663 566	0.1	-153
-29 52 37	19.0	CIV 4674 137	4567? 125?	2?	9?
00 48 35.2		Ly-α 4176 447	4169 331	0.2	26
-29 49 46	19.2	CIV 5318 280	5094? 301?	4?	-8?
00 48 55.1		Ly-α 3912 176	3878 357	1	-103
-29 44 46	18.9	CIV 4972 56	NOT DETECTED	-	-
00 52 39.0		Ly-α 4082 225	4056 362	1	-61
-28 23 45	19.3	CIV 5187 86	NOT DETECTED	-	-
00 59 57.4		Ly-α 3957 140	3955 204	0.1	-46
-26 57 52	18.9	CIV 5029 144?	NOT DETECTED	-	-
01 00 33.0		Ly-α 3407 548?	3483? 550?	-2?	-0.4?
-28 09 45	19.3	CIV 4360 127	NOT DETECTED	-	-
		CIII] 5325 99?	NOT DETECTED	-	-
01 00 35.2		CIV 3760 148	3743 108	0.5	27
-27 39 46	19.2	CIII] 4613 68	NOT DETECTED	-	-
01 03 54.6		OVI 3933 72	NOT DETECTED	-	-
-29 13 07	18.6	Ly-α 4639 419	4675 403	-0.8	4

TABLE 4.4.1 Comparison of the PDS spectra with IPCS spectra. Wavelengths and equivalent widths are in Å.

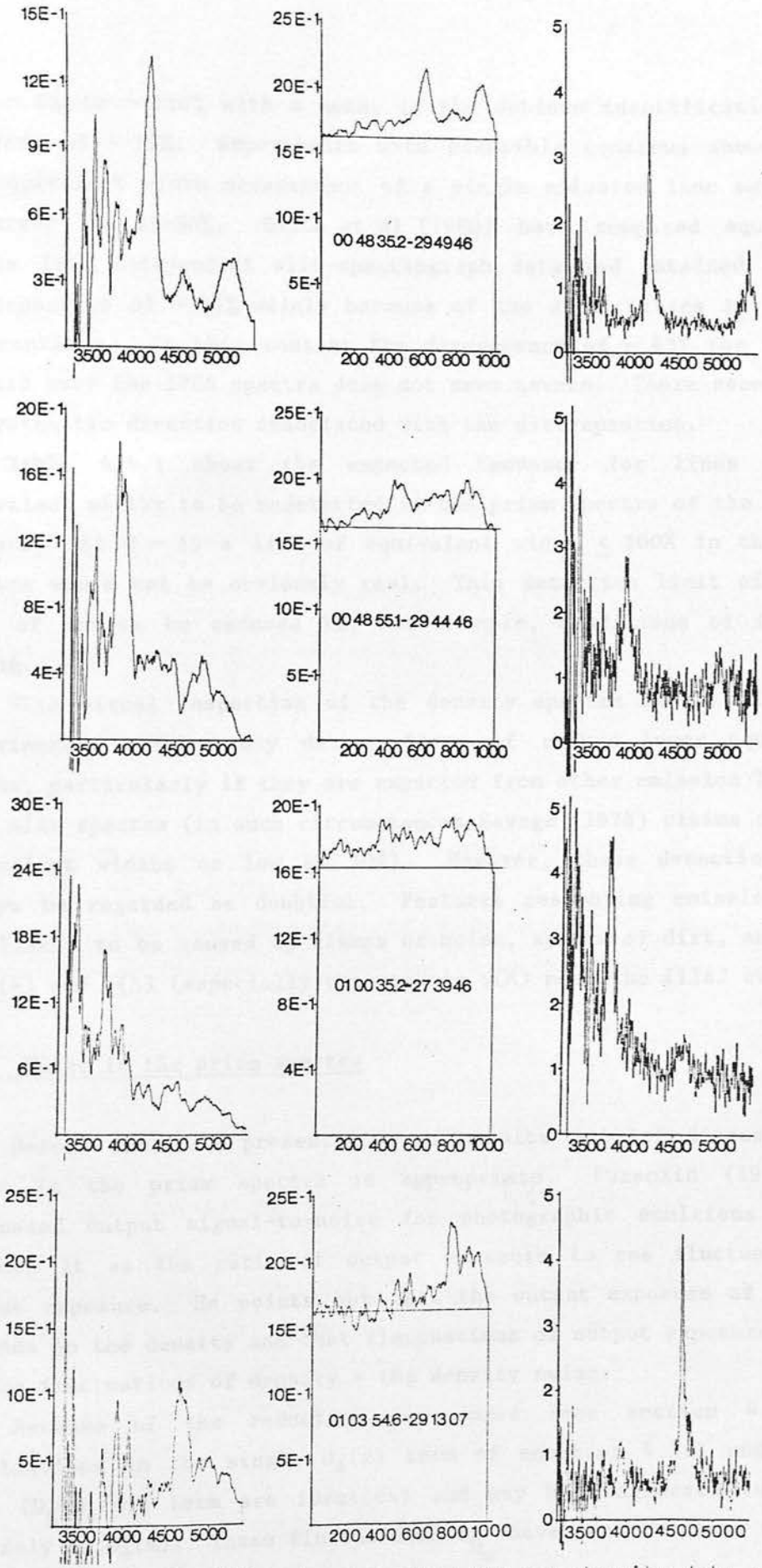

Fig.4.4.1 The PDS reduced spectra, the raw density data, and the IPCS spectra for four quasars. The horizontal line at D=1.63 in the density data denotes the level of the mean sky background. Note that $g(\lambda)$ has not been included. Fluxes are per unit wavelength with an arbitrary scale.

from ~ 0% to ~ 150% with a mean, if the dubious identifications are ignored, of ~ 43%. Experiments with plausible continua showed that the equivalent width measurement of a single emission line may carry an error of 15-30%. Smith et al (1980) have compared equivalent widths from independent slit-spectrograph data and obtained typical discrepancies of ~ 35% mainly because of the difficulties in setting the continua. In this context the discrepancy of ~ 43% for the PDS spectra over the IPCS spectra does not seem severe. There seems to be no systematic direction associated with the discrepancies.

Table 4.4.1 shows the expected tendency for lines of low equivalent widths to be undetected in the prism spectra of the fainter quasars. At B ~ 19 a line of equivalent width $\lesssim$ 100Å in the prism spectra would not be obviously real. This detection limit of ~ 100Å will of course be reduced in, for example, conditions of improved seeing.

With visual inspection of the density spectra on the plate the experienced searcher may detect lines of rather lower equivalent widths, particularly if they are expected from other emission lines or from slit spectra (in such circumstances Savage (1978) claims detected equivalent widths as low as 10Å). However, these detections must always be regarded as doubtful. Features resembling emission lines are likely to be caused by clumps of noise, specks of dirt, and peaks in $\gamma(\lambda)$ and $g(\lambda)$ (especially the peak in $\gamma(\lambda)$ near the IIIaJ cut-off).

4.5 Noise in the prism spectra

Before the full presentation of results a brief discussion of noise in the prism spectra is appropriate. Furenlid (1978) has discussed output signal-to-noise for photographic emulsions and he defines it as the ratio of output exposure to rms fluctuation in output exposure. He points out that the output exposure of course, depends on the density and that fluctuations of output exposure depend on the fluctuations of density - the density noise.

Because of the reduction procedures (see section 4.3) the fluctuations in the single $D_*(x)$ term of equation 4.3.1 and in the term $(D_B - D_*(x))$ term are identical and may be considered to reside entirely in $D_*(x)$. These fluctuations σ_{D_*} have contributions from the

spectra and from the local smoothed sky background.

Consequently, start from equation 4.3.1 after correction for the transmission of the telescope and the atmosphere:

$$E_{*}(x) = \{1-10^{(D_B-D_{*}(x))/\gamma_s}\} \frac{10^{D_{*}(x)/\gamma(x)}}{g(x)A(x)T(x)} \qquad [4.5.1]$$

Differentiation with respect to D_{*} and subsequent multiplication by $\sigma_{D_{*}}$ gives the fluctuation in output exposure as

$$\sigma_{E_{*}} \simeq \sigma_{D_{*}} \frac{10^{D_{*}(x)/\gamma(x)}}{g(x)A(x)T(x)} \ln 10 \cdot \{\frac{1}{\gamma(x)}[1-10^{(D_B-D_{*}(x))/\gamma_s}] + \frac{1}{\gamma_s} 10^{(D_B-D_{*}(x))/\gamma_s}\} \qquad [4.5.2]$$

and the output noise-to-signal ratio is consequently

$$\frac{\sigma_{E_{*}}}{E_{*}} \simeq \sigma_{D_{*}} \ln 10 \{\frac{1}{\gamma(x)} + \frac{1}{\gamma_s[10^{(D_{*}(x) - D_B)/\gamma_s}-1]}\} \qquad [4.5.3]$$

Equation 4.5.3 shows that the signal-to-noise ratio depends on wavelength and, with the trend for higher γ at longer wavelengths, favours the longer wavelengths. At short wavelengths where there is frequently very little signal and the signal-to-noise ratio is small, equation 4.5.2 shows that the transmission functions cause the amplitude of the output noise to be large. A further increase in amplitude is caused by subsequent scrunching.

Furenlid et al (1977) show that the noise σ_D of an emulsion type is a particular function of absolute density and that this function is almost independent of the hypersensitisation treatment. In Furenlid et al (1977) and Furenlid (1978) D - σ_D data are given for a total of seven emulsion types, including IIIaJ. The values are for diffuse densities with a 1000μm² aperture. In the data reduction of the prism spectra the sky scans also had, effectively, an aperture of 1000μm² while the spectral scans had an aperture of 400μm². Furenlid (1978) cites the relation for scaling the noise according to aperture size. For the prism spectra the noise as a function of D_{*} is given in Table 4.5.1. The data were obtained from the IIIaJ list in Furenlid (1978);

D_*	σ_{D_*}
0.18	0.052
0.45	0.055
0.71	0.059
0.98	0.061
1.25	0.066
1.65	0.070
2.31	0.080
2.98	0.089
3.64	0.093

TABLE 4.5.1

Accumulated noise as a function of D_*. D_* is above fog and densities are PDS. The data can be used only for UJ3682P.

When the emission line ΔD is small the expression for output signal-to-noise ratio is much simpler and can be obtained directly from equation 4.5.3:

$$\frac{\Delta E_*}{\sigma_{E_*}} \sim \frac{\Delta D}{\sigma_{D_*}} \qquad [4.5.9]$$

4.6 Presentation of the Data

The density spectra $D_*(\lambda)$ of the quasar candidates and the resulting products $g(\lambda)I_*(\lambda)$ are shown in the Appendix. Identification is by right ascension and declination and for each quasar $D_*(x)$ and $g(\lambda)I_*(\lambda)$ appear on the left and right respectively. A density of 1.63 represents the mean sky background on UJ3682P.

Table 4.6.1 again identifies the quasars by their positions and lists the data that were deduced from the prism spectra that included the relative $g(\lambda)$. The discussion of section 4.5 was used for Table 4.6.1 to impose a reality condition on emission lines - namely that their signal-to-noise ratios exceeded two. Features with ratios less than two have been taken to be of doubtful reality and they are not included in the table.

In the comparison of the prism spectra with IPCS spectra (section 4.4) the equivalent widths and wavelengths were obtained using interactive programs. In Table 4.6.1 the equivalent widths and wavelengths were obtained with a ruler and a calculator to avoid appropriating the computer for many hours (for the twelve comparison quasars Table 4.6.1 is consistent and lists the ruler and calculator measurements). The equivalent widths were calculated from

$$w = \int\{ \frac{I_*(\lambda)}{C_*(\lambda)} - 1\} \, d\lambda \qquad [4.6.1]$$

where $C_*(\lambda)$ is the assumed flux from the continuum and $I_*(\lambda)$ is the flux from the emission line plus the continuum. The numerical integrations used 50Å segments.

The continuum fluxes (C) in Table 4.6.1 were measured in

arbitrary units for the assumed continua at wavelengths between 4500Å and 5000Å, which is where $\gamma(\lambda)$ and relative $g(\lambda)$ are best known and where problems with noise in the continuum are least.

The prism spectra of quasars frequently show only one convincing emission line, partly because of the small wavelength range of IIIaJ emulsion (the use of IIIaF will extend the wavelength range but only at the expense of increased influence of the sky background) and partly because lines other than Ly-α are likely to be too faint to be seen. Consequently, in Table 4.6.1, a single-line redshift depends on an experienced guess of the identity of the single line. For objects without a blue continuum a strong line may be guessed, almost always correctly, to be Ly-α. An IPCS spectrum was used to identify the line in Q01 00 35.2 - 27 39 46 only.

The B magnitudes in Table 4.6.1 were obtained from COSMOS data of the plate B3499 (IIaO emulsion, GG385 filter, 60 minute exposure, 15/16 August 1977), using a calibration curve supplied by Gerry Gilmore and Neill Reid and programs by Harvey MacGillivray. These B magnitudes carry errors of $\sim \pm 0.2$ and $\sim \pm 0.4$ when respectively brighter and fainter than 19^m. The magnitudes were found by predicting the COSMOS x, y positions of the quasars from their α, δ values and taking the objects nearest to the calculated positions to be the quasars; possible misidentifications are indicated by a question mark in Table 4.6.1.

The data in Table 4.4.1 when compared with the counterparts of Table 4.6.1 show that the ruler and calculator method overestimates the equivalent widths (numerical integration within SDRSYS uses smaller wavelength steps) but the wavelength discrepancies are essentially unchanged. The equivalent widths would perhaps have been better measured with a planimeter, but none was available.

Regardless of the method of numerical integration the measurement of equivalent widths in these prism spectra is made difficult firstly by the uncertainty in the level of the continuum that arises from the plate noise and secondly by the uncertainty in the slope of the continuum that arises from the small wavelength range of IIIaJ. The use of IIIaF emulsion with the new, higher dispersion prism will alleviate this latter difficulty.

TABLE 4.6.1

QUASAR	EMISSION LINE	Z	C	B	COMMENTS
00 45 04.8 -30 02 51			0.47	17.9	BLUE
00 45 18.0 -26 14 02			0.30	19.3	
00 45 20.1 -29 14 48			0.14	20.1	
00 45 25.4 -28 29 24	3600,325 L?	1.95 ?	0.30	19.4	Z=L
00 45 41.4 -28 50 27	3924,291 L?	2.22 ?	0.40	18.9	Z=L AAT
00 45 49.9 -26 04 06	4137,137 MG?	0.48 ?	0.41	18.6	Z=MG AAT
00 45 55.2 -28 00 53	3847,1003 L?	2.15 ?	0.16	19.7	Z=L
00 46 01.7 -28 12 39	4200,152 CIV 5116,29 CIII	1.71 1.68	0.72	18.1	AAT

00 46 21.0			0.37	18.9	
-26 16 41					
00 46 41.5	4028,418 L?	2.30	0.18	20.1	Z=L
-28 21 01		?			
00 46 44.9	3877,767 L	2.18	0.13	19.5	
-29 22 34	4936,229 CIV	2.19			
00 46 51.9	4313,273 L?	2.54	0.18	19.1	Z=L
-26 45 53		?			
00 47 00.3			0.11	20.0	
-29 11 06					
00 47 03.3	4014,550 L?	2.29		19.9	Z=L
-26 21 25		?			
00 47 15.0	3794,499 L?	2.11	0.26	19.5	Z=L AAT
-29 21 33		?			
00 47 45.6			0.07	20.2	
-26 33 48					
00 47 49.7	3806,690 L	2.12	0.67	18.2	AAT
-27 59 36	4819,151 CIV	2.11			
00 48 16.3	3617,587 L	1.96	0.29	19.0	AAT
-29 52 37	4573,191 CIV	1.95			

00 48 21.8 -26 05 39			0.19	19.2	
00 48 22.5 -27 59 40	3567,412 CIII 5208,108 MG	0.87 0.86	0.18	19.8	
00 48 26.4 -27 34 26	3507,1062 L 4477,275 CIV 4978,113 ?	1.87 1.89	0.13	19.8	ABS?FLAWS?
00 48 31.6 -26 45 34	5090,254 L?	3.17 ?	0.11	20.2	Z=L
00 48 35.2 -29 49 46	4176,509 L 5077,194 CIV?	2.42 2.28	0.23	19.2	AAT CIV WRONG?
00 48 42.5 -26 08 34	3951,527 L 4635,141 OIV 5100,173 CIV	?	0.23	19.0	POOR LINE FIT
00 48 46.9 -28 04 17	3542,144 CIII 5153,79 MG	0.86 0.84	1.23	17.6	AAT
00 48 48.5 -26 59 17	5200,496 L?	3.26 ?	0.12	20.0	Z=L
00 48 50.7 -29 57 41	4021,196 ? 5049,45 ?		0.36		POSSIBLY L,CIV

00 48 51.9 -26 56 26	4100,314 L?	2.36 ?	0.13	20.1	Z=L
00 48 52.0 -29 07 20	4167,164 CIV 5075,93 CIII	1.69 1.66	0.17	19.7	
00 48 52.3 -27 09 05	3465,817 ?		0.20	19.7	LINE NOT REAL
00 48 55.1 -29 44 46	3889,484 L?	2.19 ?	0.28	18.9	Z=L AAT
00 49 01.4 -28 20 54	3633,67 ? 3964,456 L 5017,58 CIV	2.25 2.24	0.96	18.1	
00 49 29.4 -27 14 01	4244,572 L?	2.48 ?	0.27	19.1	Z=L
00 49 29.8 -29 00 43	3934,224 L?	2.22 ?	0.63	18.8	Z=L
00 49 30.1 -26 06 48	3732,428 L?	2.06 ?	0.16	19.2	Z=L ABS?
00 49 32.8 -26 53 44			0.34	18.9	

00 49 44.5 -27 36 11			0.46	19.0 BLUE
00 50 05.9 -28 04 27	3879,426 L?	2.18 ?	0.18	20.1 Z=L
00 50 10.3 -28 07 11	4170,187 L?	2.42 ?	0.32	18.9 Z=L
00 50 19.1 -26 40 40	3933,279 L?	2.22 ?	0.13	20.1 Z=L
00 50 27.9 -26 34 48	3791,481 L?	2.11 ?	0.22	19.1 Z=L
00 50 37.6 -28 25 30			0.22	19.9
00 50 49.6 -28 06 30	3479,145 L?	1.85 ?	0.58	19.0 Z=L AAT
00 50 55.2 -28 43 14	4243,368 L?	2.48 ?	0.16	19.6 Z=L
00 51 02.7 -30 01 57	3965,959 L?	2.25 ?	0.14	19.5 Z=L
00 51 10.8 -26 47 39			0.11	

00 51 12.9	3423,739 ?		0.20		NO LINE
-27 15 38	5100,172 ?				FIT.ABS?
00 51 14.4	4042,108 CIV	1.61	0.40	18.8	
-27 33 45	5029,74 CIII	1.63			
00 51 17.6	3583,842 L?	1.94	0.09	19.6	Z=L
-28 55 10		?			
00 51 25.8	3819,320 L?	2.13	0.17		Z=L
-26 30 00		?			
00 51 27.2	3611,868 L	1.96	0.22		POOR
-26 49 12	4035,238 OIV	1.88			FIT-OIV
	4564,239 CIV	1.95			
00 51 40.1	3640,383 CIV	1.35	0.33	19.3	
-28 46 47	4500,97 CIII	1.36			
00 51 40.6	3587,323 CIV	1.32	0.14		
-26 37 32	4444,153 CIII	1.33			
00 51 43.2	3493,181 OIV	1.50	0.39		
-28 01 20	3877,339 CIV	1.50			
	4796,70 CIII	1.51			
00 51 47.2	3917,338 ?		0.53	18.9	NO LINE
-28 11 54	4885,167 ?				FIT

00 51 51.1 -27 24 54	4468,500 CIV?	1.88 ?	0.09		Z=CIV
00 51 52.6 -26 34 34	3678,334 L?	2.01 ?	0.25		Z=L
00 51 54.0 -26 39 50	4028,114 ?		0.30?		ABS?
00 52 14.5 -29 24 14			0.30		DIRT AT 3400
00 52 16.6 -28 32 32	3833,354 ? 4800,215 ?		0.18	19.9	NO LINE FIT
00 52 21.2 -27 34 12	3486,144 ? 3732,233 ?		0.23	20.1	ODD SPECTRUM
00 52 31.6 -26 37 27			0.21		OVERLAPS
00 52 39.0 -28 23 45	4039,506 L?	2.31	0.27	19.3	Z=L AAT
00 52 57.9 -29 42 06			0.20	19.8	
00 53 06.1 -28 21 14	5200,55 ?		0.30	19.5	NO LINE FIT

00 53 20.0 -29 21 53	3750,257 L?	2.07	0.28	19.6	Z=L
00 53 20.3 -28 13 50	3486,322 L? 4450,265 CIV?	1.86 1.87	0.24	19.9	
00 53 38.5 -27 09 14	3838,65 ? 4793,47 ?		0.64	18.6	NO LINE FIT.ABS?
00 54 06.5 -27 33 34	3877,57 MG?	0.39	0.50	18.4	Z=MG.BLUE
00 54 18.7 -26 50 00			0.10	19.3	
00 54 22.5 -28 10 27	3430,202 CIII 4176,55 CII 4958,89 MG	0.80 0.80 0.77	0.34	19.4	
00 54 33.1 -29 34 04	3674,293 L?	2.01	0.16	19.4	Z=L.ABS? NARROW LINE
00 54 55.4 -26 01 52			0.50	18.9	WRONG OBJECT?
00 55 07.1 -27 54 29	4172,55 CIV 5148,53 CIII	1.69 1.70	0.34	19.1	ABS

00 55 09.1 -27 06 22			0.21	20.0	
00 55 42.6 -28 50 11	4236,211 ? 4986,90 ?		0.21	19.6	NO LINE FIT
00 56 03.2 -27 16 17	3983,152 ?		0.24	19.7	NO LINE FIT
00 56 21.7 -29 15 35			0.48		BLUE CONTINUOUS
00 56 22.6 -29 11 23			0.27		
00 56 35.2 -29 05 31	4334,89 ?		0.21	19.5	NO FIT NARROW
00 57 04.7 -27 59 49	5134,206 ?		0.10	19.9	NO FIT BLUE
00 57 12.2 -29 21 17	4059,77 ?		0.31	19.2	NO FIT' ABS?
00 57 18.9 -27 54 40	3825,200(OIV?) 4200,96(CIV?)		0.18	19.4	BLUE.ABS? VERY NARROW
00 57 37.4 -28 20 02	4200,124 CIV?	1.71	0.31	19.3	Z=CIV

00 58 43.4 -26 43 27	4688,190 L?	2.84 ?	0.31	19.0	Z=L OVERLAP
00 58 57.6 -27 05 41			0.29	19.2	ABS?ODD SPECTRUM
00 59 12.3 -28 48 46	3604,123 ? 4641,108 ? 5000,123 ?		0.19	19.8	NO LINE FIT
00 59 14.3 -26 55 09	3900,381 ?		0.36	18.9	NO FIT.ODD SPECTRUM
00 59 15.6 -29 43 52	3919,823 L?	2.21 ?	0.12	20.1	Z=L
00 59 26.1 -29 09 20			0.17	20.2	
00 59 27.6 -26 25 07	3800,300 L?	2.11 ?	0.55	18.5	Z=L.ABS AT 4275
00 59 57.4 -26 57 52	3944,269 L?	2.23 ?	0.32	18.9	Z=L AAT
01 00 02.3 -28 04 12	3974,538 L? 5000,144 CIV?	2.26 2.23	0.16	19.7	POOR FIT

01 00 16.2 -29 10 21	4105,179 L 5142,99 CIV	2.36 2.32	0.35	19.0	CIV + CUT-OFF
01 00 32.6 -29 09 20	4233,58 CIII?	1.22 ?	0.38	19.1	Z=CIII
01 00 33.0 -28 09 45			0.33	19.3	AAT
01 00 35.2 -27 39 46	3744,193 CIV?	1.42 ?	0.28	19.2	Z=CIV AAT Z=1.42
01 00 57.9 -28 06 10			0.14	20.1	
01 01 00.4 -29 17 54	3584,545 CIV 4447,169 CIII	1.31 1.33	0.14	19.9	
01 01 02.0 -27 08 49			0.13	19.2	ABS?
01 01 03.3 -28 01 31			0.11	20.0	
01 01 14.5 -29 32 04	3684,215 ?		0.25	19.0	NO FIT BLUE
01 01 18.3 -29 15 44			0.08	19.9	

01 01 40.1 -29 59 58	3600,605 CIV 4467,302 CIII	1.32 1.34	0.10	20.1	
01 02 56.7 -26 34 16			0.67	18.2	
01 02 57.6 -29 41 04	4642,162 L?	2.80 ?	0.27	19.7	Z=L.ABS IS FLAW
01 03 02.7 -29 05 53	3944,214 L?	2.23 ?	0.20	19.6	Z=L,COULD BE CIV
01 03 03.5 -27 38 38	3619,309 L 4590,159 CIV	1.97 1.96	0.23	19.4	ABS?
01 03 08.0 -27 07 36	3877,181 L? 4940,209 CIV?	2.18 2.19	0.30	19.0	ODD SPECTRUM
01 03 11.8 -29 25 19	3900,532 L? 4894,142 CIV?	2.20 2.16	0.22	19.4	ABS AT Z=2.06
01 03 15.3 -29 27 12	3863,408 L 4877,94 CIV	2.17 2.15	0.22	19.7	CIV IS' MARGINAL
01 03 26.9 -26 40 23			0.21	19.3	
01 03 51.7 -26 34 29			0.09	20.3	

01 03 54.6 -29 13 07	4676,325 L? ?	2.83	0.40	18.6	Z=L AAT
01 03 57.2 -27 49 52	3813,159 ? 5045,74 ?		0.48	18.7	NO FIT HII REGION?
01 04 01.9 -27 34 14	4200,395 L? ?	2.44	0.27	18.9	Z=L AAT
01 04 12.5 -26 49 00	4208,125 ? 5071,28 ?		0.21		LINES ARE MARGINAL
01 04 13.1 -27 28 59	3556,576 L? ?	1.91	0.19	19.8	Z=L
01 04 15.4 -28 10 00	3931,240 L? ?	2.22	0.51	18.5 ?	Z=L
01 04 21.3 -27 08 09	3700,962 L? ?	2.03	0.28		Z=L
01 04 22.7 -26 35 02	3528,777 L? ?	1.89	0.16		Z=L
01 04 26.5 -27 17 14			0.21		
01 04 39.7 -26 59 59			0.11		BLUE.NARROW LINES?

01 04 43.1	3940,226 CIV	1.54	0.21	
-28 30 38	4405,99 ?			
	4838,188 CIII	1.53		
01 04 50.1	3986,594 L?	2.27	0.21	POOR
-29 11 20	5000,166 CIV?	2.23		FIT
01 04 55.6			0.35	ABS?
-29 35 18				

KEY TO TABLE 4.6.1

L=LYMAN-ALPHA 1216 +NV 1240
OIV=OIV+SIIV 1400
CIV=CIV 1549
CIII=CIII] 1909
CII=CII] 2326
MG=MGII 2798

?=UNCERTAINTY OR UNIDENTIFIED LINE
ABS=ABSORPTION
Z=* MEANS Z ASSUMES LINE IDENTIFICATION *
AAT=OBJECT OBSERVED WITH AAT+IPCS

EMISSION LINE=WAVELENGTH,EQUIVALENT WIDTH
BOTH IN ANGSTROMS

5. Spectrogram Data

This chapter is concerned with the presentation of the data on the variation of γ and g with wavelength from ~ 3950Å to the emulsion cut-off.

5.1 The variation of γ with wavelength - $\gamma(\lambda)$

The variations with wavelength of the emulsion properties were determined from UKSTU calibration spectrograms with the implicit assumption that there were no changes in the dependences within an emulsion batch. No calibration could then be imposed on the prism plate during its exposure in the telescope.

To prepare a calibration spectrogram a cut plate is exposed in a conventional calibration spectrograph, which has a 12-stepped aperture slit. Details of the step widths and of the wavelength scale are given in the UKST Handbook. Bromage (1972) has shown that the exposure varies linearly (hence "geometrical exposure") with the step width only for the steps that are wider than 150μm, for which diffraction effects are unimportant.

The usable wavelength range of the spectrograms extends from ~ 3950Å (or at best 3800Å) to the emulsion cut-off. The present lack of information for wavelengths shorter than 3950Å is a serious difficulty because of the suspected changes in the trends of both $\gamma(\lambda)$ and $g(\lambda)$.

The spectrograms were measured by the PDS using a square scanning aperture of side 20μm (as were the prism spectra). The deduced values of $\gamma(\lambda)$ at intervals of 150Å are listed in Table 5.1.1; they are appropriate to PDS densities above fog.

For the emulsion batch 2C7, which corresponds to the plate UJ3682P, two spectrograms were available, one hypersensitised (H) and one unhypersensitised (UH); spectrograms for the other batches were all on hypersensitised emulsion (H). The hypersensitisation is written in Table 5.1.1 as, for example, 39N + 6H + 3, which means 39 days of soaking in nitrogen at 20°C followed by 6 hours of soaking in hydrogen at 20°C and 3 days of cold storage in (gaseous) nitrogen. Data for the batch 2L8 are given in Table 5.1.1 for two

λ	2C7 UH	2C7 H	1B8 H	2I6 H	2J6 H	2L8 H1	2L8 H2
3650	2.46						
3800	3.33			1.86?		1.85	1.67?
3950	4.27	3.10	2.50	2.36	2.79	2.44	2.38
4100	4.51	3.70	3.04	2.79	2.83	2.90	2.83
4250	4.41	3.83	3.11	2.89	3.11	3.13	2.94
4400	4.14	3.95	3.40	3.14	3.54	3.13	2.97
4550	4.21	3.84	3.88	3.22	3.62	3.11	3.03
4700	3.89	3.95	3.71	3.22	3.48	3.04	3.09
4850	3.67	3.86	3.88	3.46	3.53	3.08	2.97
5000	4.07	4.19	3.91	3.54	3.70	3.11	2.91
5150	4.13	4.15	3.92	3.38	3.85	3.10	3.17
5300	4.62	4.62	4.35	3.77	3.98	3.33	3.25
5450	5.15	3.43?	3.79?	2.86?	2.50?	3.58	4.03
FOG DENSITY	0.20	0.47	0.47	1.30	0.90	-	0.96
SPECTROGRAM NUMBER	36	41	52	18	24	74	79

2C7	UH :		60 mins	2.1 ND
2C7	H :	39N + 6H + 3	60 mins	3.9 ND
1B8	H :	56N + 10H + 0	60 mins	3.9 ND
2I6	H :	34N + 9H + 2	60 mins	3.9 ND
2J6	H :	14N + 4½H + 7	60 mins	3.9 ND
2L8	H1 :	15N + 10H + 1	60 mins	3.0 ND
2L8	H2 :	37N + 9H + 1	60 mins	3.0 ND

TABLE 5.1.1 Values of $\gamma(\lambda)$ for IIIaJ emulsion batches. A question mark indicates that the measured points might not be on the linear characteristic.

hypersensitisations but the differences are not marked. However for batch 2C7 hypersensitisation has altered the shape of the $\gamma(\lambda)$ curve (Fig 5.1.1). It has also reduced the exposure time by a factor of 20 at a density of 1 and a wavelength of 4550Å (for the further hypersensitisation of batch 2L8 the reduction factor is only 1.06).

For hypersensitised IIIaJ two properties of the $\gamma(\lambda)$ curves seem to be general : a peak at long wavelengths near the emulsion cut-off and what appears to be the start of a rapid decline with decreasing wavelength at short wavelengths (although 2J6 is possibly an exception). At intermediate wavelengths $\gamma(\lambda)$ is either roughly flat or slowly increasing. The possible decline of $\gamma(\lambda)$ beyond the long wavelength peak is uncertain because $g(\lambda)$ declines rapidly there and the measured points might not be on the linear characteristic. The height and sharpness of the long wavelength peak at ~ 5300Å varies from batch to batch. During searches of prism spectra for quasars a high peak may be mistaken for a further emission line when one is clearly seen at shorter wavelengths.

The linear characteristic of hypersensitised IIIaJ emulsion is, in general, accurately linear between typical densities of 1.5 and 3; very occasionally there appears to be no strictly linear section but only a point of inflection. In Table 5.1.1 the errors in $\gamma(\lambda)$ should not exceed ~ 0.1. The geometrical exposures have been used throughout but the resulting errors in $\gamma(\lambda)$ are unimportant because the $\gamma(\lambda)$ values are mainly determined from the larger steps.

The $\gamma(\lambda)$ values in Table 5.1.1 are appropriate to PDS densities. An interobservatory calibration plate (set 32, wedge 3 : IIIaJ) was scanned by the PDS with the 20μm square scanning aperture. The calibration plate has ANSI diffuse densities for a 1000μm^2 aperture : to convert the PDS densities to these and the PDS $\gamma(\lambda)$ to ANSI $\gamma(\lambda)$ divide by 1.33.

Some people adopt the Baker density, $B = \log (10^D - 1)$ to extend the linear part of the characteristic curve but for IIIaJ the extension is slight. The densities of the prism spectra lay on the linear characteristic.

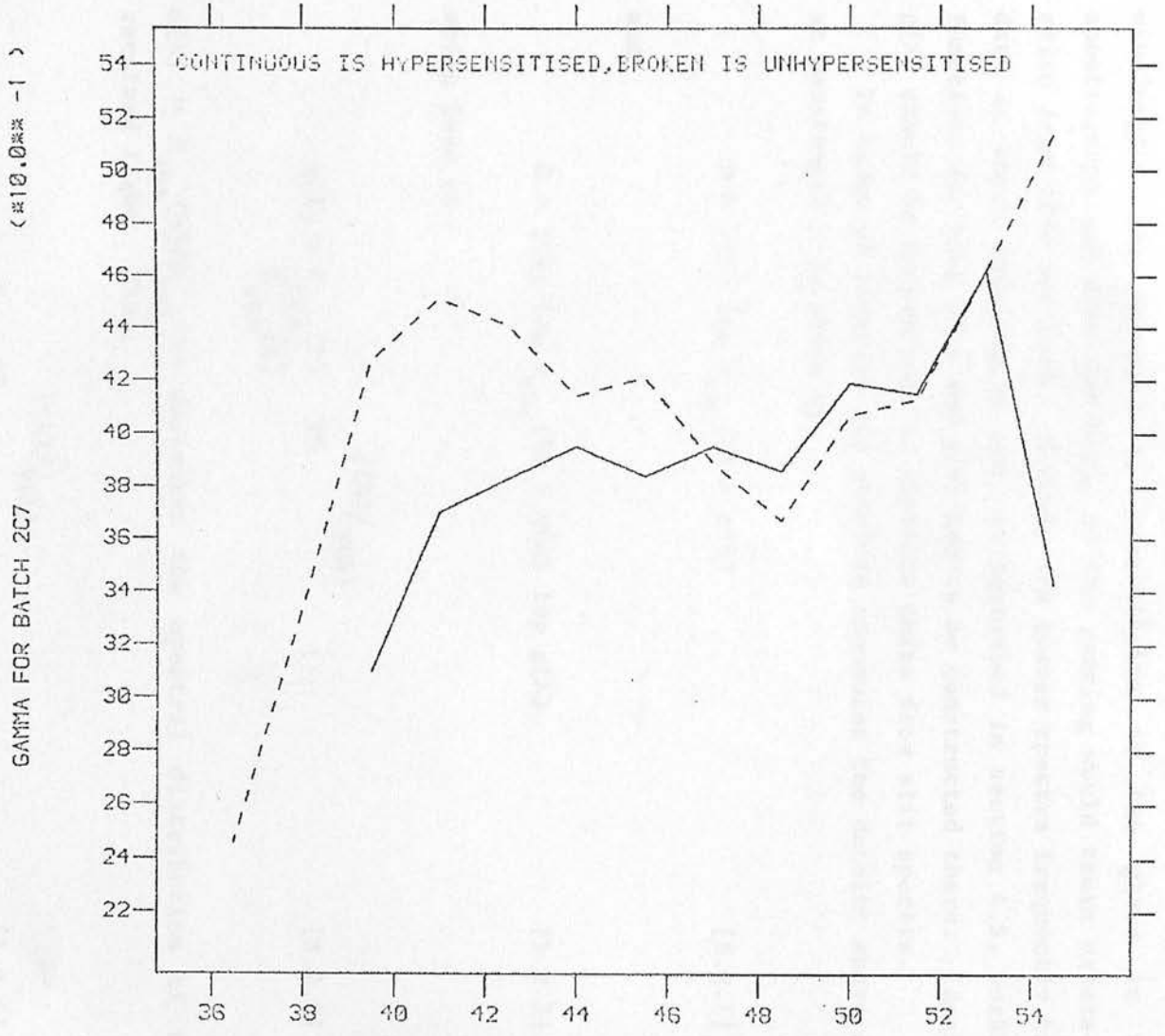
CONTINUOUS IS HYPERSENSITISED,BROKEN IS UNHYPERSENSITISED
GAMMA FOR BATCH 2C7
(*10.0** -1)
54
52
50
48
46
44
42
40
38
36
34
32
30
28
26
24
22
36
38
40
42
44
46
48
50
52
54
WAVELENGTH(A)
(*10.0** 2)

FIG.5.1.1

5.2 The variation of g with wavelength - g(λ)

The grain response function g(λ) cannot easily be obtained from spectrogram data because knowledge of the spectral distribution of the light received by the test plate is required. In the absence of such knowledge approximate results may be obtained for relative g(λ) by assuming that the spectrograph lamp (a quartz halogen lamp) has a blackbody distribution corresponding to some particular temperature (3100K was used). If there were any spectrogram data at short wavelengths the decrease in transmission of the glass in the spectrograph and also the blaze of the grating would cause errors to arise from this approach. However the quasar spectra frequently have data at short wavelengths and, as described in section 4.3, working functions for both γ(λ) and g(λ) had to be constructed there. Ideally g(λ) should be determined, in absolute units from slit spectra.

In terms of relative and absolute exposures the density above fog at wavelength λ is given by

$$D = \gamma(\lambda) \log E_{rel}(\lambda) + c(\lambda) \qquad [5.2.1]$$

and

$$D = \gamma(\lambda) \log E_{abs}(\lambda) + \gamma(\lambda) \log g(\lambda) \qquad [5.2.2]$$

which lead to

$$g(\lambda) = \frac{E_{rel}(\lambda)}{E_{abs}(\lambda)} \quad 10^{c(\lambda)/\gamma(\lambda)} \qquad [5.2.3]$$

$\alpha(\lambda) = E_{abs}(\lambda)/E_{rel}(\lambda)$ describes the spectral distribution of the received light. Then,

$$g(\lambda) = \frac{1}{\alpha(\lambda)} \quad 10^{c(\lambda)/\gamma(\lambda)} \qquad [5.2.4]$$

λ	2C7 UH	2C7 H	1B8 H	2I6 H	2J6 H	2L8 H1	2L8 H2
3650	0.73						
3800	0.82			1.05?		0.68	0.57?
3950	0.84	1.42	1.09	1.19	1.11	0.78	0.65
4100	0.89	1.21	1.13	1.24	1.33	0.80	0.71
4250	0.89	1.05	1.17	1.14	1.22	0.80	0.78
4400	0.98	0.95	1.09	1.05	1.00	0.90	0.91
4550	1.00	1.00	1.00	1.00	1.00	1.00	1.00
4700	1.23	1.00	1.09	1.00	1.00	1.08	1.06
4850	1.48	1.05	1.00	0.95	1.00	1.12	1.22
5000	1.25	0.95	1.00	0.90	1.00	1.13	1.34
5150	1.41	1.00	1.13	1.05	1.00	1.30	1.23
5300	0.98	0.74	0.74	0.67	0.67	0.95	1.00
5450	0.23	0.21?	0.22?	0.24?	0.22?	0.23?	0.18

TABLE 5.2.1 Values of $g(\lambda)$ for IIIaJ emulsion batches (glass transmission and grating blaze are not included). A question mark indicates that the measured points might not be on the linear characteristic.

$\gamma(\lambda)$ and $c(\lambda)$ are the constants in the equation of the linear characteristic at wavelength λ and they are easily found from the spectrogram data; $\alpha(\lambda)$ describes the spectral distribution of the light source and includes the transmission of the glass and the blaze of the grating. $\alpha(\lambda)$ is likely to be known only relatively (if at all) and therefore so is $g(\lambda)$: absolute calibration requires spectrophotometric standards. The involved theory of blazed gratings is given by Madden and Strong (1958) and a verbal summary is given by Wilkinson and Martin (1967).

Table 5.2.1 is the counterpart of Table 5.1.1 and it lists the values of $g(\lambda)$ relative to g(4550Å) that were calculated using equation 5.2.4. $\alpha(\lambda)$ was assumed to be simply the distribution that corresponds to a blackbody at 3100K. The data of Table 5.1.1 are certainly more reliable than those of Table 5.2.1.

For the hypersensitised batch 2C7 attempts to obtain $g(\lambda)$ in absolute units by spectrophotometry of faint blue objects were frustrated in 1978 and 1979 by poor weather at the AAT.

The distributions of $g(\lambda)$ in Table 4.2.1 show very similar trends for hypersensitised batches 2C7, 1B8, 2I6 and 2J6 but hypersensitised 2L8 and unhypersensitised 2C7 are greatly different.

If $\gamma(\lambda)$ does decrease with decreasing wavelength below 3950Å then the available IPCS spectra suggest that $g(\lambda)$ would increase.

6. Selection Effects

The chapter describes a quantitative specification of the selection effects that operate in the searches for quasars on objective-prism plates.

6.1 Introduction

The objective-prism method of finding quasars is regarded as the most efficient in the sense that it produces large numbers of them. However the value of a large sample is severely reduced and the efficiency is not a great advantage if the selection effects cannot be quantified. Two fields of quasars cannot be compared correctly unless the quasars are re-selected in terms of magnitude, redshift and emission-line equivalent width to form a class that is not selected against in either field. If, for example, the properties of one plate and the atmospheric conditions restrict the selected quasars to $m < 19.5$, $z \sim 2$ and $w > 100$ while for the other plate $m < 18.5$, $z \sim 2$ and $w > 150$ the differences in the numbers of quasars would probably not indicate anisotropy of the universe. If the quasars from both plates were restricted to $m < 18.5$, $z \sim 2$ and $w > 150$ then a meaningful comparison of the numbers of quasars could be made. The re-selection may be done by incorporating the technique for objective-prism spectrophotometry and the following quantification of selection effects.

6.2 Description of the Selection Effects

Previous work on the selection effects that operate in the searches for quasars on objective-prism plates (Carswell and Smith (1978)) has not specifically formulated the dependence of the emission-line equivalent width upon wavelength, continuum flux, plate and photon noise, seeing and sky background. The work of chapter 3 makes such a formulation possible.

Consider an idealised, triangular emission line of observed FWZI $\Delta\lambda$ and equivalent width $W(\lambda)$ at wavelength λ. λ and the corresponding x refer to the peak of the line. The exposure at λ from line and

continuum is $E_*(\lambda)$ and the exposure from the continuum only is $C_*(\lambda)$. Because the line has a triangular profile, and assuming that the continuum is flat, the expression for equivalent width becomes

$$E_*(\lambda)\ \Delta\lambda = C_*(\lambda)\Delta\lambda + 2C_*(\lambda)W(\lambda)$$

or

$$E_*(x) = C_*(x) + 2C_*(x)\ \frac{W(\lambda)}{\Delta\lambda} \qquad [6.2.1]$$

Idealise the spectrum on the plate to one with a rectangular profile across the dispersion (that is, D is not a function of y). In this way define the width of the profile as the diameter d of the seeing disc. Then, integrating across the spectrum, equation 3.2.22 leads to

$$E(x) = \{1-10^{(D_B-D)/\gamma_s}\}\ \frac{10^{D/\gamma(x)}}{g(x)}\ .d \qquad [6.2.2]$$

and D is, of course, a function of x. The functions and symbols are defined in Chapter 3 except that equation 6.2.2 redefines E, E_* and C_* (they now contain a factor d). Equation 6.2.2 may be written as

$$D = \gamma_s \log \{g(x)E(x)h^{D}(x)/d\ + g_s\ E_B\} \qquad [6.2.3]$$

where
$$h(x) = 10^{(1/\gamma_s\ -\ 1/\gamma(x))} \qquad [6.2.4]$$

and
$$g_sE_B = 10^{D_B/\gamma_s} \qquad [6.2.5]$$

The equation 6.2.3 may be solved analytically when $\gamma_s = \gamma(x)$ so that $h(x) = 1$.

The equivalent width that can be detected on a prism spectrum of a given density is determined by the density noise at that density. The density noise arises from plate noise and photon noise. Suppose that line, continuum and background produce density D_l at x and that continuum and background produce D_c. Then, using 6.2.3 and writing

$\Delta D = D_l - D_c$,

$$10^{\Delta D/\gamma_s} = \frac{g(x)E_*(x)h^{D_l}(x) + g_s E_B d}{g(x)C_*(x)h^{D_c}(x) + g_s E_B d} \qquad [6.2.6]$$

For the detection of weak lines ΔD is small so that $h^{D_l}(x) \simeq h^{D_c}(x)$. Using equation 6.2.1 for the equivalent width leads to

$$\frac{W(\lambda)}{\Delta\lambda} = \tfrac{1}{2}\left\{1 + \frac{g_s E_B d}{g(x)C_*(x)h^{D_c}(x)}\right\}\{10^{\Delta D/\gamma_s} - 1\} \qquad [6.2.7]$$

The observed line width $\Delta\lambda$ may be written in terms of the rest frame width and wavelength : $\Delta\lambda = (\frac{\lambda}{\lambda_o})\Delta\lambda_o$. If the density detection limit is ΔD then the equivalent widths of detected lines are given by

$$W(\lambda) > \tfrac{1}{2}(\frac{\lambda}{\lambda_o})\Delta\lambda_o \left\{1 + \frac{g_s E_B d}{g(x)C_*(x)h^{D_c}(x)}\right\}\{10^{\Delta D/\gamma_s} - 1\} \qquad [6.2.8]$$

ΔD is related to the density noise through the signal-to-noise ratio. Now $C_*(x) = A(\lambda)T(\lambda)I_*(\lambda)\frac{d\lambda}{dx}tS$

and $E_B = \phi_B \eta^2 tS$

where t is the exposure time, S is the telescope aperture, η is the plate scale (arcsec m^{-1}) and ϕ_B is the sky flux at the telescope (Wm^{-2} per square arcsec). Equation 6.2.8 becomes

$$W(\lambda) > \tfrac{1}{2}(\frac{\lambda}{\lambda_o})\Delta\lambda_o \left\{1 + \frac{g_s \phi_B \eta\rho \frac{dx}{d\lambda}}{g(\lambda)A(\lambda)T(\lambda)I_*(\lambda)h^{D_c}(\lambda)}\right\}\{10^{\Delta D/\gamma_s} - 1\} \qquad [6.2.9]$$

and $\rho = \eta d$ is the diameter of the seeing disc in arcsec.

The condition 6.2.9 strictly applies only between the lower flux limit that corresponds to continuum detection and the upper limit that corresponds to the upper limit of the linear characteristic. Even a

very strong emission line would pass unnoticed if there was no continuum. Following the same procedure as above the lower limit to the continuum is described by

$$A(\lambda)T(\lambda)I_{*}(\lambda) > \frac{g_s \phi_B \eta \rho \frac{dx}{d\lambda}}{g(\lambda)h^{D_B}(\lambda)} \{10^{\Delta D/\gamma_s} - 1\} \qquad [6.2.10]$$

and the upper limit by

$$A(\lambda)T(\lambda)I_{*}(\lambda) = \frac{\rho \frac{dx}{d\lambda}}{\eta t S g(\lambda) h^{D_S}(\lambda)} \{10^{D_S/\gamma_s} - 10^{D_B/\gamma_s}\} \qquad [6.2.11]$$

D_s is the saturation density and it is independent of wavelength (strictly, D_s is the upper limit to linearity).

The values of the density limit ΔD in equations 6.2.9 and 6.2.10 may be found from Furenlid et al (1977). They find that the density noise is a function of density only and not hypersensitisation. This implies that a given density depends on a particular number per unit area of perceived photons and that hypersensitisation simply affects the time necessary to perceive those photons. Then the density noise data of Furenlid et al (1977) and Furenlid (1978) include both plate noise and photon noise. Density noise is assumed to be independent of wavelength.

Of course the selection effects described by 6.2.9 do not refer to the relatively few, lower redshift quasars that are identified by their ultraviolet continua on prism plates rather than by emission lines.

The data for the equivalent widths of Ly-α + NV or assumed Ly-α + NV from Table 4.6.1 combined with the relative continuum fluxes may be used to test the discussion of selection effects. Detection generally depends on Ly-α + NV and if these lines are observed on the discovery plates then the equivalent widths of any other line in, for example, the spectrophotometric data of the CTIO Curtis Schmidt survey (Osmer and Smith (1980)) and the CTIO-4m survey (Osmer (1980)) would be inappropriate.

For the data in Table 4.6.1 consider the relations 6.2.8 and

6.2.10 in the following forms:

$$W(\lambda) > \tfrac{1}{2}\left(\frac{\lambda}{\lambda_o}\right)\Delta\lambda_o \left\{1 + \frac{g_s E_B d\frac{dx}{d\lambda}}{g(\lambda)C_*(\lambda)h^{D_C}(\lambda)}\right\} \left\{10^{\Delta D/\gamma_s} - 1\right\} \qquad [6.2.12]$$

$$C_*(\lambda) = \frac{g_s E_B d\frac{dx}{d\lambda}}{g(\lambda)h^{D_B}(\lambda)} \left\{10^{\Delta D/\gamma_s} - 1\right\} \qquad [6.2.13]$$

In this simplified treatment the wavelength dependences are ignored, $g_s/g(\lambda)$ and $h(\lambda)$ are set to 1, the mean redshift is taken to be 2.2, and $\Delta\lambda_o$ is taken to be 80Å. The last two equations then become

$$W(\lambda) > 128 \left\{\frac{1 + E_B d\frac{dx}{d\lambda}}{C_*(\lambda)}\right\} \left\{10^{\Delta D/\gamma_s} - 1\right\} \qquad [6.2.14]$$

$$C_*(\lambda) = E_B d\frac{dx}{d\lambda} \left\{10^{\Delta D/\gamma_s} - 1\right\} \qquad [6.2.15]$$

The UK Schmidt SGP quasars in Table 4.6.1 have been re-selected so that the equivalent widths are for lines with signal-to-noise ratios greater than two. Consequently the ΔD to be used in 6.2.14 is greater than the ΔD in 6.2.15. From Furenlid et al (1977) and Furenlid (1978), with a resolution element of 20μm, the ΔD for continuum detection is 0.05 (signal-to-noise ratio = 1) and the ΔD for line detection (Table 4.5.1) is at least 0.14 (signal-to-noise ratio = 2) and increases with density. With only small errors this latter ΔD may be taken to be constant at 0.14. The well-defined faint limit of 0.1 for the continuum flux (see Fig 6.2.1) was used in equation 6.2.15 to obtain $E_B d\frac{dx}{d\lambda}$ in the same arbitrary units as $C_*(\lambda)$. This $E_B d\frac{dx}{d\lambda}$ was then used in 6.2.14 to give the selection effect curve that is shown in Fig 6.2.1, which plots the continuum flux in arbitrary units against the equivalent width of Ly-α + NV or assumed Ly-α + NV. The curve suggests that the selection effects are indeed correctly described by the above procedure.

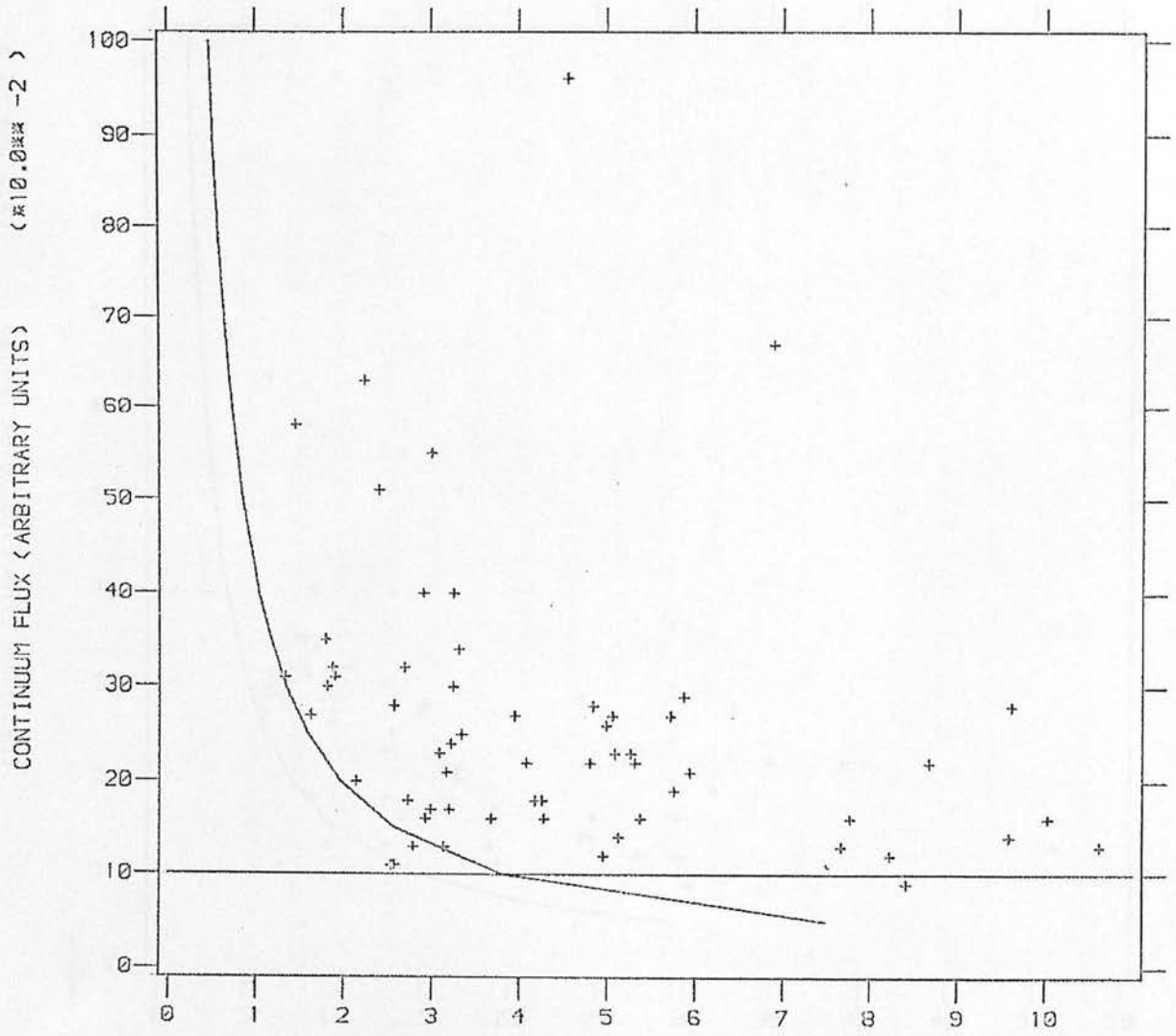

FIG.6.2.1 UKS LY EW(A) (*10.0** 2)

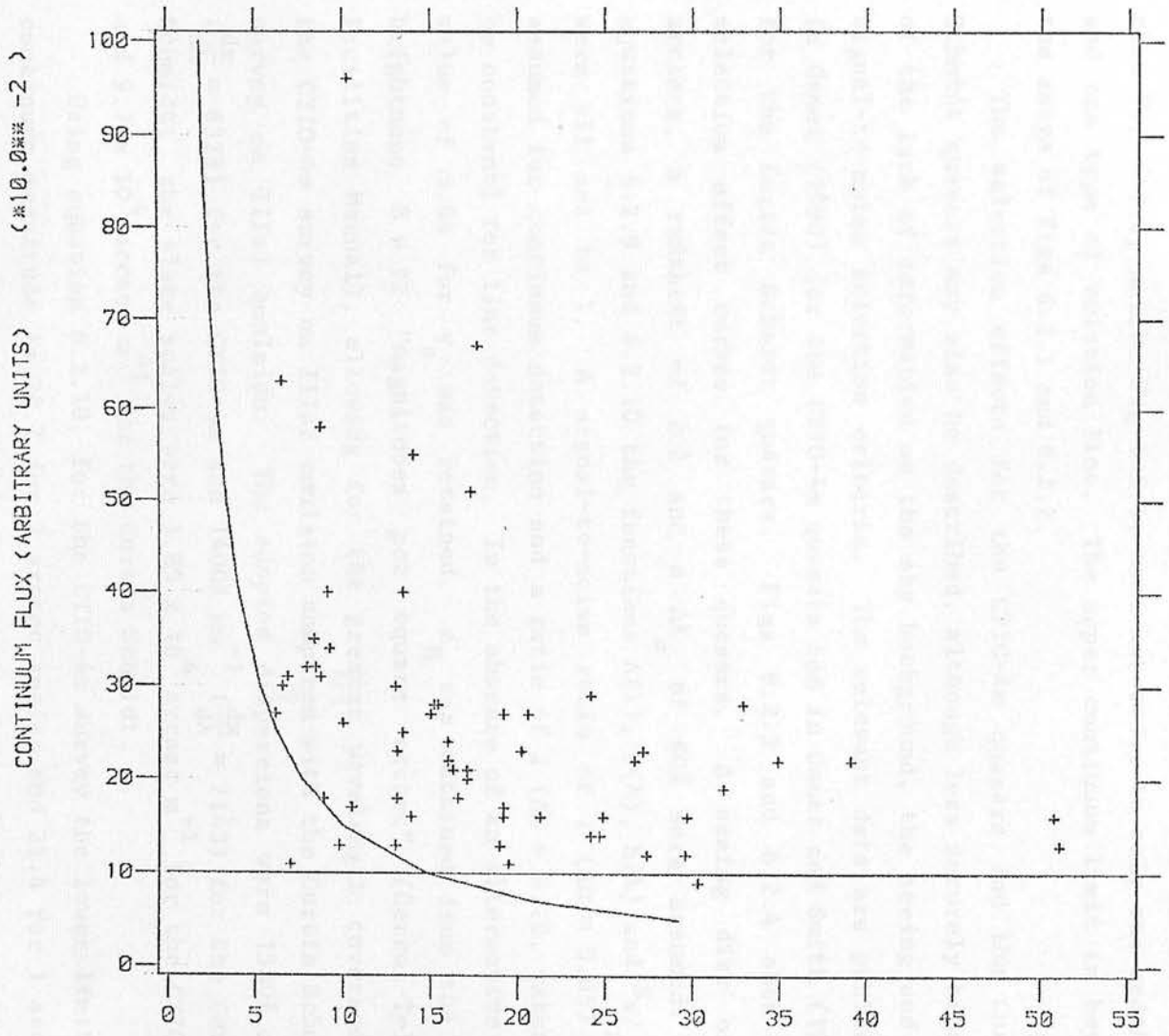

FIG.6.2.2 UKS LY EW/FWZI

The use of a fixed $\Delta\lambda_o$ is convenient but inessential. Osmer (1980) points out that for the CTIO-4m quasars the widest Ly-α + NV at FWZI has twice the width of the narrowest. Consequently the ratio of the observed equivalent width $W(\lambda)$ to the observed FWZI $\Delta\lambda$ (see equations 6.2.7 and 6.2.12, the latter with $(\frac{\lambda}{\lambda_o})\ \Delta\lambda_o = \Delta\lambda$) is superior to the equivalent width alone for describing the selection effects. Fig 6.2.2 plots continuum flux against $W(\lambda)/\Delta\lambda$ for the quasars of Fig 6.2.1. The selection effect curve in Fig 6.2.2 again used the observed faint limit for the determination of $E_B d\frac{dx}{d\lambda}$ and again took ΔD to be constant at 0.14. The agreement appears to be good. Notice that Fig 6.2.2, unlike Fig 6.2.1, need not refer to only one redshift and one type of emission line. The upper continuum limit is beyond the range of Figs 6.2.1 and 6.2.2.

The selection effects for the CTIO-4m quasars and the Curtis Schmidt quasars may also be described, although less securely because of the lack of information on the sky background, the seeing and the signal-to-noise selection criteria. The relevant data are published in Osmer (1980) for the CTIO-4m quasars and in Osmer and Smith (1980) for the Curtis Schmidt quasars. Figs 6.2.3 and 6.2.4 show the selection effect curves for these quasars. A seeing disc of 2 arcsecs, a redshift of 2.2 and a $\Delta\lambda_o$ of 80Å were assumed. In equations 6.2.9 and 6.2.10 the functions $A(\lambda)$, $T(\lambda)$, $h(\lambda)$ and $g_s/g(\lambda)$ were all set to 1. A signal-to-noise ratio of 1 ($\Delta D = 0.05$) was assumed for continuum detection and a ratio of 2 ($\Delta D = 0.10$, taken to be constant) for line detection. In the absence of an alternative the value of 3.84 for γ_s was retained. ϕ_B was obtained from the sky brightness B = 22 "magnitudes per square arcsec" (Cerro Tololo Facilities Manual), allowing for the greater wavelength coverage of the CTIO-4m survey on IIIaF emulsion compared with the Curtis Schmidt survey on IIIaJ emulsion. The adopted dispersions were 1580Å mm^{-1} ($\frac{dx}{d\lambda} = 6329$) for the CTIO-4m and 1400Å mm^{-1} ($\frac{dx}{d\lambda} = 7143$) for the Curtis Schmidt; the plate scales were 1.85×10^4 arcsec m^{-1} for the CTIO-4m and 9.7×10^4 arcsec m^{-1} for the Curtis Schmidt.

Using equation 6.2.10, for the CTIO-4m survey the lower limiting continuum magnitude is 20.7 for 2 arcsec seeing and 21.4 for 1 arcsec seeing; for the Curtis Schmidt survey the lower limiting continuum magnitude is 19.4 for 2 arcsec seeing and 20.1 for 1 arc seeing.

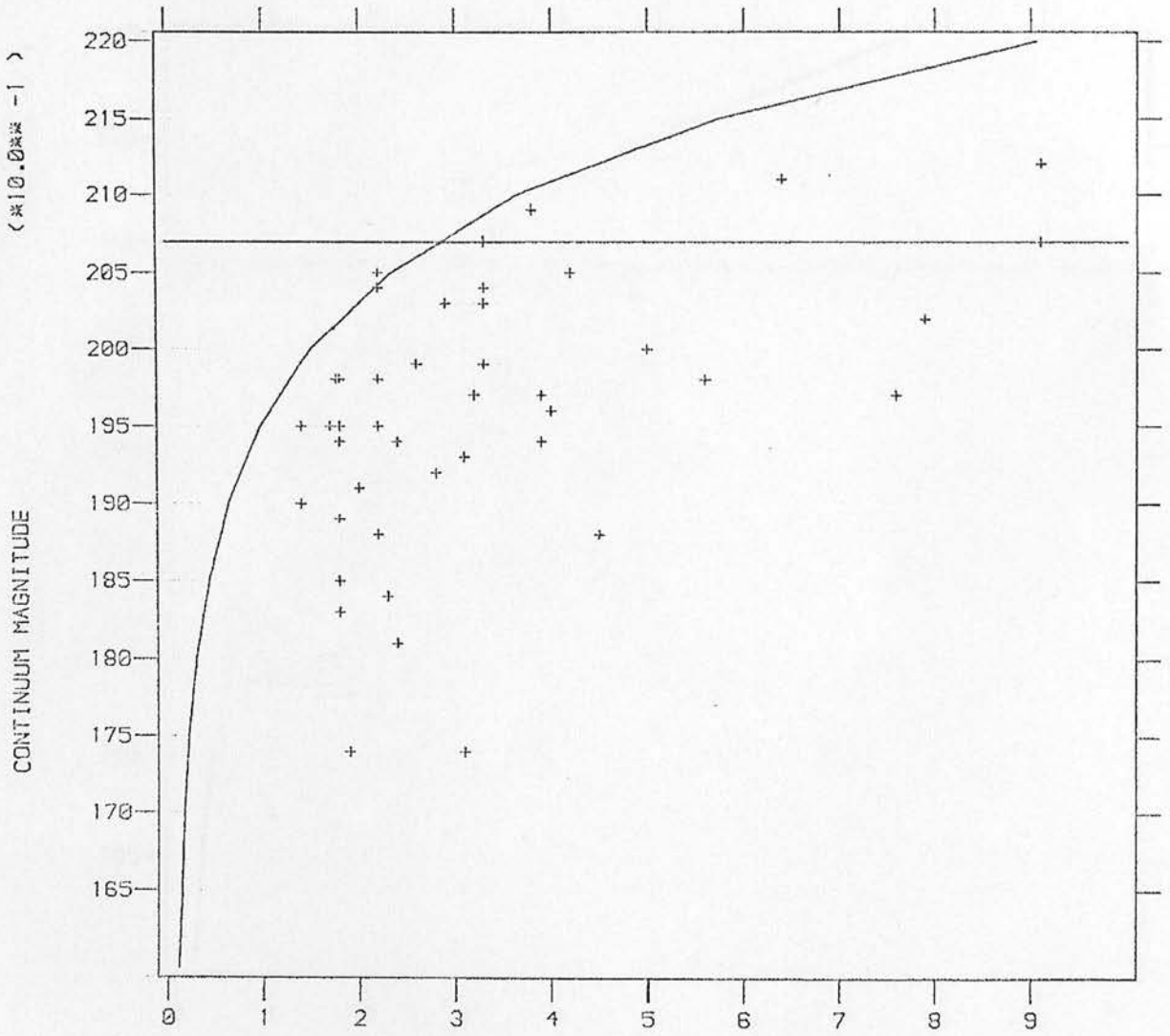

FIG.6.2.3 CTIO-4M LY EW(A) (*10.0** 2)

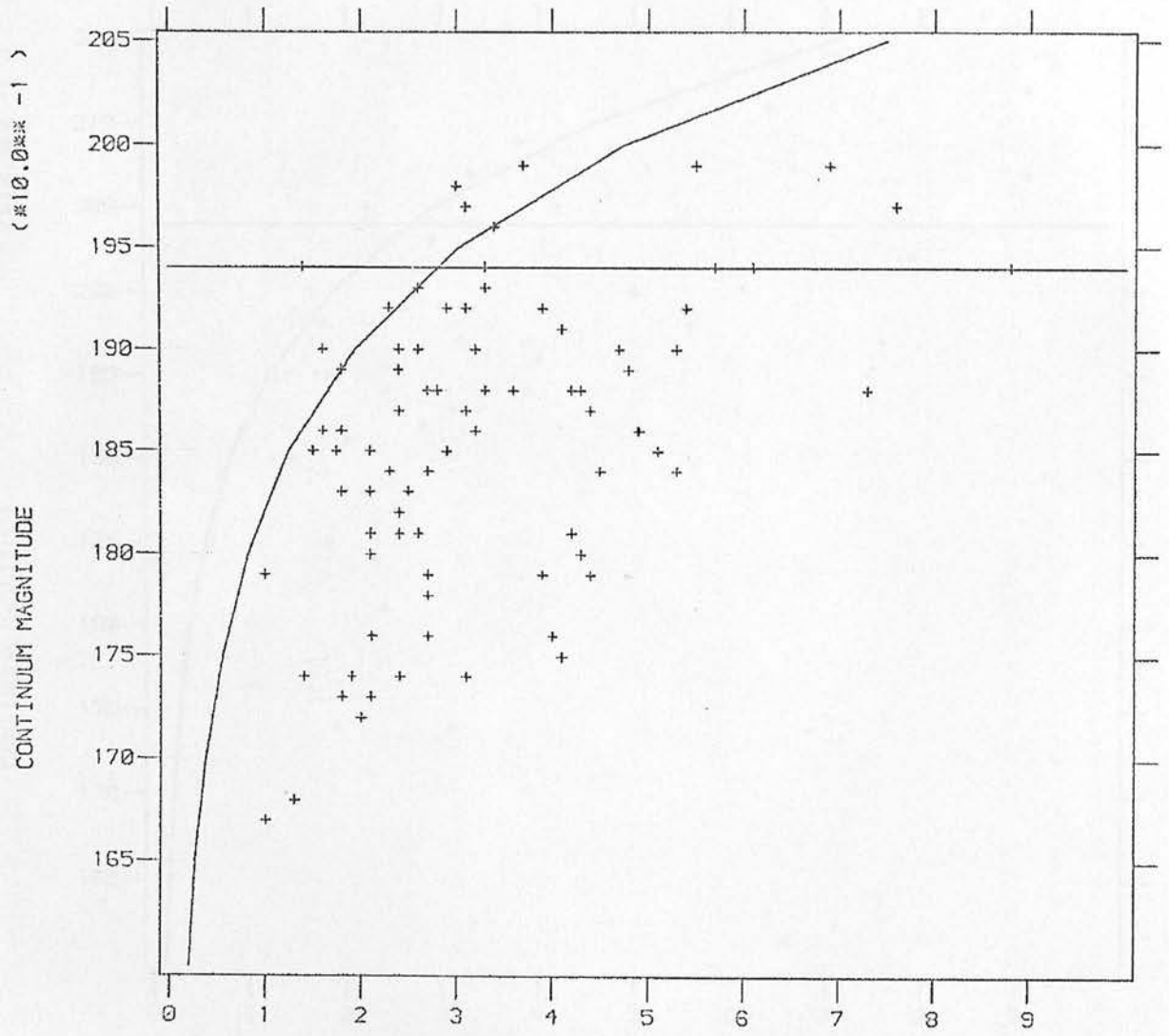

FIG.6.2.4 CS LY EW(A) (*10.0** 2)

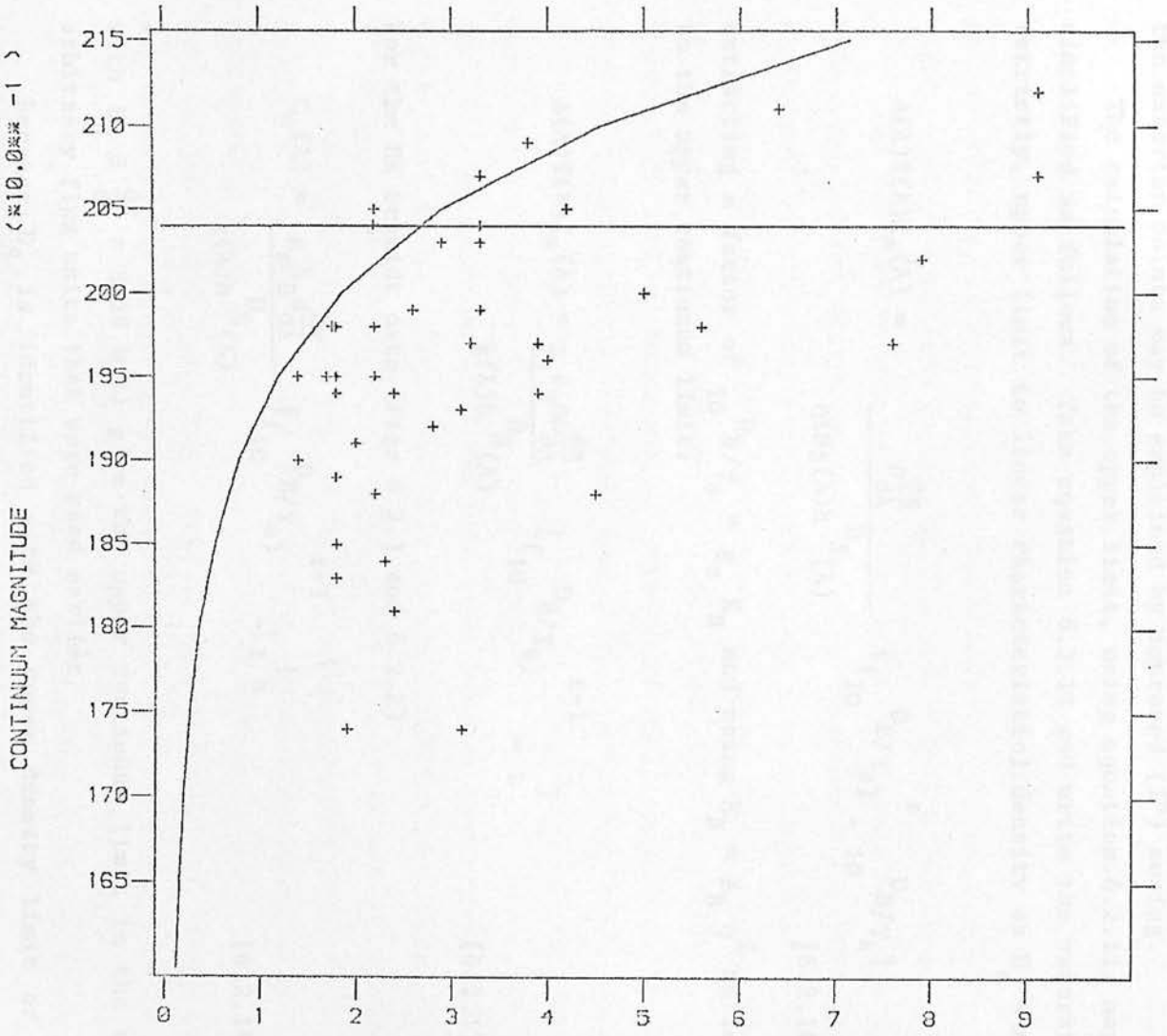

FIG.6.2.5 CTIO-4M LY EW(A) (*10.0** 2)

These values and the selection curves (Figs 6.2.3 and 6.2.4) agree quite well with the observations; the few points outside the curves may be explained by detection on plates with improved (1") seeing. The fit for the CTIO-4m survey is poorer than that for the Curtis Schmidt survey. This could, for example, be because the sky background has been underestimated over the greater wavelength coverage of IIIaF or because no allowance has been made for the grating "transmission"; assuming the latter possibility and adopting a mean "transmission" of 80% Fig 6.2.3 is revised to Fig 6.2.5. Again the exterior points may be explained by improved (1") seeing.

The calculation of the upper limit, using equation 6.2.11, may be simplified as follows. Take equation 6.2.11 and write the saturation (strictly, upper limit to linear characteristic) density as $D_s = \varepsilon D_B$:

$$A(\lambda)T(\lambda)I_*(\lambda) = \frac{\rho\frac{dx}{d\lambda}}{\eta tSg(\lambda)h^{D_S(\lambda)}} \left\{ \left(10^{D_{B/\gamma_s}}\right)^{\varepsilon} - 10^{D_{B/\gamma_s}} \right\} \qquad [6.2.16]$$

Extracting a factor of $10^{D_{B/\gamma_s}} = g_s E_B$ and using $E_B = \phi_B \eta^2 tS$ leads to the upper continuum limit:

$$A(\lambda)T(\lambda)I_*(\lambda) = \frac{g_s\phi_B\eta\rho\frac{dx}{d\lambda}}{g(\lambda)h^{D_S(\lambda)}} \left\{ \left(10^{D_{B/\gamma_s}}\right)^{\varepsilon-1} - 1 \right\} \qquad [6.2.17]$$

For the UK Schmidt data (Figs 6.2.1 and 6.2.2)

$$C_*(\lambda) = \frac{g_s E_B d\frac{dx}{d\lambda}}{g(\lambda)h^{D_S(\lambda)}} \left\{ \left(10^{D_{B/\gamma_s}}\right)^{\varepsilon-1} - 1 \right\} \qquad [6.2.18]$$

with $E_B \; d\,\frac{dx}{d\lambda} = 3.29$ will give the upper continuum limit in the same arbitrary flux units that were used earlier.

Because D_S is identified with the upper density limit of the linear characteristic rather than with complete saturation then adopting $D_S \simeq 3$ and consequently $\varepsilon = {}^{D_S}/_{D_B} \simeq 1.84$ in equation 6.2.18

with the usual approximations leads to an upper limit to the continuum flux, in arbitrary units, of 4.2 for the UK Schmidt quasars. This value is beyond the range of Figs 6.2.1 and 6.2.2. Adopting the same ε and without including the grating "transmission" in equation 6.2.17 the upper limit for the CTIO-4m survey is $m_v = 16.6$ for 2 arcsec seeing and $m_v = 17.4$ for 1 arcsec seeing; for the Curtis Schmidt survey it is $m_v = 16.1$ for 1 arcsec seeing.

Although the wavelength dependence of the selection effects has been formulated in this section its application is restrained by the absence of data on $\gamma(\lambda)$, $g(\lambda)$ and consequently $h(\lambda)$ at short wavelengths, where rapid changes are suspected. When such data become available the selection parameter $W(\lambda)/\Delta\lambda$ will be particularly appropriate because it does not depend on a specific emission line or on the redshift. A convenient approximation will be the adopting of a fixed, typical continuum density in the term $h^D C(\lambda)$ of equation 6.2.9.

Some qualitative comments may easily be made about the wavelength dependence of the selection effects. The functions $A(\lambda)$, $T(\lambda)$ and $\frac{d\lambda}{dx}$ increase with increasing wavelength so that line detection is favoured at long wavelengths. For a particular emission line this trend will be opposed by the increase of line width with redshift. These dependences will be modified, of course, by $\gamma(\lambda)$ and $g(\lambda)$. The sharp peak in $\gamma(\lambda)$ near the emulsion cut-off will, through $h(\lambda)$, enhance line detection there. For grism quasars the blaze of the grating should be included.

This discussion of the selection effects has continued the approximation that the seeing disc in the direction of dispersion can be regarded as a delta function. This approximation is certainly appropriate to the typical prism and grism quasars for which the redshifts are $z \sim 2$ and the FWZI's of the emission lines are consequently much greater than the wavelength-widths of the seeing disc in good (FWZI $\lesssim$ 2 arcsec) seeing. However, in poor seeing (FWZI $\gtrsim$ 3 arcsec), and particularly for emission lines that lie close to the emulsion cut-off, a correction for the spread of the seeing disc may be made by increasing $\Delta\lambda$ by a factor $\sim \sqrt{2}$ when the widths of the lines and the seeing disc are comparable.

6.3 Comparison of the CTIO-4m and Curtis Schmidt Surveys

The previous section contains a description of the selection effects that operate in the Curtis and UK Schmidt surveys and in the CTIO-4m survey for quasars. The selection curves now contribute to a discussion of the different surface densities that result from the CTIO-4m and Curtis Schmidt surveys. The slit spectra and deduced data for these surveys are given in Osmer (1980) and Osmer and Smith (1980).

Osmer's (1980) Figure 7 shows that the surface density of CTIO-4m quasars is ~ 10 times greater than the surface density of Curtis Schmidt quasars "at a magnitude where they might be expected to overlap". The CTIO-4m quasars were discovered in an area of 5.1 square degrees and the Curtis Schmidt quasars in the 340 square degrees of the high galactic latitude zone ($b < -50°$).

Osmer (1980) did not allow for the ability of the CTIO-4m plates to show weaker lines at a given continuum magnitude than the Curtis Schmidt plates. In Fig 6.3.1 such allowance is made by superimposing the Curtis Schmidt selection curves on the CTIO-4m data (as usual the plot is for the detection of Ly-α + NV). Then, in Fig 6.3.1, only those CTIO-4m quasars with $m_V \leq 19.4$ and to the right of the selection curve (definition: those quasars in the Curtis Schmidt "free region") could, with 2 arcsec seeing, also be detected with the Curtis Schmidt. The surface density of those CTIO-4m quasars only should be compared with the surface density of Curtis Schmidt quasars. In this way Fig 6.3.1 gives 13 quasars (actually 12 because a nearby bright star caused the spectrophotometry of Q21 12 10 - 40 43 to be uncertain and no data were given in Osmer (1980); data for this quasar were given in Osmer and Smith (1980)) in 5.1 square degrees or 2.5 quasars per square degree for the CTIO-4m survey in the Curtis Schmidt free region while Fig 6.2.4 leads to 66 quasars in 340 square degrees or 0.2 quasars per square degree for the Curtis Schmidt survey (Fig 6.2.4 actually gives 70 points in the free region; each of 7 points corresponds to 2 quasars so there are really 77 quasars in the free region; of these 77, 11 were discovered in fields at low galactic latitudes ($b > -50°$) that were not part of the 340 square degrees). Thus at first sight the surface density of CTIO-4m quasars appears to

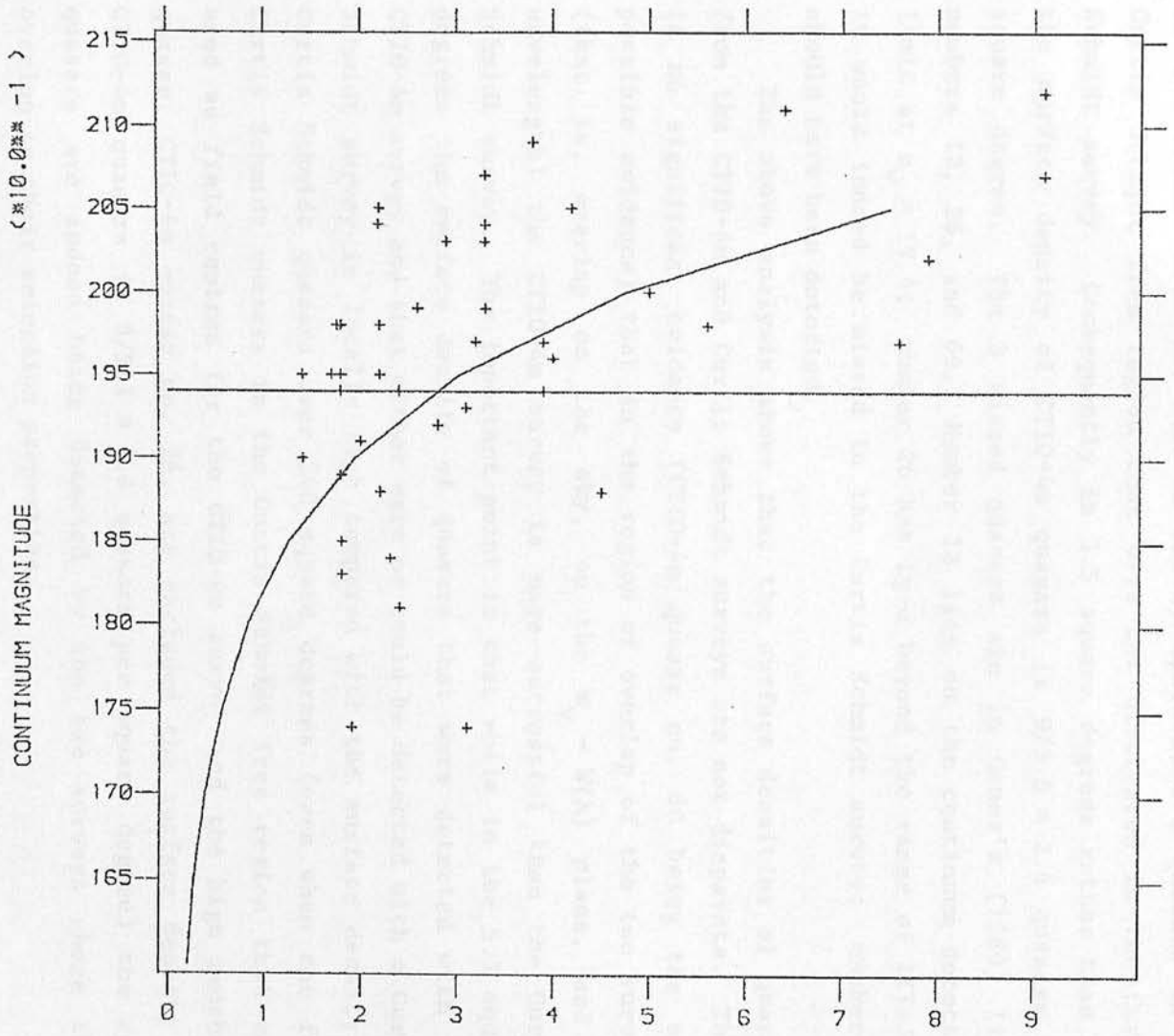

FIG.6.3.1 CTIO-4M LY EW(A);CS CURVES (*10.0** 2)

be ~ 13 times greater than that of the Curtis Schmidt quasars. However the discrepancy is actually the consequence of an incorrect argument. According to Osmer the CTIO-4m and Curtis Schmidt surveys have ~ 3.5 square degrees of sky in common. The CTIO-4m survey finds 6 Curtis Schmidt quasars (including Q21 12 10 - 40 43 and three other quasars that were also used a field centres) in the common area of sky and in the Curtis Schmidt free region so that the local surface density of Curtis Schmidt quasars is 6/3.5 = 1.7 quasars per square degree. Surface densities of 1.7 and 2.5 are certainly compatible. In the common area the CTIO-4m survey discovered 3 quasars in the Curtis Schmidt free region that were not discovered in the Curtis Schmidt survey. Consequently in 3.5 square degrees rather than 5.1 the surface density of CTIO-4m quasars is 9/3.5 = 2.6 quasars per square degree. The 3 missed quasars are in Osmer's (1980) list, numbers 12, 26, and 60. Number 12 lies on the continuum detection limit at $m_V = 19.4$; number 26 has Ly-α beyond the range of IIIaJ so it would indeed be missed in the Curtis Schmidt survey; number 60 should have been detected.

The above analysis shows that the surface densities of quasars from the CTIO-4m and Curtis Schmidt surveys are not disparate. There is no significant evidence (CTIO-4m quasar no. 60 being the only possible evidence) that in the region of overlap of the two surveys (that is, overlap on the sky, on the $m_V - W(\lambda)$ plane, and in wavelength) the CTIO-4m survey is more successful than the Curtis Schmidt survey. The important point is that while in the 5.1 square degrees the surface density of quasars that were detected with the CTIO-4m survey and that either were or could be detected with a Curtis Schmidt survey is locally high compared with the surface density of Curtis Schmidt quasars over 340 square degrees (even when the four Curtis Schmidt quasars in the Curtis Schmidt free region that were used as field centres for the CTIO-4m survey and the high redshift quasar, CTIO-4m quasar no. 26, are excluded the surface density of CTIO-4m quasars is 8/5.1 = 1.6 quasars per square degree) the same quasars are indeed being detected by the two surveys where they overlap in their selection properties.

The CTIO-4m survey and even the Curtis Schmidt survey do not obviously represent the whole sky.

The present lack of an absolute calibration for the PDS spectrophotometry of the UK Schmidt quasars prevents a real comparison of their surface density with that of the Curtis Schmidt survey. An estimate based on Fig 6.2.1 and an assumed sky brightness of B = 22 ("magnitudes per square arcsec") is that the surface density of the UK Schmidt quasars that should be detected with a Curtis Schmidt survey is ~ 1 per square degree.

6.4 The Cumulative Apparent Luminosity Function

In this section the cumulative apparent luminosity function is discussed for the CTIO-4m and Curtis Schmidt surveys. The slit spectra that are available for all of the constituent quasars makes these surveys a useful source of data for comparing the cumulative apparent luminosity functions of quasars (that were discovered by slitless spectroscopy) before and after the inclusion of selection effects.

Only those quasars that were discovered primarily by Ly-α + NV are considered. The redshifts are therefore in the range $1.6 \leq Z \leq 3.4$. The quasar Q21 12 10 - 40 43 has been included although its spectrophotometry was believed to have been affected by a nearby bright star. As usual the relevant data for the two surveys are given in Osmer (1980) and Osmer and Smith (1980).

A short program was written to count the numbers of quasars that were at or brighter than a given apparent magnitude and that exceeded a given equivalent width limit.

For 2 arcsec seeing the work of section 6.2 gives the limiting continuum magnitude of the Curtis Schmidt survey as $m_V = 19.4$, and at this magnitude the limiting equivalent width is 277Å. For the CTIO-4m survey with 2 arcsec seeing and including 80% grating "transmission" the limiting continuum magnitude is $m_V = 20.4$, and at this magnitude the limiting equivalent width is 268Å. Consequently, if equivalent widths are restricted to $W(\lambda) > 277$Å the Curtis Schmidt and CTIO-4m surveys are, in principle, complementary (however, the approximations in the quantification of the selection effects and the possibly unrepresentative areas of the sruveys should not be forgotten). With this restriction the cumulative counts are shown in the lower curves

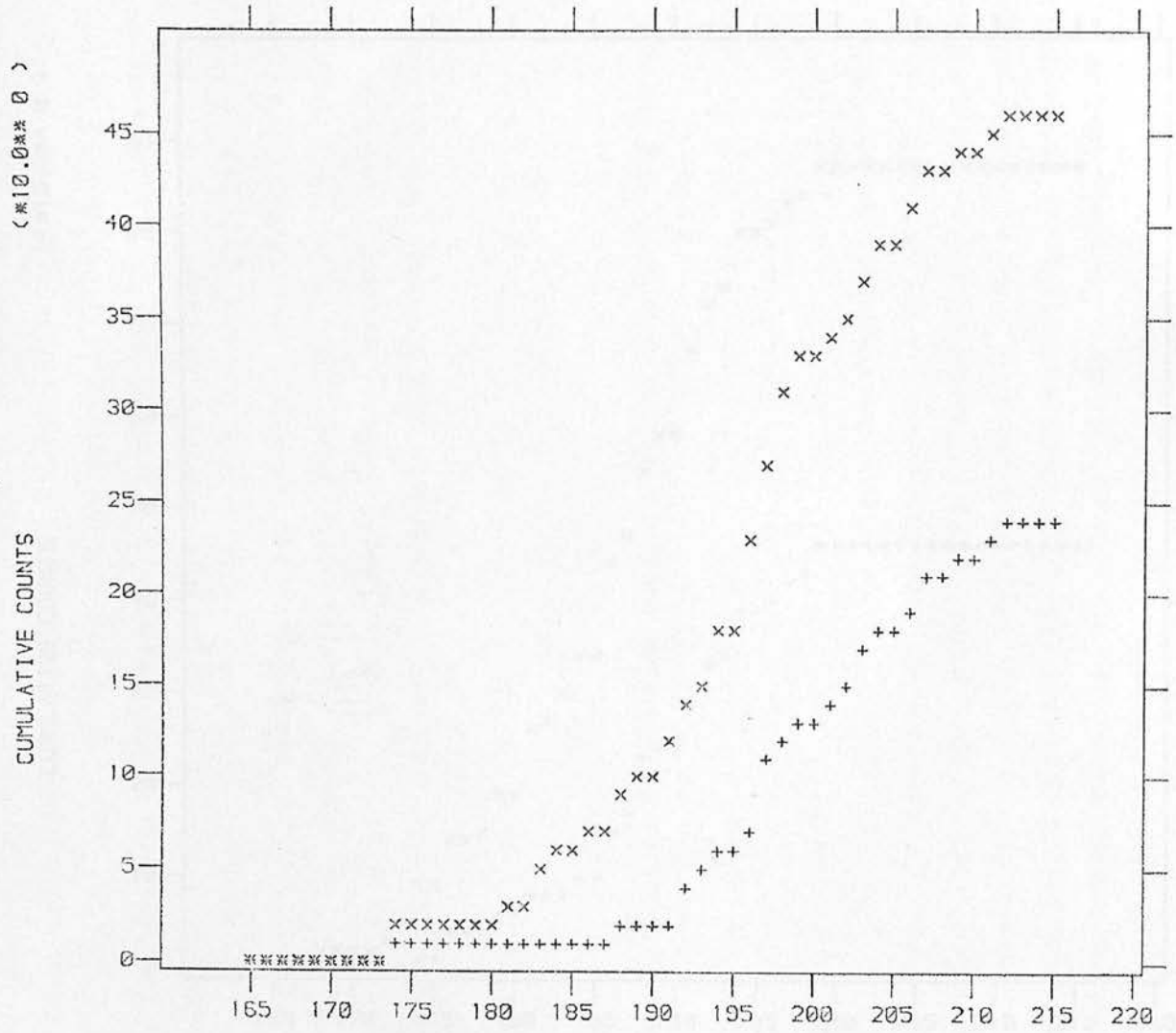

FIG.6.4.1 CTIO-4M CONT MAG (*10.0** -1)

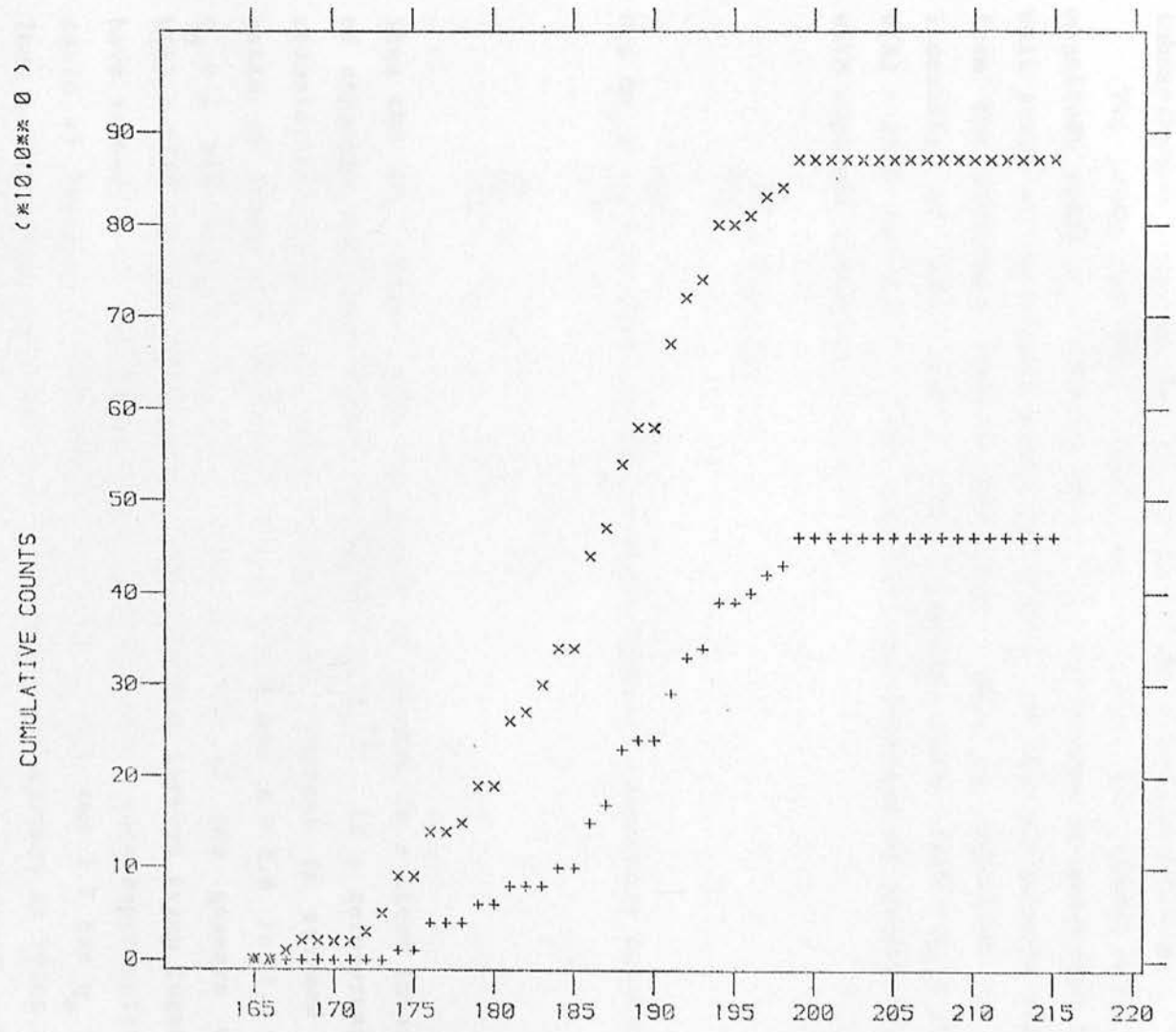

FIG.6.4.2 CS CONT MAG

of Figs 6.4.1 and 6.4.2 for the CTIO-4m and Curtis Schmidt surveys respectively. The upper curves show the cumulative counts for all the Ly-α + NV detections regardless of equivalent widths.

For both surveys the plots of cumulative counts against continuum magnitude appear to have a linear section for the quasars that are restricted to $W(\lambda) > 277$Å. The unrestricted ($W(\lambda) > 0$) plot for the CTIO-4m survey is similar to that of the Curtis Schmidt survey but is, of course, shifted to fainter magnitudes; neither plot possesses a linear section. These unrestricted plots must reflect the inhomogeneous sampling that is caused by the selection effects.

The plots for $W(\lambda) > 277$Å taken together are linear over the magnitude range $m_v \sim 18.4$ to 20.4. The difference in gradients (per unit area) at the common point ($m_v = 19.4$) of the two surveys arises from the different surface densities. What is important is the linearity of the plots: for quasars with $18.4 \leq m_v \leq 20.4$, $W(\lambda) > 277$Å and $1.6 \leq z \leq 3.4$ the rate of increase of quasar counts with apparent continuum magnitude is

$$\frac{\Delta N}{\Delta m_v} = \text{constant}$$

Now $\Delta m_v \propto \frac{-\Delta f_v}{f_v}$ so that the differential apparent luminosity function is

$$\frac{dN}{df_v} \propto -f_v^{-1}$$

Thus the data suggest that the number of quasars in a fixed interval of apparent continuum luminosity varies as f_v^{-1}. If a zero-pressure cosmological model with zero cosmological constant is assumed the ratio of luminosity distances for $z = 3.4$ and $z = 1.6$ is 2.1 for $q_o = 1$ and 3.2 for $q_o = 0$. However, 75% of the quasars with $W(\lambda) > 277$Å from the CTIO-4m and Curtis Schmidt surveys taken together have redshifts in the range 2.0 to 2.8 so that a more representative ratio of luminosity distance is 1.4 for $q_o = 1$ and 1.7 for $q_o = 0$. Then a very crude approximation is to regard the quasars as lying in a thin shell for which no cosmological model need be assumed and in which no evolution with redshift need be considered. This would then

tentatively suggest that the differential absolute luminosity function has the same dependence: $\frac{dN}{dF} \propto F_v^{-1}$.

Smith (1978) and Carswell and Smith (1978) have commented on the inclusion of the Baldwin effect in the luminosity function. The Baldwin effect (Baldwin (1977) and Baldwin et al (1978)) claims, at least for the CIV line in radio-selected quasars with flat radio spectra, that the larger rest frame equivalent widths occur in the intrinsically fainter quasars. Such an effect would cause the luminosity function to be a function of equivalent width. However, even without considering the restrictions to the available area of the m_v - $W(\lambda)$ plane caused by the selection effects the data for the equivalent widths of Ly-α + NV and CIV in the CTIO-4m and Curtis Schmidt surveys do not support the Baldwin effect (see Osmer (1980) and Smith (1978)).

The differential apparent luminosity function does not legitimately relate directly to the differential absolute luminosity function. The former contains the latter and influences from the cosmological model (through the thickness of the shell) and from luminosity or density evolution. To eliminate the variation of factors that depend on redshift the considered range of redshift needs to be narrowed and the total number of quasars needs to be increased. The implied prism or grism survey, which must be automated to be feasible and which must contain all the information for a description of the selection effects, should provide the data for the determination of the luminosity function in several thin shells at different redshifts. An alternative and very appropriate survey technique would be the use of interference filters to detect quasars at particular redshifts. Interference filters at two neighbouring wavelengths would give plates to be searched, using automatic measuring machines (e.g. COSMOS), for images brighter with one filter than with the other. The results would be mostly Ly-α detections at two distinct redshifts.

Finally, note that the linearity of the plots for quasars with $W(\lambda) > 277$Å in Figs 6.4.1 and 6.4.2 does not apparently extend to all quasars. Consideration of the upper curves for the unrestricted data shows that the existence of quasars in the region of the m_v - $W(\lambda)$ plane that is excluded by the selection effects would cause the

cumulative counts to increase even more rapidly at the fainter magnitudes and would therefore cause still greater departures from linearity.

7. Observations of Quasars in the Fields SGP and 345

Several quasars in the fields SGP and 345 were observed with the Image Photon Counting System on the Anglo-Australian Telescope. The chapter describes the instruments, the observations and the results.

7.1 Introduction

The observations of quasars in the fields SGP and 345 were obtained in collaboration with Alec Boksenberg, Russell Cannon, Ann Savage, Malcolm Smith and Jasper Wall. The original intention was to obtain absolute spectrophotometry for the calibration of the objective-prism spectrophotometry. However the weather during the usable nights was usually suitable only for the reserve programme of the confirmation of quasar candidates and observations of individually interesting quasars. Three quasars with broad absorption were observed and two of them have now been published in Clowes et al (1979). Three high-redshift ($z \lesssim 2.8$) quasars were observed and they are included in a paper (Smith et al (1980)) on the Lyman limit in quasars.

The earlier and mostly unpublished observations by Cannon, Smith and Boksenberg of quasars in these two fields are not given here but some of them have been used in the comparison of the objective-prism and PDS spectra with the corresponding IPCS spectra (section 4.4). Those observations are not absolutely calibrated.

7.2 The Anglo-Australian Telescope and the Image Photon Counting System

The Anglo-Australian Telescope is situated near Coonabarabran in New South Wales, Australia at an altitude of 1164m and on the same mountain as the UK Schmidt Telescope.

The clear aperture of the hyperboloidal primary mirror is approximately 3.9m and the focal length is 12.70m so that the prime focus is ~ f/3.3. Other foci are the f/8 Cassegrain, the f/15 Cassegrain and the f/36 Coudé.

The RGO spectrograph, which mounts at the f/8 focus (scale = 6.70

arcsec mm^{-1}) was used with the 25cm, f/1.67 camera for all the observations. The detector was the Image Photon Counting System. The slit of the spectrograph is 38mm long and lengths of it from 0.15mm may be isolated by dekker masks. The slit width may be varied from 0.07 to 16.75 arcsec (10μm to 2.5mm). Neutral density and colour filters may be inserted into the light path. A copper-argon arc lamp is available for wavelength calibration and a tungsten continuum lamp for determining the spatial variations of image tube sensitivity.

The IPCS can detect, locate and count individual photon events. The system provides a two-dimensional array of ~ 10^6 pixels but the number of them that is actually used depends on the storage requirements (before the introduction of the external memory the computer core limited the number of usable pixels to ~ 18000). The IPCS may be used in its 1D or 2D modes, but with the external memory the latter is usual.

The sky-subtracted accumulated counts may be displayed throughout an integration so that the observer knows when sufficient data have been acquired. Data are normally written to magnetic tape.

The IPCS counting rate of ~ 1 sec^{-1} $Å^{-1}$ near 5500Å for a star at V = 15 indicates that ~ 1% of the available photons there are detected. The response of the system peaks at ~ 4100Å.

The telscope manual contains information on the RGO spectrograph and the IPCS but there are also separate manuals that describe those instruments in greater detail.

7.3 The Observations

The observations were made in 1978 and 1979 using grating 250B (grating 4), with nominal reciprocal dispersion of 156Åmm^{-1}, except for the observations of the broad absorption quasar Q2240.9-3702 on 20/21 October 1978 when grating 1200V (grating 1), with nominal reciprocal dispersion of 33Åmm^{-1}, was used. The gratings were used blaze-to-collimator and with the 25cm camera. Each frame line or channel corresponded to ~ 15μm and each line increment (X-gain low) corresponded to 2.5 arcsec (User's Guide to the RGO spectrograph). The spectral resolution was ~ 10Å except for the observations of Q2240.9-3702 on 20/21 October 1978 when it was ~ 2Å.

The journal of the observations is given in Table 7.3.1. Whether the observations were taken in the 1D or 2D modes of the IPCS is indicated there. In both cases two apertures, A and B, were defined for object plus sky and sky alone. Objects were observed for equal times in each aperture so that asymmetries in the spatial response of the detector would not cause incorrect sky subtraction : each object plus sky integration had a matching sky integration (except for 331 seconds of the integration on 2227.4-4107). Standard stars were observed in the same way (but through neutral density filters) to determine the wavelength dependence of the detector response. Correction for atmospheric extinction used a standard function in SDRSYS, and consequently there could be errors, particularly at short wavelengths.

Exposures of the copper-argon arc were obtained for wavelength calibration. Because of the relative weakness of ultraviolet lines compared with red the wavelengths of the spectra obtained in 1978 might be in error below ~ 3500Å. For the 1979 observations the ultraviolet arc lines were enhanced by filtering out the red lines during part of the arc exposures. Frequent arc exposures were taken to correct possible wavelength shifts caused by the floppy image tube (see AAO Newsletter no. 13 (1980)). The data were reduced using the AAO data reduction system SDRSYS.

Table 7.3.2 gives further details of the observed objects. The redshifts deduced from the IPCS spectra, and the COSMOS B magnitudes, where available, are given. The redshifts are typically accurate to ~ 1%. For the three quasars with broad absorption troughs the redshifts are based only on the CIII] λ1909 lines. The "confirmed" column of Table 7.3.2 indicates whether the IPCS spectra confirm the objects as quasars. The "prob. quasar" column indicates the objects that were selected as probable quasars and that were consequently listed in Table 2.3.2 or Table 2.3.3. The "obj. prism" column indicates whether the objects have objective-prism spectrophotometry and the "refs" column indicates papers that include particular spectra.

This section contains illustrations of the F_λ spectra of the objects 2217.7-3830, 2220.0-3904, 2227.4-4107, 0042.9-2657, 0045.8 -2604, 0048.8-2804, 0050.8-2806, Q0100.5-2809, Q0101.5-3025 and

TABLE 7.3.1 Journal of AAT observations

NAME	1950 RA, DEC	DATE	DWELL(s)	SLIT(")	1D/2D	SEEING(")
2217.7 - 3830	22 17 43.0 -38 30 35	29/30 AUG 79	4000	1.5	2D	1.5
2220.0 - 3904	22 21 01.2 -39 04 10	29/30 AUG 79	2000	1.5	2D	1/1.5
2227.4 - 4107	22 27 21.2 -41 07 08	29/30 AUG 79	2331	1.5	2D	1.5
2231.8 - 4154	22 31 48.8 -41 54 04	29/30 SEPT 78	600	2.5	1D	6
2235.1 - 4004	22 35 09.0 -40 04 12	29/30 SEPT 78	2000	2.5	1D	6
2238.9 - 4115	22 38 55.5 -41 15 10	29/30 SEPT 78	4000	2.5	1D	6
2240.9 - 3702	22 40 55.5 -37 02 50	29/30 SEPT 78	4000	2	1D	4
2240.9 - 3702	22 40 55.5 -37 02 50	20/21 OCT 78	11200	1.5	1D	1.5/2
0042.9 - 2657	00 42 51.9 -26 57 20	30 SEPT/1 OCT 78	2000	2.5	1D	3
0045.8 - 2604	00 45 49.8 -26 04 10	29/30 AUG 79	1238	1.5	2D	1/1.5
0048.8 - 2804	00 48 46.9 -28 04 22	29/30 AUG 79	4000	7	2D	1.5
0050.8 - 2806	00 50 49.2 -28 06 30	29/30 AUG 79	4000	6.5	2D	1
0100.5 - 2809	01 00 32.6 -28 09 50	30 SEPT/1 OCT 78	2000	2.5	1D	3
0101.5 - 3025	01 01 30.5 -30 25 57	30 SEPT/1 OCT 78	4000	1.5/2.5	1D	3
0103.9 - 2913	01 03 54.0 -29 13 11	30 SEPT/1 OCT 78	2000	2.5	1D	3

TABLE 7.3.2 Summary of Observed Objects

NAME	Z	COSMOS B	CONFIRMED	PROB. QUASAR	OBJ. PRISM	REFS	COMMENTS
2217.7 - 3830	1.52*		YES	YES			Broad Absorption at z = 1.46
2220.0 - 3904	0.36?		YES				Single Line at 3800Å
2227.4 - 4107							Spectrum Variable? - see text
2231.8 - 4154				YES			
2235.1 - 4004							
2238.9 - 4115	1.83*		YES	YES		1	Broad Absorption
2240.9 - 3702	1.82*		YES	YES		1	Broad Absorption
0042.9 - 2657	2.90		YES	YES		3	
0045.8 - 2604	0.49?	18.6	YES	YES	YES		Single Weak Feature at 4160Å
0048.8 - 2804	0.85	17.6	YES	YES	YES		
0050.8 - 2806	1.82	19.0	YES	YES	YES		
0100.5 - 2809	1.80	19.3	YES	YES	YES		
0101.5 - 3025	3.16	18.8	YES	YES		3	
0103.9 - 2913	2.80	18.6	YES	YES	YES	2,3	

1 Clowes et al (1979)

2 Clowes et al (1980)

3 Smith et al (1980)

*Redshifts based on CIII] λ1909 only.

See text for further details

Q0103.9-2913 in Fig 7.3.1 (the names of the objects are on the left edges of the plots and although they are generally of different formats from the names in Tables 7.3.1 and 7.3.2 they are immediately recognisable). F_ν spectra of Q2240.9-3702 and Q2238.9-4115 are given in Clowes et al (1979) (an offprint is included in this thesis) and in Fig 7.3.2.

The spectra of 2231.8-4154 and 2235.1-4004 are not shown because the objects were not confirmed as quasars although the former was listed in Table 2.3.3 as a "probable quasar". Presumably they are stars.

The object 2227.4-4107 was not selected as a probable quasar and indeed was not confirmed as a quasar. The IPCS spectrum is given in Fig 7.3.1, however, because it does not obviously correspond to the density spectrum on UJ2461P. On the plate UJ2461P (July 1976) the density spectrum of 2227.4-4107 indicated a sharp discontinuity in the spectrum at ~ 4700Å with the stronger intensity being at the longer wavelengths. The feature was much less marked on UJ4512P (September 1978) but there was no obvious change in the continuum at shorter wavelengths. The IPCS spectrum (August 1979) is quite flat and shows no feature at ~ 4700Å. Quantitative work on the prism spectra is required to confirm that the spectrum of 2227.4-4107 has varied (unfortunately there is no calibration spectrogram for the emulsion batch of UJ2461P).

The object Q2220.4-3904 was not selected as a probable quasar (rather, a possible quasar - but on re-examining the spectrum on UJ2461P the classification does seem rather cautious) but was found to be a quasar. It has a single emission line at 3800Å, which is presumably MgII λ2798 at a redshift of 0.36. The quasar Q0045.8-2604 has a single convincing emission line at 4106Å, which is again presumably MgII λ2798 but at a redshift of 0.49. The identification of this object as a quasar on UJ2461P was reinforced by the strong continuum in the blue.

Another moderately low redshift ($z = 0.85$) quasar is Q0048.8-2804. This quasar was detected more by its strong blue continuum than by its emission lines.

The three high-redshift quasars Q0042.9-2657, Q0101.5-3025 and Q0103.9-2913 are discussed in the paper by Smith et al (1980), which

Fig 7.3.1 F_λ spectra of the objects 2217.7-3830, 2220.0-3904, 2227.4-4107*, 0042.9-265**, 0045.8-2604, 0048.8-2804, 0050.8-2806, 0100.5-2809, 0101.5-3025 and 0103.9-2913. Flux scales are unnormalised and wavelengths are in Angstroms.

* Identified as UKS 2227-411

** Identified as Q0042.8-2657

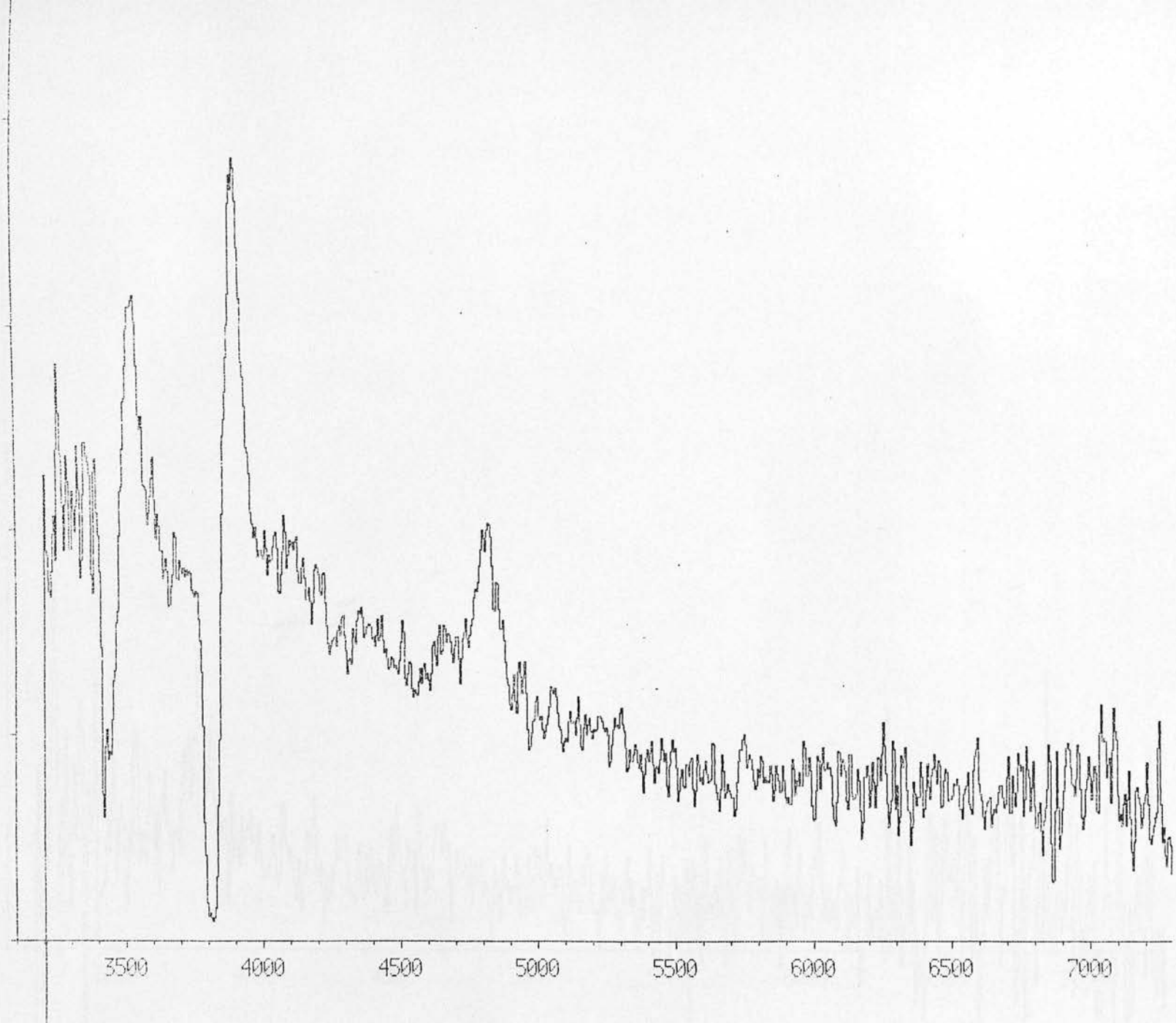

2217-3830

3500
4000
4500
5000
5500
6000
6500
7000

7000
6500
6000
5500
5000
4500
4000
3500

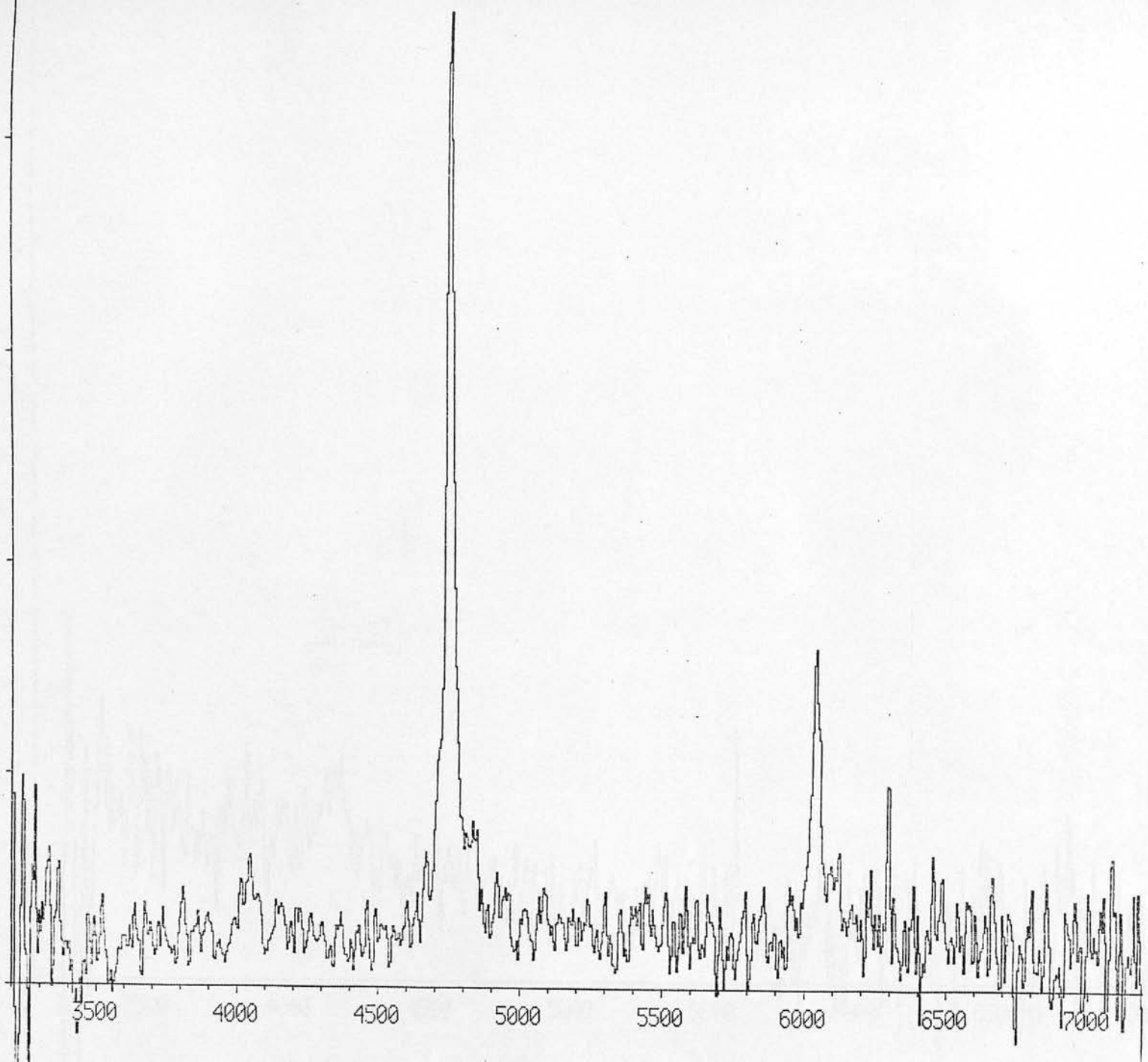

Q0042. 8-2657

3500
4000
4500
5000
5500
6000
6500
7000

0048-2804

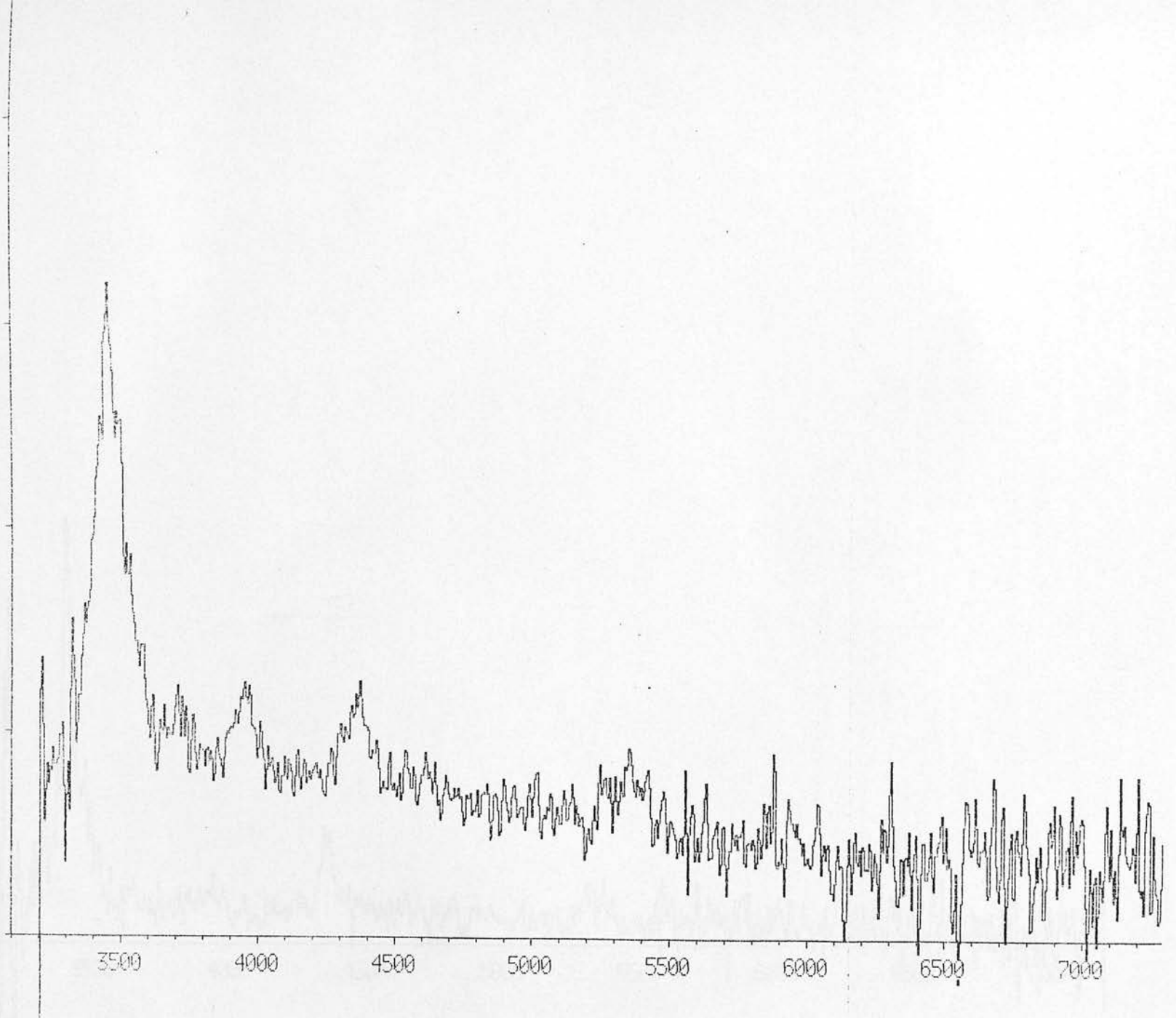

0030-2806

Q0100. 5-2809

Q0101. S-3025

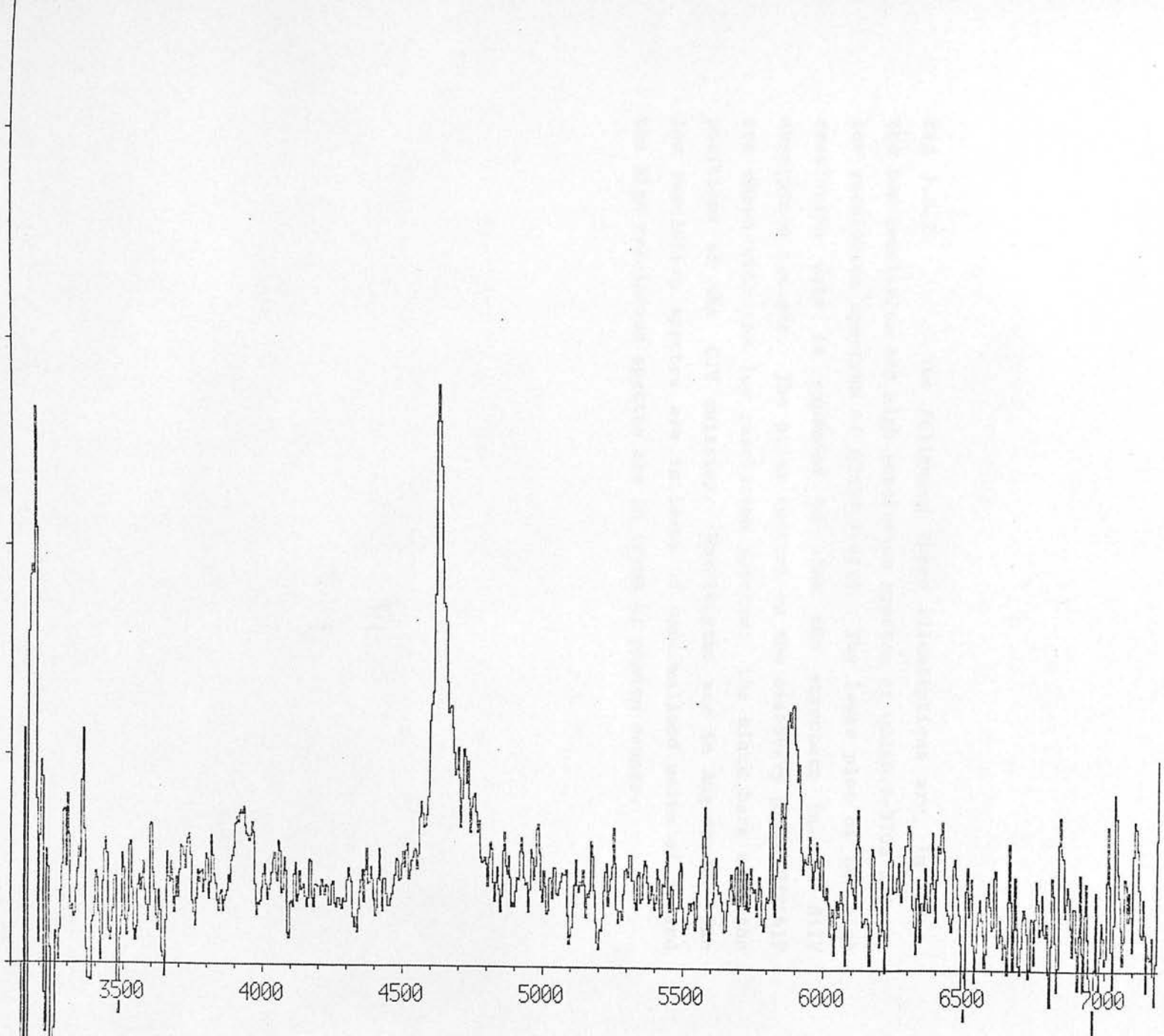

Q0103. 9-2913

Fig 7.3.2 The following three illustrations are, in order, the low resolution and high resolution spectra of Q2240.9-3702 and the low resolution spectrum of Q2238.9-4115. The lower plot of the high resolution data is expanded to show the structure in the SiIV absorption troughs. The prism spectra on the discovery plate UJ2461P are shown with the low resolution spectra; the black bars mark the positions of the CIV emission. Wavelengths are in Angstroms. The low resolution spectra are in terms of unnormalised units of F_v and the high resolution spectra are in terms of photon counts.

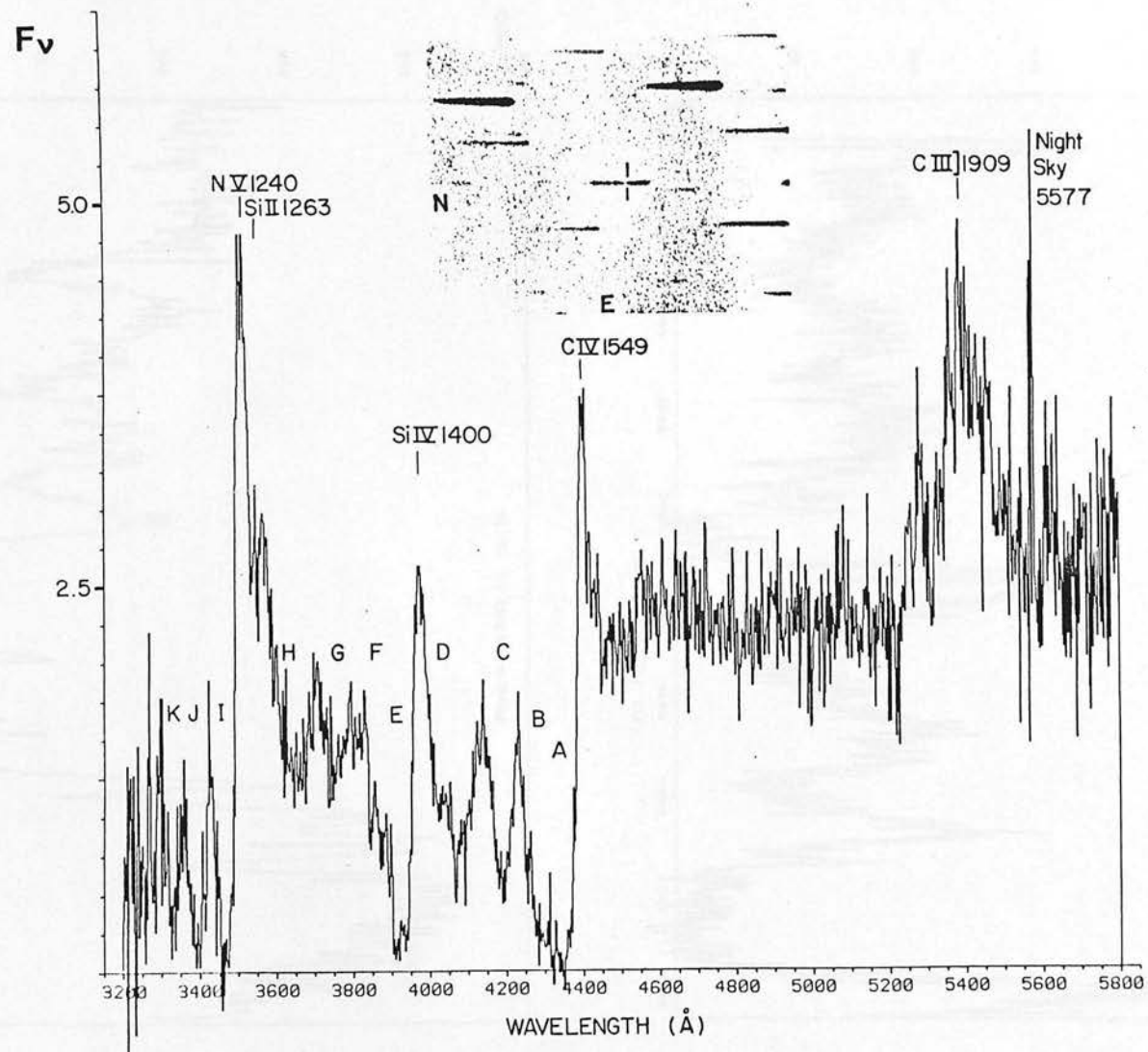
Fν
5.0
2.5
N V 1240
Si II 1263
C IV 1549
Si IV 1400
C III] 1909
Night
Sky
5577
N
E
K J I H G F E D C B A
3200 3400 3600 3800 4000 4200 4400 4600 4800 5000 5200 5400 5600 5800
WAVELENGTH (Å)

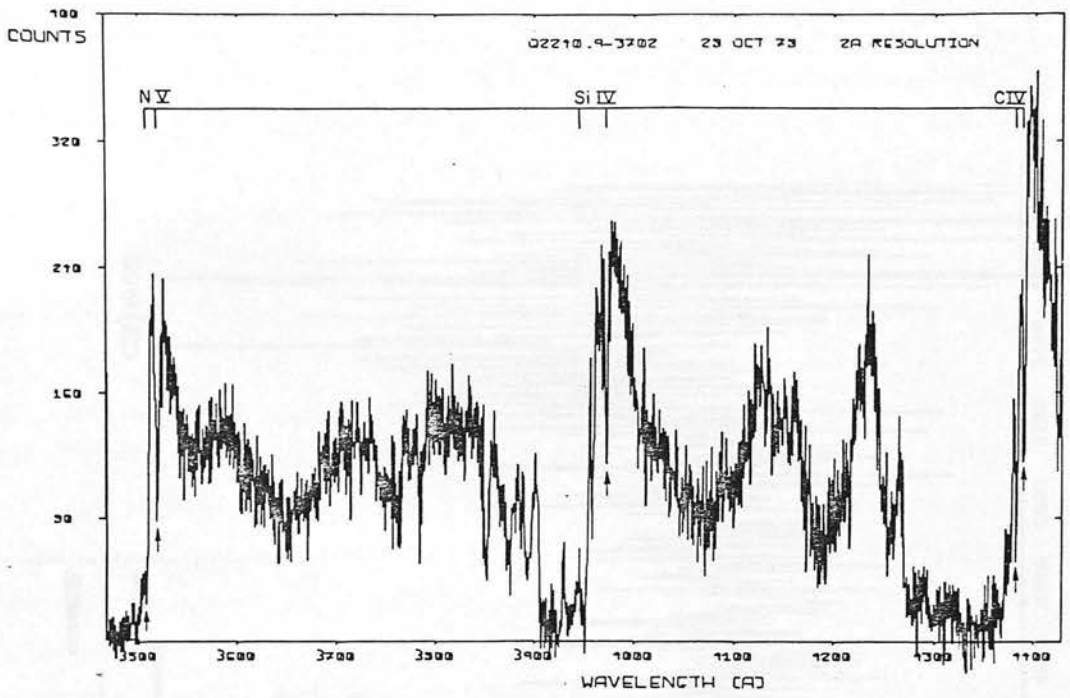
COUNTS
02210.9-3702 23 OCT 73 2A RESOLUTION
N V
Si IV
C IV
WAVELENGTH (A)

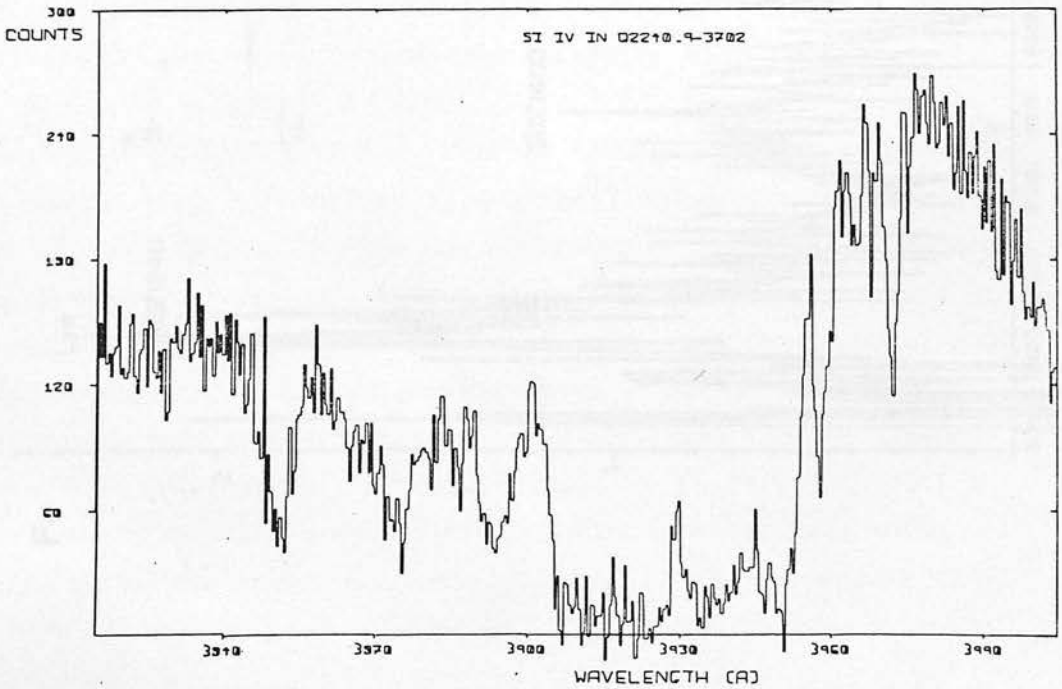
COUNTS
SI IV IN 02210.9-3702
WAVELENGTH (A)

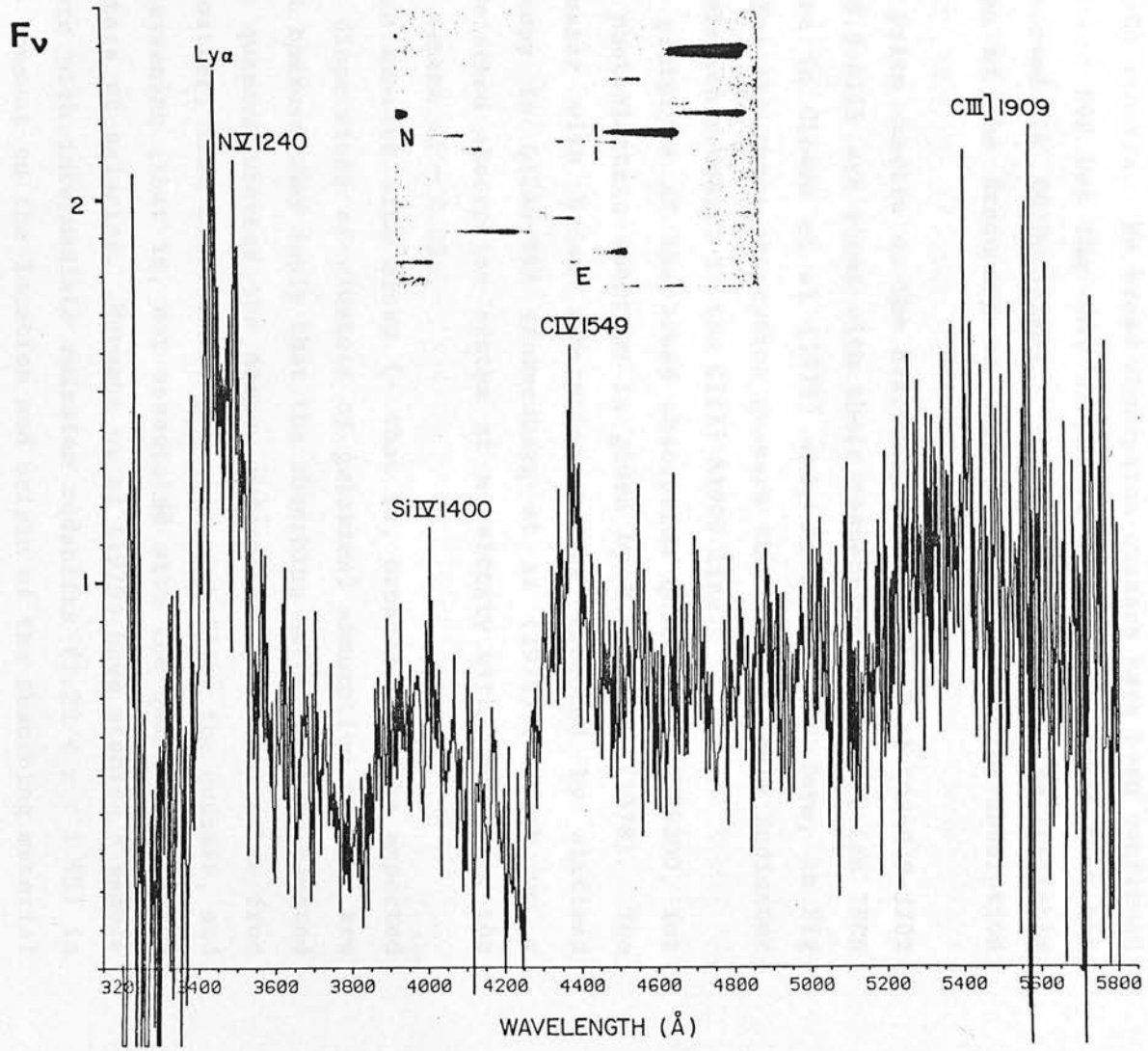
F_ν
Lyα
NV 1240
SiIV 1400
CIV 1549
CIII] 1909
N
E
2
1
3200
3400
3600
3800
4000
4200
4400
4600
4800
5000
5200
5400
5600
5800
WAVELENGTH (Å)

is concerned with observations of the Lyman limit in quasars and the location and covering factor of absorbing clouds.

7.4 The Quasars With Broad Absorption Troughs

The three quasars Q2217.7-3830, Q2240.9-3702 and Q2238.9-4115, all in field 345, were believed to have broad absorption troughs visible in their prism spectra and these troughs were indeed confirmed by the IPCS spectra. No broad absorption quasars have been confirmed in the field SGP but the only suspected absorption quasar that has been observed is Q0100.5-2809. There is presently no reliable indication of the frequency of occurrence of the broad absorption quasars.

The prism spectra on the discovery plate UJ2461P of Q2240.9-3702 and Q2238.9-4115 are shown with their respective low-resolution IPCS F_ν spectra in Clowes et al (1979) and, in a degraded form, in Fig 7.3.2. For the three absorption quasars the only reliable indicator of the emission redshift is the CIII] λ1909 line.

The prototype of the broad absorption quasars is PHL5200, for which a photoelectric spectrum is given by H.E. Smith (1978). The first quasar with broad absorption to be detected by slitless spectroscopy is Q1246-057 (Boksenberg et al (1978)), which has a single detached absorption system at a velocity with respect to the emission system of ~ 0.05c.

These quasars with broad (- that is, broader than the expected velocity dispersions of clusters of galaxies) absorption troughs are important because they imply that the absorbing matter must be ejected from the quasars whereas the narrow absorption lines can arise from ejected matter, from clusters of galaxies containing the quasars, and from intervening (that is, not associated with the quasars) galaxies and clusters of galaxies. Weymann et al (1979) have studied a sample of quasars with intermediate emission redshifts ($1.20 < z < 1.95$) in order to comment on the location and origin of the absorbing material that produces narrow-lined absorption systems. They conclude that systems with velocities or equivalent velocities V with respect to the emission system are

(i) typically due to either ejected or independent intervening matter when $3000\text{kms}^{-1} \lesssim V \lesssim 20000\text{kms}^{-1}$,

(ii) typically due to clusters containing the quasars when $V \lesssim 3000\text{kms}^{-1}$,

(iii) typically due to intervening galaxies and clusters when $V \gtrsim 20000\text{kms}^{-1}$.

Weymann et al (1979) interpret the broad absorption troughs as the consequences of short-lived explosive events rather than continuous outflows. They tentatively relate the explosions to the outbursts in radio and optically active quasars. Furthermore, they interpret the absorbing matter that causes the narrow-lined, ejected absorption systems as the debris, after dissipation, cooling and condensation, of the explosions that cause the broad absorption troughs. Rees (1970) discusses a process of condensation into filaments.

Structure in the broad absorption troughs of a quasar was first observed in the high resolution data of Q2240.9-3702 (Clowes et al (1979) and Fig 7.3.2). There is consequently evidence but not proof that such a condensation process is occurring in this quasar. The arrows in the upper plot of the high resolution data indicate a clear, narrow-lined absorption system at a redshift of 1.8316. Although this system apparently has $Z_{abs} > Z_{em}$ the uncertainty in Z_{em} is such that the absorption system cannot be said to be blueshifted with respect to the emission system.

Q2240.9-3702 is certainly an extreme quasar. Between the emission lines of NV λ1240 and CIV λ1549 there are at least 8 broad absorption troughs (labelled A to H in Fig 7.3.2) visible in the low resolution spectrum and they form pairs of SiIV λ1400 and CIV λ1549 in 4 absorption systems with redshifts ~ 1.62, 1.70, 1.76 and 1.80. The velocities relative to the emission system ($z \sim 1.82$) of the absorption systems may be calculated from

$$\frac{V_{rel}}{c} = \frac{(1 + Z_{em})^2 - (1 + Z_{abs})^2}{(1 + Z_{em})^2 + (1 + Z_{abs})^2}$$

which gives ~ 0.07c (22000kms^{-1}), 0.04c (13000kms^{-1}), 0.02c

(6400kms^{-1}) and 0.01c (2100kms^{-1}) for the above absorption redshifts. There is the possibility that the SiIV absorption troughs contain contributions from CIV absorption at ejection velocities greater than 22000kms^{-1} (also, in a different quasar, Q1309-056, there is evidence (AAO Newsletter no. 11 (1979)) for the ejection of absorbing material at velocities ~ 0.12c (35000kms^{-1})). Weymann et al (1979) expect that "there should be very few PHL5200-type absorption systems with ejection velocities much in excess of 18000kms^{-1}".

The 4 absorption systems in Q2240.9-3702 are certainly a simplification of the real structure: for example, the high resolution data clearly show smaller-scale structure in the troughs E and F. The trough D might consist of two features in the same way that the combined troughs A+B and E+F respectively consist of A,B and E,F; the lack of a counterpart in trough H could be due to confusion from line emission.

Ly-α λ1216 emission is absorbed by Ly-α and NV in the highest redshift absorption systems (troughs I and J) and it does not appear above the level of the extrapolated continuum.

Notice that each of the troughs J and K corresponds to Ly-α and NV absorption in different pairs of absorption systems (for the details see Clowes et al (1979)).

An interesting issue is whether the absorption systems in Q2240.9-3702 arise from a single explosion or from repeated explosions. The absorption system with the highest redshift, and consequently the lowest relative velocity, is nearly black so the absorbing gas must nearly cover the emission line region and the continuum source. If the gas has been decelerated and has passed through the emission line region this system may be interpreted as the oldest. If the higher velocity systems are within the emission line region (which is suggested by their smoother absorption profiles) then the interpretation is consistent with at least two independent explosions.

In the quasar Q2238.9-4115 only two (asymmetric) absorption troughs can be identified. They are SiIV and CIV at a redshift of ~ 1.70, which, given the emission redshift of ~ 1.83, indicates an ejection velocity of ~ 0.05c (14000kms^{-1}). Smaller-scale structure could exist in the troughs but it would not be seen in the low signal

-to-noise spectrum.

Q2217.7-3830 has an emission redshift of 1.52 and a single, clear absorption system at a redshift of 1.46, indicating an ejection velocity of $\sim 0.02c$ ($7200 kms^{-1}$). The velocity dispersions of the troughs in Q2240.9-3702 and Q2238.9-4115 may be obtained from Clowes et al (1979). The FWHM values for Q2217.7-3830 are $\sim 5000 kms^{-1}$.

Summary

The thesis shows how the low-resolution, conventional F_λ spectra of quasars may be obtained from their density spectra on objective-prism plates. The full expression for the extraction of the quasar spectrum from the combined monochromatic (at a point) quasar and broadband sky exposures is successfully approximated by taking γ_s to be a constant. The objective-prism spectrophotometry is presently limited by the lack of data for $\gamma(\lambda)$ and $g(\lambda)$ at short wavelengths. With the adopted $\gamma(\lambda)$ and $g(\lambda)$ the equivalent widths of emission lines are, on average, within ~ 40% of the values obtained from IPCS spectra.

Wavelengths were assigned using the dispersion curve and fixed wavelength points were located by transformation from the images on a direct plate. The redshifts from the objective-prism spectrophotometry are, on average, within ~ 1% of the IPCS values.

The technique of objective-prism spectrophotometry leads to a quantification, based on the signal-to-noise ratios necessary for the detection of emission lines and continua, of the selection effects that operate in the searches for quasars or other emission line objects on objective-prism or grism plates. The dependences of the minimum equivalent width that can be detected on continuum flux, wavelength, sky background, plate noise, dispersion, seeing, plate scale, emulsion functions, atmospheric transmission and telescope transmission are formulated. The quantification of the selection effects is used to demonstrate that the CTIO-4m and Curtis Schmidt surveys find the same quasars where the "free" regions of the surveys overlap. The surface density of "Curtis Schmidt" quasars in the 5.1 square degrees of the CTIO-4m survey is locally high compared with the surface density of quasars from the 340 square degrees of the Curtis Schmidt survey, but the CTIO-4m survey is not more successful than the Curtis Schmidt survey where the surveys overlap.

For a complete sample extracted from the CTIO-4m and Curtis Schmidt surveys the data suggest that the number of quasars in a fixed interval of apparent continuum luminosity is inversely proportional to apparent continuum luminosity.

Data on the functions $\gamma(\lambda)$ and $g(\lambda)$ for several batches of

emulsion IIIaJ are presented. The peak in $\gamma(\lambda)$ near the emulsion ($g(\lambda)$) cut-off leads to the detection of lines with lower equivalent widths than would otherwise occur.

AAT/IPCS observations are presented and particular attention is given to the extreme absorption line quasar Q2240.9-3702, in which matter is apparently being ejected at velocities up to $\sim$ 22000kms^{-1} (0.07c).

Acknowledgements

Many people have advised and helped me during the course of this work. I wish to thank

my supervisors : David Emerson, Russell Cannon, Malcolm Smith and Ann Savage

the staff of the UK Schmidt Telescope, especially Peter Standen and John Dawe

Don Morton and the staff of the AAO for hospitality while I was the research student at AAO

the AAO software group : Pat Wallace, Bryony Wallace, John Straede and Helen Darling

John Barrow, John Cooke, Ken Elliott, Gerry Gilmore, Steve Heathcote, Harvey MacGillivray, David Malin, Bruce Peterson and Neill Reid

Linda Robertson for typing this thesis

the Science Research Council and PATT.

References

ALTMAN, J.H. 1977 in The Theory of the Photographic Process ed JAMES, T.H. 4th edition p. 513 Macmillan.

ARP, H. 1980 ApJ 239, 463.

BAHCALL, J.N. & SONEIRA R.M. 1980 ApJ 238, L17.

BALDWIN, J.A. 1977 ApJ 214, 679.

BALDWIN, J.A., BURKE, W.L., GASKELL, C.M. & WAMPLER, E.J. 1978 Nature 273, 431.

BALDWIN, J.A. 1979 in Active Galactic Nuclei p 51 eds HAZARD, C. & MITTON, S. CUP.

BENTLEY, M., HAVES, P., SPENCER, R.E. & STANNARD, D. 1976 MNRAS 176, 275.

BOHUSKI, T.J. & WEEDMAN, D.W. 1979 ApJ 231, 653.

BOKSENBERG, A., CARSWELL, R.F., SMITH, M.G. & WHELAN, J.A.J. 1978 MNRAS 184, 773.

BRACCESI, A., ZITELLI, V., BÒNOLI, F. & FORMIGGINI, L. 1980 A&A 85, 80.

BROMAGE, G.E. 1972 Circulated report.

BROWNE, I.W.A. 1980 Nature 286, 307.

BURBIDGE, G.R., CROWNE, A.H. & SMITH, H.E. 1977 ApJ Suppl 33, 113.

BURBIDGE, G. 1979 Nature 282, 451.

CARSWELL, R.F. & SMITH, M.G. 1978 MNRAS 185, 381.

CLOWES, R.G., SMITH, M.G., SAVAGE, A., CANNON, R.D., BOKSENBERG, A. & WALL, J.V. 1979 MNRAS 189, 175.

CLOWES, R.G., EMERSON, D., SMITH, M.G., WALLACE, P.T., CANNON, R.D., SAVAGE, A. & BOKSENBERG, A. 1980 MNRAS in press.

CONDON, J.J., O'DELL, S.L., PUSCHELL, J.J. & STEIN, W.A. 1980 Nature 283, 357.

COOKE, J.A. 1980 PhD Thesis, University of Edinburgh.

ELLERY, L.A. 1980 PhD Thesis (in preparation) University of Edinburgh.

FURENLID, I., SCHOENING, W.E. & CARDER Jr., B.E. 1977 AAS Photo-Bull 16, 14.

FURENLID, I. 1978 in Modern Techniques in Astronomical Photography p. 153 eds WEST, R.M. & HEUDIER, J.L. ESO.

GILMORE, G. 1980 Preprint.

GREEN, R.F. & SCHMIDT, M. 1978 ApJ 220, L1.

HEWITT, A. & BURBIDGE, G.R. 1980 ApJ Suppl 43, 57.

HOAG, A.A. & SMITH, M.G. 1977 ApJ 217, 362.

LEWIS, W.C., BABCOCK, T.A. & JAMES, T.H. 1971 AAS Photo-Bull 3, 7.

LEWIS, D.W., MacALPINE, G.M. & WEEDMAN, D.W. 1979 ApJ 233, 787.

MacALPINE, G.M., SMITH, S.B. & LEWIS, D.W. 1977a ApJ Suppl 34, 95.

MacALPINE, G.M., SMITH, S.B. & LEWIS, D.W. 1977b ApJ Suppl 35, 197.

MacALPINE, G.M., LEWIS, D.W., & SMITH S.B. 1977 ApJ Suppl 35, 203.

MacALPINE, G.M. & LEWIS, D.W. 1978 ApJ Suppl 36, 587.

MacALPINE, G.M. & WILLIAMS, G.A. 1980 ApJ Suppl in press.

MADDEN, R.P. & STRONG, J. 1958 Appendix P in STRONG, J. Concepts of Classical Optics Freeman.

MURDOCH, H.S. 1978 Proc. ASA 3, 282.

NANDY, K., REDDISH, V.C., TRITTON, K.P., COOKE, J.A. & EMERSON, D. 1977 MNRAS 178, 63P.

OSMER, P.S. 1977 ApJ 214, 1.

OSMER, P.S. 1980 ApJ Suppl 42, 523.

OSMER, P.S. & SMITH, M.G. 1980 ApJ Suppl 42, 333.

OSTERBROCK, D.E. 1979 in Active Galactic Nuclei p. 25 eds HAZARD, C. & MITTON, S. CUP.

REES, M.J. 1970 ApJ 160, L29.

RICHSTONE, D.O. & SCHMIDT, M. 1980 ApJ 235, 361.

SAVAGE, A. 1978 PhD Thesis, University of Sussex.

SAVAGE, A. & BOLTON, J.G. 1979 MNRAS 188, 599.

SCHMIDT, M. 1972 ApJ 176, 273.

SCHMIDT, M. 1976 ApJ 209, L55.

SCHMIDT, M. 1978 Physica Scripta 17, 329.

SELDNER, M. & PEEBLES, P.J.E. 1979 ApJ 227, 30.

SETTI, G. & ZAMORANI, G. 1978 A&A 66, 249.

SETTI, G. & WOLTJER, L. 1979 A&A 76, L1.

SIM, M.E. 1978 in Modern Techniques in Astronomical Photography p. 23 eds WEST, R.M. & HEUDIER, J.L. ESO.

SMITH, M.G. 1975 ApJ 202, 591.

SMITH, M.G. 1978 Vistas Astr 22. 321.

SMITH, H.E. 1978 Mercury 7, 27.

SMITH M.G. & WRIGHT, A.E. 1980 MNRAS 191, 871.

SMITH, M.G. CARSWELL, R.F., WHELAN, J.A.J., BOKSENBERG, A., CLOWES, R.G., SAVAGE, A., CANNON, R.D. & WALL, J.V. 1980 MNRAS Submitted.

SRAMEK, R.A. & WEEDMAN, D.W. 1978 ApJ 221, 468.

SRAMEK, R.A. & WEEDMAN, D.W. 1980 ApJ 238, 435.

STEWART, N.J. & HAWKINS, M.R.S. 1978 Nature 276, 163.

TAPIA, M. & CATCHPOLE, R. 1980 Observatory 100, 71.

VAN KREVELD, A. 1934 Zeits. f. Wiss. Photophysik u. Photochemie 32, 222.

WALL, J.V. 1975 Observatory 95, 196.

WALSH, D., CARSWELL, R.F. & WEYMANN, R.J. 1979 Nature 279, 381.

WEBB, J.H. 1936 J. Opt. Soc. Am. 26, 12.

WEEDMAN, D.W. 1980 ApJ 237, 326.

WEYMANN, R.J., WILLIAMS, R.E., PETERSON, B.M. & TURNSHEK, D.A. 1979 ApJ 234, 33.

WEYMANN, R.J., LATHAM, D., ANGEL, J.R.P., GREEN, R.F., LIEBERT, J.W., TURNSHEK, D.A., TURNSHEK, D.E. & TYSON, J.A. 1980 Nature 285, 641.

WILKINSON, G.R. & MARTIN, D.H. 1967 in Spectroscopic Techniques p. 75 ed MARTIN, D.H. North-Holland.

WILLS, D. & LYNDS, R. 1978 ApJ Suppl 36, 317.

WILLS, D. 1978 Physica Scripta 17, 333.

WILLS, D. 1979 Nature 281, 405.

APPENDIX

Illustrations of the density spectra (left hand side) and the deduced intensity (F_λ) spectra (right hand side) for quasars on UJ3682P (see Chapter 4). The intensity spectra have not been divided by $g(\lambda)$ and are consequently $g(\lambda)I_*(\lambda)$ rather than $I_*(\lambda)$. Densities are with respect to chemical fog and are PDS densities rather than ANSI diffuse densities. The mean density of the sky background is 1.63. The intensity scale is unnormalised. The density spectra are plotted against channel number and the F_λ spectra against wavelength in Angstroms.

Note that 00 45 25.4-28 29 24 is misidentified as 00 45 20.3-28 29 24.

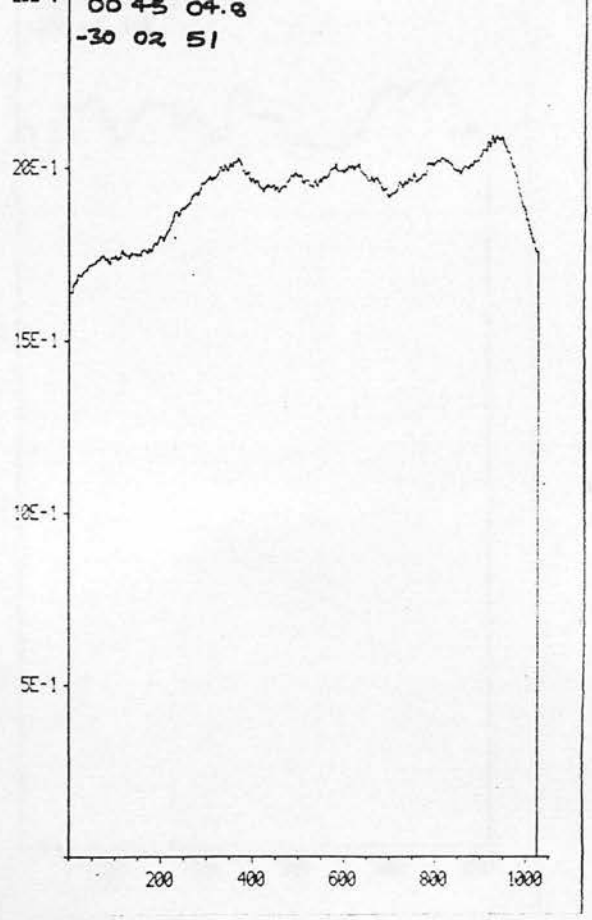
00 45 04.8
-30 02 51
20E-1
15E-1
10E-1
5E-1
200
400
600
800
1000

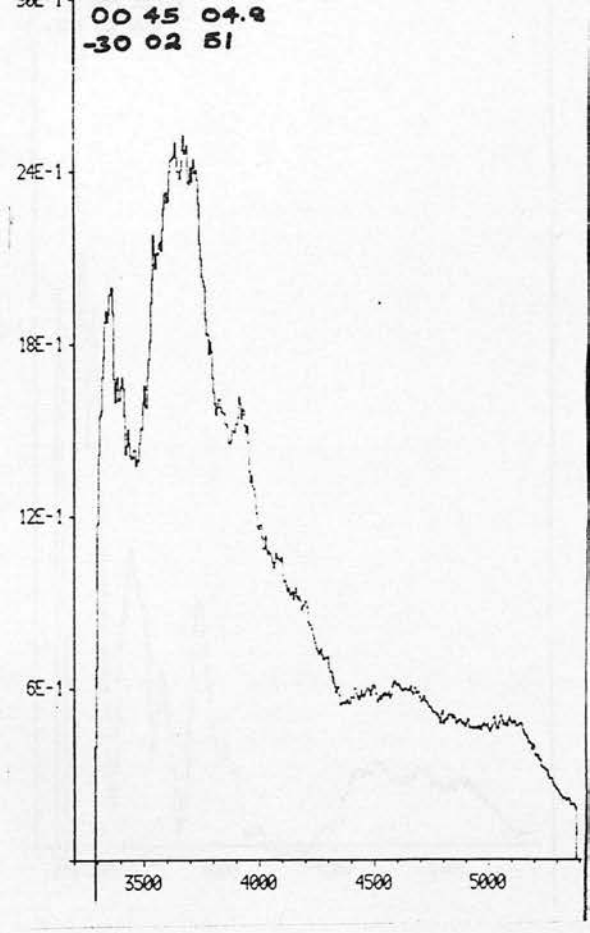
00 45 04.8
-30 02 51
24E-1
18E-1
12E-1
6E-1
3500
4000
4500
5000

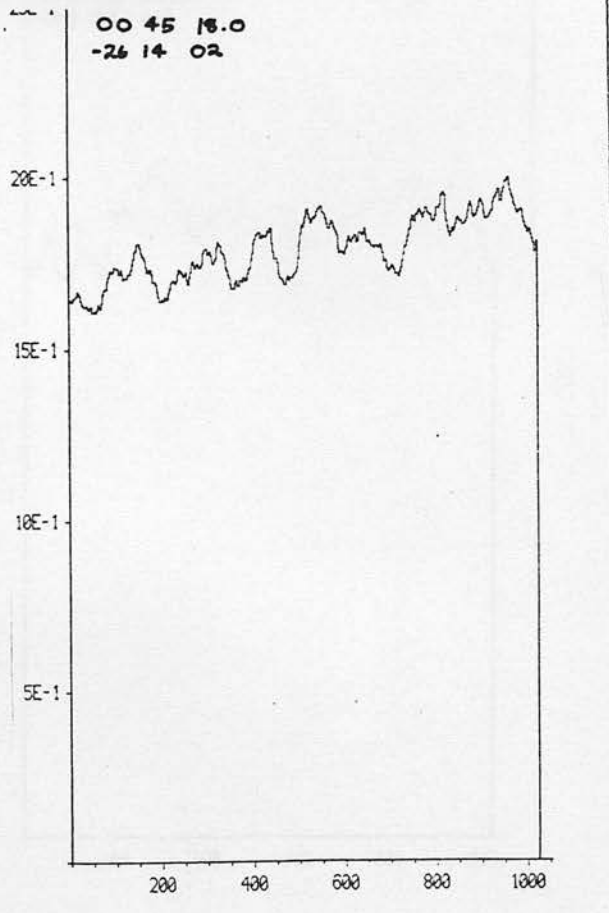
00 45 16.0
-26 14 02
20E-1
15E-1
10E-1
5E-1
200
400
600
800
1000

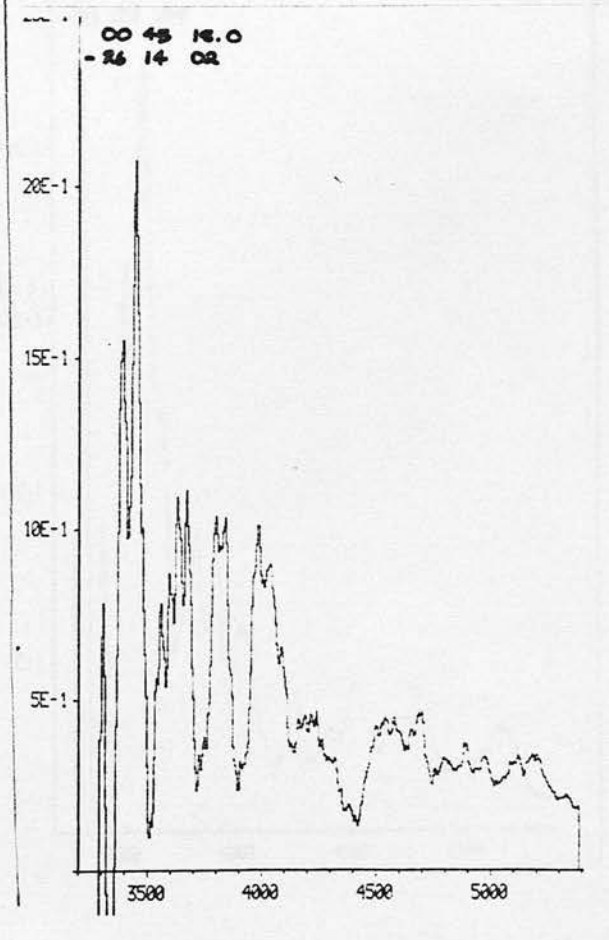
00 45 16.0
-26 14 02
20E-1
15E-1
10E-1
5E-1
3500
4000
4500
5000

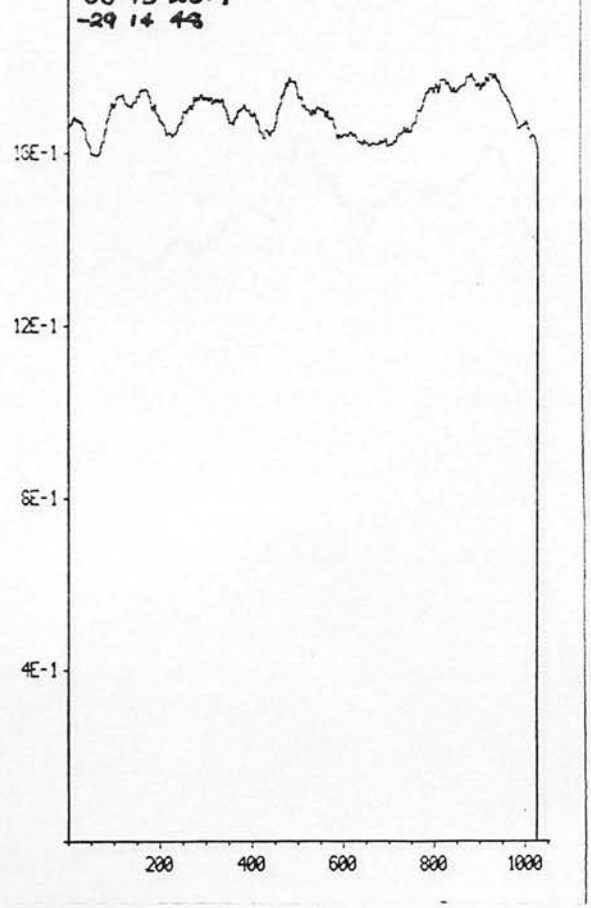
00 45 20.1
-29 14 48
16E-1
12E-1
8E-1
4E-1
200
400
600
800
1000

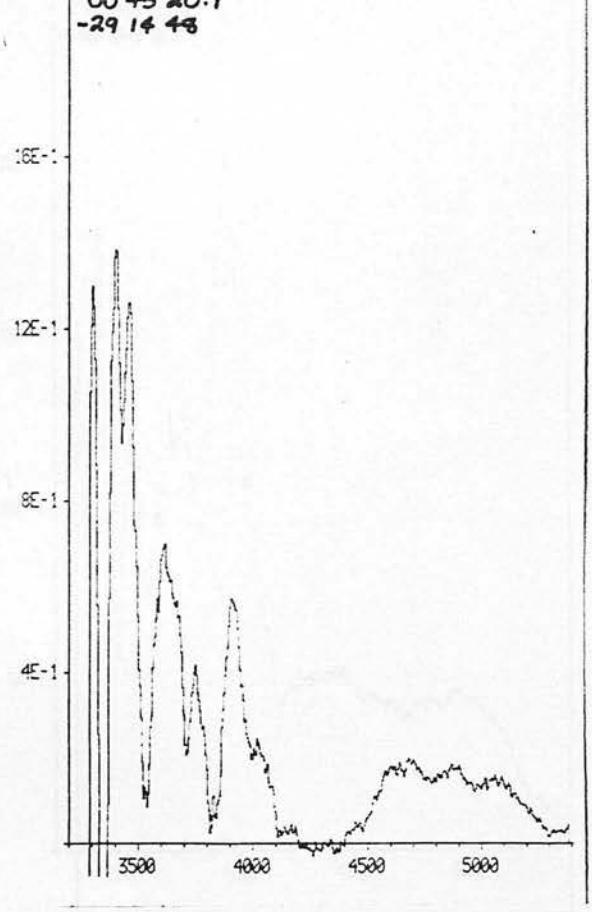
00 45 20.1
-29 14 48
16E-1
12E-1
8E-1
4E-1
3500
4000
4500
5000

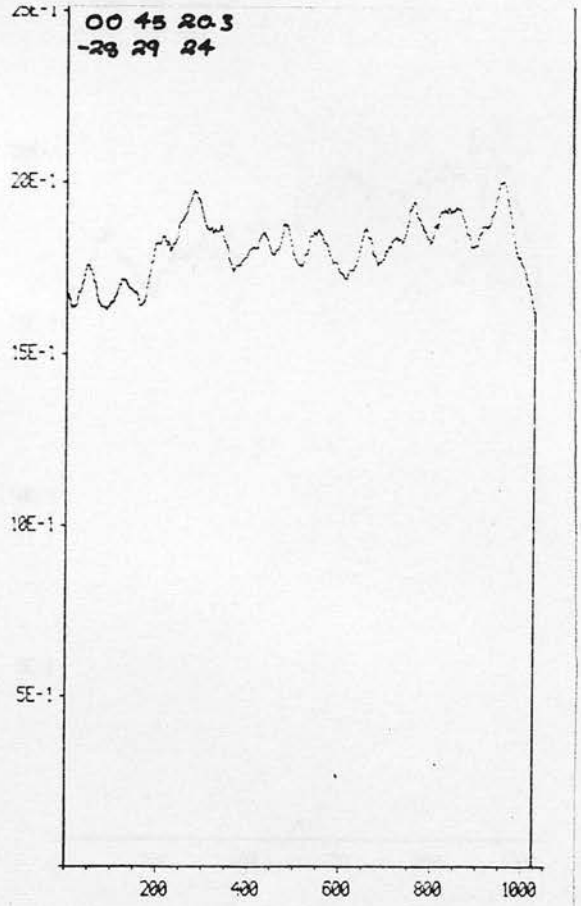
00 45 20.3
-28 29 24
20E-1
15E-1
10E-1
5E-1
200
400
600
800
1000

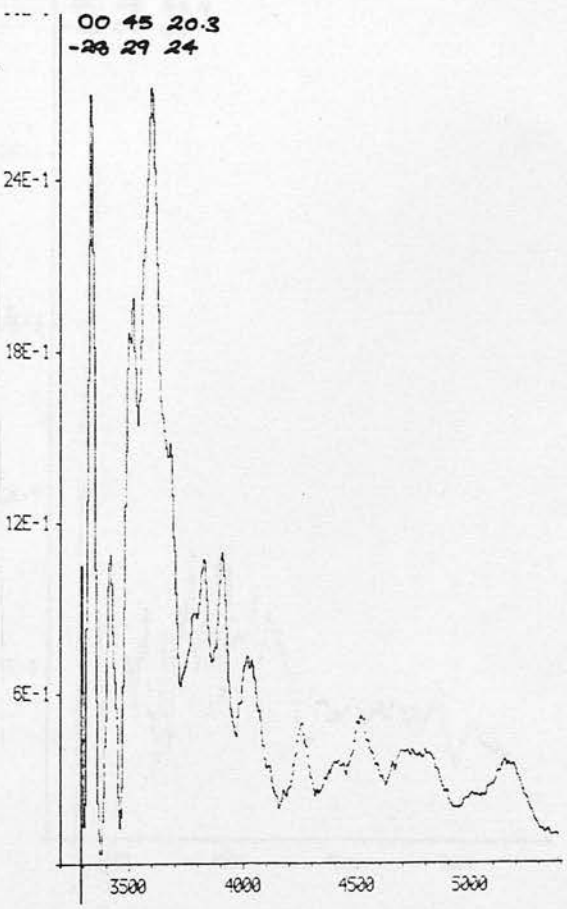
00 45 20.3
-28 29 24
24E-1
18E-1
12E-1
6E-1
3500
4000
4500
5000

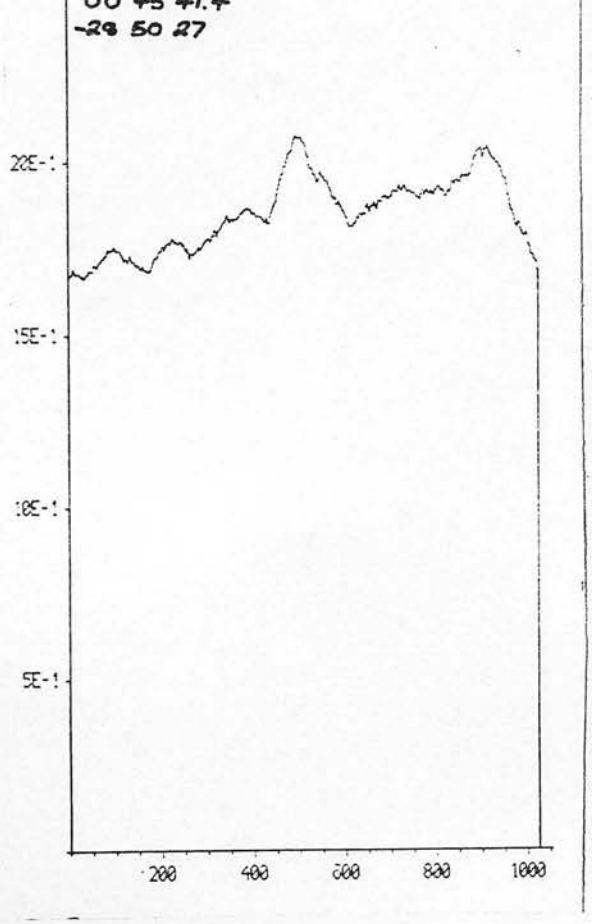
00 45 41.4
-28 50 27
2E-1
15E-1
1E-1
5E-1
200
400
600
800
1000

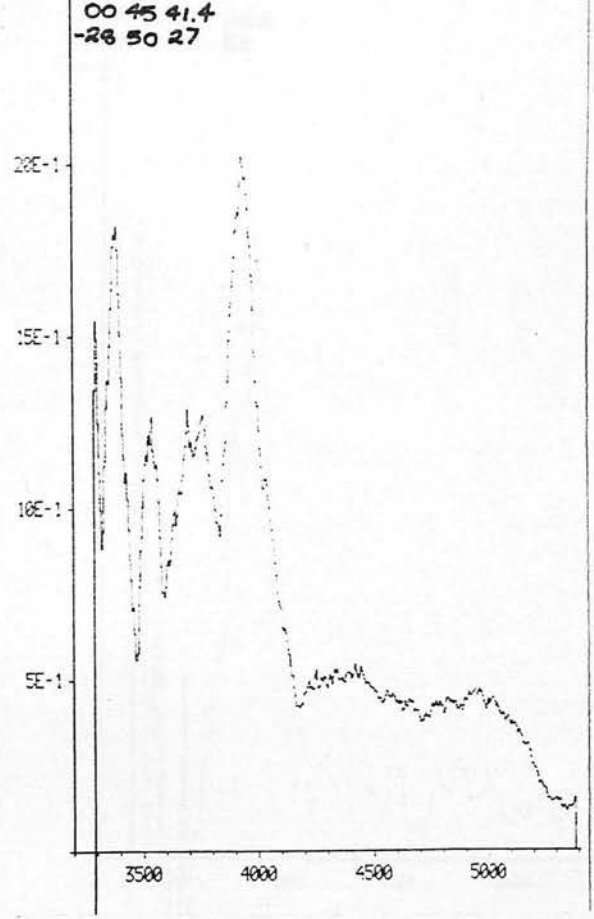
00 45 41.4
-28 50 27
2E-1
15E-1
1E-1
5E-1
3500
4000
4500
5000

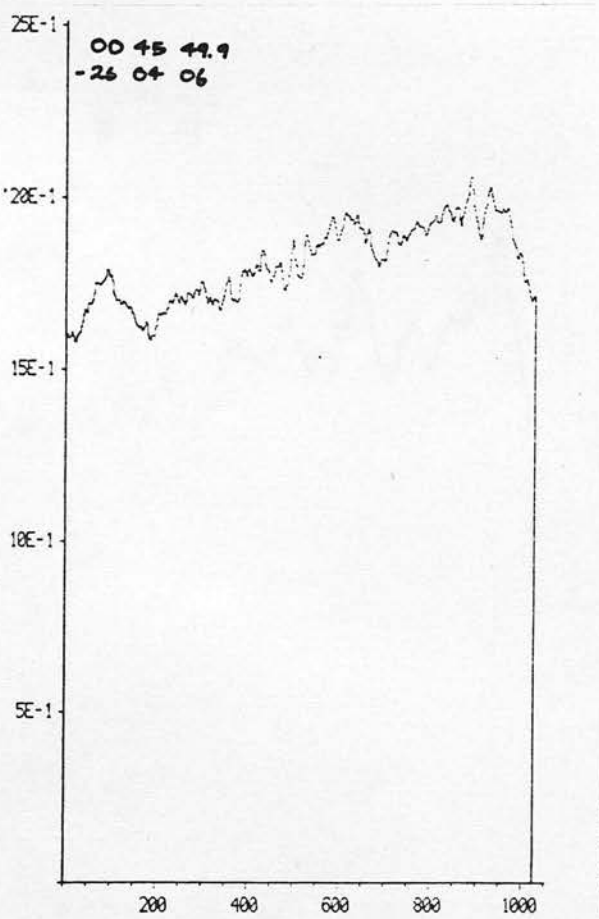
00 45 49.9
-26 04 06
25E-1
2E-1
15E-1
1E-1
5E-1
200
400
600
800
1000

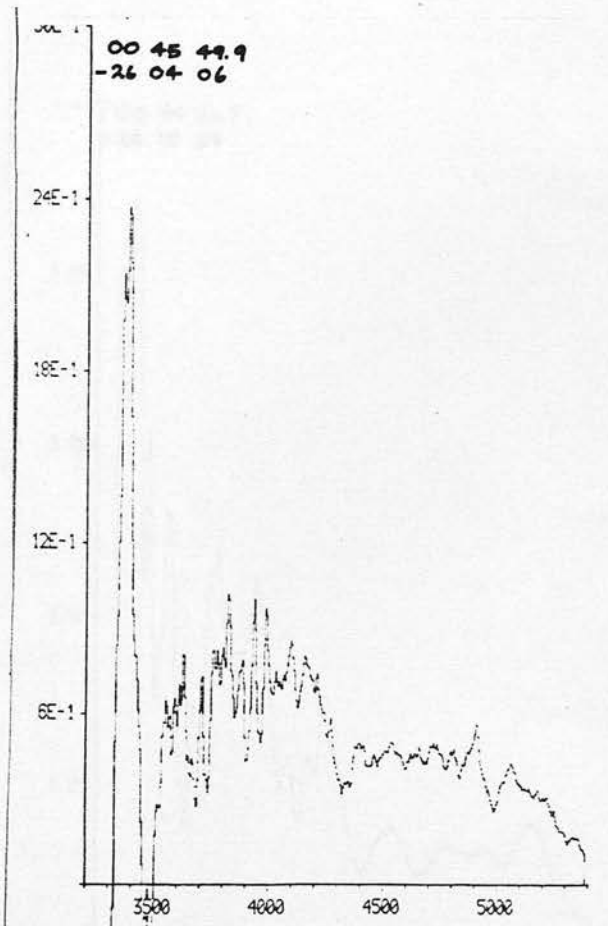
00 45 49.9
-26 04 06
24E-1
18E-1
12E-1
6E-1
3500
4000
4500
5000


00 45 55.2
-28 00 53
20E-1
15E-1
10E-1
5E-1
200
400
600
800
1000

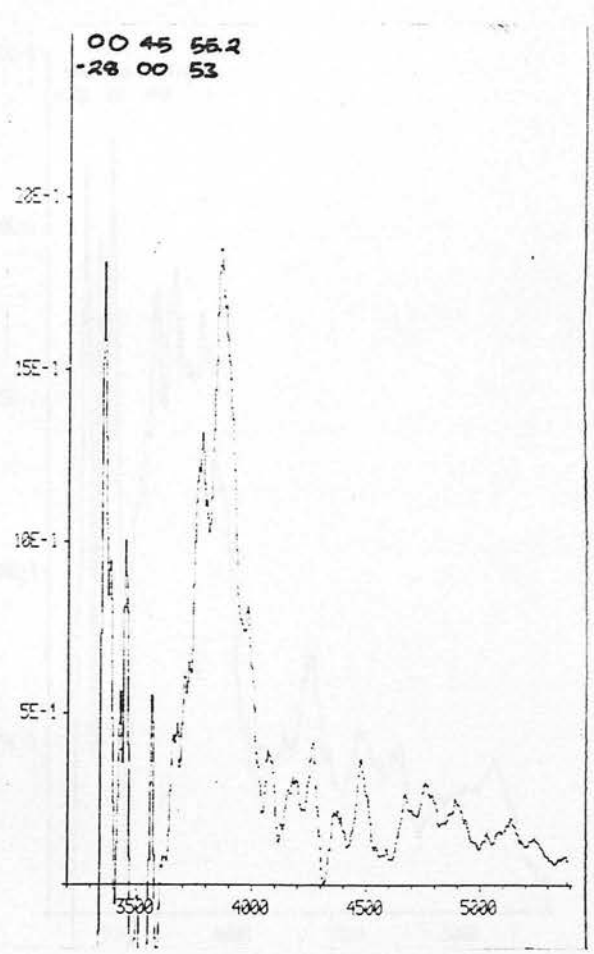
00 45 55.2
-28 00 53
20E-1
15E-1
10E-1
5E-1
3500
4000
4500
5000

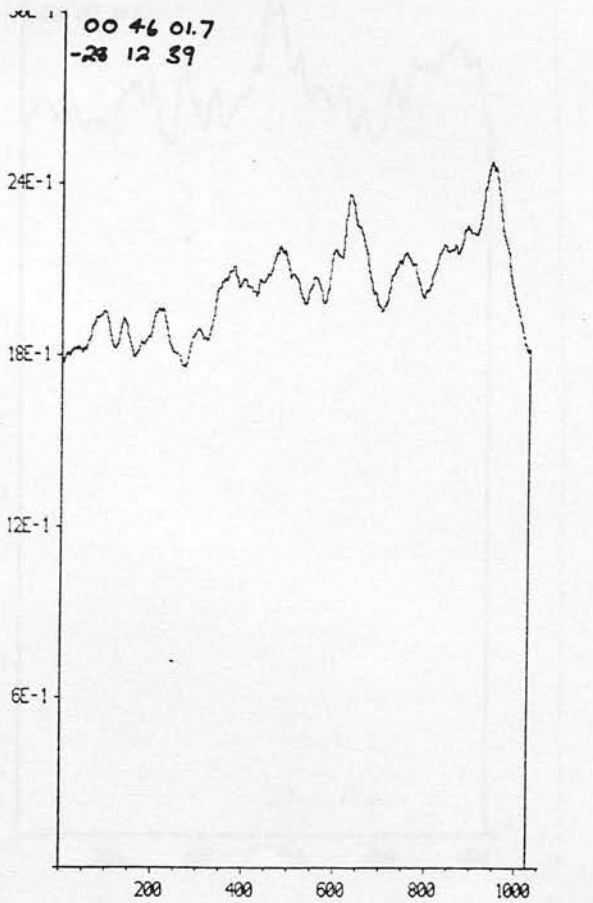
00 46 01.7
-28 12 59
24E-1
18E-1
12E-1
6E-1
200
400
600
800
1000

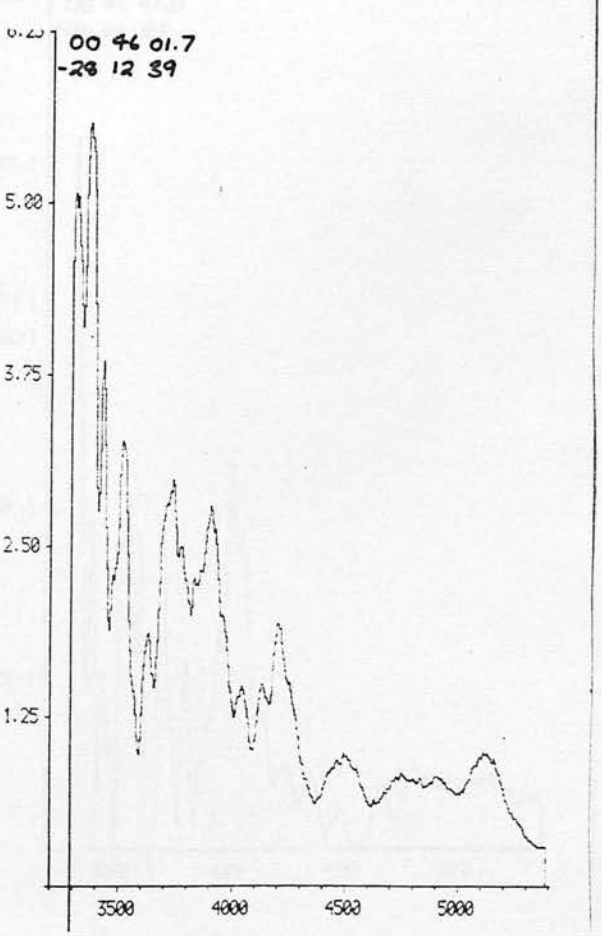
00 46 01.7
-28 12 59
5.00
3.75
2.50
1.25
3500
4000
4500
5000

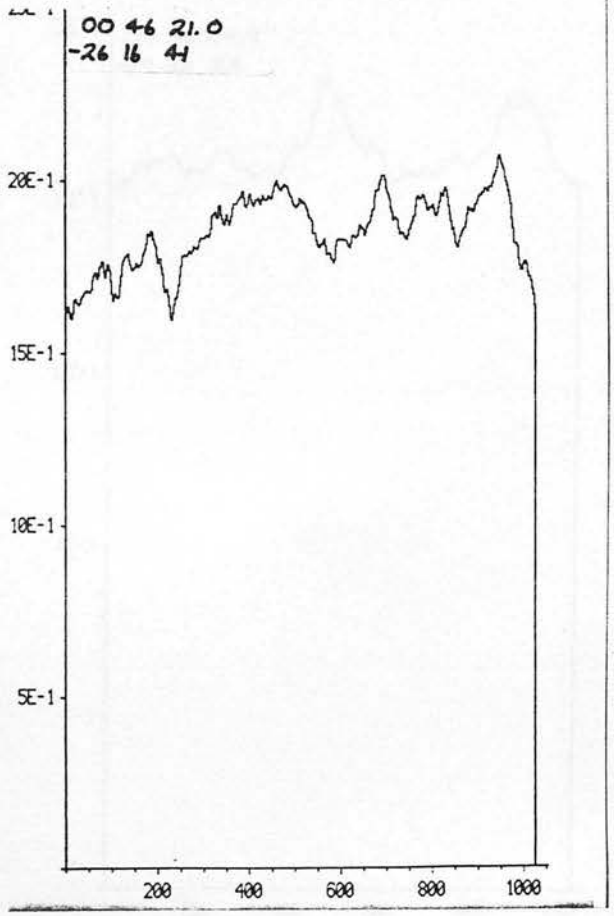
00 46 21.0
-26 16 41
20E-1
15E-1
10E-1
5E-1
200
400
600
800
1000

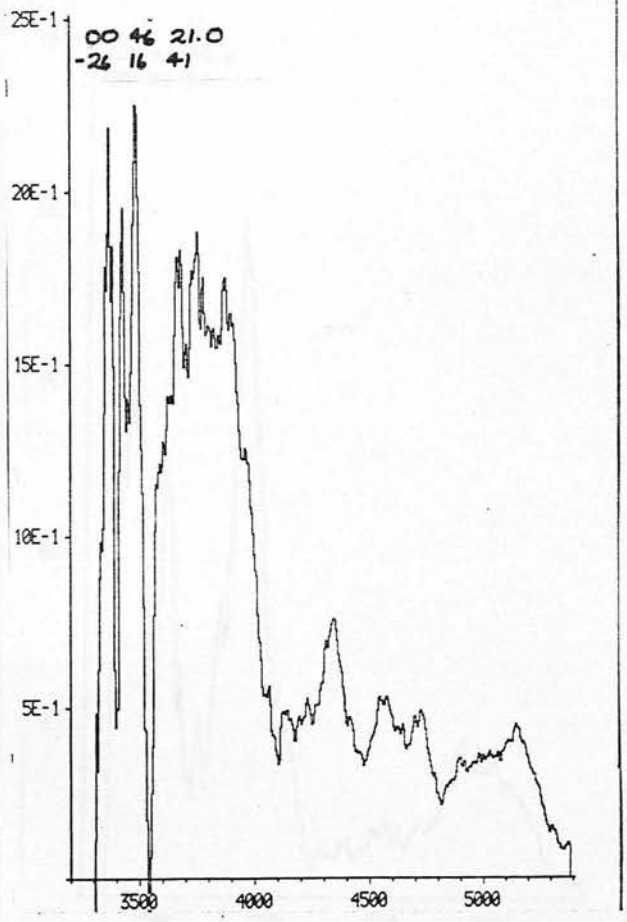
00 46 21.0
-26 16 41
25E-1
20E-1
15E-1
10E-1
5E-1
3500
4000
4500
5000

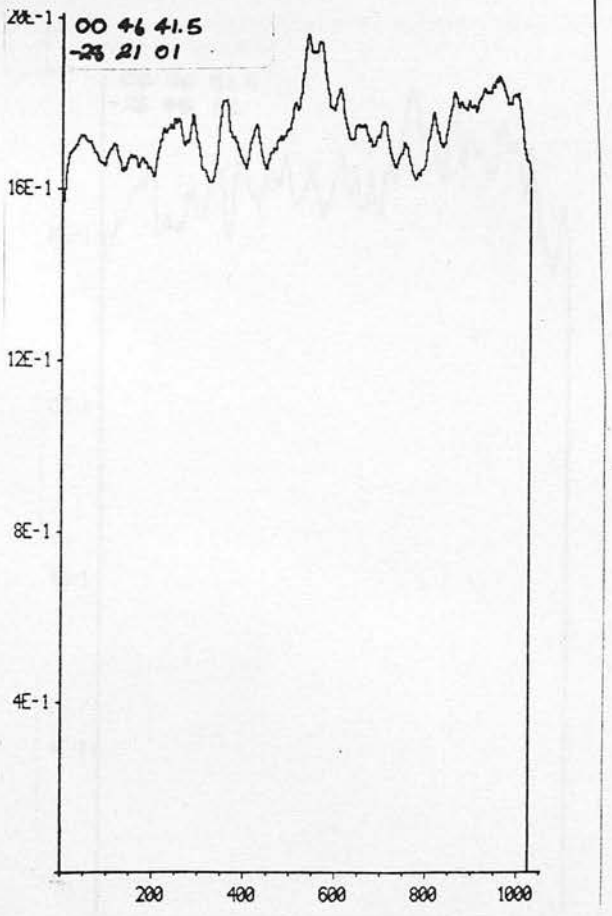
00 46 41.5
-28 21 01
16E-1
12E-1
8E-1
4E-1
200
400
600
800
1000

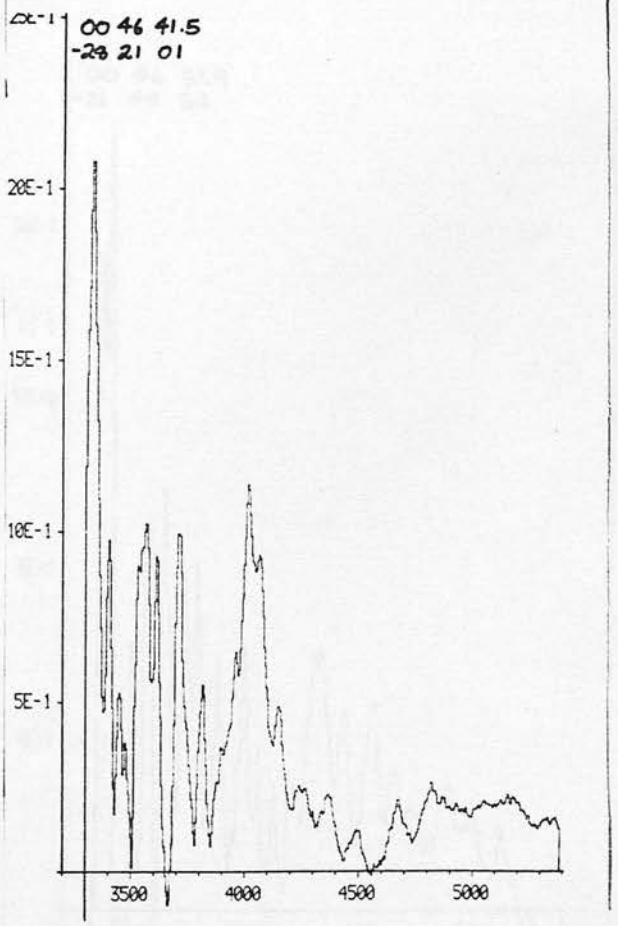
00 46 41.5
-28 21 01
20E-1
15E-1
10E-1
5E-1
3500
4000
4500
5000

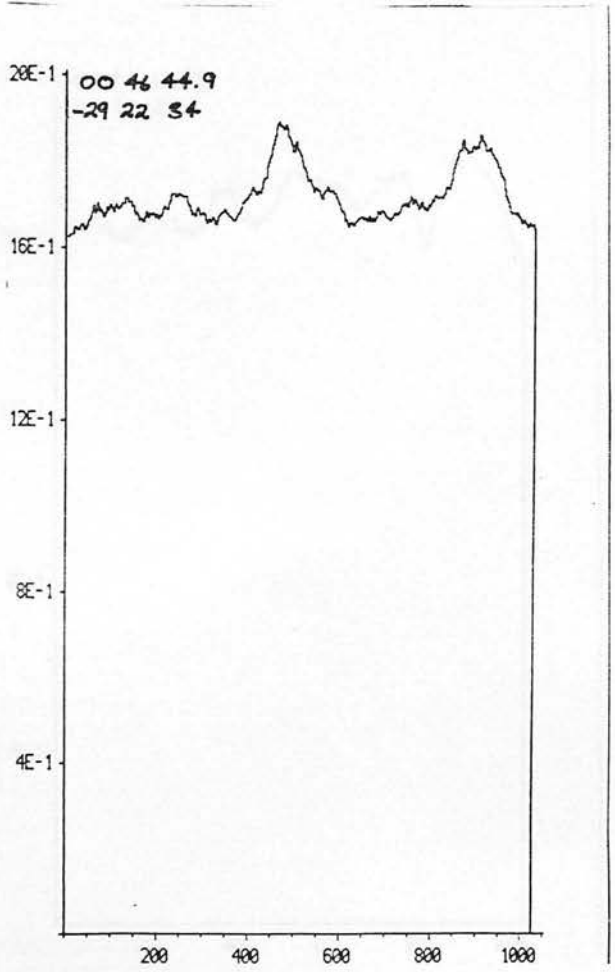
00 46 44.9
-29 22 34
20E-1
16E-1
12E-1
8E-1
4E-1
200
400
600
800
1000

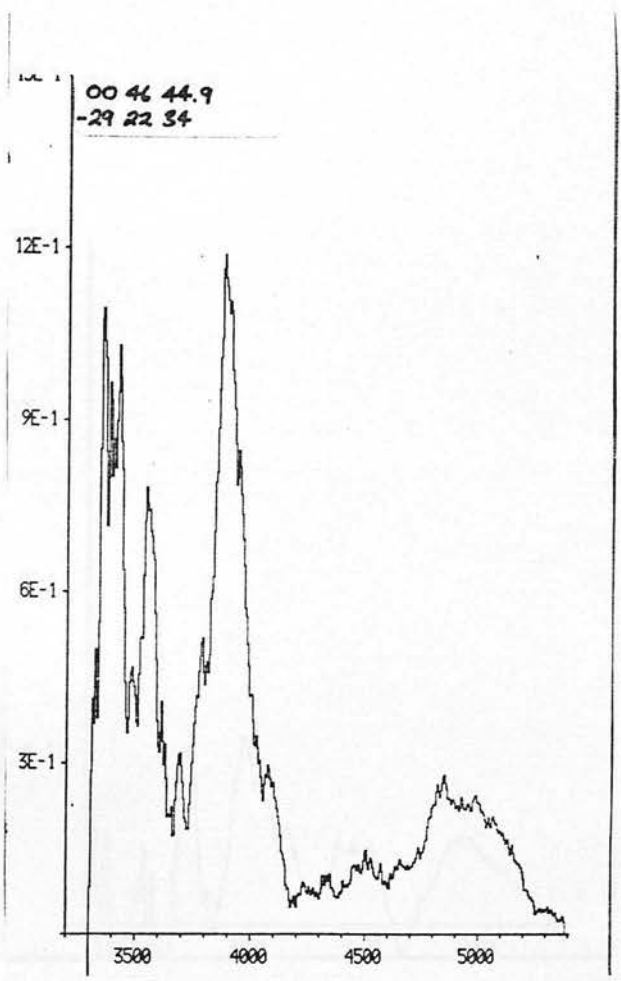
00 46 44.9
-29 22 34
12E-1
9E-1
6E-1
3E-1
3500
4000
4500
5000

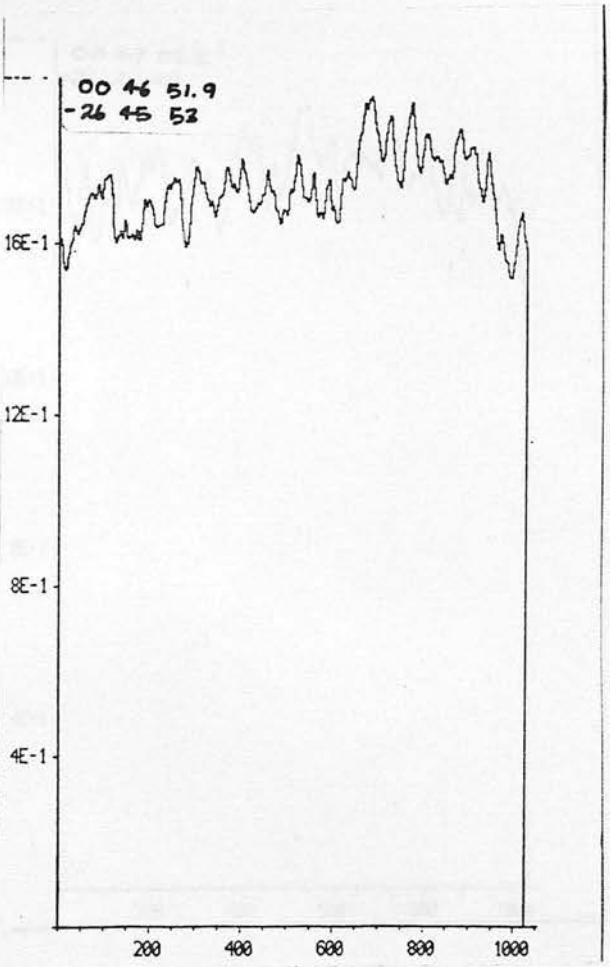
00 46 51.9
-26 45 52
16E-1
12E-1
8E-1
4E-1
200
400
600
800
1000

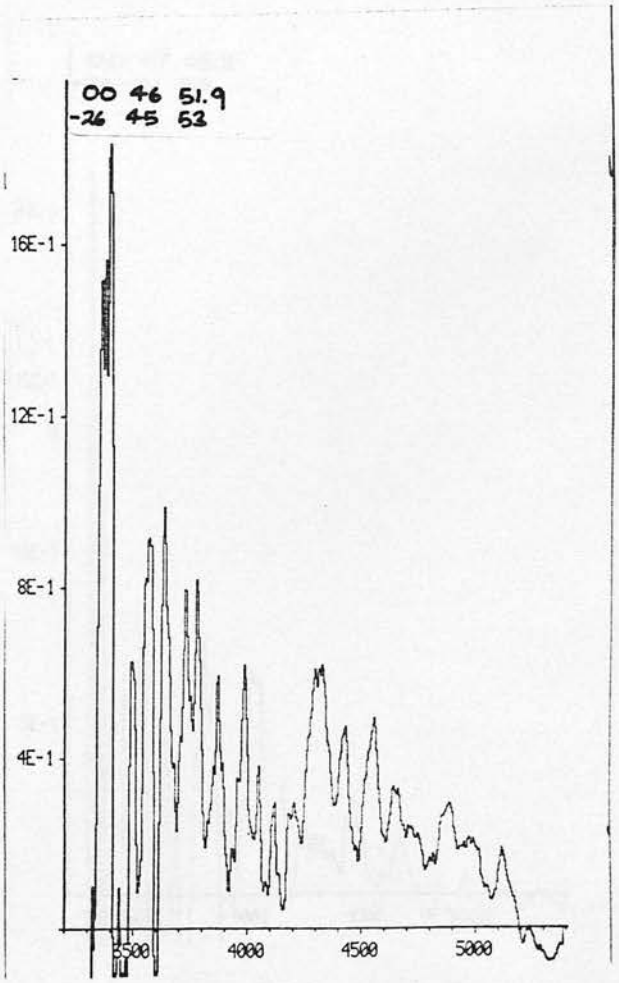
00 46 51.9
-26 45 52
16E-1
12E-1
8E-1
4E-1
3500
4000
4500
5000

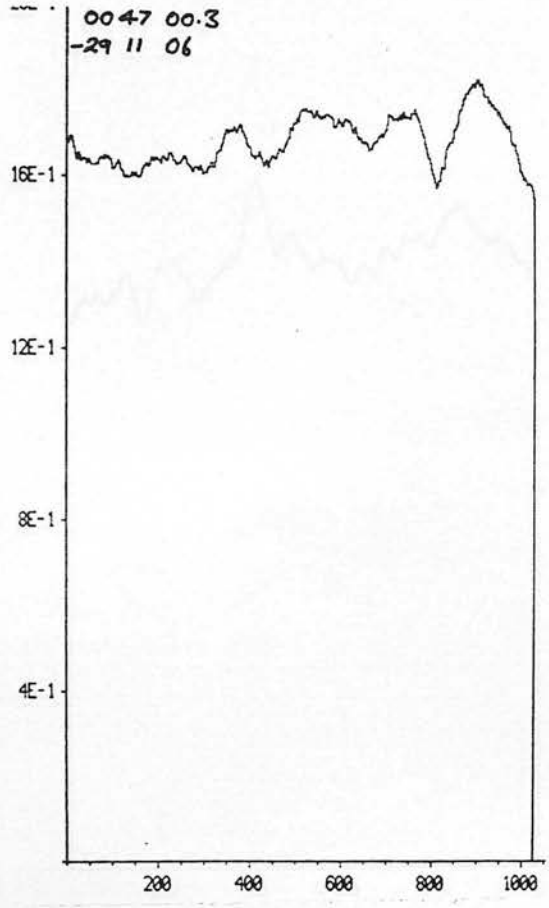
00 47 00.3
-29 11 06
16E-1
12E-1
8E-1
4E-1
200
400
600
800
1000

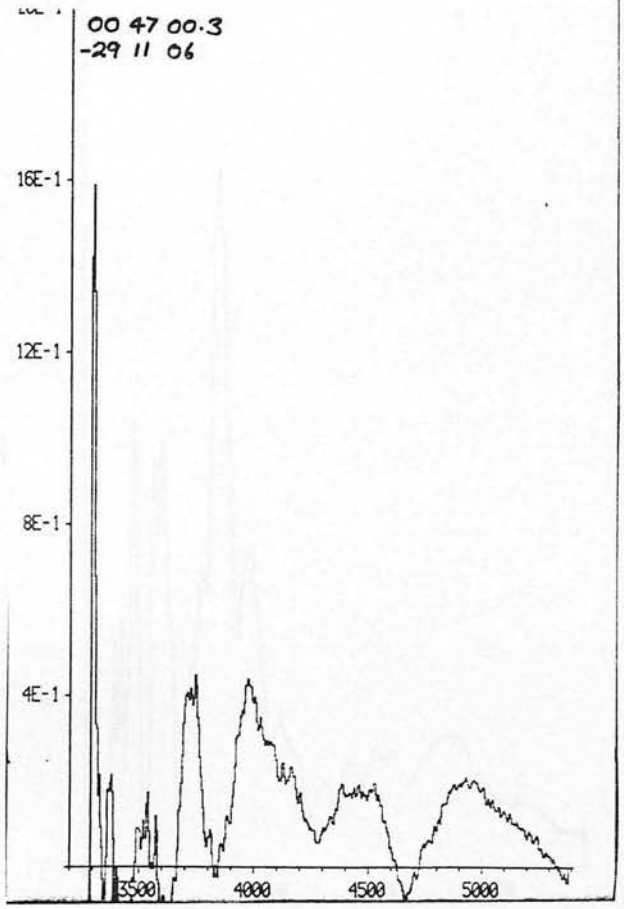
00 47 00.3
-29 11 06
16E-1
12E-1
8E-1
4E-1
3500
4000
4500
5000

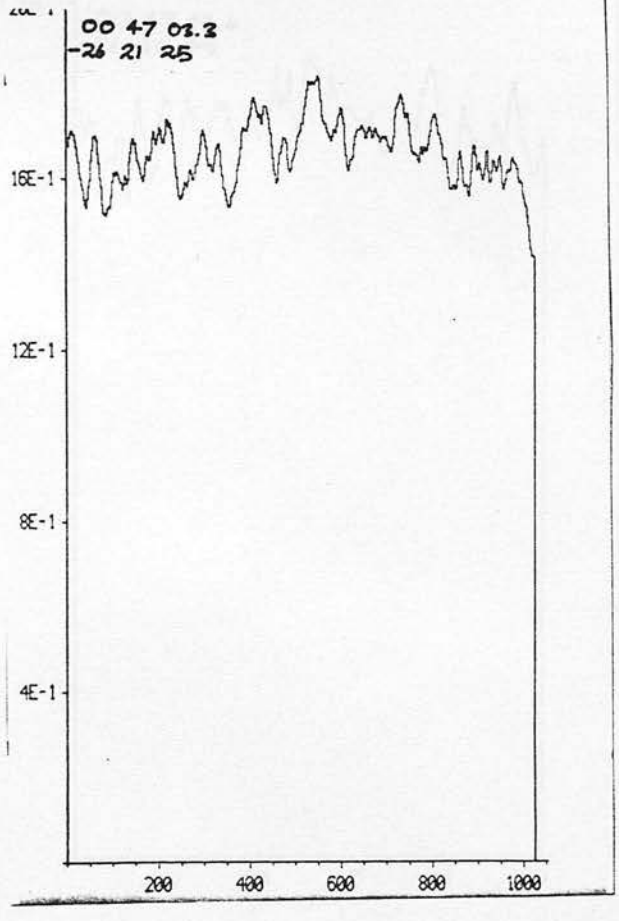
00 47 03.3
-26 21 25
16E-1
12E-1
8E-1
4E-1
200
400
600
800
1000

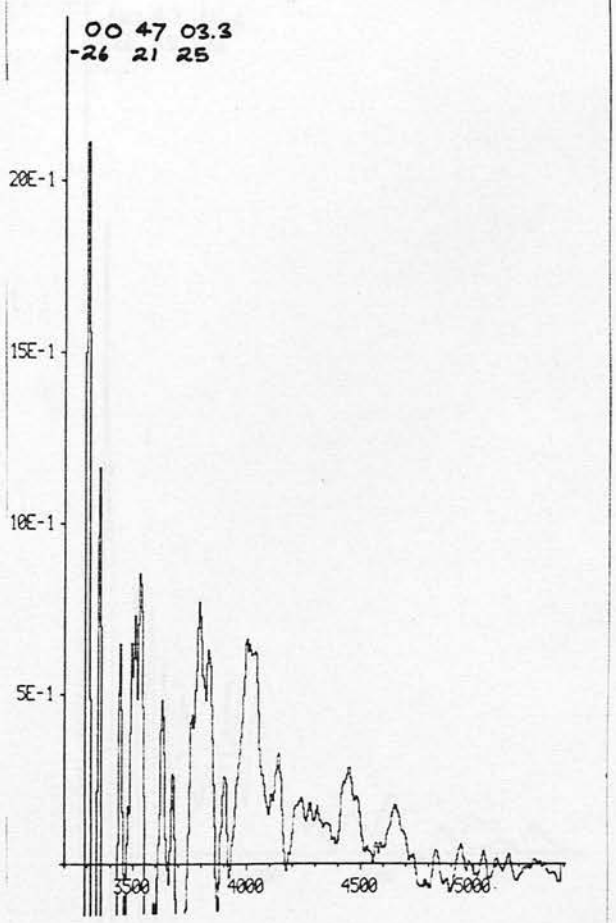
00 47 03.3
-26 21 25
20E-1
15E-1
10E-1
5E-1
3500
4000
4500
5000

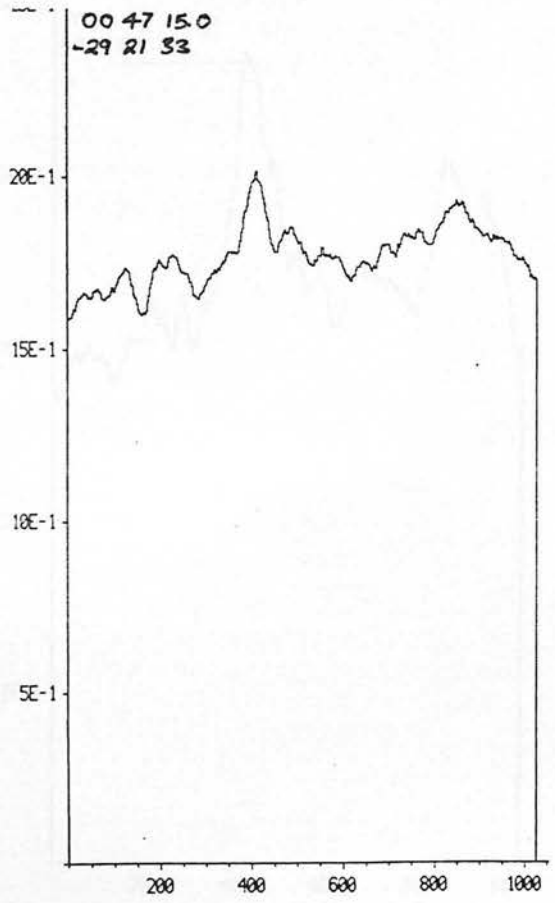
00 47 15.0
-29 21 33
20E-1
15E-1
10E-1
5E-1
200
400
600
800
1000

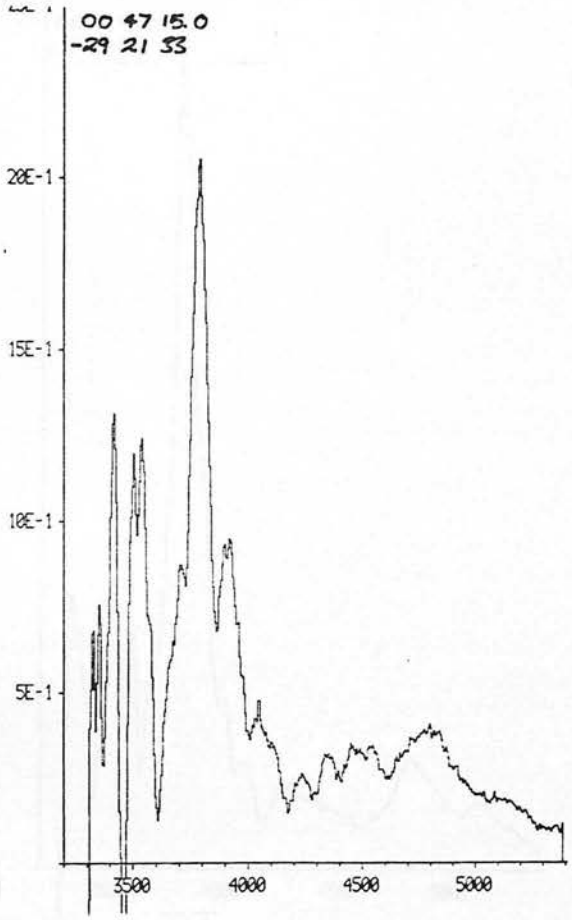
00 47 15.0
-29 21 33
20E-1
15E-1
10E-1
5E-1
3500
4000
4500
5000

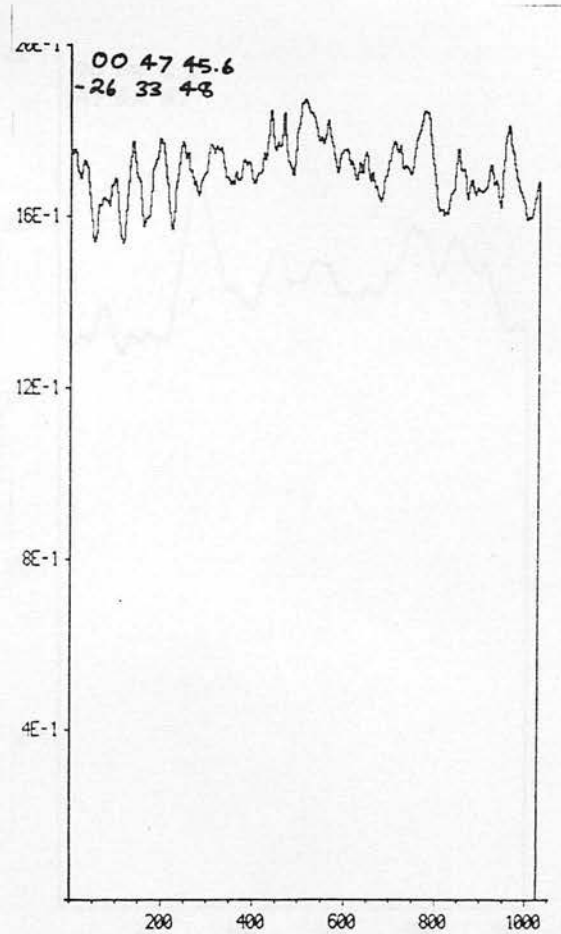
00 47 45.6
-26 33 48
16E-1
12E-1
8E-1
4E-1
200
400
600
800
1000

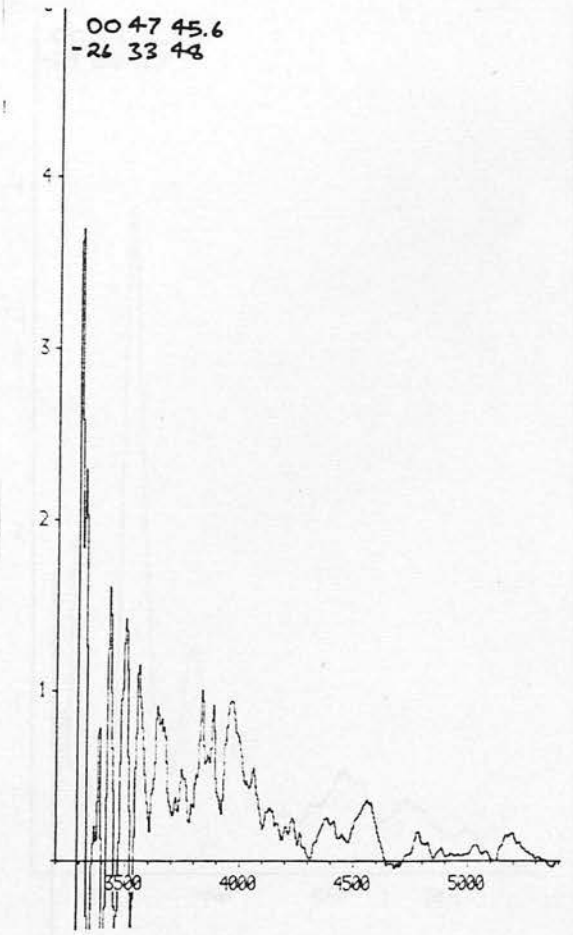
00 47 45.6
-26 33 48
4
3
2
1
3500
4000
4500
5000

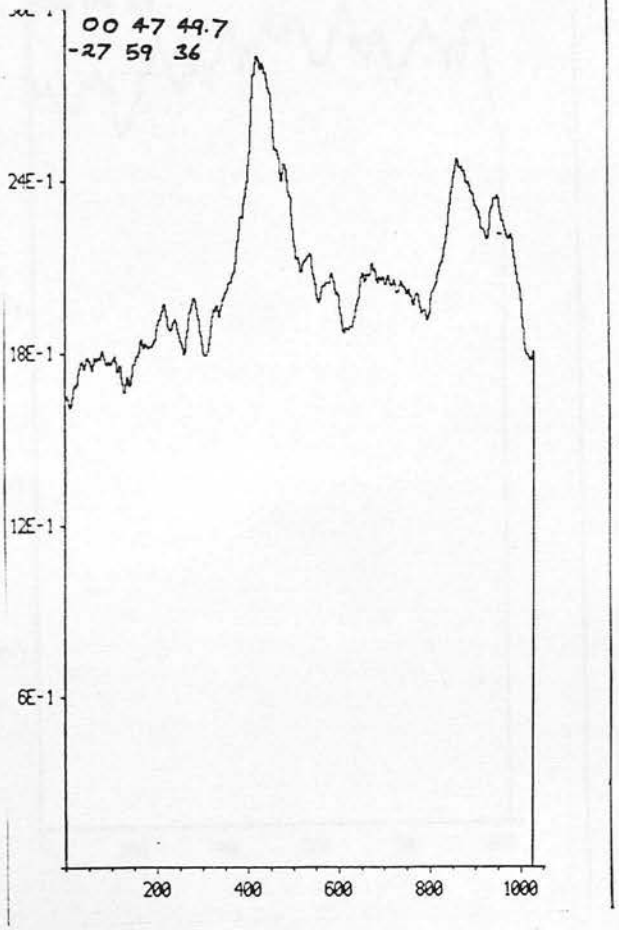
00 47 49.7
-27 59 36
24E-1
18E-1
12E-1
6E-1
200
400
600
800
1000

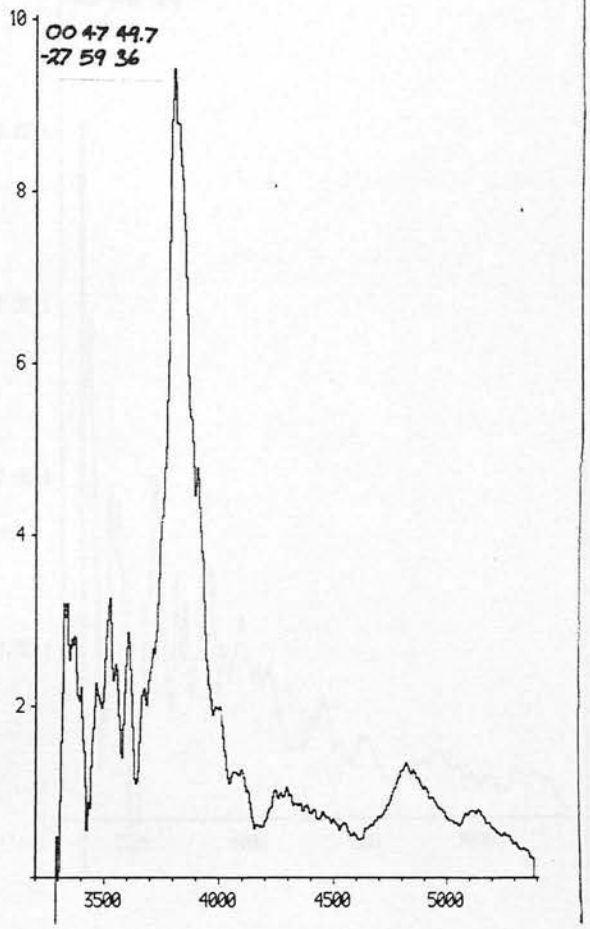
00 47 49.7
-27 59 36
10
8
6
4
2
3500
4000
4500
5000

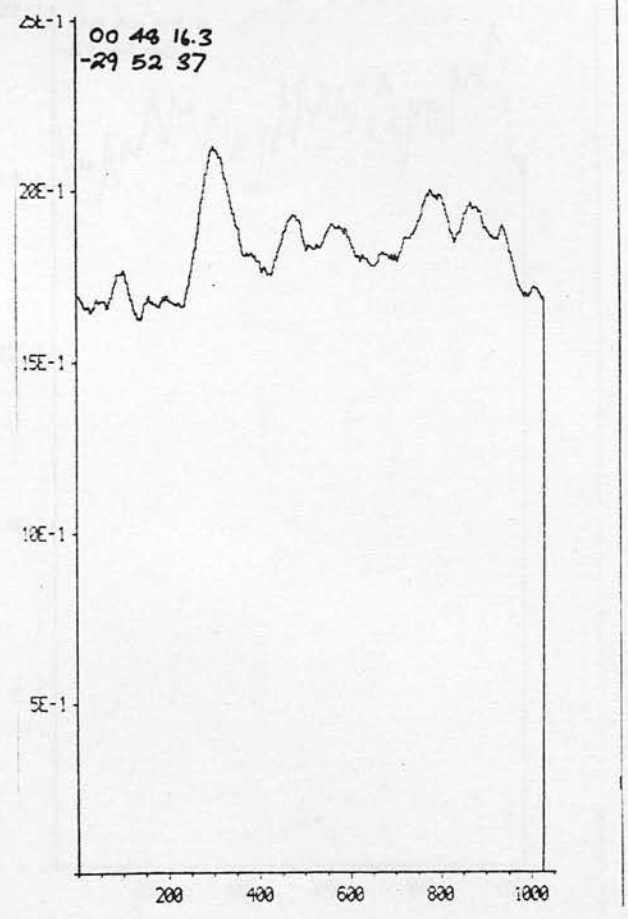
00 46 16.3
-29 52 37
25E-1
20E-1
15E-1
10E-1
5E-1
200
400
600
800
1000

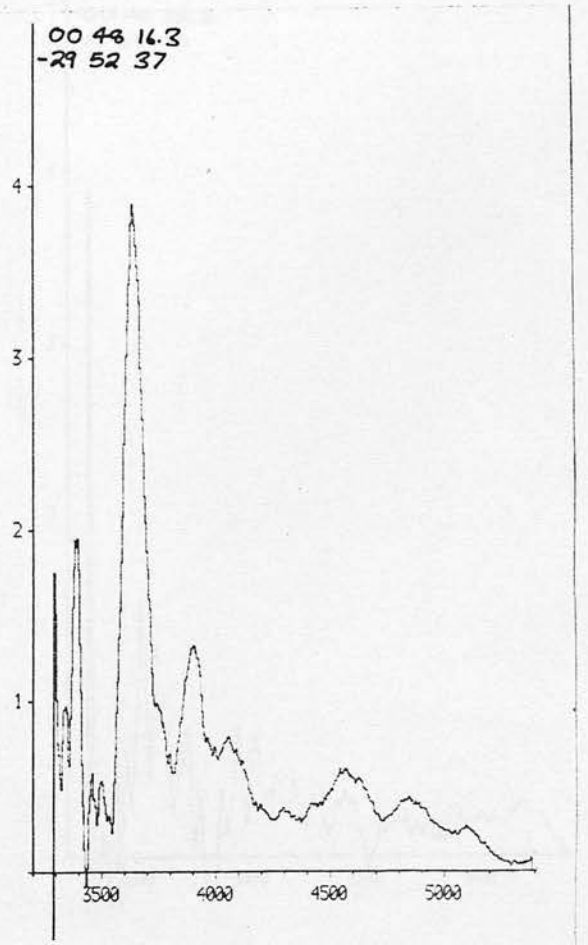
00 46 16.3
-29 52 37
4
3
2
1
3500
4000
4500
5000

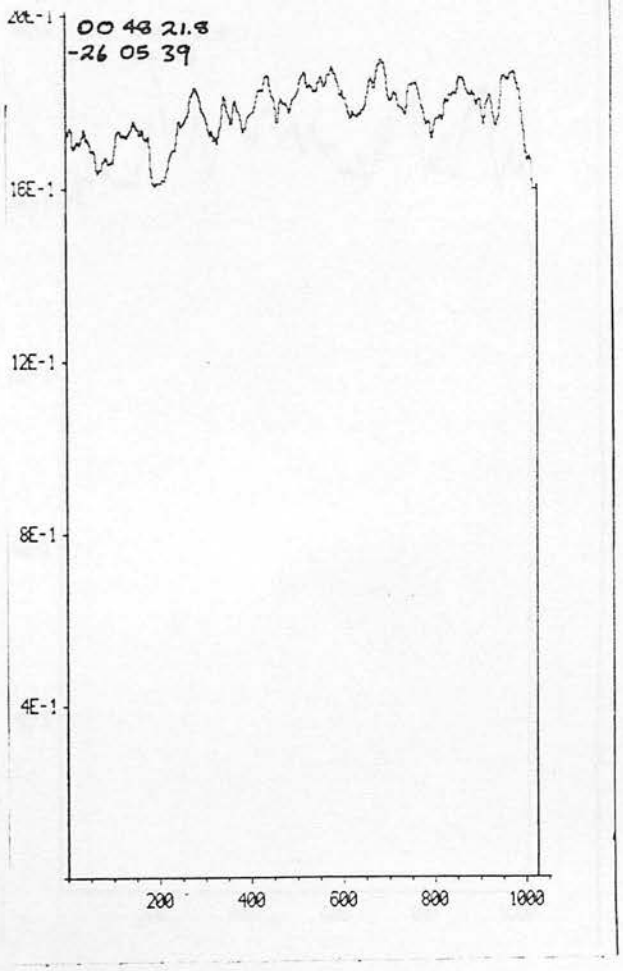
00 48 21.8
-26 05 39
16E-1
12E-1
8E-1
4E-1
200
400
600
800
1000

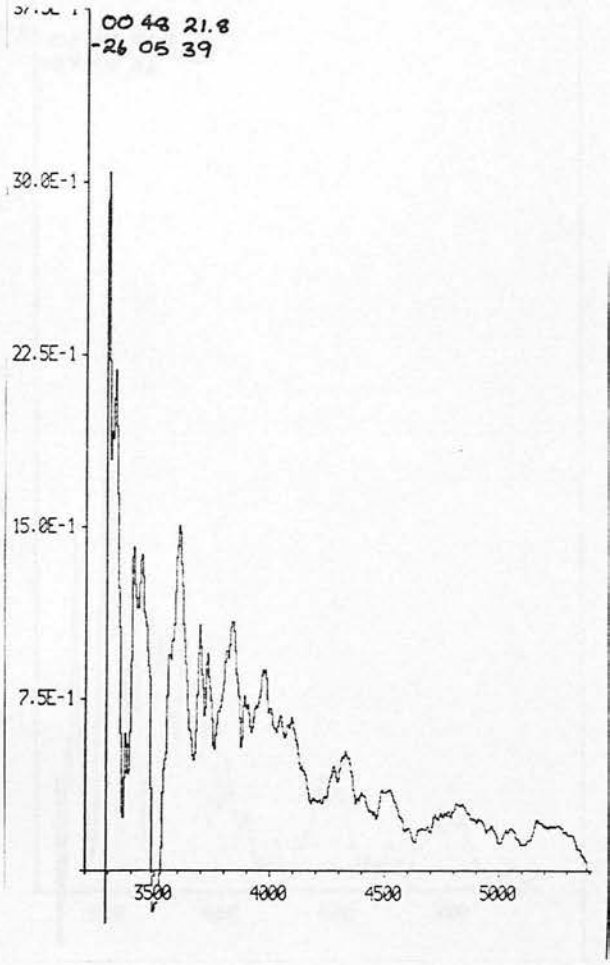
00 48 21.8
-26 05 39
30.0E-1
22.5E-1
15.0E-1
7.5E-1
3500
4000
4500
5000

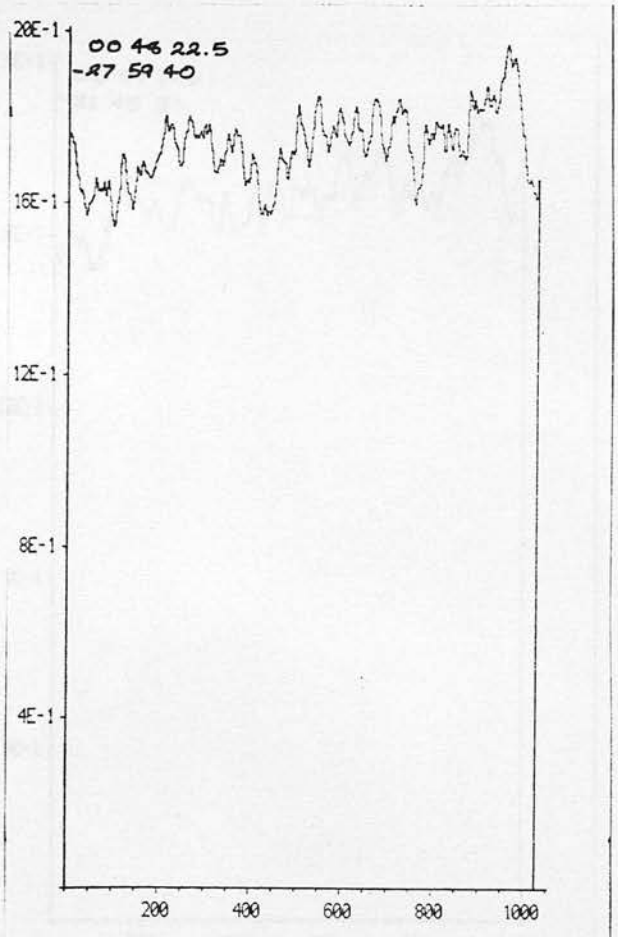
00 48 22.5
-27 59 40
20E-1
16E-1
12E-1
8E-1
4E-1
200
400
600
800
1000

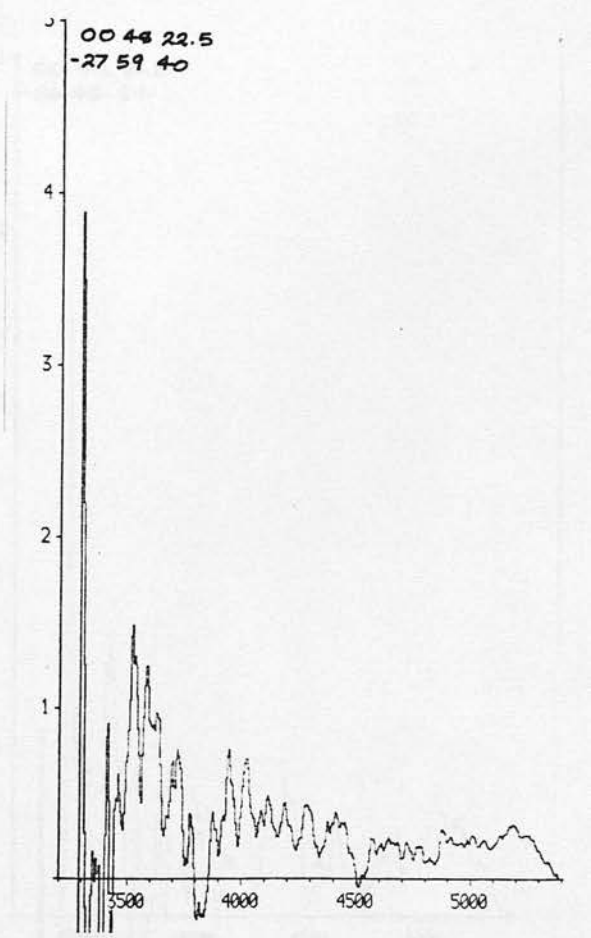
00 48 22.5
-27 59 40
4
3
2
1
3500
4000
4500
5000

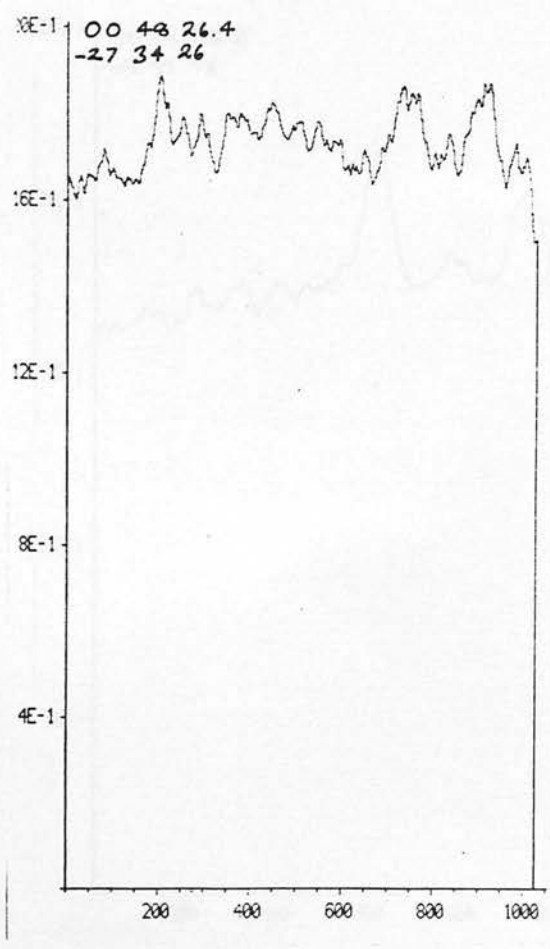
00 48 26.4
-27 34 26
20E-1
16E-1
12E-1
8E-1
4E-1
200
400
600
800
1000

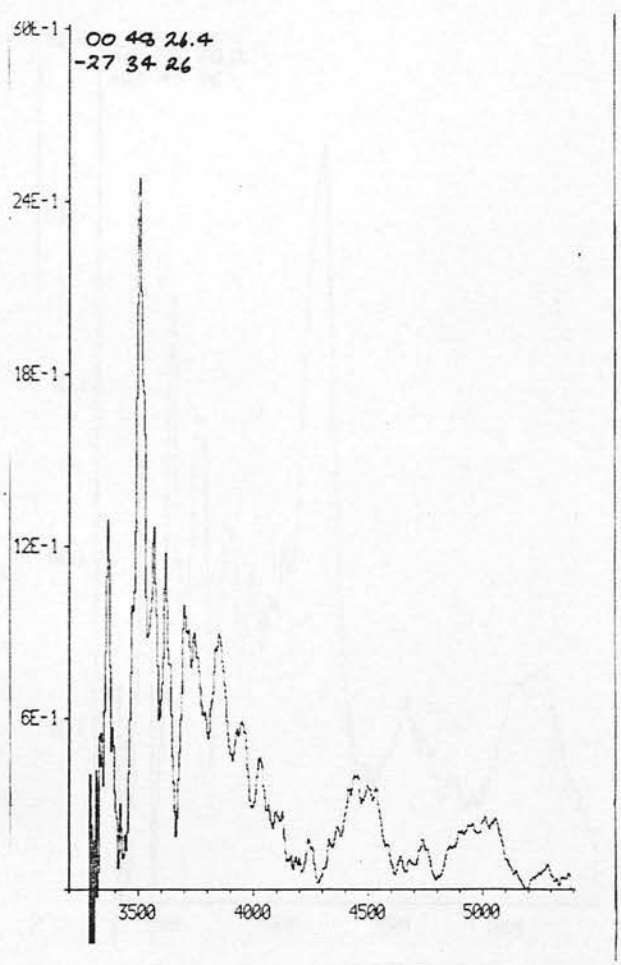
00 48 26.4
-27 34 26
30E-1
24E-1
18E-1
12E-1
6E-1
3500
4000
4500
5000

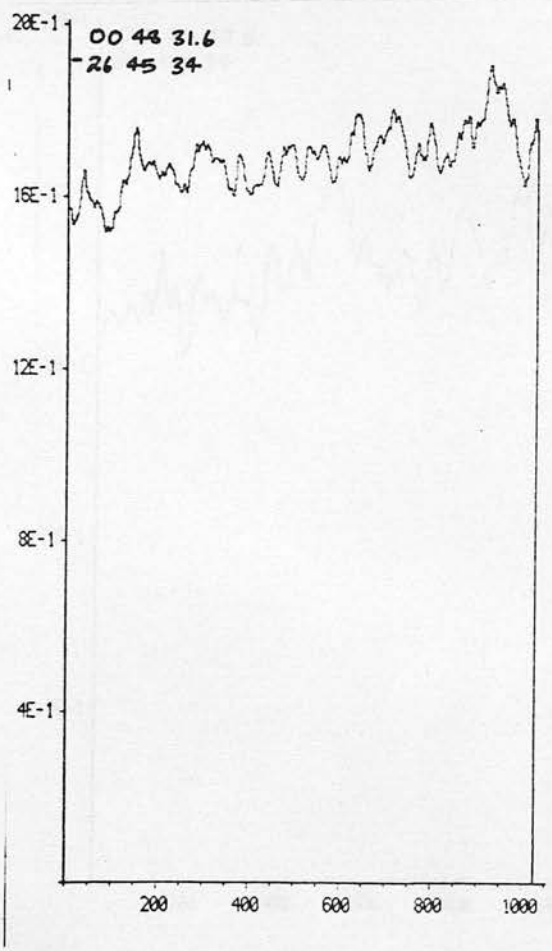
00 48 31.6
-26 45 34
20E-1
16E-1
12E-1
8E-1
4E-1
200
400
600
800
1000

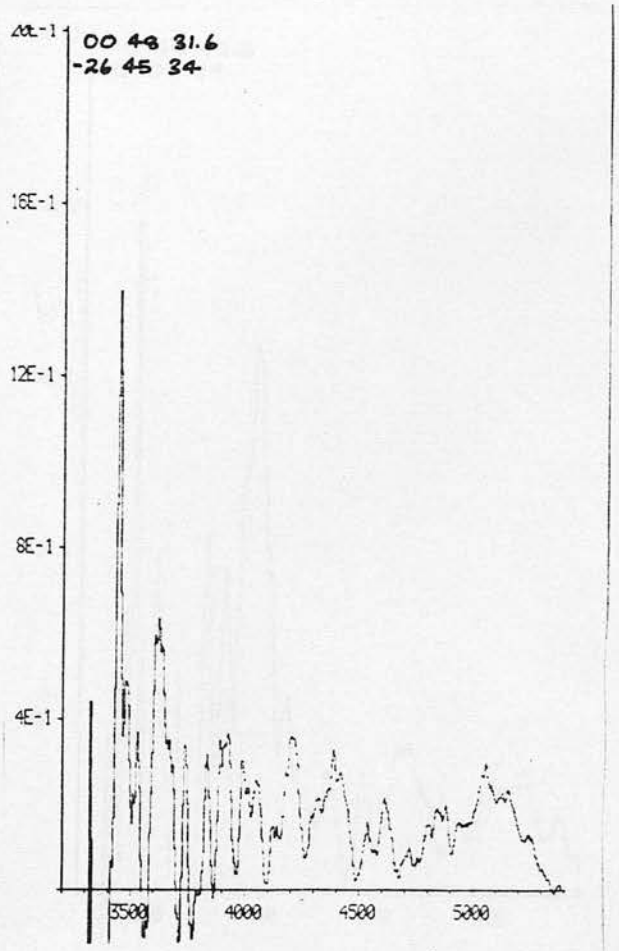
00 48 31.6
-26 45 34
20E-1
16E-1
12E-1
8E-1
4E-1
3500
4000
4500
5000

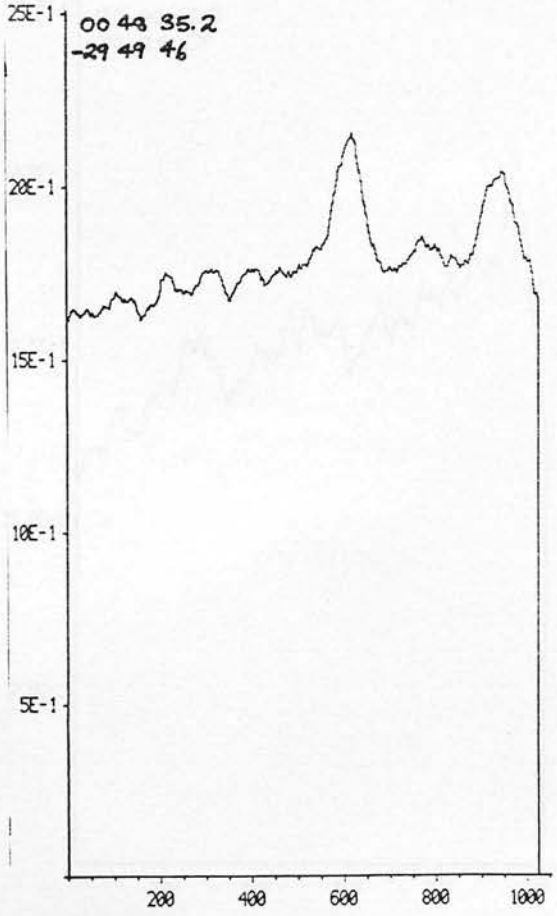
00 48 35.2
-29 49 46
25E-1
20E-1
15E-1
10E-1
5E-1
200
400
600
800
1000

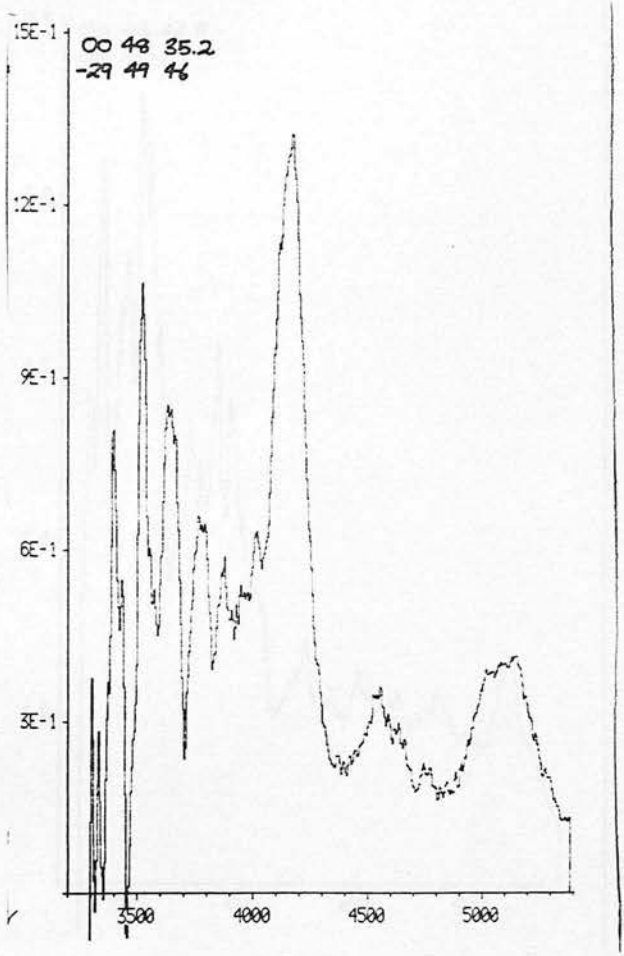
00 48 35.2
-29 49 46
15E-1
12E-1
9E-1
6E-1
3E-1
3500
4000
4500
5000

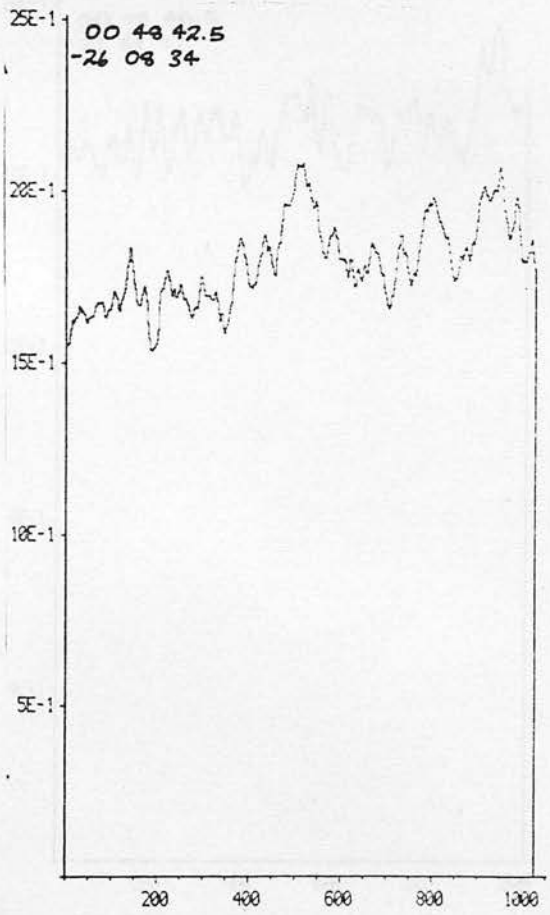
00 48 42.5
-26 08 34
25E-1
20E-1
15E-1
10E-1
5E-1
200
400
600
800
1000

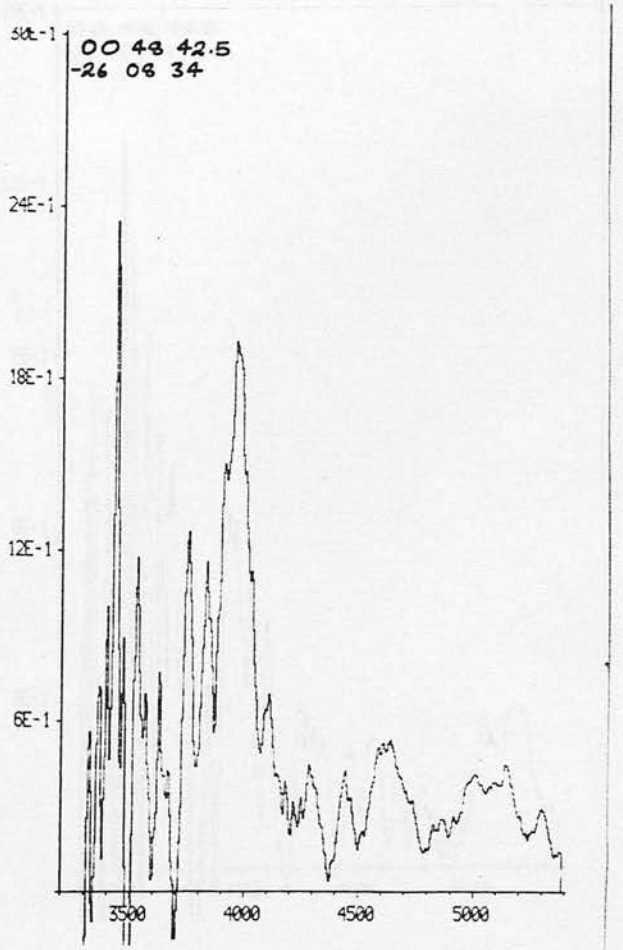
00 48 42.5
-26 08 34
30E-1
24E-1
18E-1
12E-1
6E-1
3500
4000
4500
5000

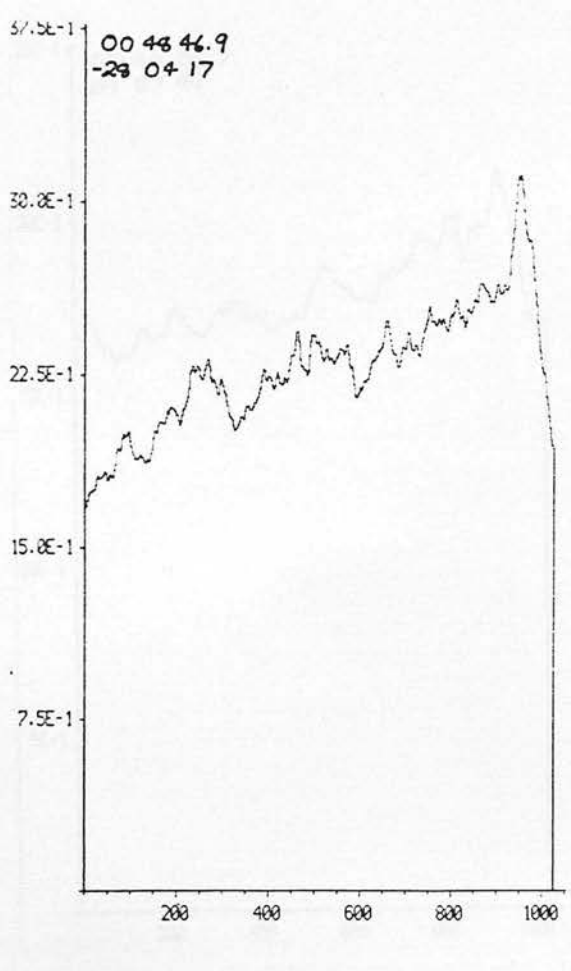
00 48 46.9
-28 04 17
30.0E-1
22.5E-1
15.0E-1
7.5E-1
200
400
600
800
1000

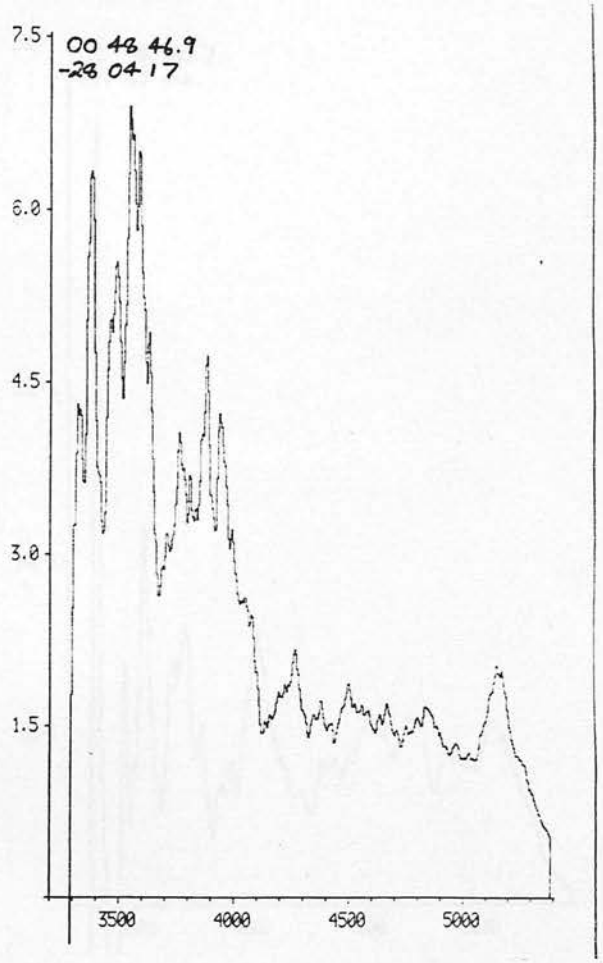
00 48 46.9
-28 04 17
7.5
6.0
4.5
3.0
1.5
3500
4000
4500
5000

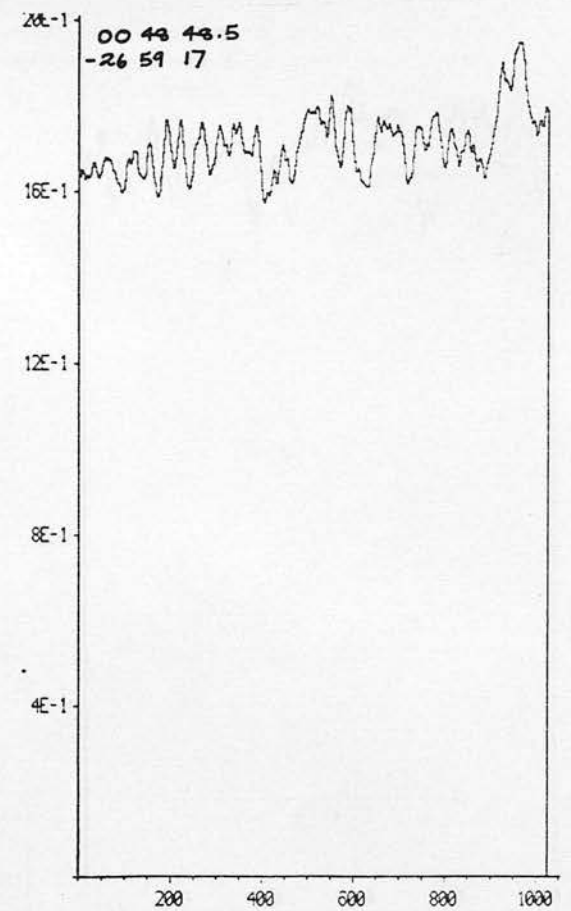
00 48 48.5
-26 59 17
16E-1
12E-1
8E-1
4E-1
200
400
600
800
1000

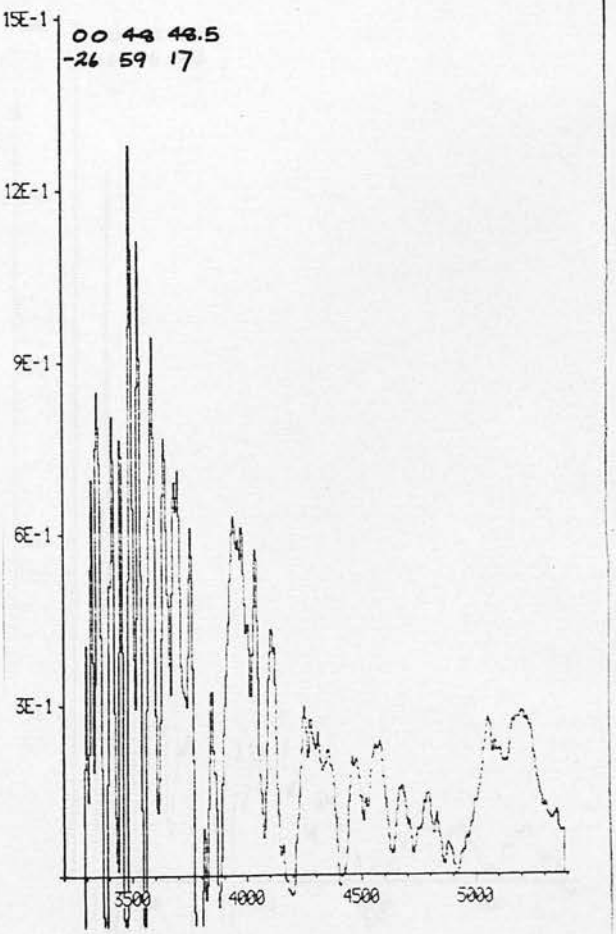
00 48 48.5
-26 59 17
15E-1
12E-1
9E-1
6E-1
3E-1
3500
4000
4500
5000

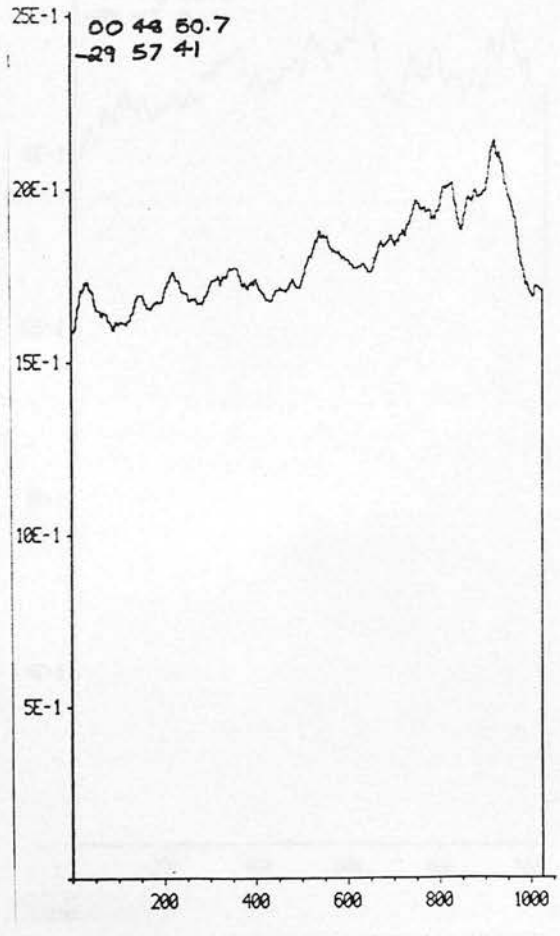
00 48 50.7
-29 57 41
25E-1
20E-1
15E-1
10E-1
5E-1
200
400
600
800
1000

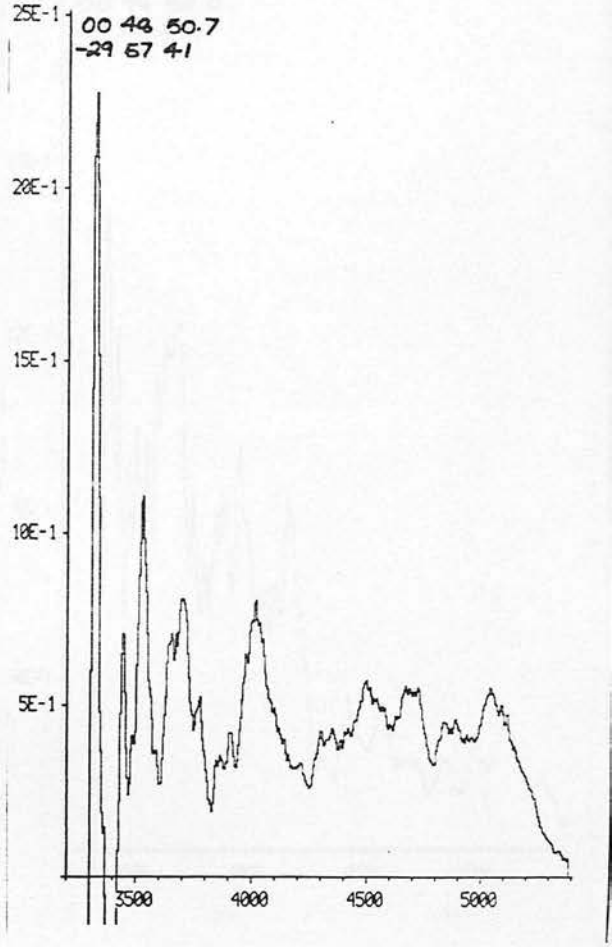
00 48 50.7
-29 57 41
25E-1
20E-1
15E-1
10E-1
5E-1
3500
4000
4500
5000

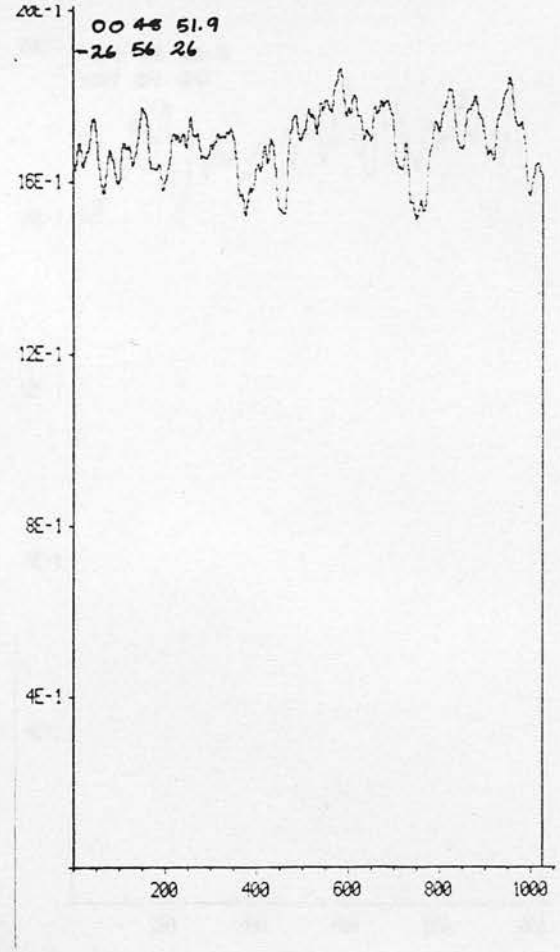
00 48 51.9
-26 56 26
16E-1
12E-1
8E-1
4E-1
200
400
600
800
1000

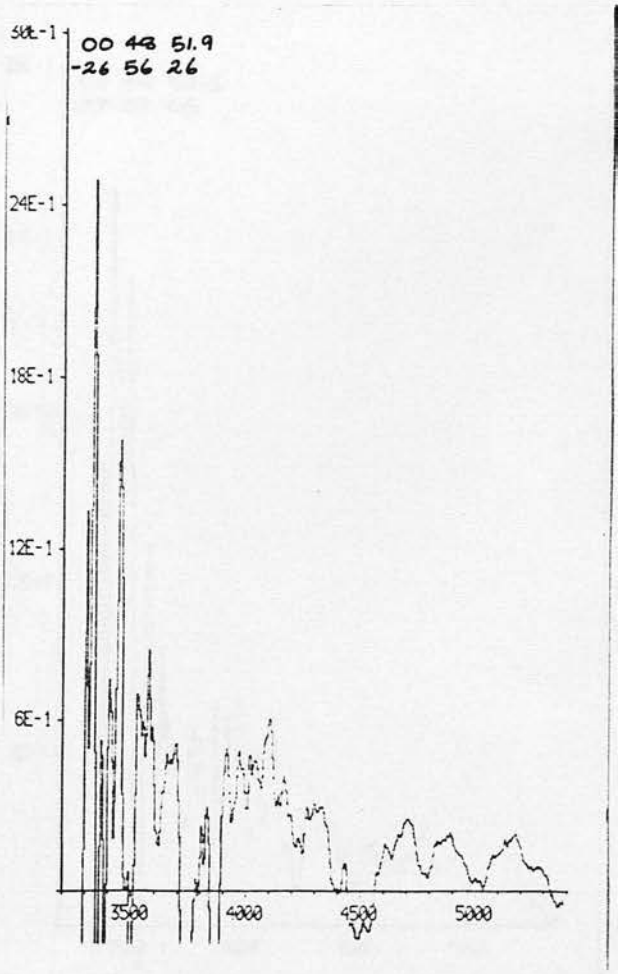
00 48 51.9
-26 56 26
24E-1
18E-1
12E-1
6E-1
3500
4000
4500
5000

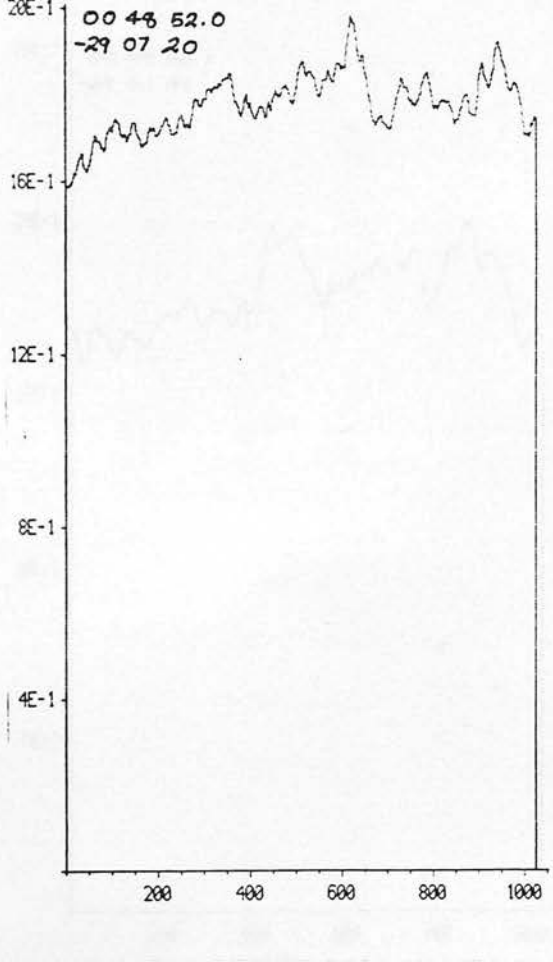
00 48 52.0
-29 07 20
20E-1
16E-1
12E-1
8E-1
4E-1
200
400
600
800
1000

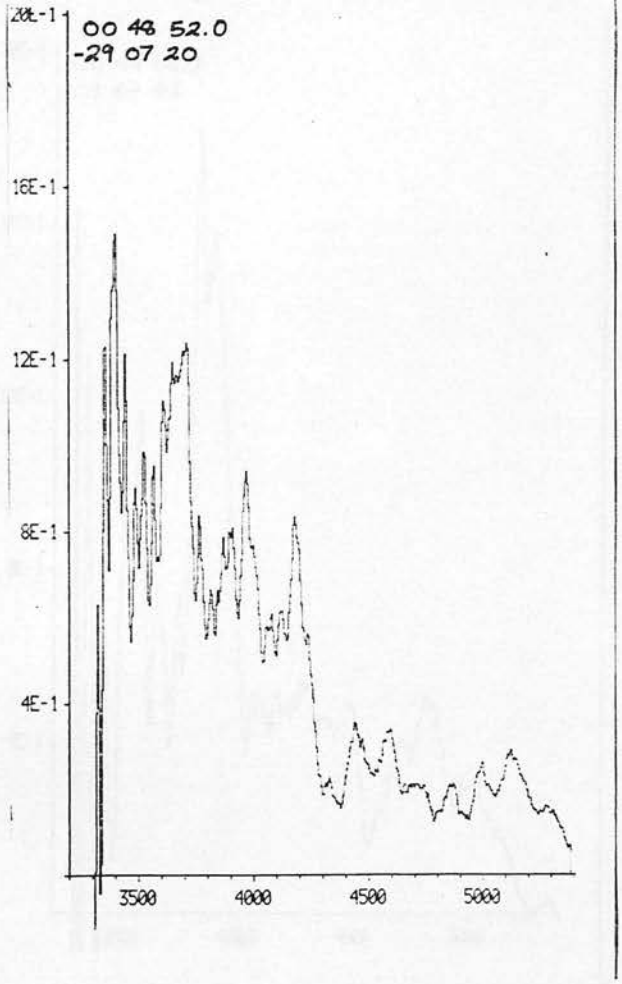
00 48 52.0
-29 07 20
20E-1
16E-1
12E-1
8E-1
4E-1
3500
4000
4500
5000

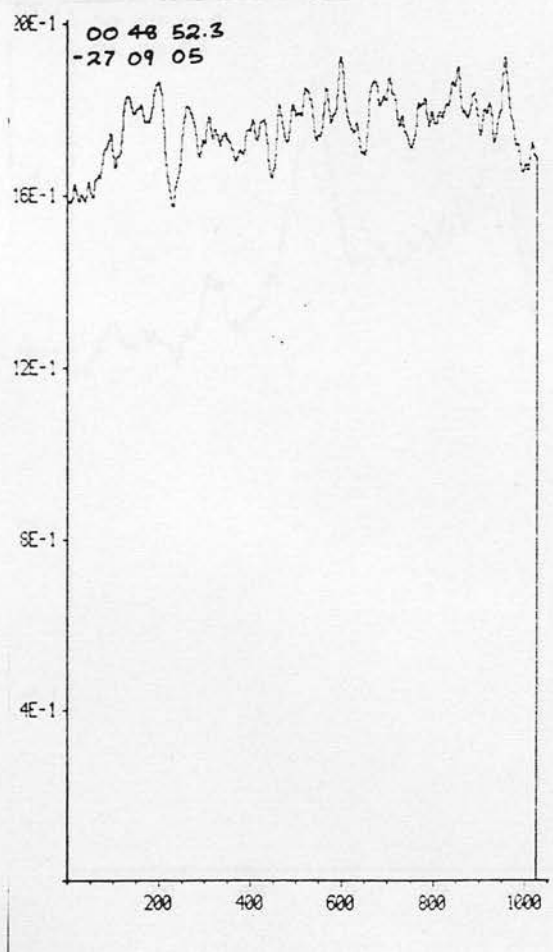
00 48 52.3
-27 09 05
20E-1
16E-1
12E-1
8E-1
4E-1
200
400
600
800
1000

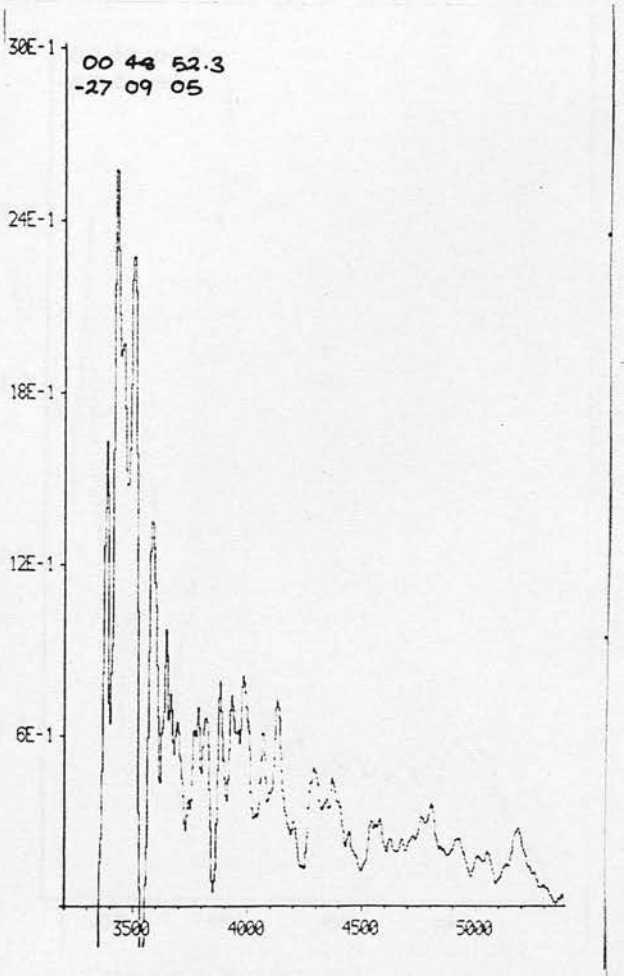
00 48 52.3
-27 09 05
30E-1
24E-1
18E-1
12E-1
6E-1
3500
4000
4500
5000

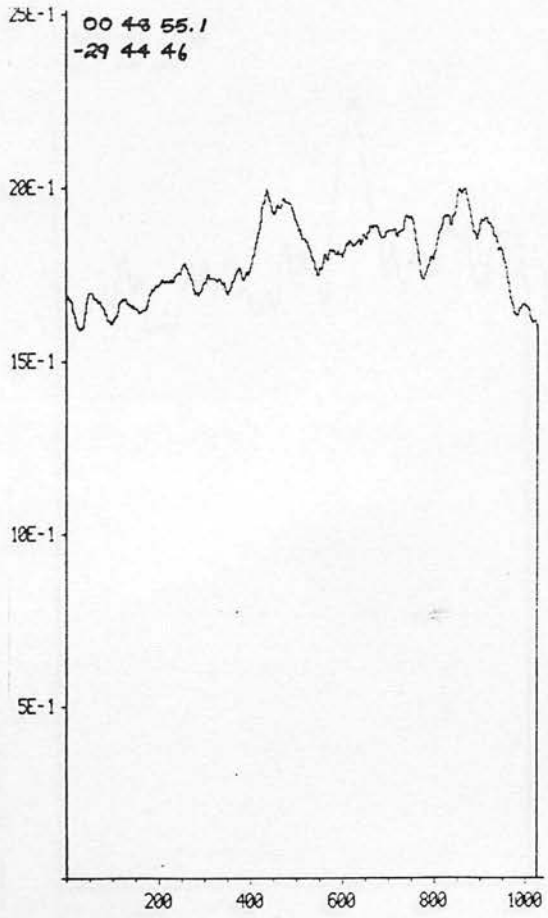
00 48 55.1
-29 44 46
25E-1
20E-1
15E-1
10E-1
5E-1
200
400
600
800
1000

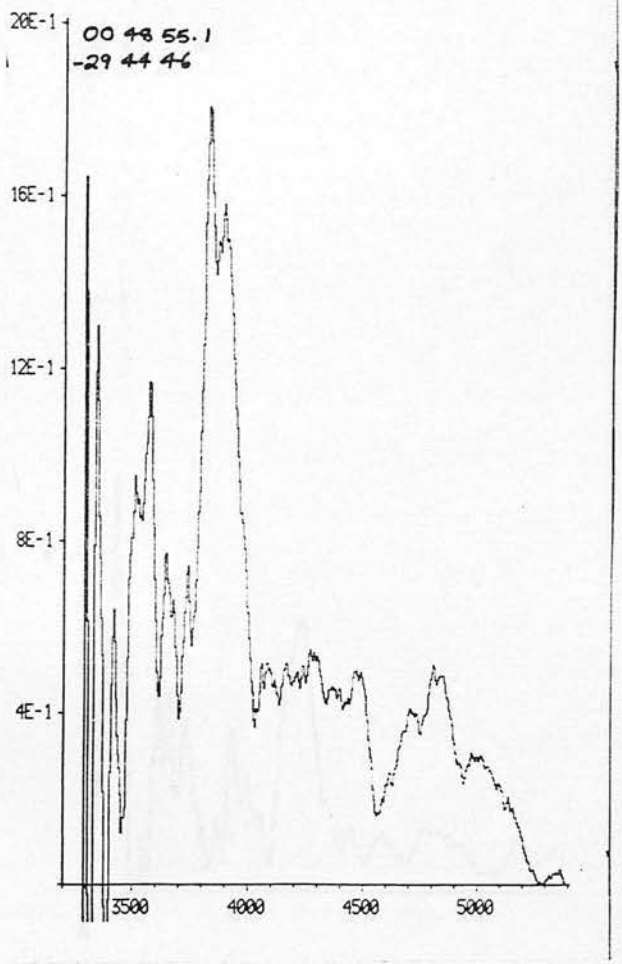
00 48 55.1
-29 44 46
20E-1
16E-1
12E-1
8E-1
4E-1
3500
4000
4500
5000

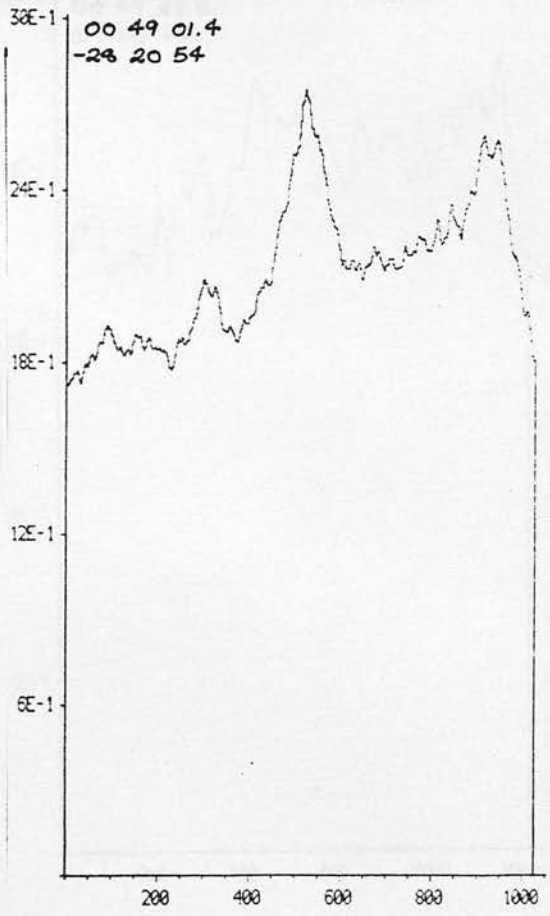
00 49 01.4
-28 20 54
30E-1
24E-1
18E-1
12E-1
6E-1
200
400
600
800
1000

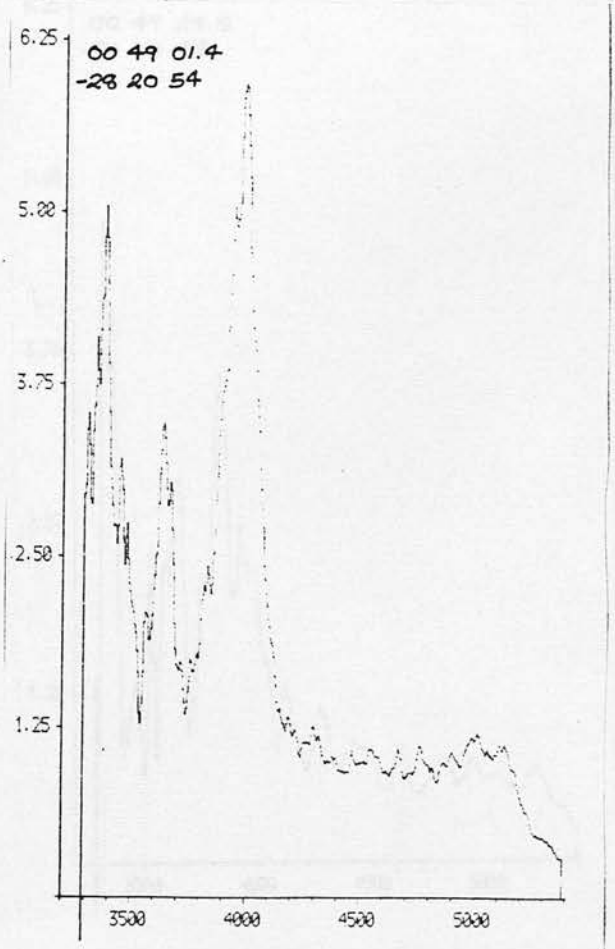
00 49 01.4
-28 20 54
6.25
5.00
3.75
2.50
1.25
3500
4000
4500
5000

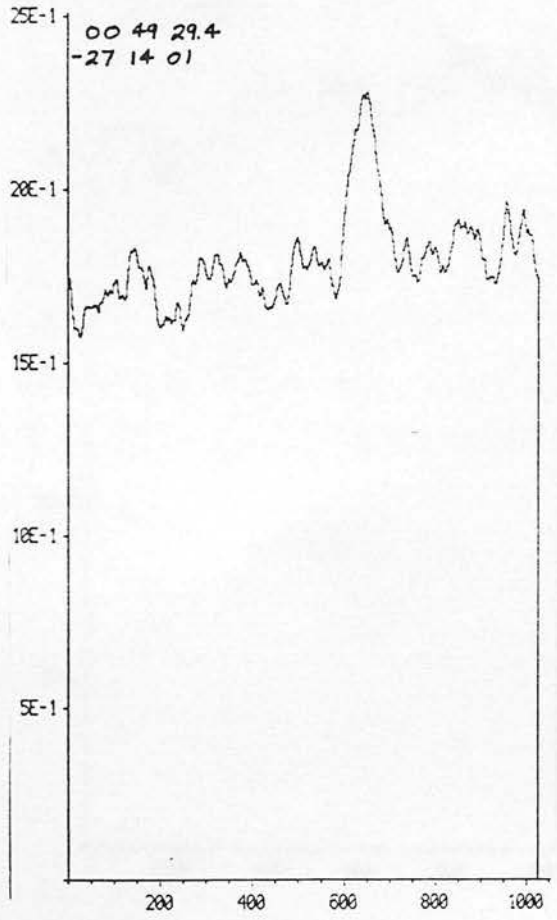
00 49 29.4
-27 14 01
25E-1
20E-1
15E-1
10E-1
5E-1
200
400
600
800
1000

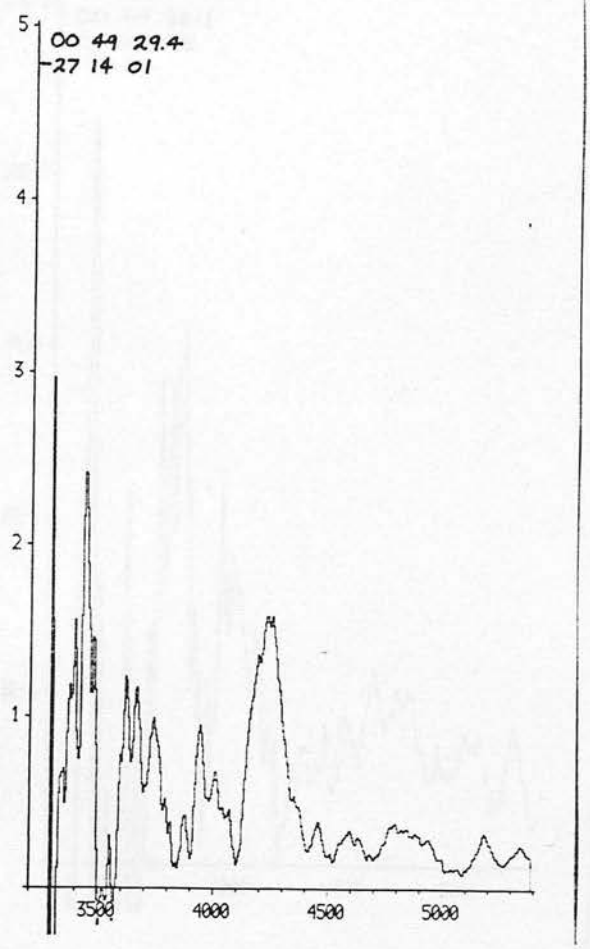
00 49 29.4
-27 14 01
5
4
3
2
1
3500
4000
4500
5000

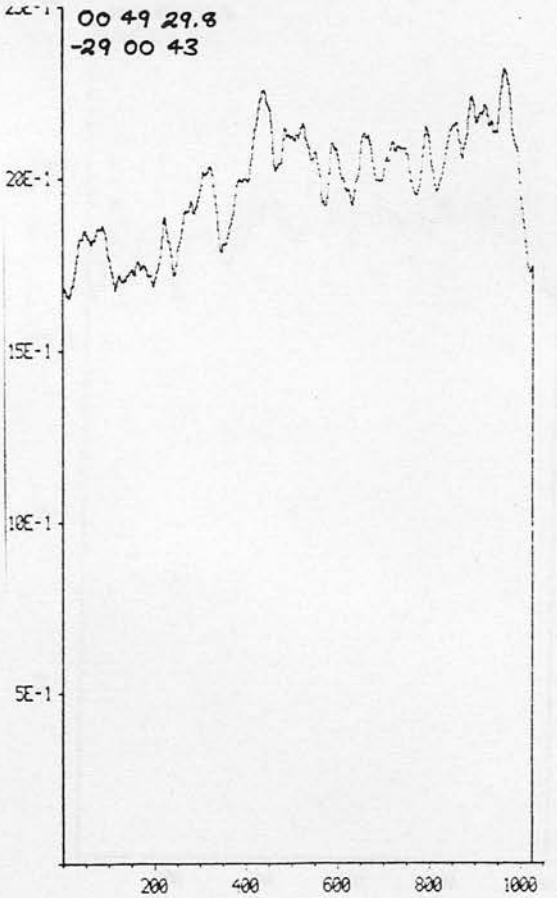
00 49 29.8
-29 00 43
20E-1
15E-1
10E-1
5E-1
200
400
600
800
1000

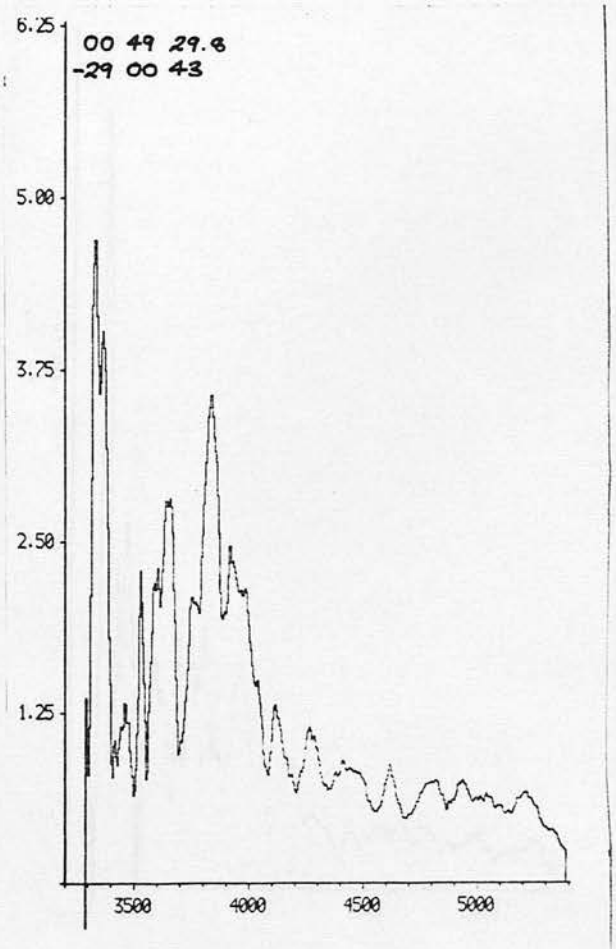
00 49 29.8
-29 00 43
6.25
5.00
3.75
2.50
1.25
3500
4000
4500
5000

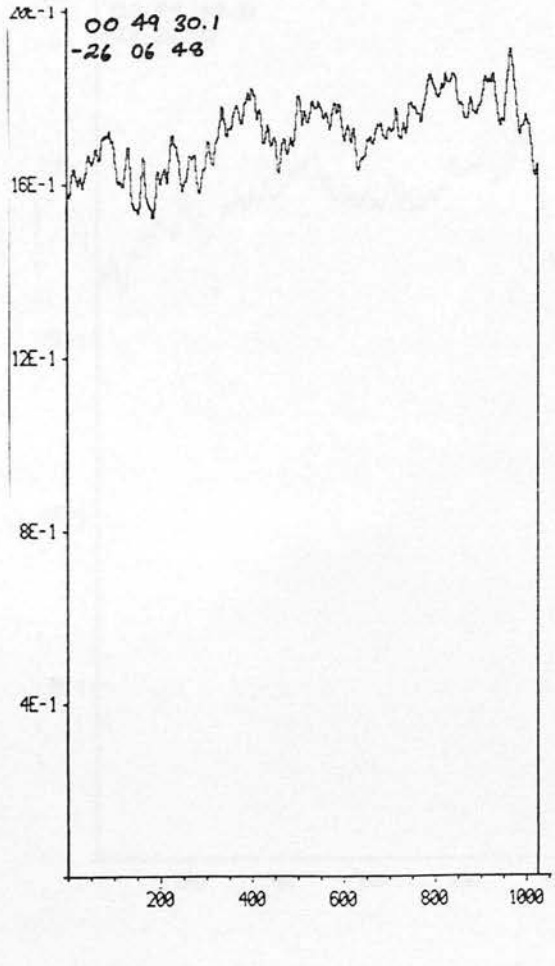
00 49 30.1
-26 06 48
16E-1
12E-1
8E-1
4E-1
200
400
600
800
1000

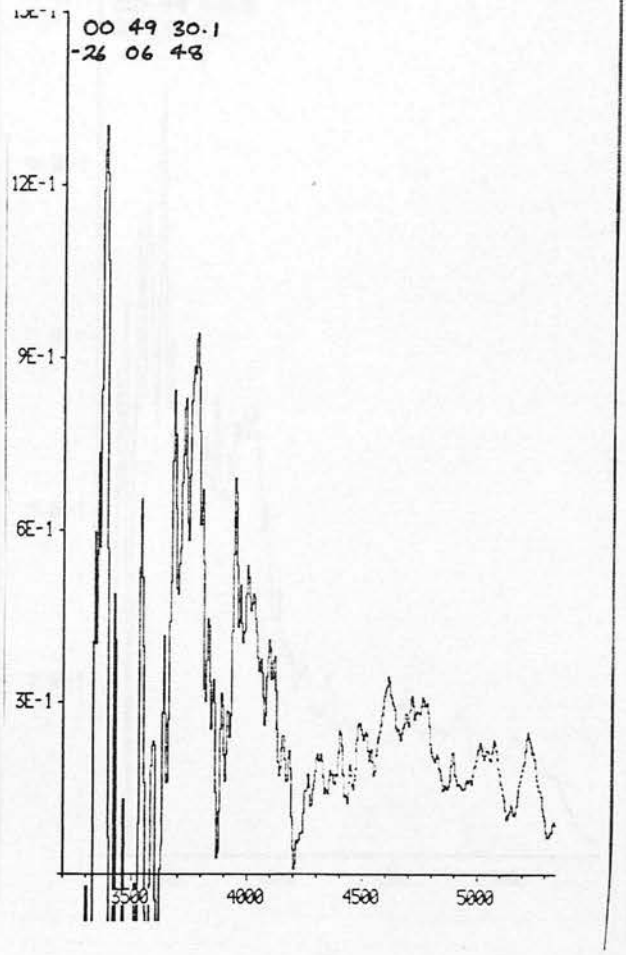
00 49 30.1
-26 06 48
12E-1
9E-1
6E-1
3E-1
3500
4000
4500
5000

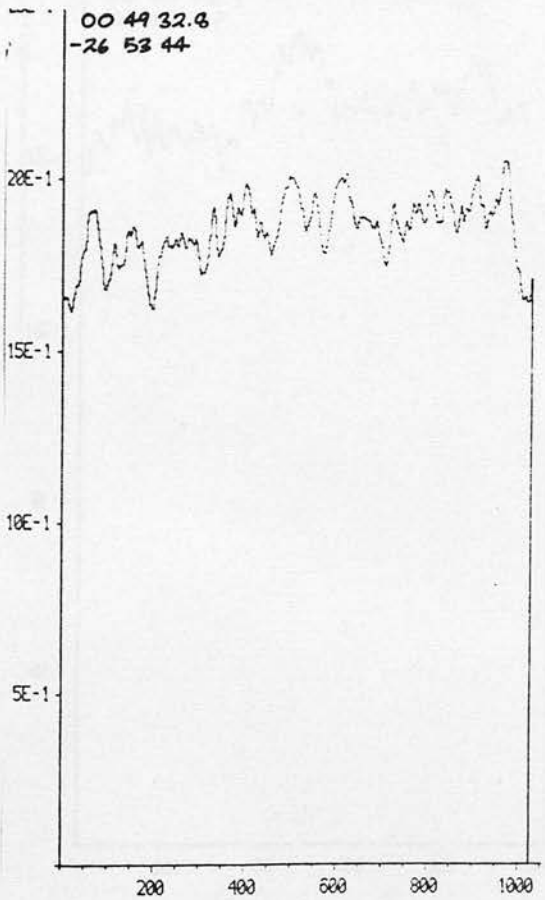
00 49 32.8
-26 53 44
20E-1
15E-1
10E-1
5E-1
200
400
600
800
1000

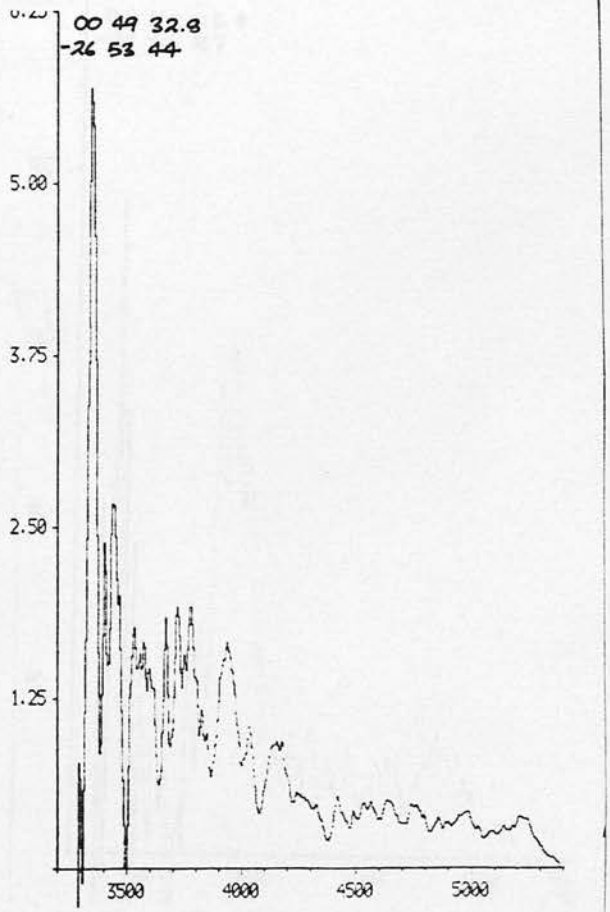
00 49 32.8
-26 53 44
5.00
3.75
2.50
1.25
3500
4000
4500
5000


00 49 44.5
-27 36 11
20E-1
15E-1
10E-1
5E-1
200
400
600
800
1000

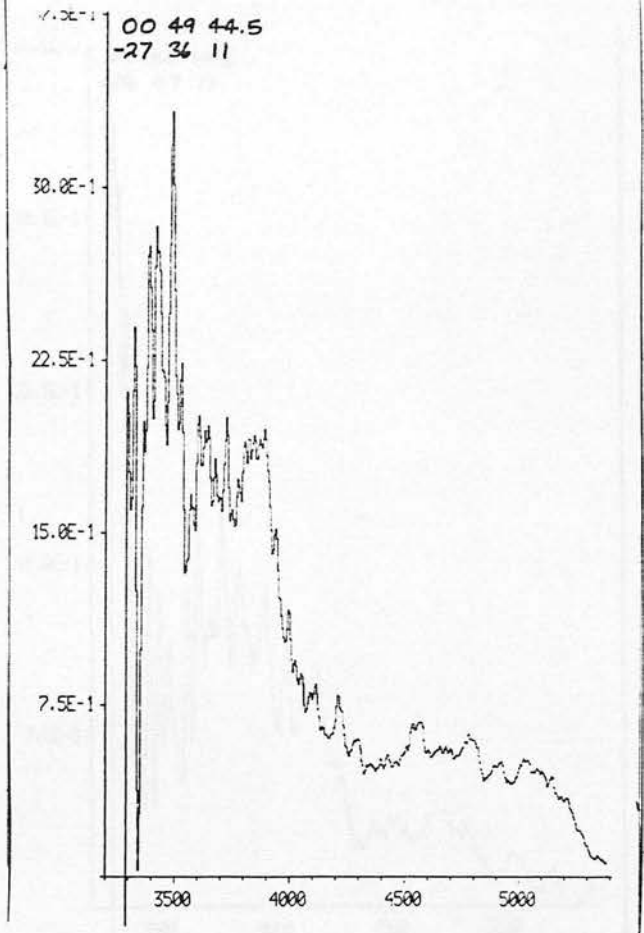
00 49 44.5
-27 36 11
30.0E-1
22.5E-1
15.0E-1
7.5E-1
3500
4000
4500
5000

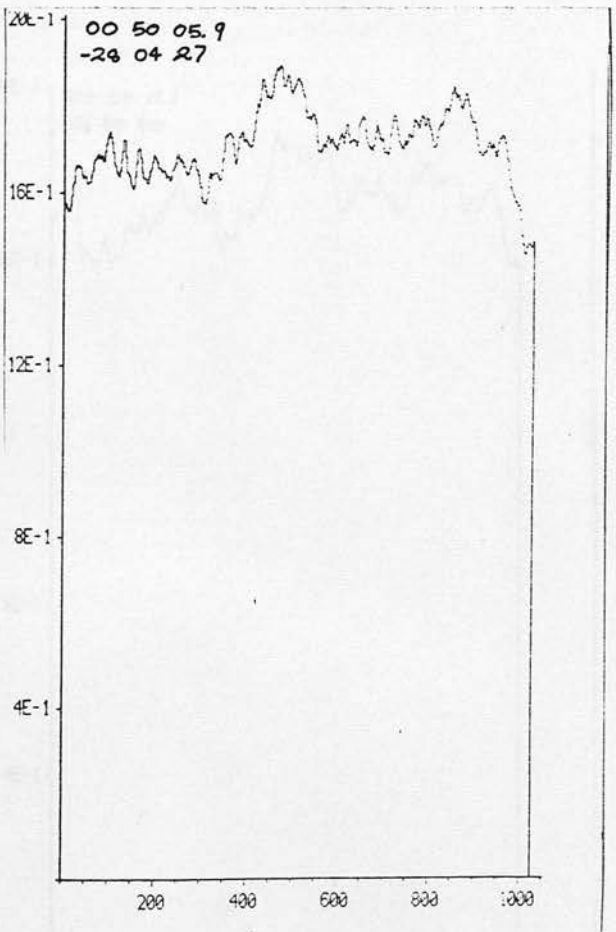
00 50 05.9
-28 04 27
16E-1
12E-1
8E-1
4E-1
200
400
600
800
1000

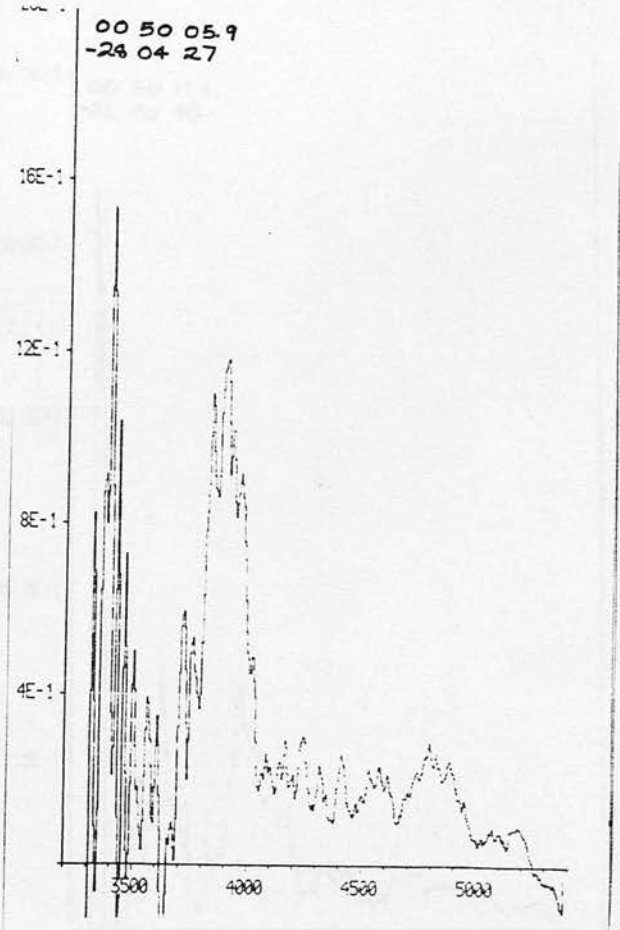
00 50 05.9
-28 04 27
16E-1
12E-1
8E-1
4E-1
3500
4000
4500
5000

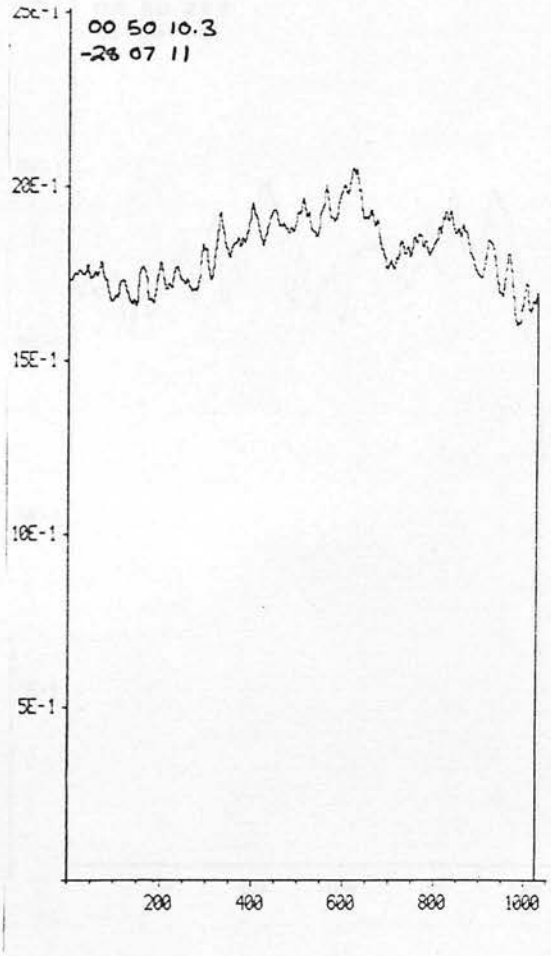
00 50 10.3
-28 07 11
20E-1
15E-1
10E-1
5E-1
200
400
600
800
1000

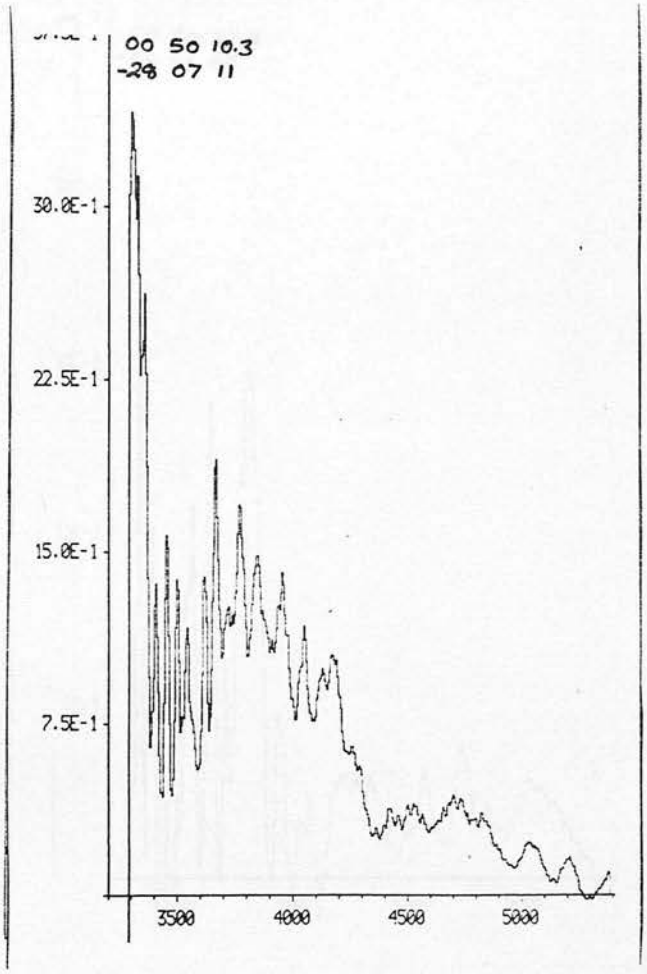
00 50 10.3
-28 07 11
30.0E-1
22.5E-1
15.0E-1
7.5E-1
3500
4000
4500
5000

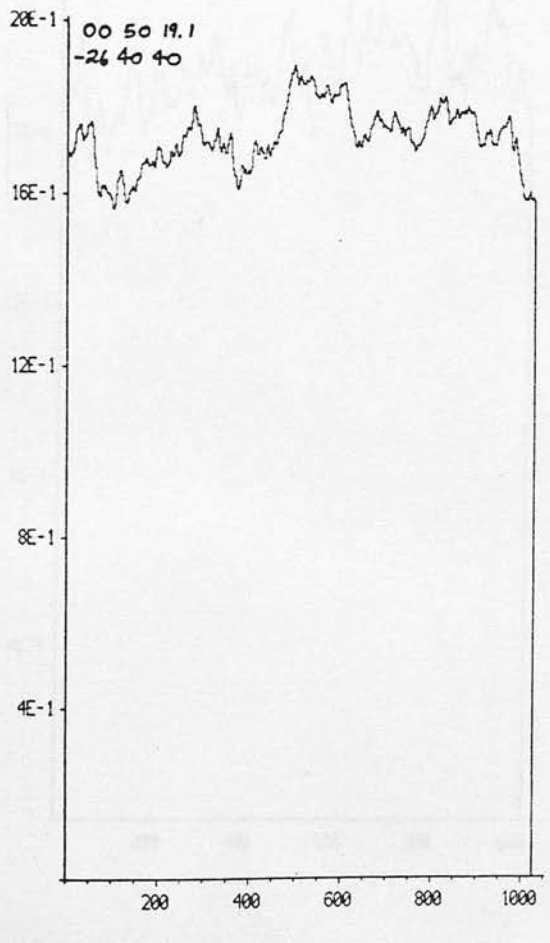
00 50 19.1
-26 40 40
20E-1
16E-1
12E-1
8E-1
4E-1
200
400
600
800
1000

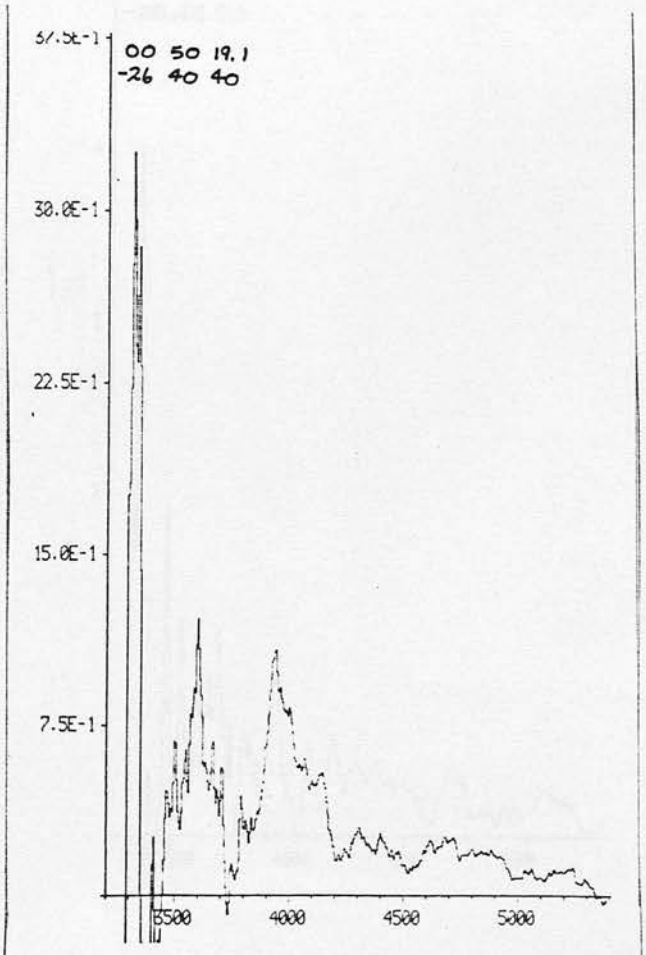
00 50 19.1
-26 40 40
30.0E-1
22.5E-1
15.0E-1
7.5E-1
3500
4000
4500
5000

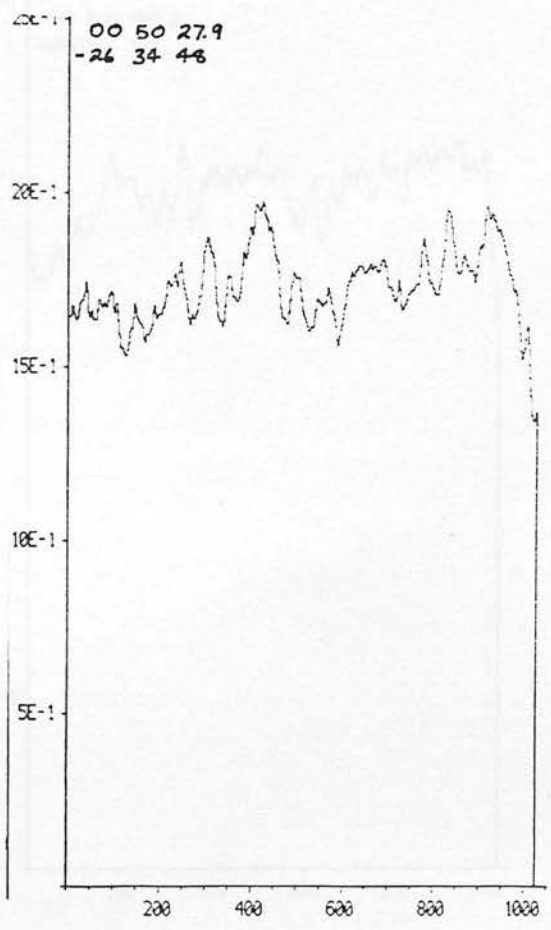
00 50 27.9
-26 34 48
20E-1
15E-1
10E-1
5E-1
200
400
600
800
1000

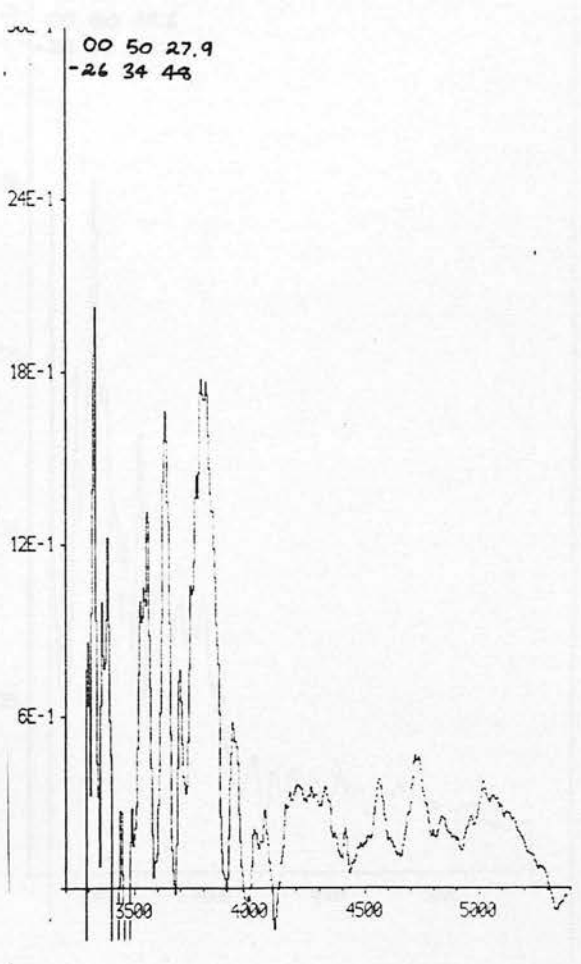
00 50 27.9
-26 34 48
24E-1
18E-1
12E-1
6E-1
3500
4000
4500
5000

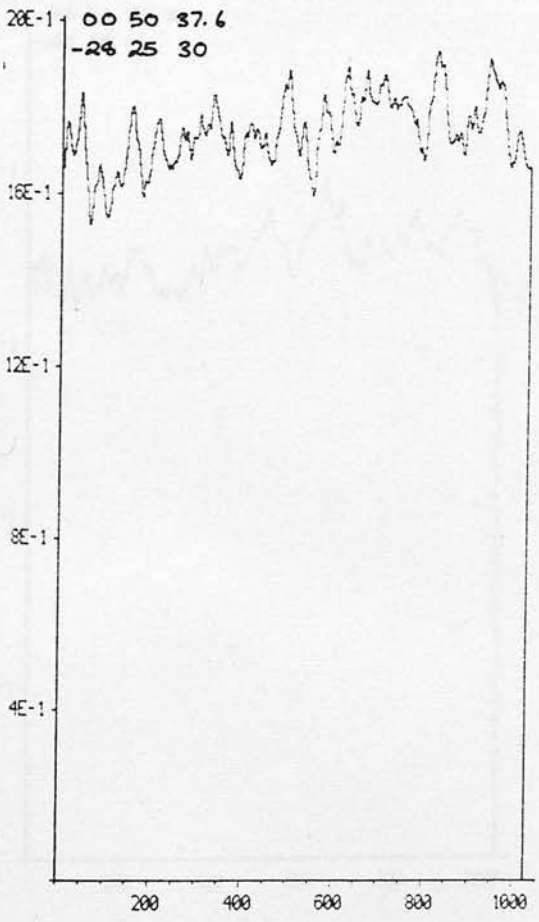
00 50 37.6
-26 25 30
20E-1
16E-1
12E-1
8E-1
4E-1
200
400
600
800
1000

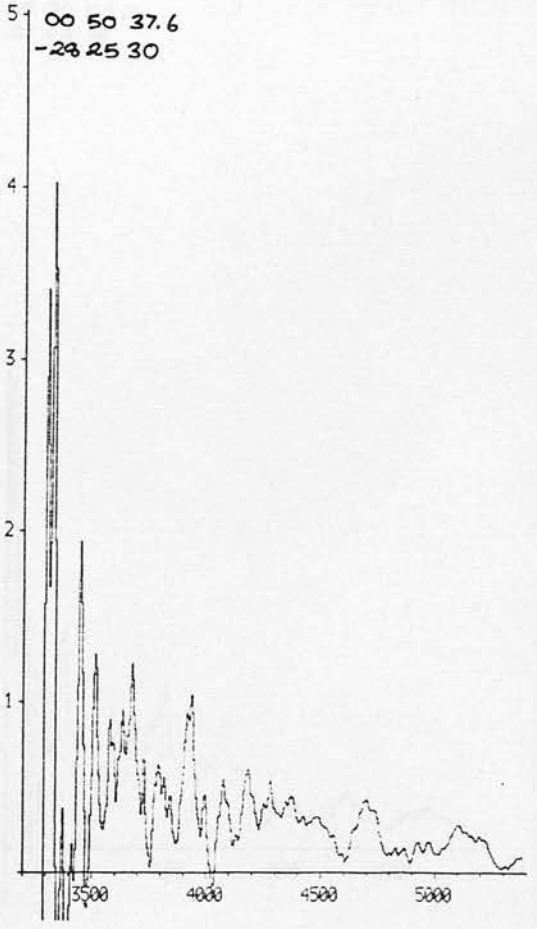
00 50 37.6
-26 25 30
5
4
3
2
1
3500
4000
4500
5000

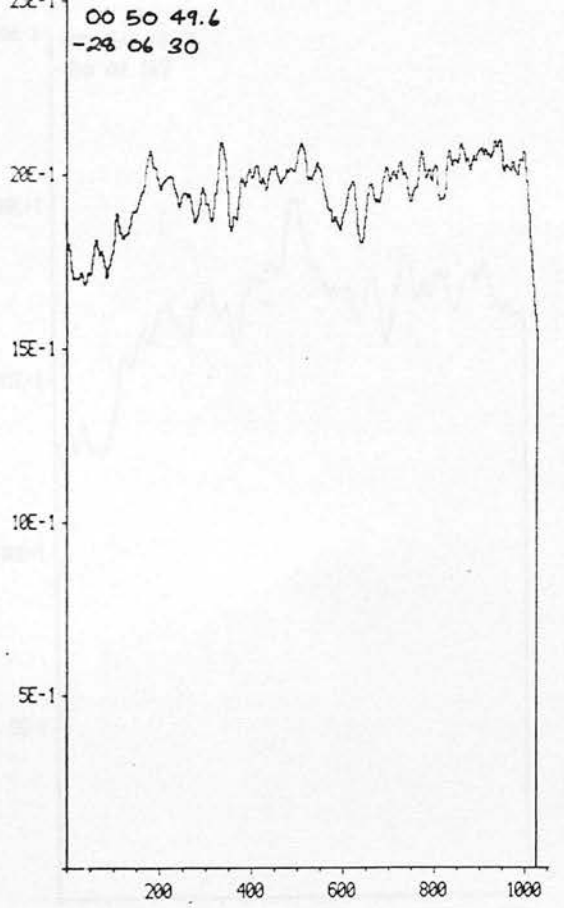
00 50 49.6
-28 06 30
25E-1
20E-1
15E-1
10E-1
5E-1
200
400
600
800
1000

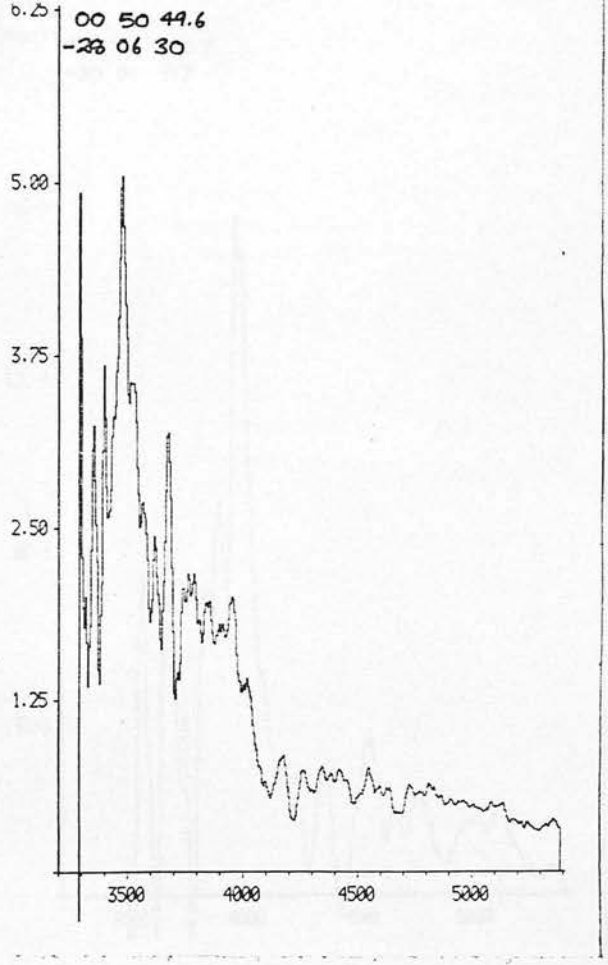
00 50 49.6
-28 06 30
6.25
5.00
3.75
2.50
1.25
3500
4000
4500
5000

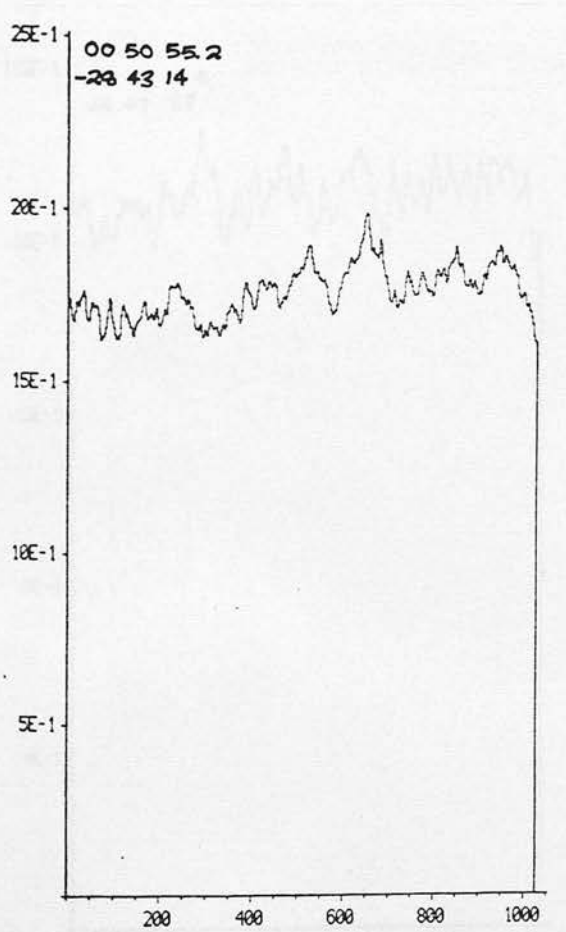
00 50 55.2
-28 43 14
25E-1
20E-1
15E-1
10E-1
5E-1
200
400
600
800
1000

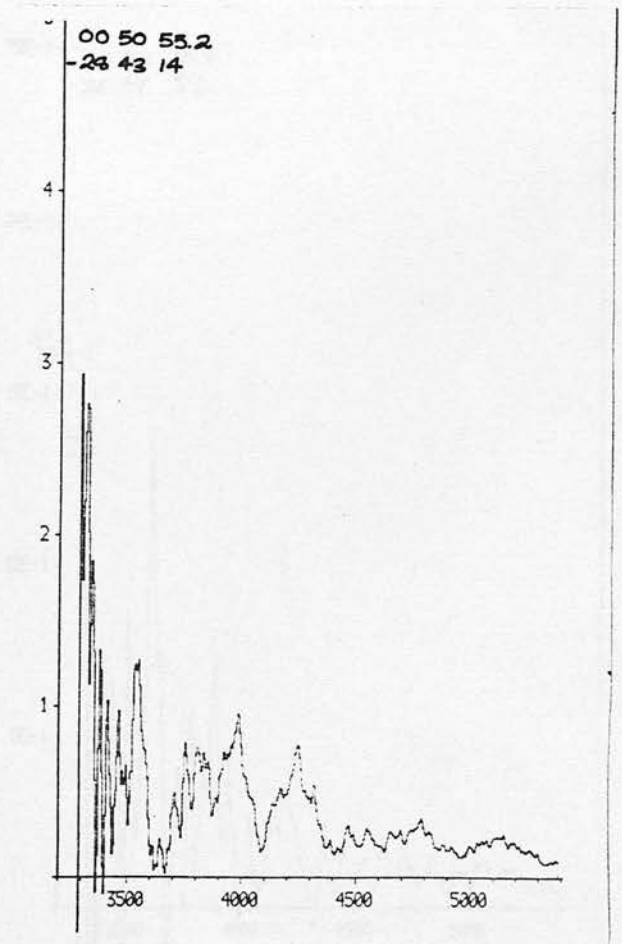
00 50 55.2
-28 43 14
4
3
2
1
3500
4000
4500
5000


00 51 02.7
-30 01 57
20E-1
15E-1
10E-1
5E-1
200
400
600
800
1000

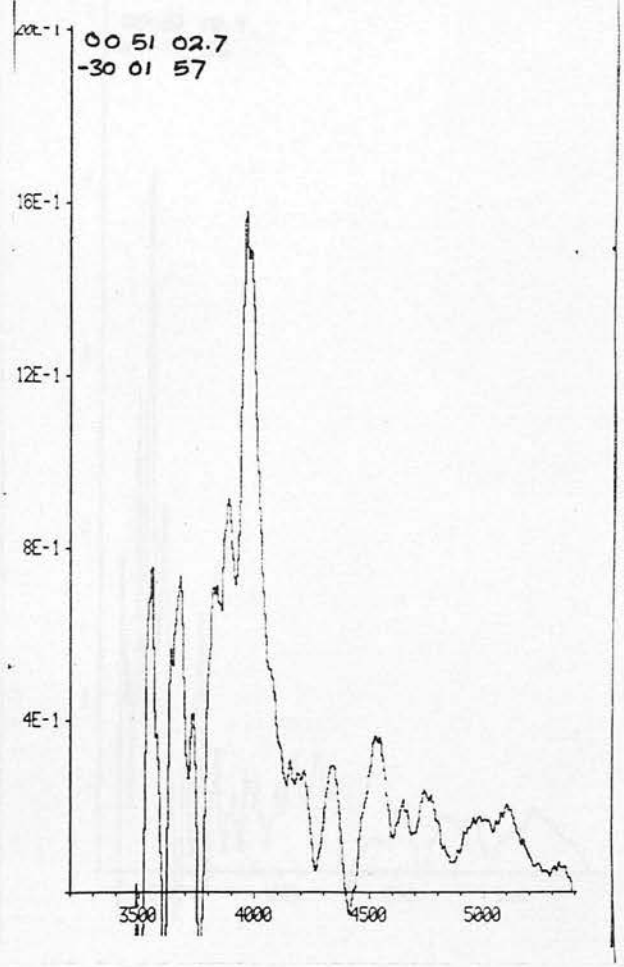
00 51 02.7
-30 01 57
16E-1
12E-1
8E-1
4E-1
3500
4000
4500
5000

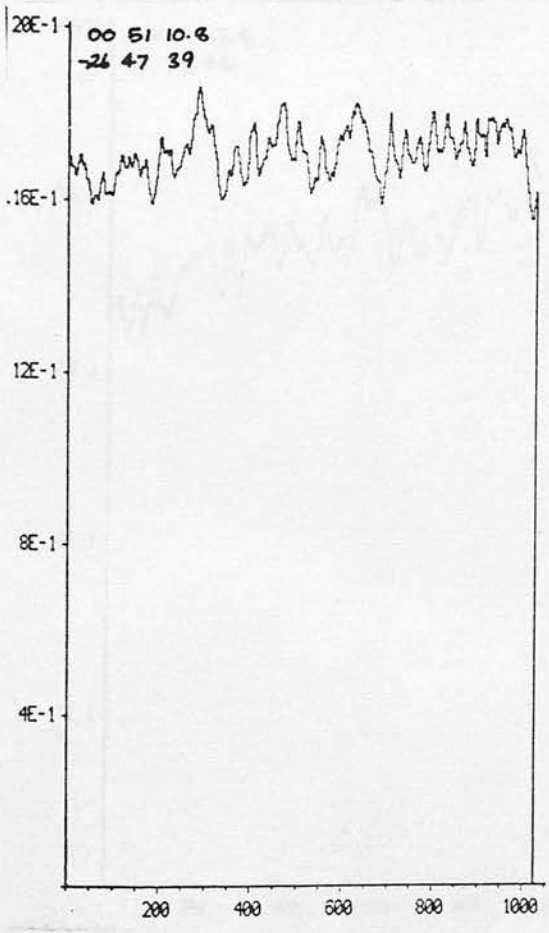
00 51 10.8
-26 47 39
16E-1
12E-1
8E-1
4E-1
200
400
600
800
1000

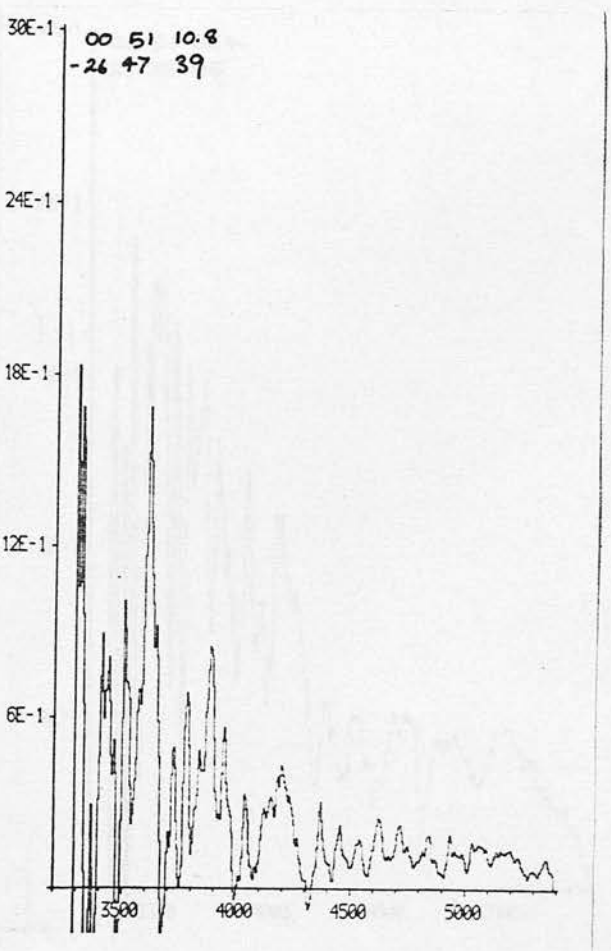
00 51 10.8
-26 47 39
30E-1
24E-1
18E-1
12E-1
6E-1
3500
4000
4500
5000

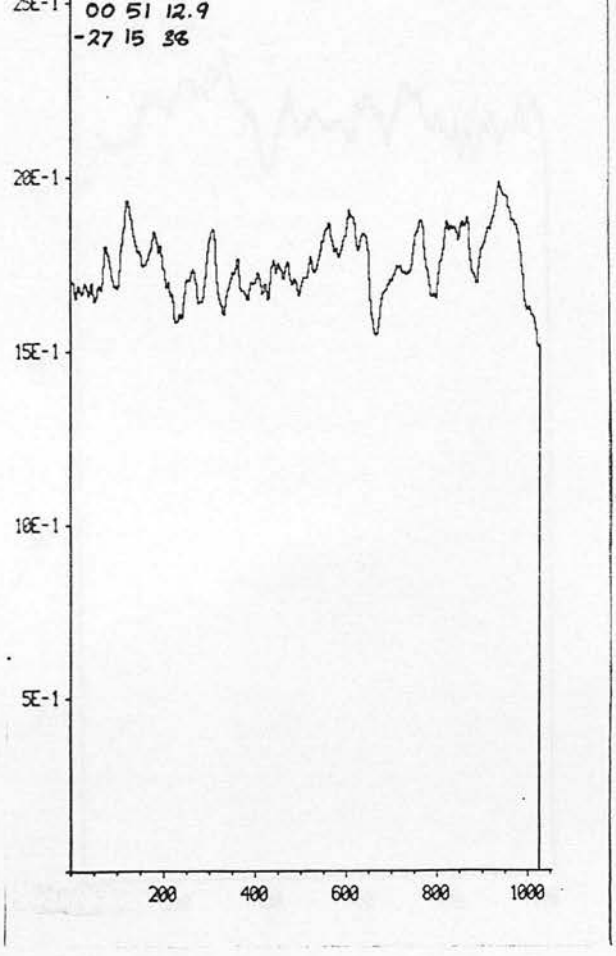
00 51 12.9
-27 15 36
25E-1
20E-1
15E-1
10E-1
5E-1
200
400
600
800
1000

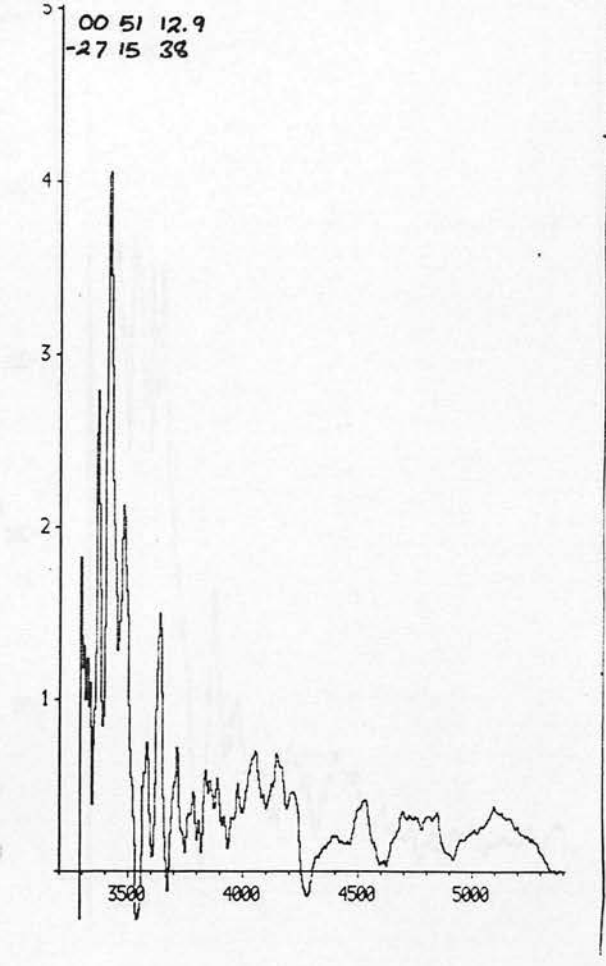
00 51 12.9
-27 15 36
5
4
3
2
1
3500
4000
4500
5000

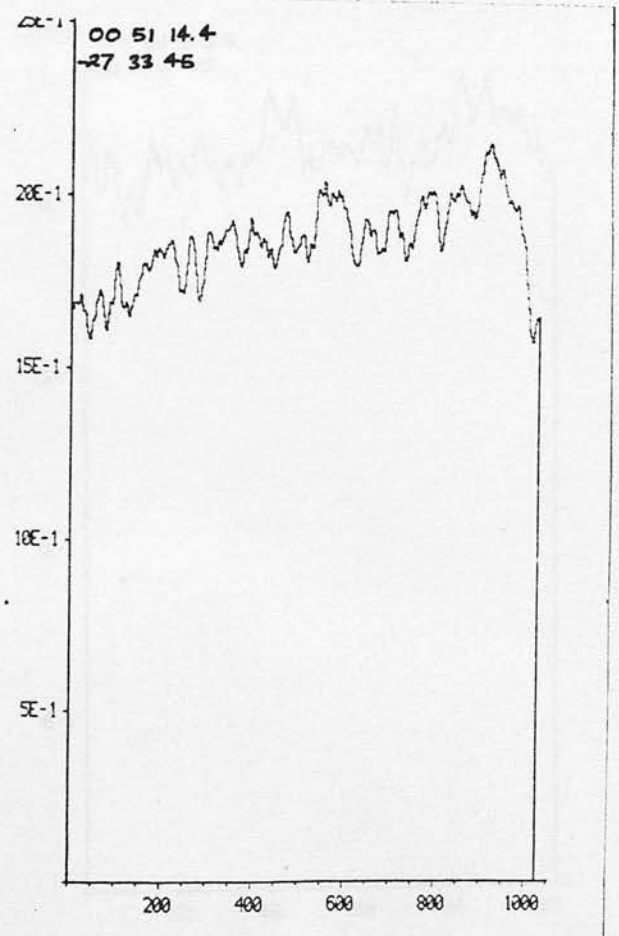
00 51 14.4
-27 33 46
20E-1
15E-1
10E-1
5E-1
200
400
600
800
1000

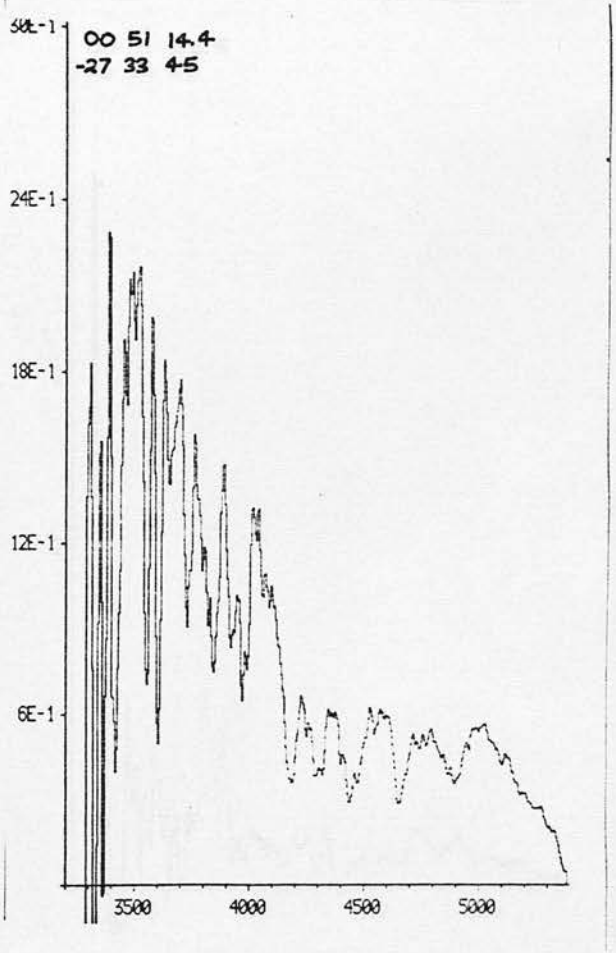
00 51 14.4
-27 33 45
30E-1
24E-1
18E-1
12E-1
6E-1
3500
4000
4500
5000

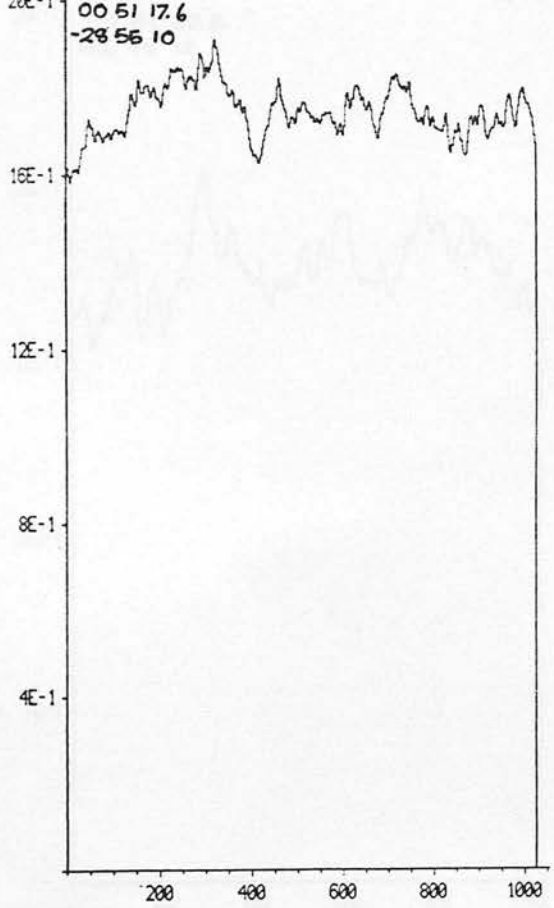
00 51 17.6
-28 56 10
16E-1
12E-1
8E-1
4E-1
200
400
600
800
1000

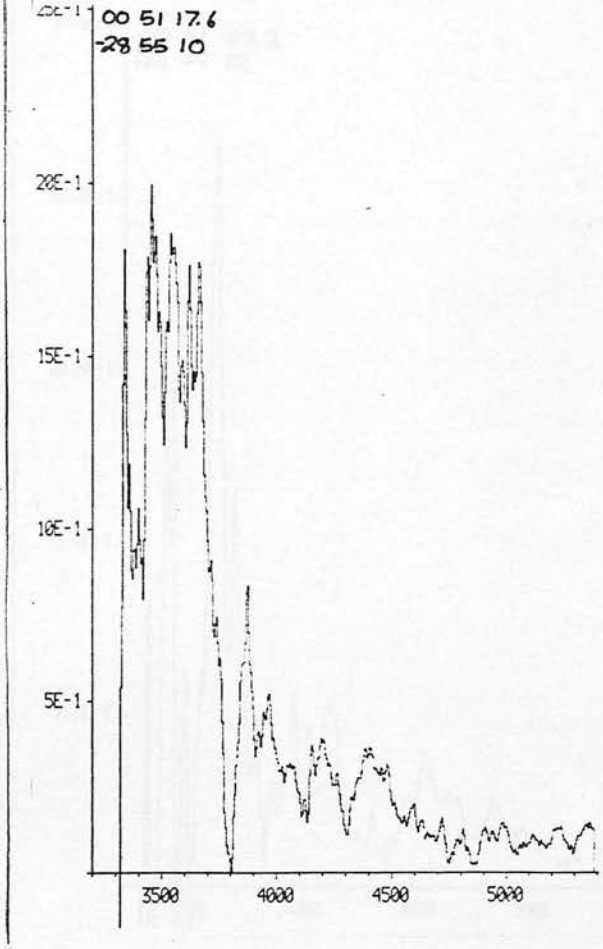
00 51 17.6
-28 55 10
20E-1
15E-1
10E-1
5E-1
3500
4000
4500
5000

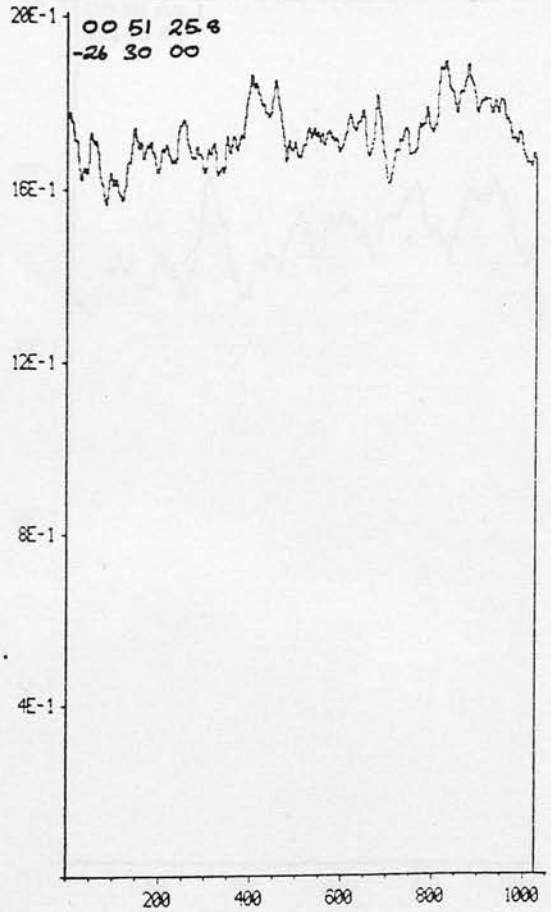
00 51 25.8
-26 30 00
20E-1
16E-1
12E-1
8E-1
4E-1
200
400
600
800
1000

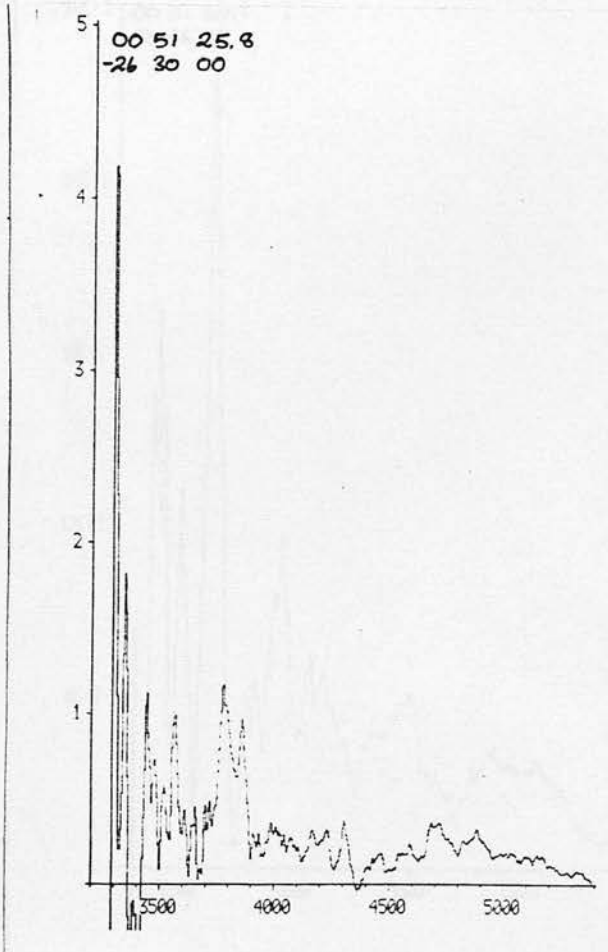
00 51 25.8
-26 30 00
5
4
3
2
1
3500
4000
4500
5000

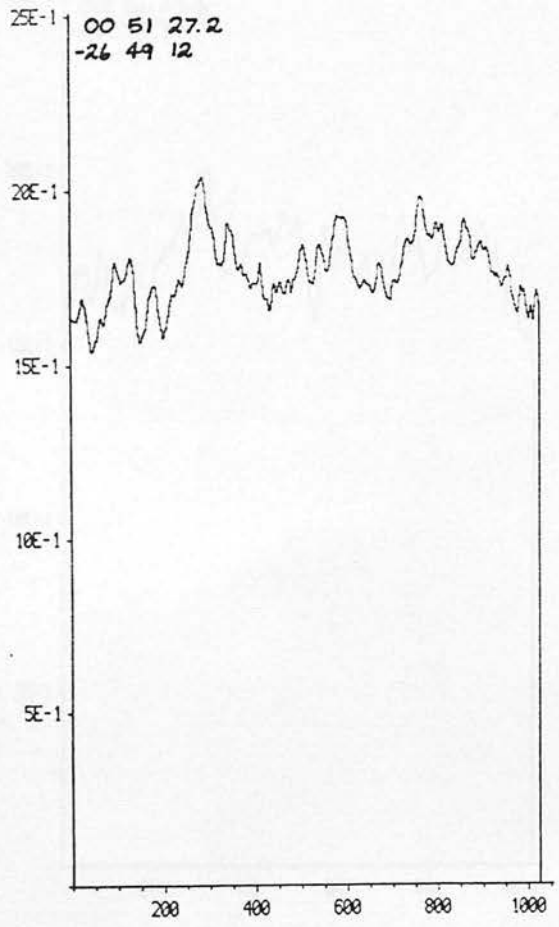
00 51 27.2
-26 49 12
25E-1
20E-1
15E-1
10E-1
5E-1
200
400
600
800
1000

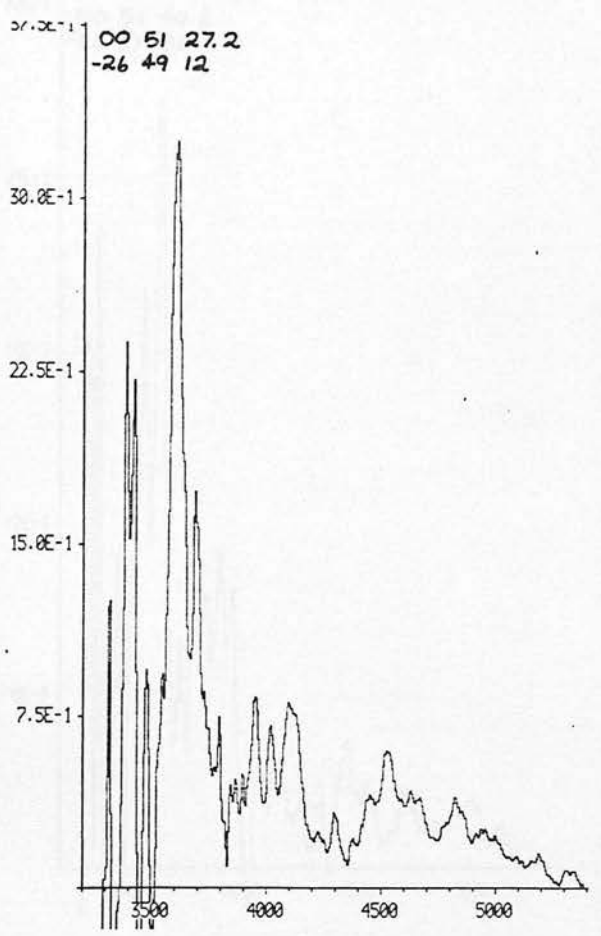
00 51 27.2
-26 49 12
30.0E-1
22.5E-1
15.0E-1
7.5E-1
3500
4000
4500
5000

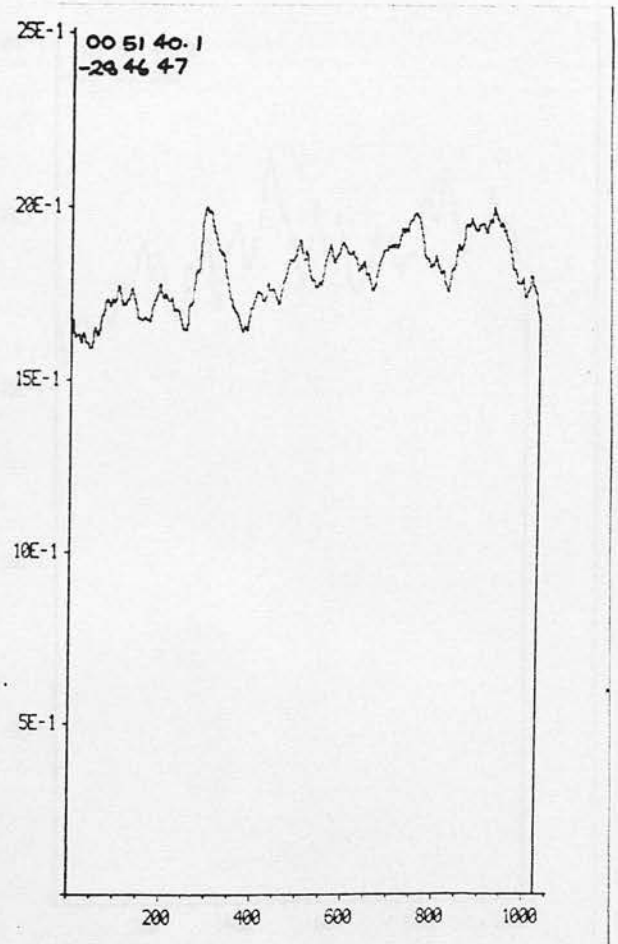
00 51 40.1
-26 46 47
25E-1
20E-1
15E-1
10E-1
5E-1
200
400
600
800
1000

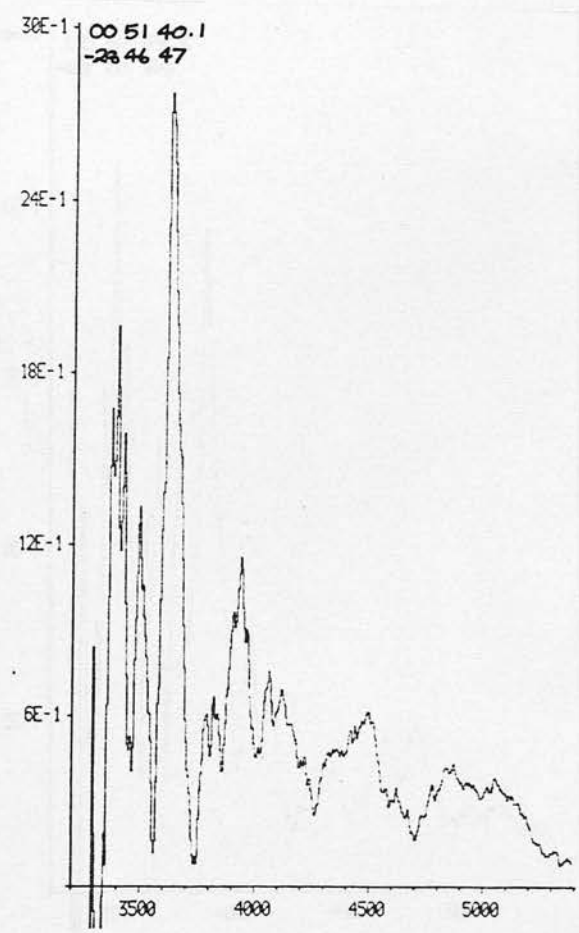
00 51 40.1
-26 46 47
30E-1
24E-1
18E-1
12E-1
6E-1
3500
4000
4500
5000

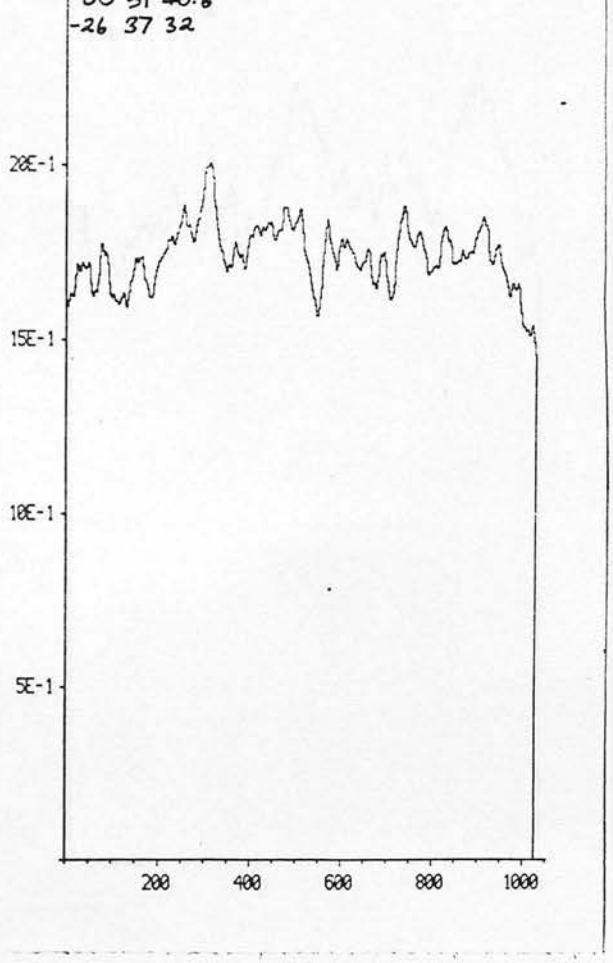
00 51 40.6
-26 37 32
20E-1
15E-1
10E-1
5E-1
200
400
600
800
1000

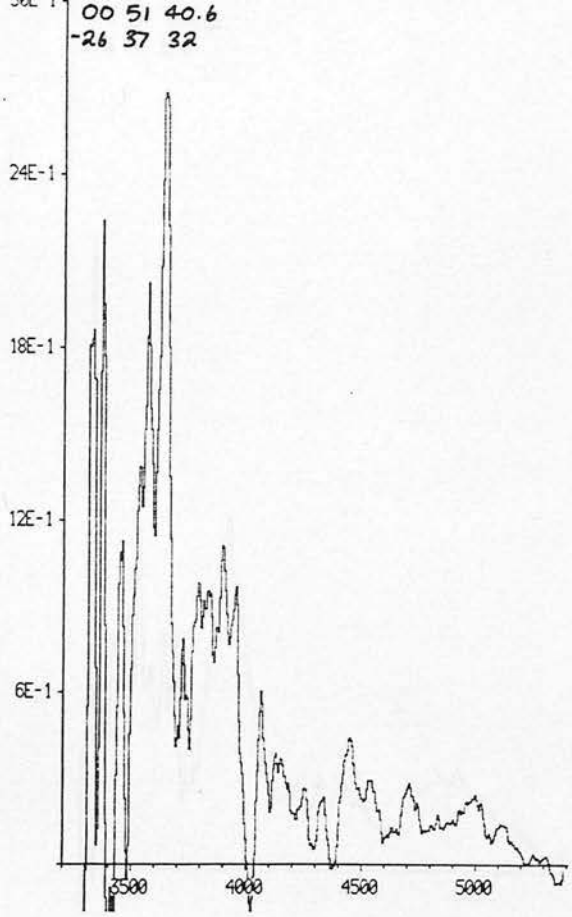
00 51 40.6
-26 37 32
24E-1
18E-1
12E-1
6E-1
3500
4000
4500
5000

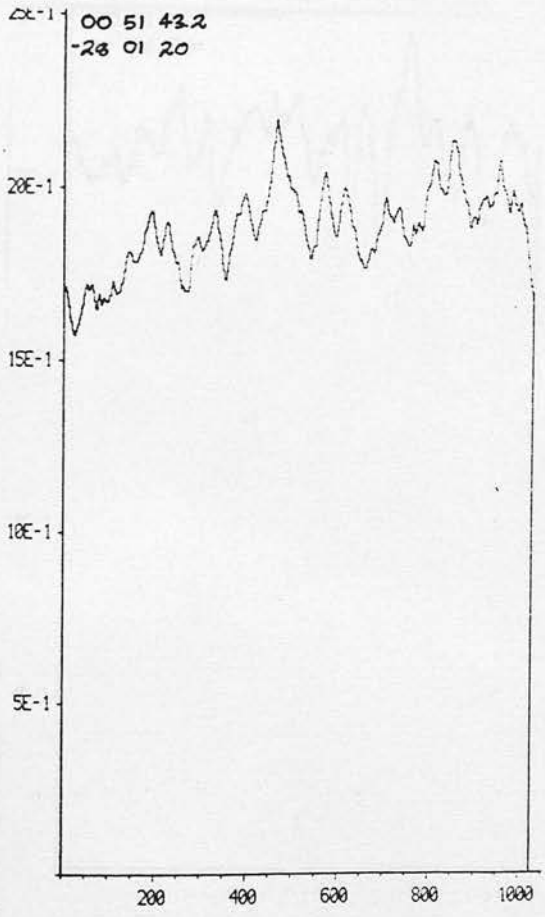
00 51 43.2
-26 01 20
20E-1
15E-1
10E-1
5E-1
200
400
600
800
1000

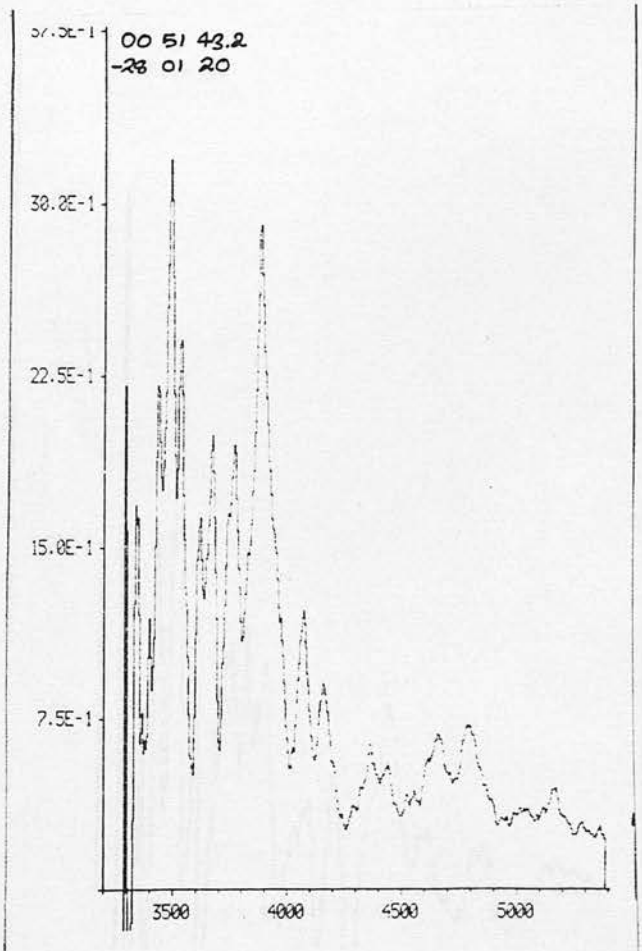
00 51 43.2
-26 01 20
30.0E-1
22.5E-1
15.0E-1
7.5E-1
3500
4000
4500
5000

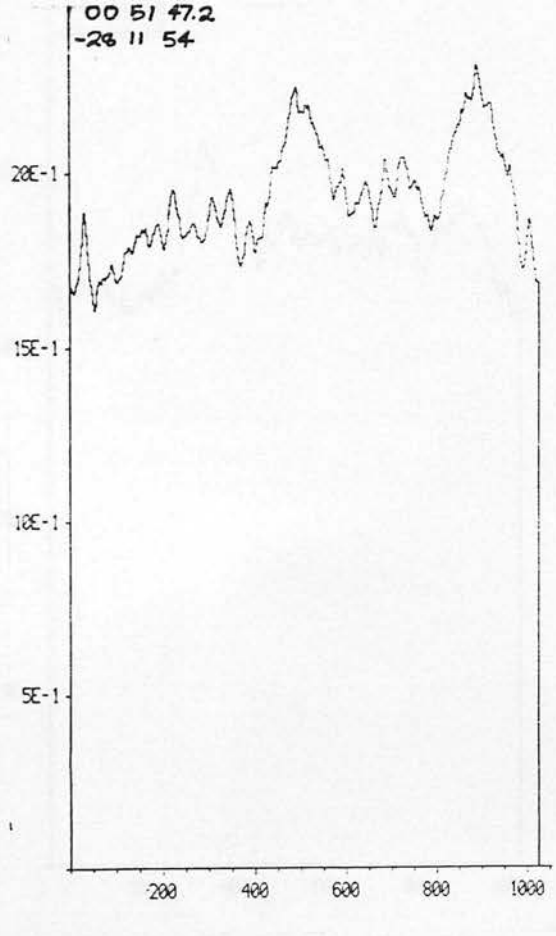
00 51 47.2
-28 11 54
20E-1
15E-1
10E-1
5E-1
200
400
600
800
1000

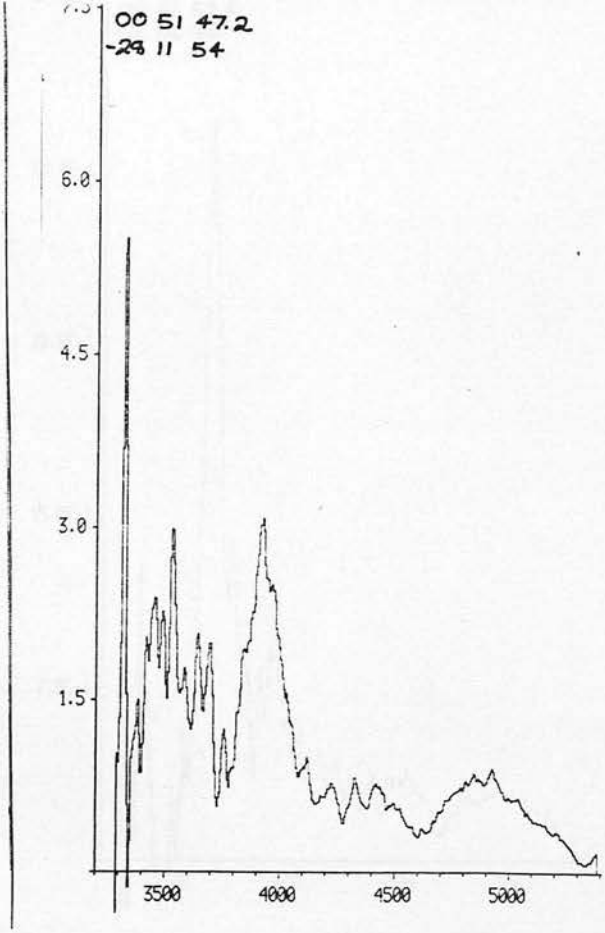
00 51 47.2
-28 11 54
6.0
4.5
3.0
1.5
3500
4000
4500
5000

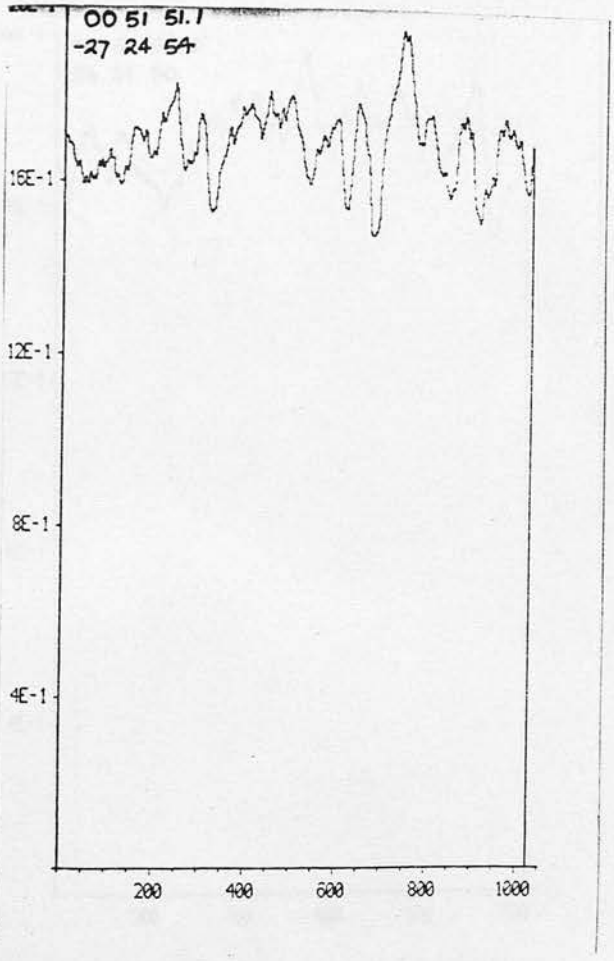
00 51 51.1
-27 24 54
16E-1
12E-1
8E-1
4E-1
200
400
600
800
1000

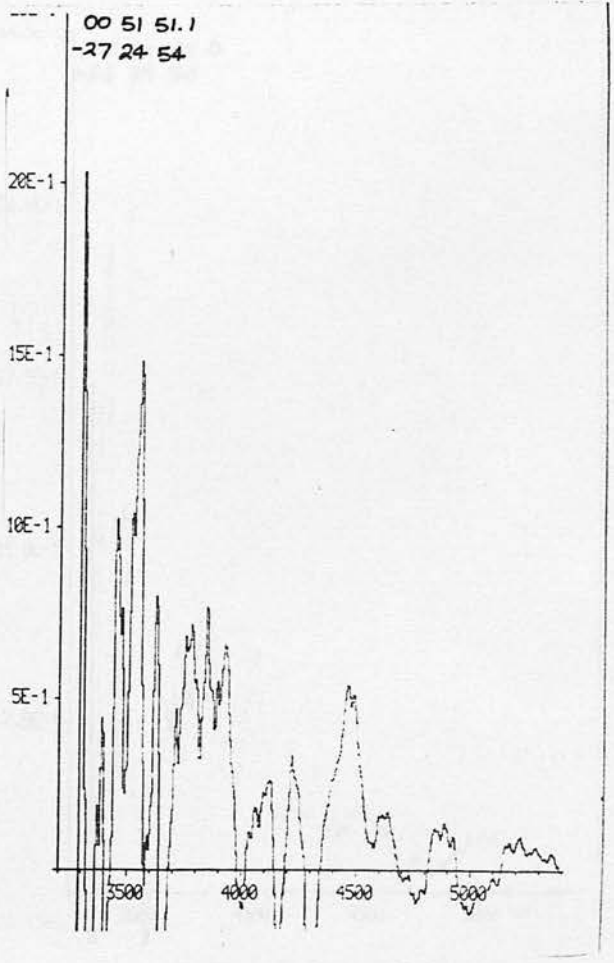
00 51 51.1
-27 24 54
20E-1
15E-1
10E-1
5E-1
3500
4000
4500
5000

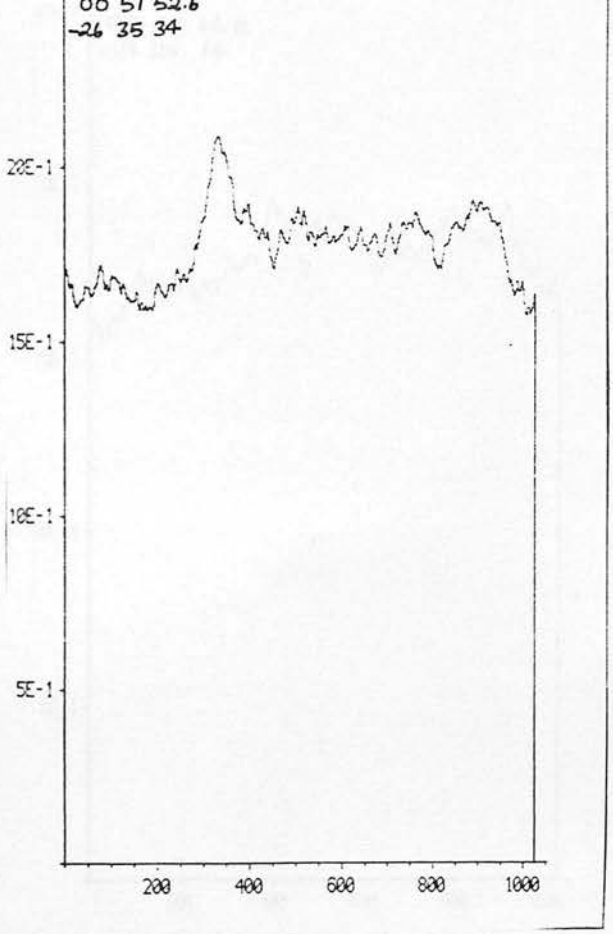
00 51 52.6
-26 35 34
20E-1
15E-1
10E-1
5E-1
200
400
600
800
1000

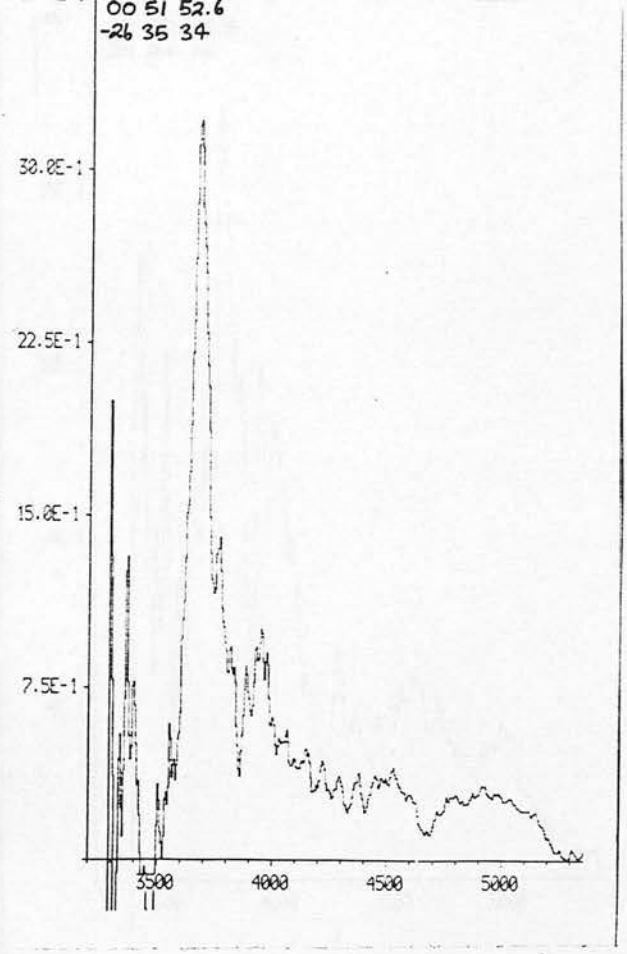
00 51 52.6
-26 35 34
30.0E-1
22.5E-1
15.0E-1
7.5E-1
3500
4000
4500
5000

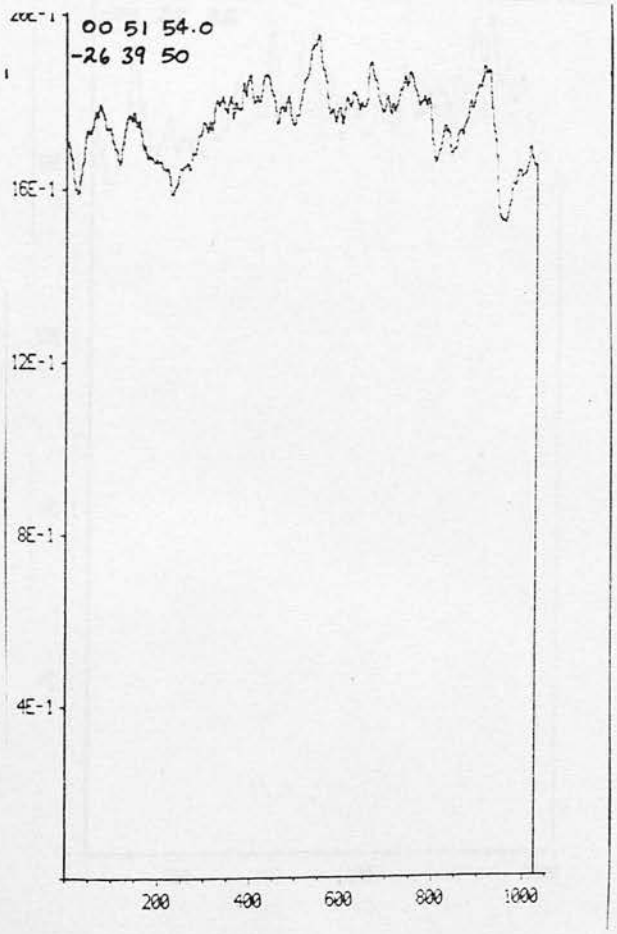
00 51 54.0
-26 39 50
16E-1
12E-1
8E-1
4E-1
200
400
600
800
1000

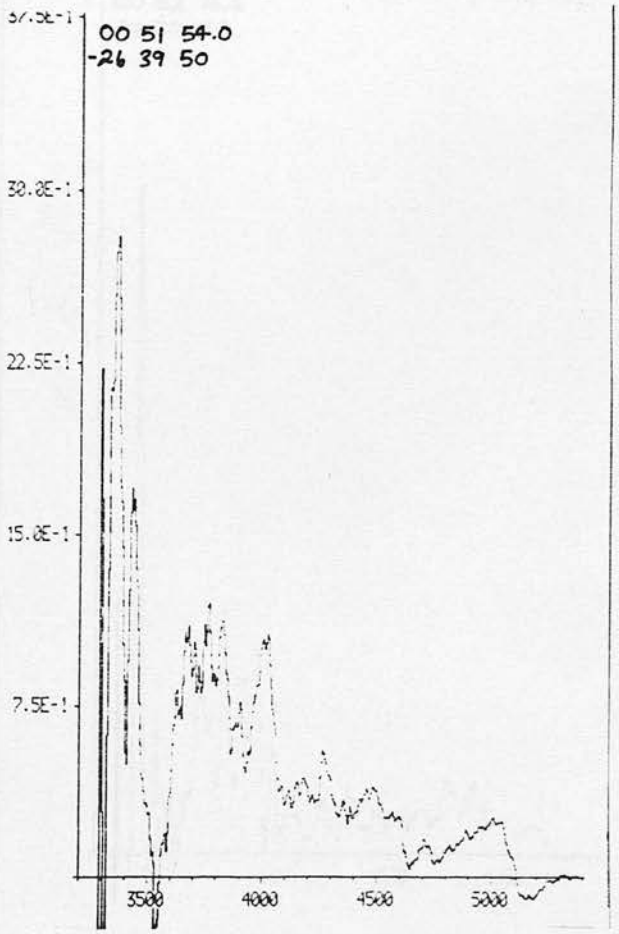
00 51 54.0
-26 39 50
30.0E-1
22.5E-1
15.0E-1
7.5E-1
3500
4000
4500
5000

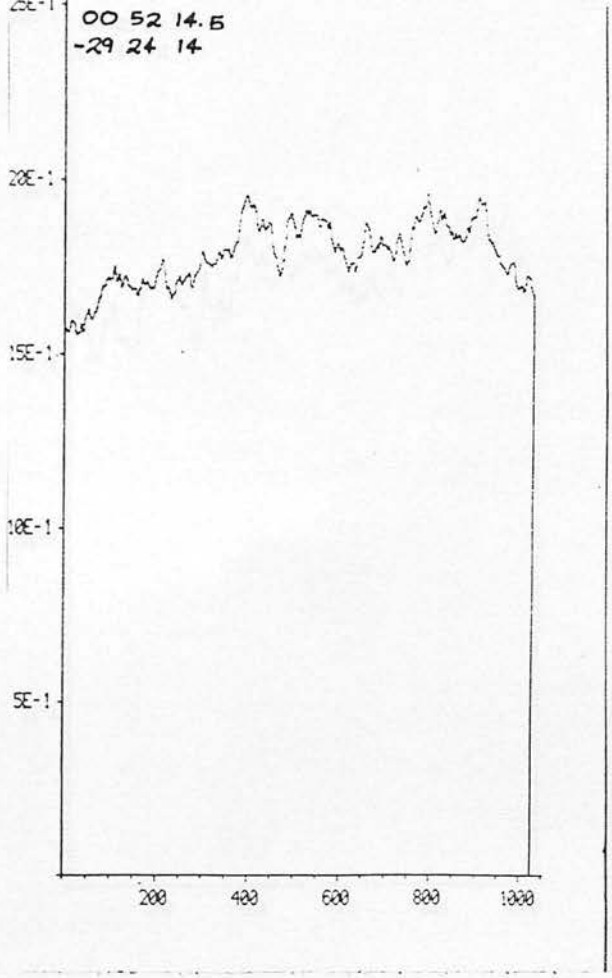
00 52 14.5
-29 24 14
25E-1
20E-1
15E-1
10E-1
5E-1
200
400
600
800
1000

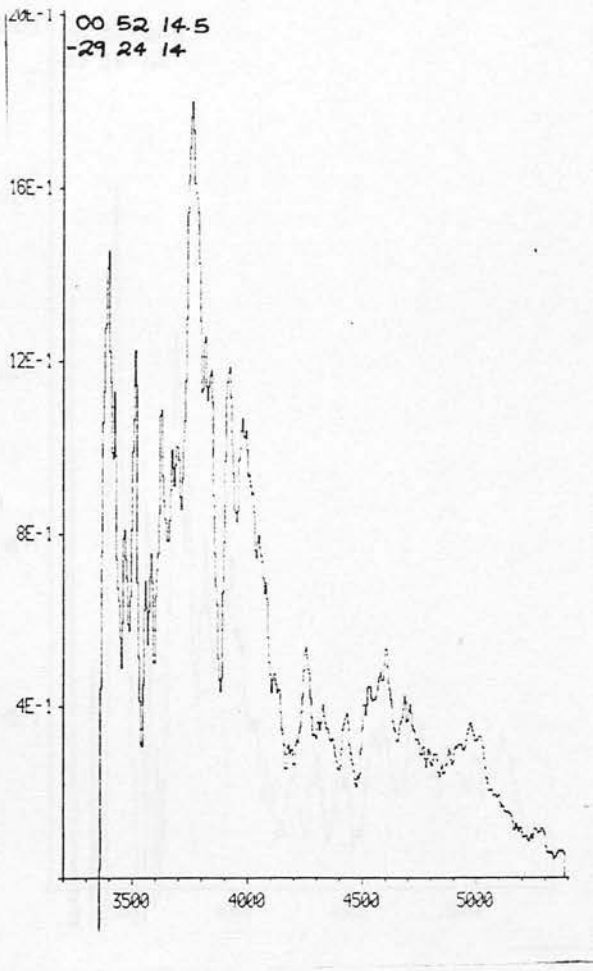
00 52 14.5
-29 24 14
20E-1
16E-1
12E-1
8E-1
4E-1
3500
4000
4500
5000

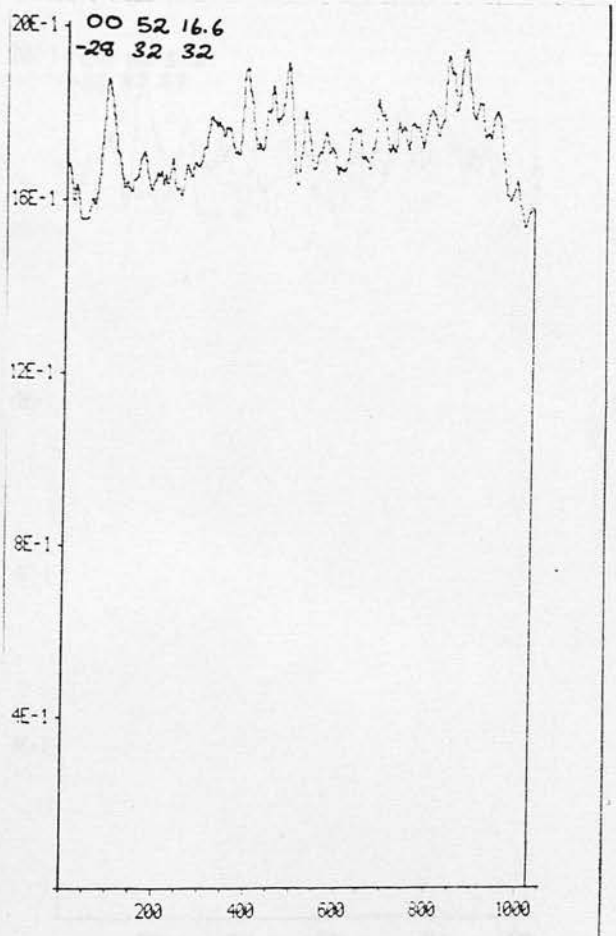
00 52 16.6
-28 32 32
20E-1
16E-1
12E-1
8E-1
4E-1
200
400
600
800
1000

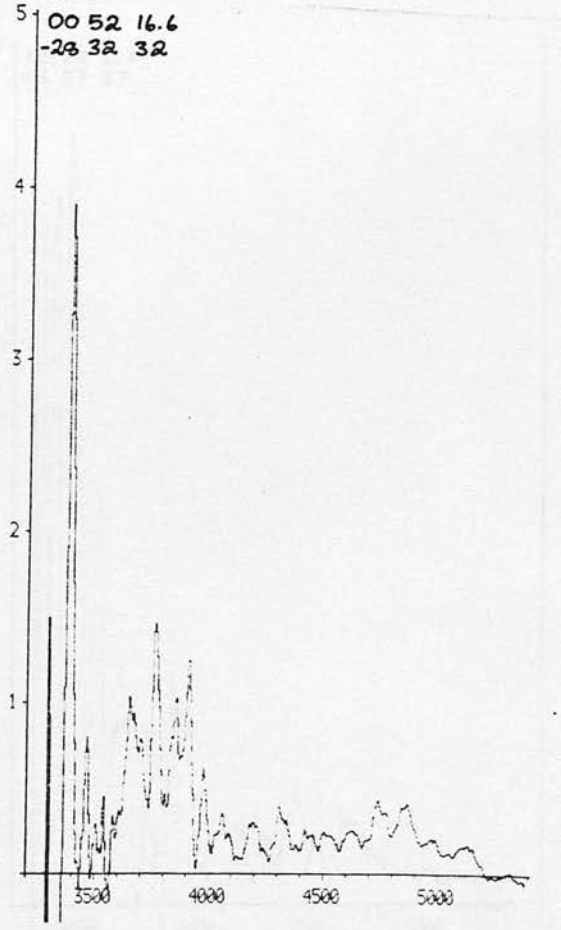
00 52 16.6
-28 32 32
5
4
3
2
1
3500
4000
4500
5000

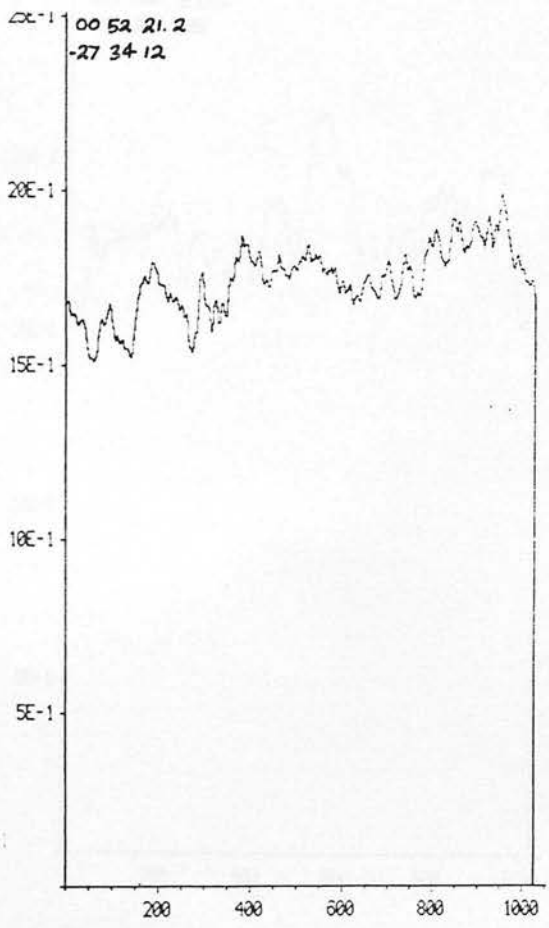
00 52 21.2
-27 34 12
20E-1
15E-1
10E-1
5E-1
200
400
600
800
1000

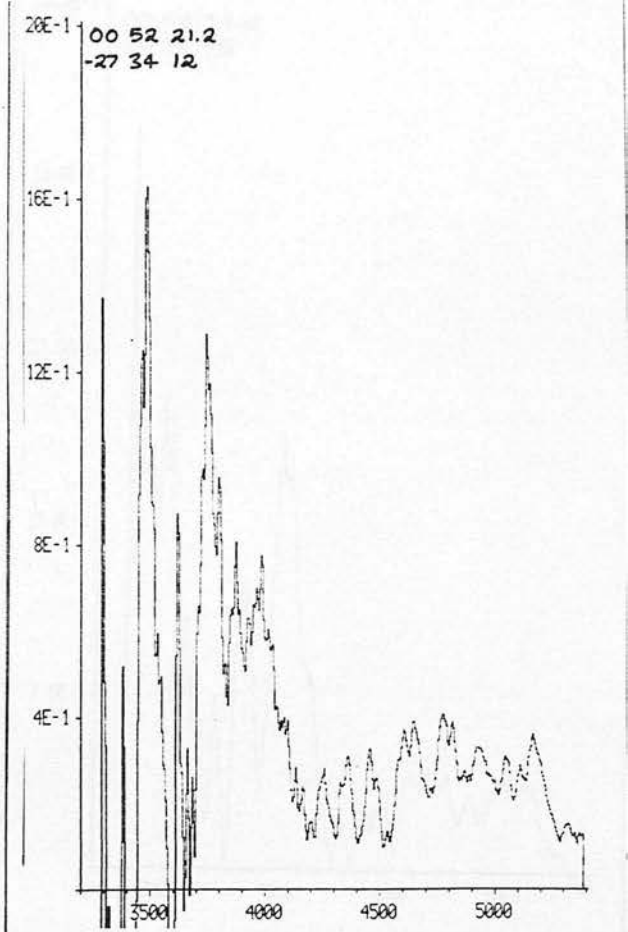
00 52 21.2
-27 34 12
20E-1
16E-1
12E-1
8E-1
4E-1
3500
4000
4500
5000

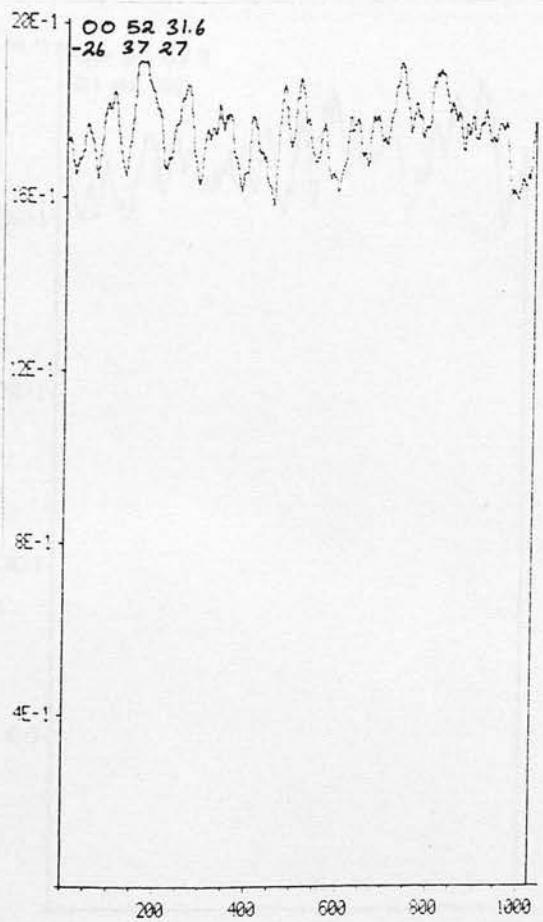
00 52 31.6
-26 37 27
20E-1
16E-1
12E-1
8E-1
4E-1
200
400
600
800
1000

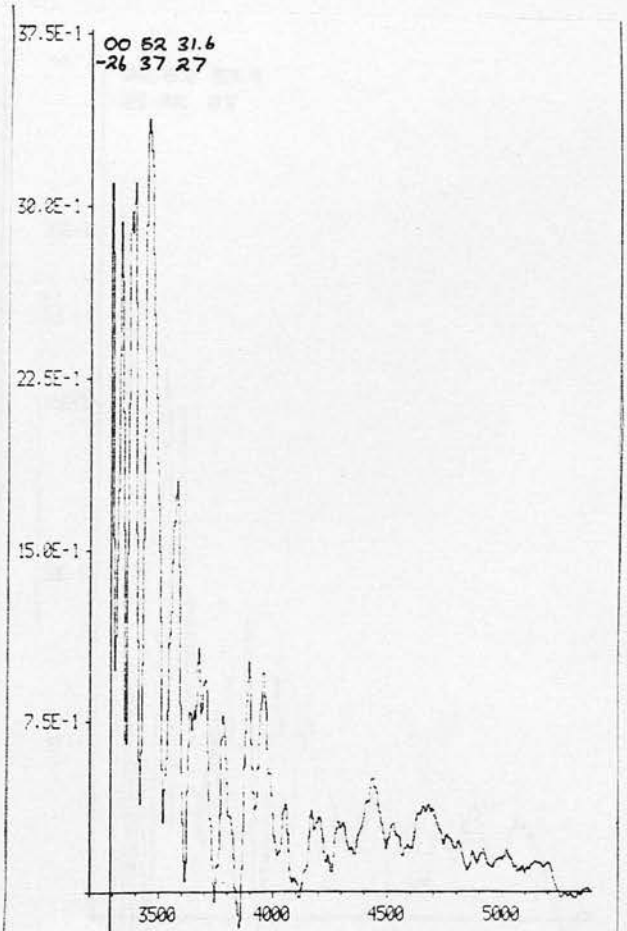
00 52 31.6
-26 37 27
37.5E-1
30.0E-1
22.5E-1
15.0E-1
7.5E-1
3500
4000
4500
5000

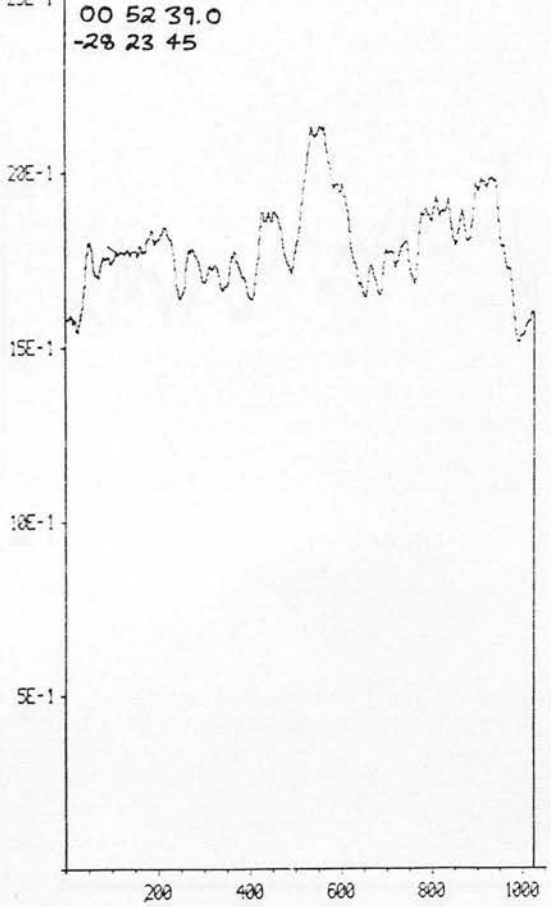
00 52 39.0
-28 23 45
20E-1
15E-1
10E-1
5E-1
200
400
600
800
1000

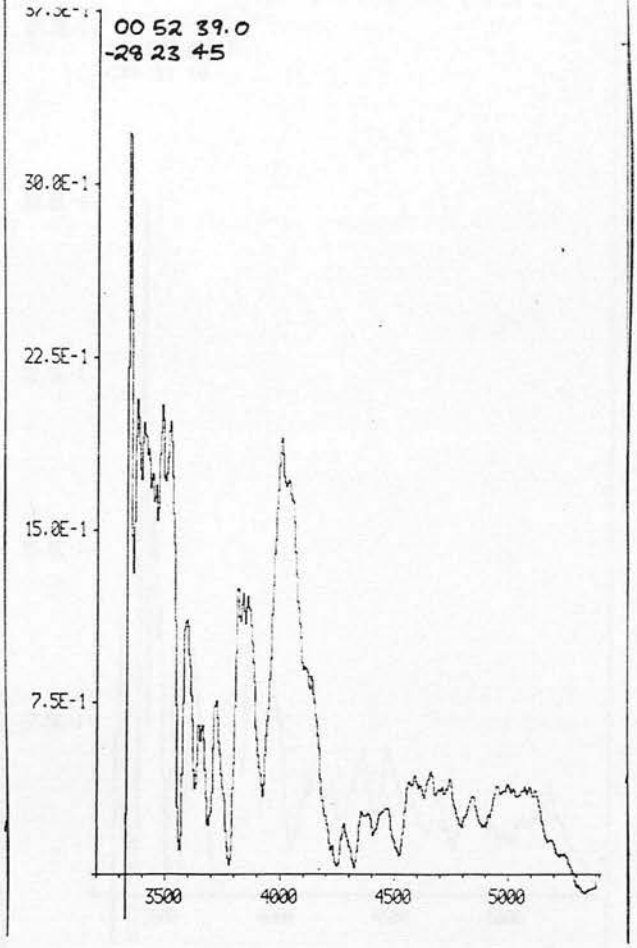
00 52 39.0
-28 23 45
30.0E-1
22.5E-1
15.0E-1
7.5E-1
3500
4000
4500
5000

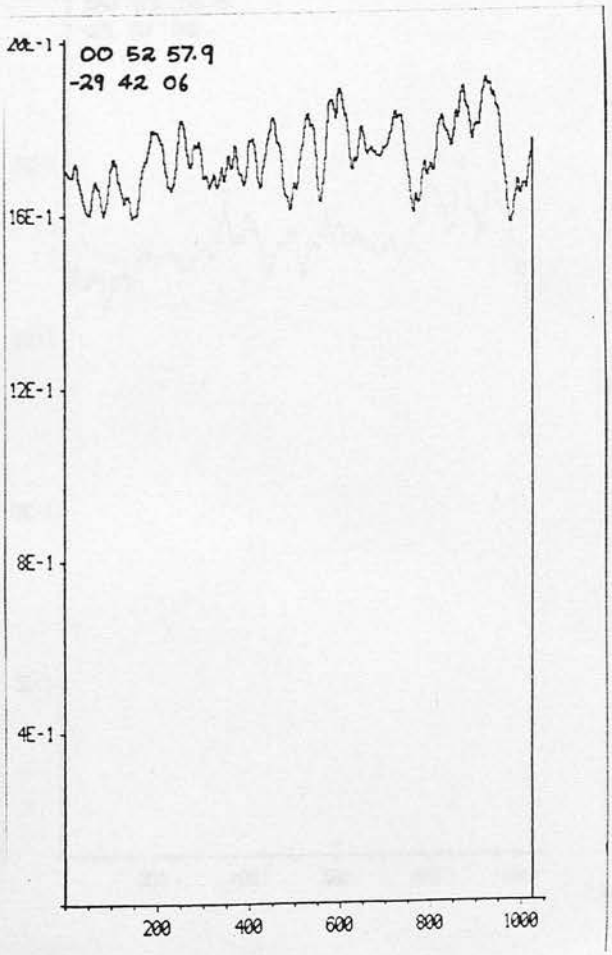
00 52 57.9
-29 42 06
16E-1
12E-1
8E-1
4E-1
200
400
600
800
1000

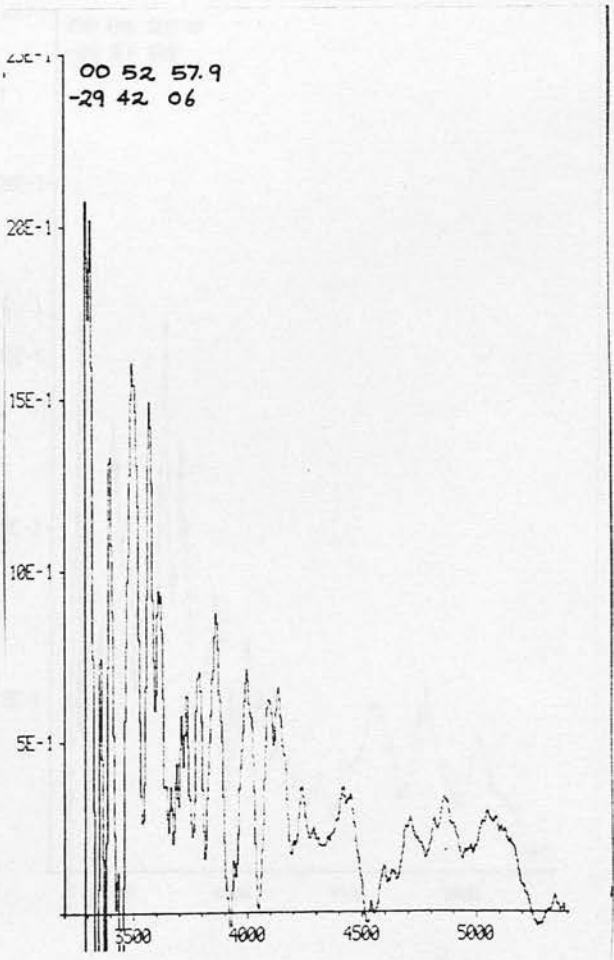
00 52 57.9
-29 42 06
20E-1
15E-1
10E-1
5E-1
3500
4000
4500
5000

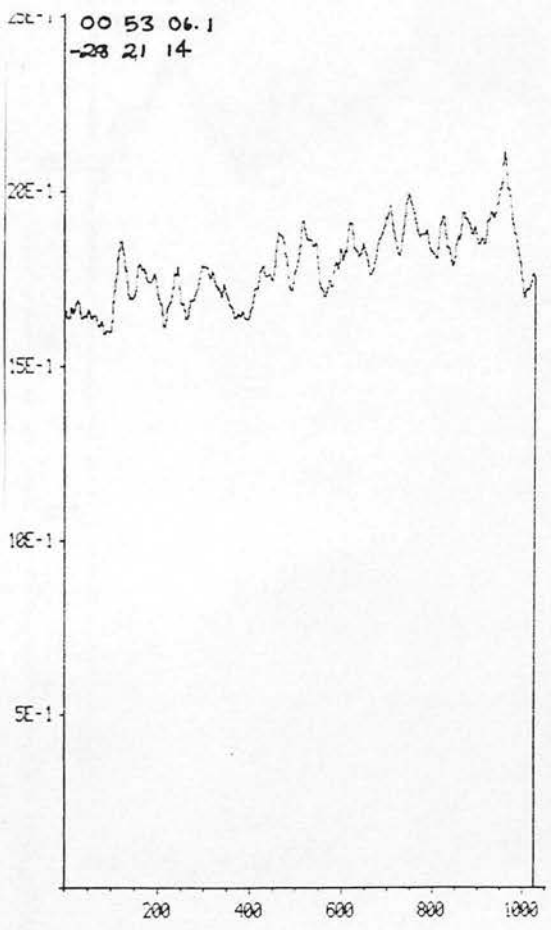
00 53 06.1
-28 21 14
20E-1
15E-1
10E-1
5E-1
200
400
600
800
1000

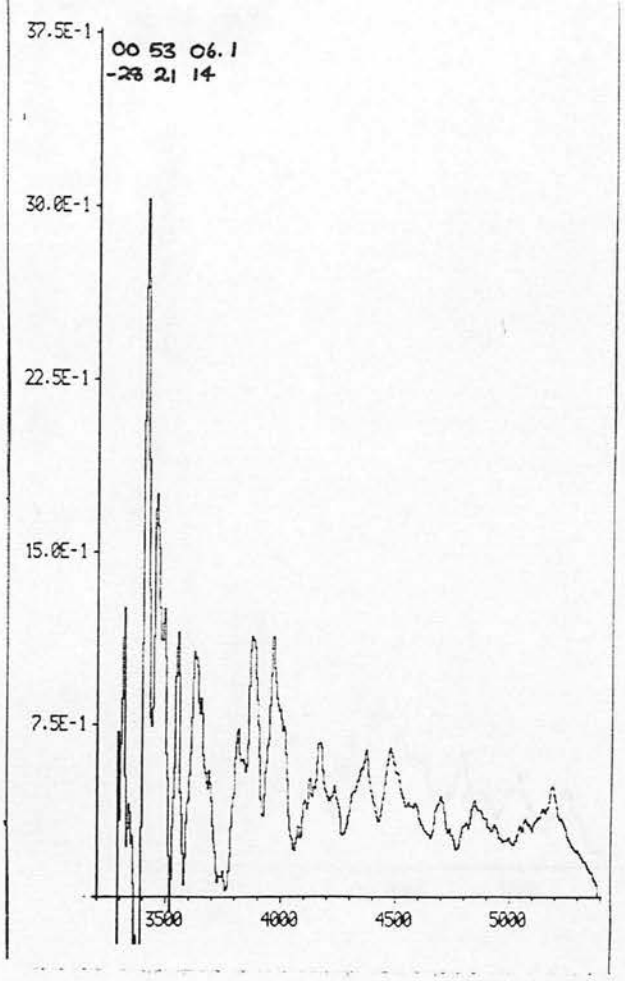
37.5E-1
00 53 06.1
-28 21 14
30.0E-1
22.5E-1
15.0E-1
7.5E-1
3500
4000
4500
5000

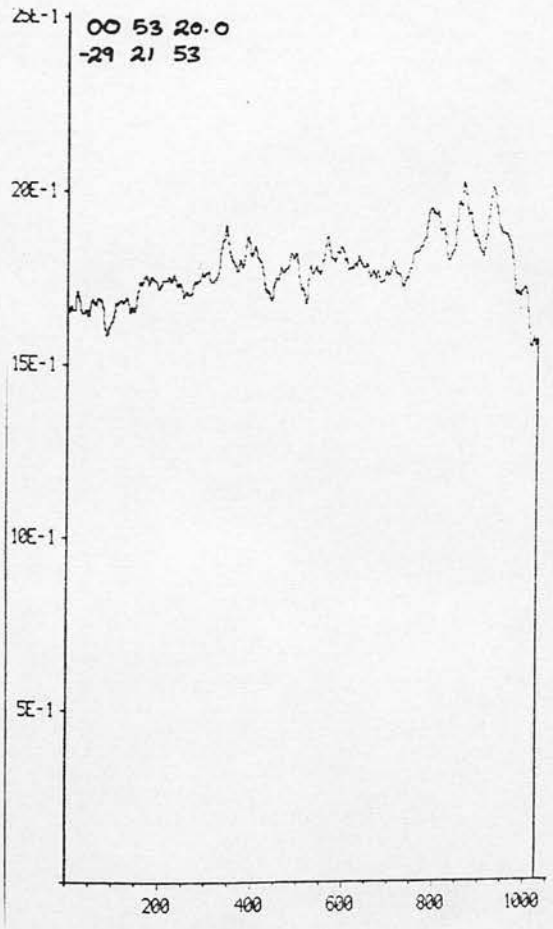
00 53 20.0
-29 21 53
20E-1
15E-1
10E-1
5E-1
200
400
600
800
1000

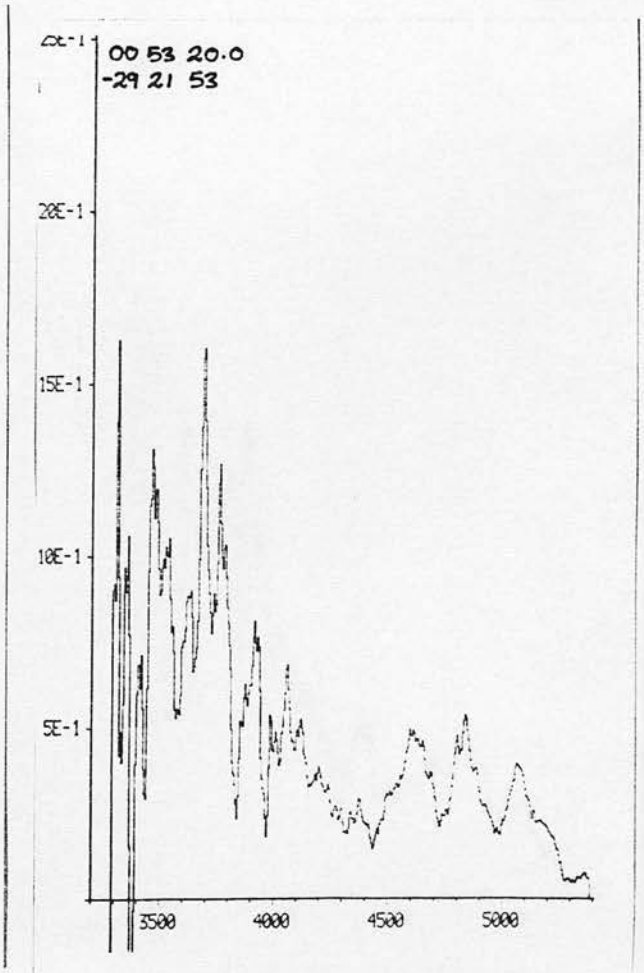
00 53 20.0
-29 21 53
20E-1
15E-1
10E-1
5E-1
3500
4000
4500
5000

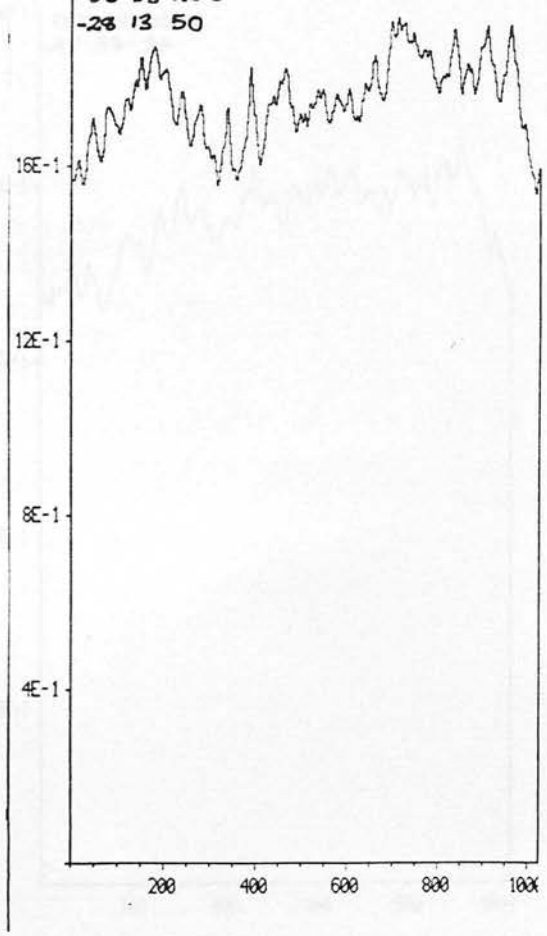
-28 13 50
16E-1
12E-1
8E-1
4E-1
200
400
600
800

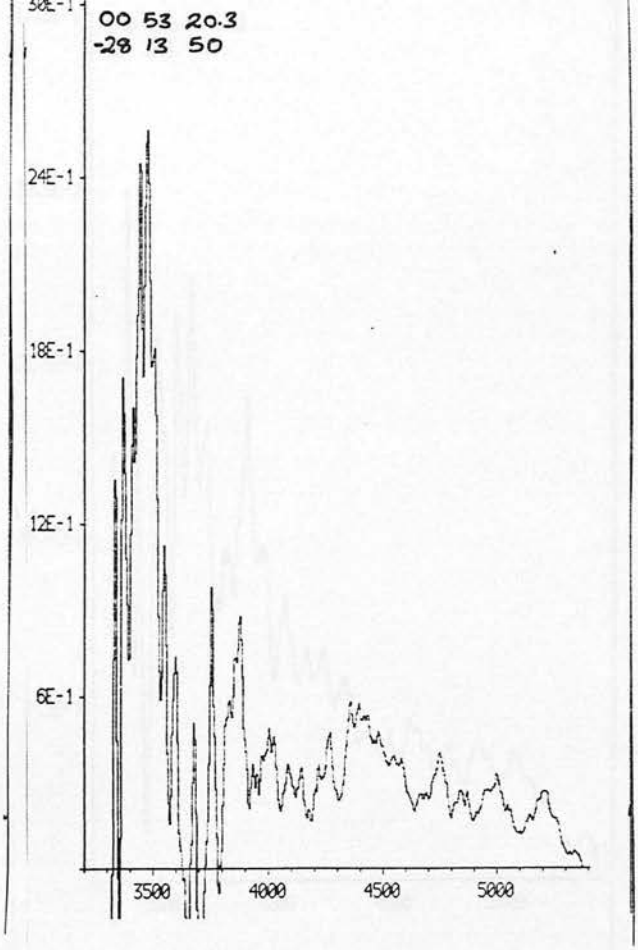
00 53 20.3
-28 13 50
24E-1
18E-1
12E-1
6E-1
3500
4000
4500
5000

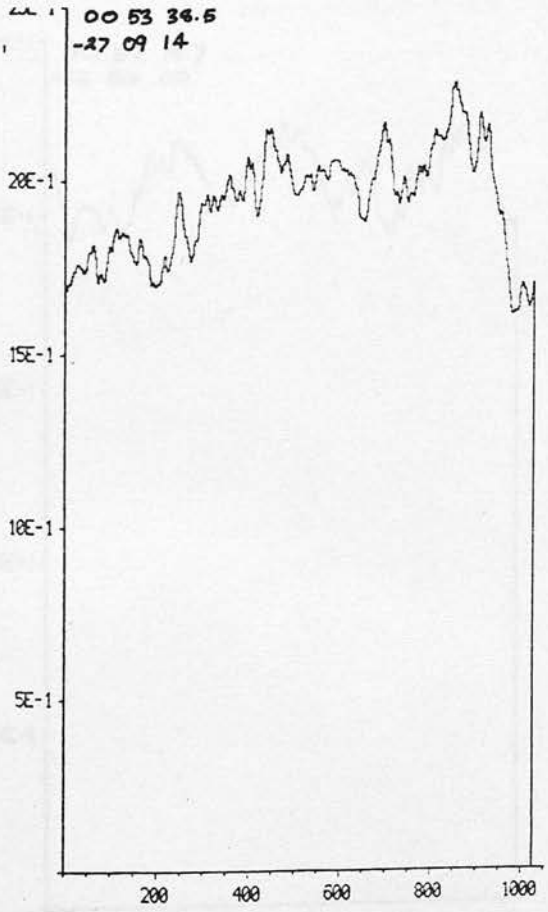
00 53 36.5
-27 09 14
20E-1
15E-1
10E-1
5E-1
200
400
600
800
1000

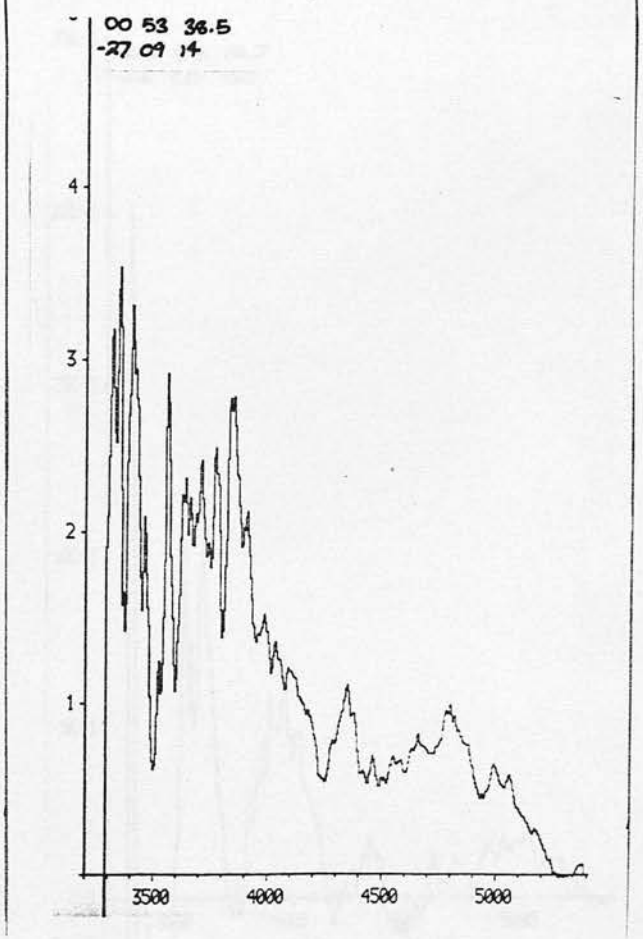
00 53 36.5
-27 09 14
4
3
2
1
3500
4000
4500
5000

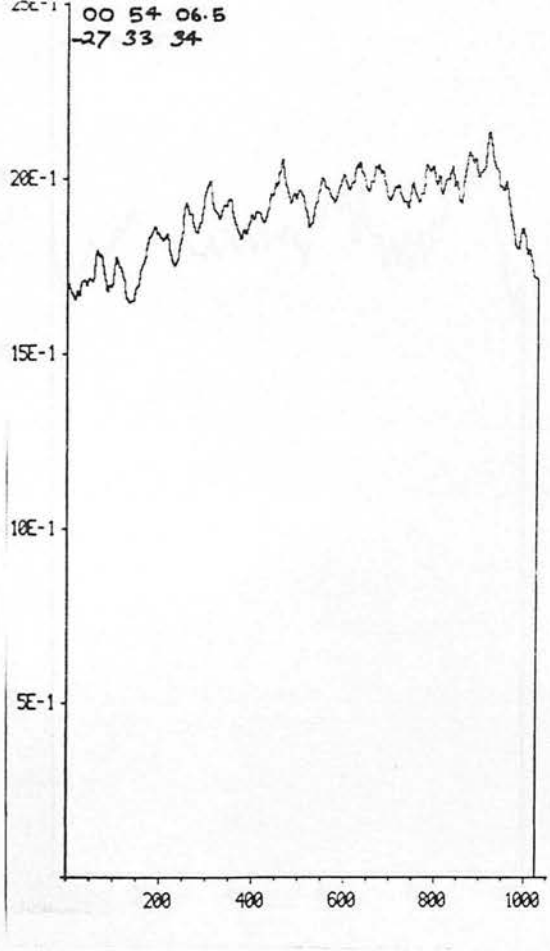
00 54 06.5
-27 33 34
20E-1
15E-1
10E-1
5E-1
200
400
600
800
1000

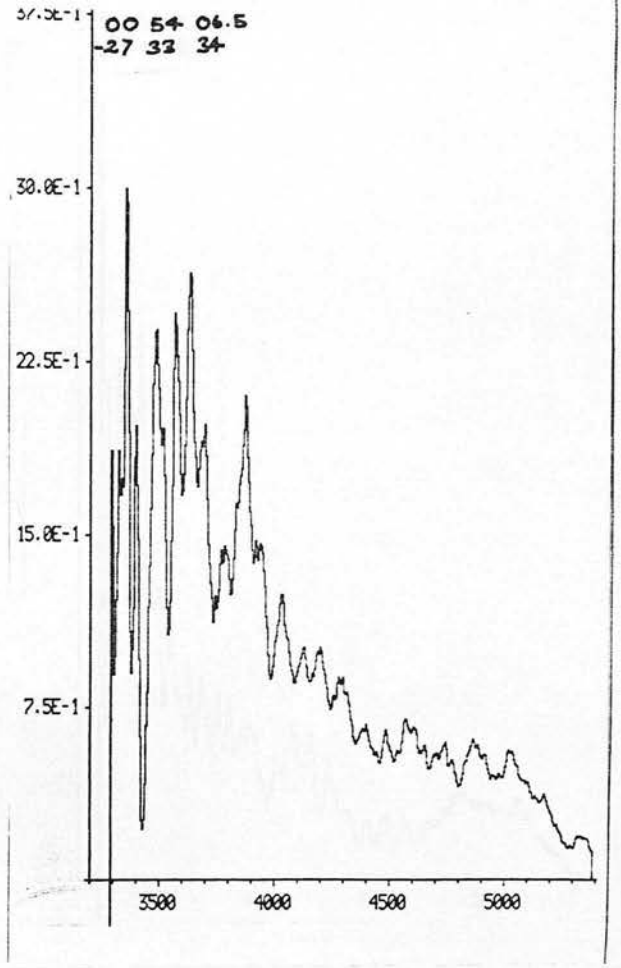
00 54 06.5
-27 33 34
30.0E-1
22.5E-1
15.0E-1
7.5E-1
3500
4000
4500
5000

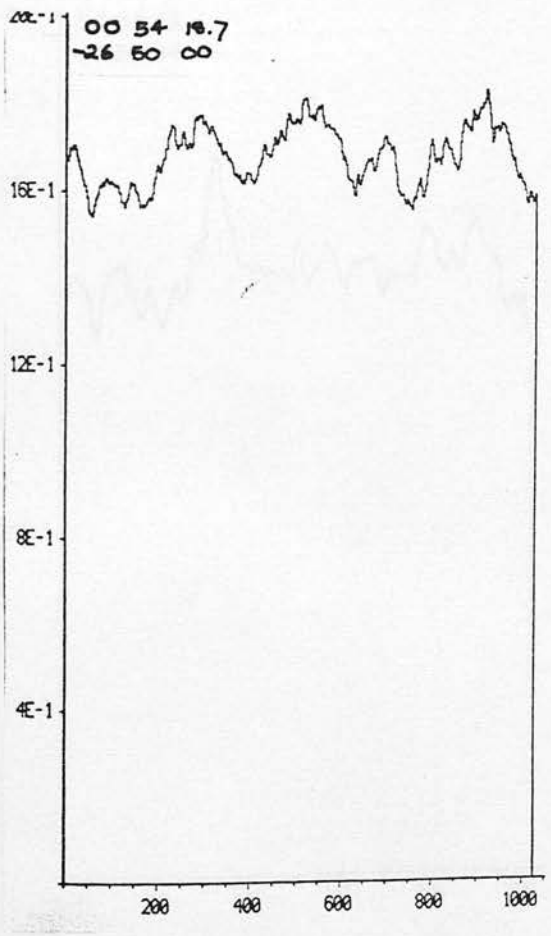
00 54 18.7
-26 50 00
16E-1
12E-1
8E-1
4E-1
200
400
600
800
1000

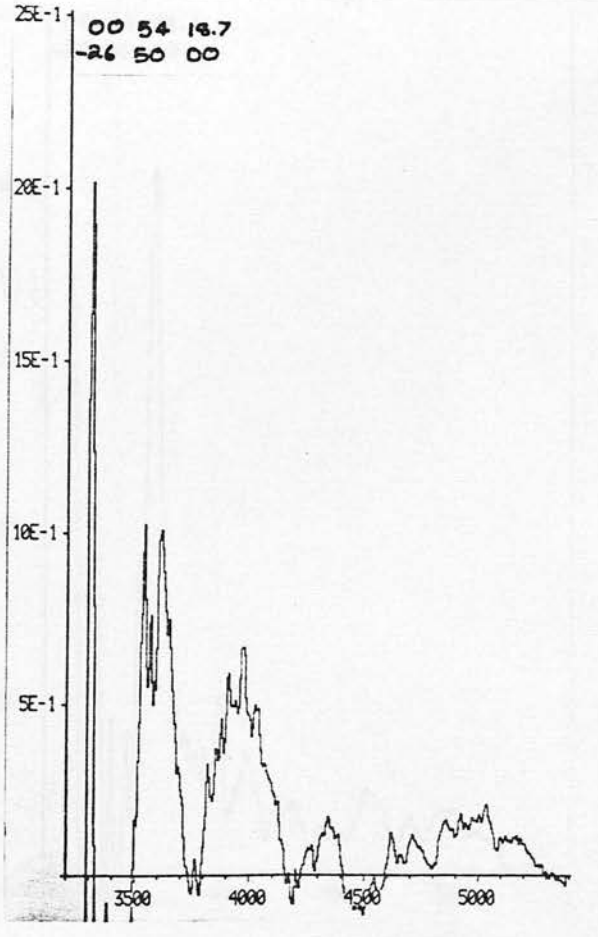
00 54 18.7
-26 50 00
25E-1
20E-1
15E-1
10E-1
5E-1
3500
4000
4500
5000

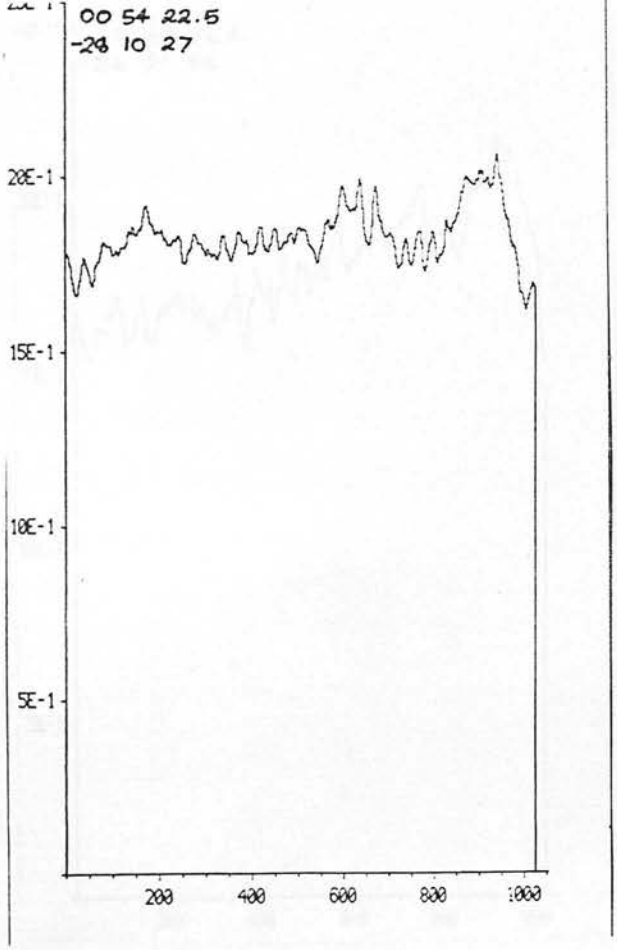
00 54 22.5
-28 10 27
20E-1
15E-1
10E-1
5E-1
200
400
600
800
1000

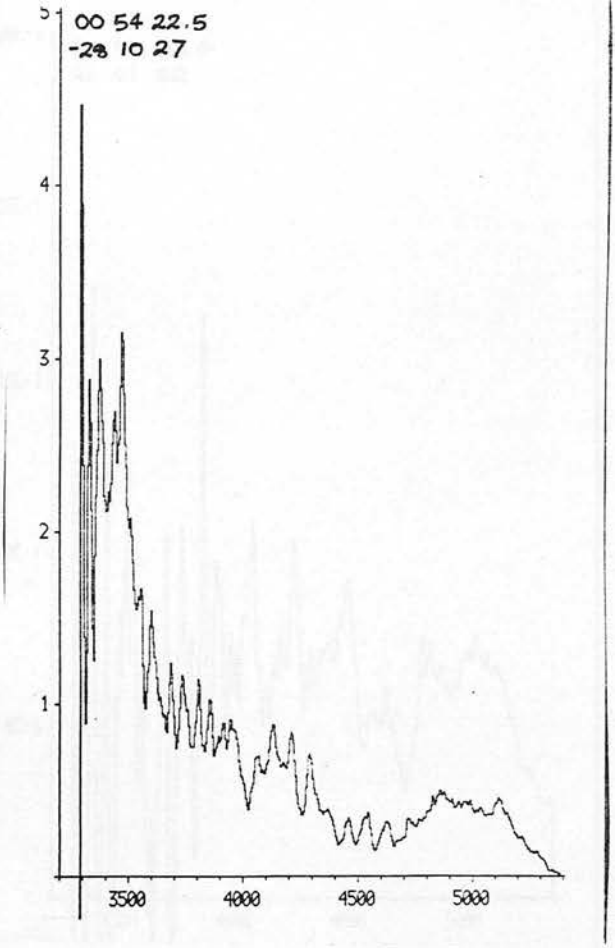
00 54 22.5
-28 10 27
4
3
2
1
3500
4000
4500
5000

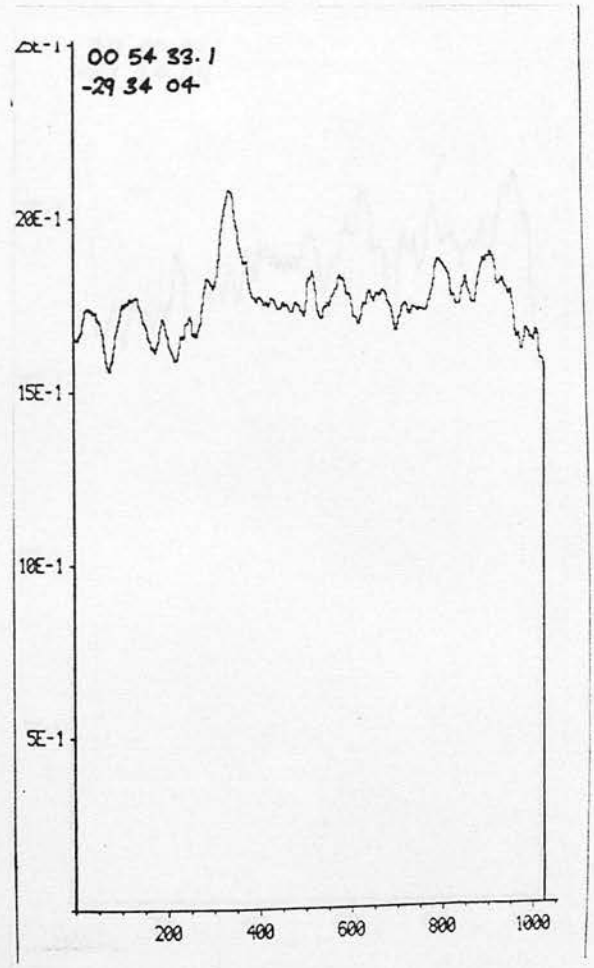
00 54 33.1
-29 34 04
20E-1
15E-1
10E-1
5E-1
200
400
600
800
1000

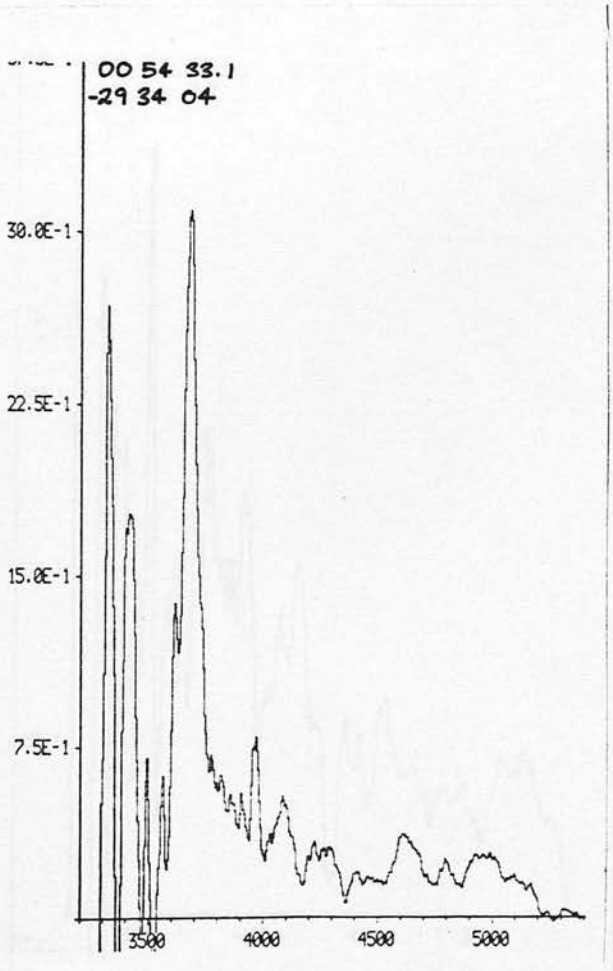
00 54 33.1
-29 34 04
30.0E-1
22.5E-1
15.0E-1
7.5E-1
3500
4000
4500
5000

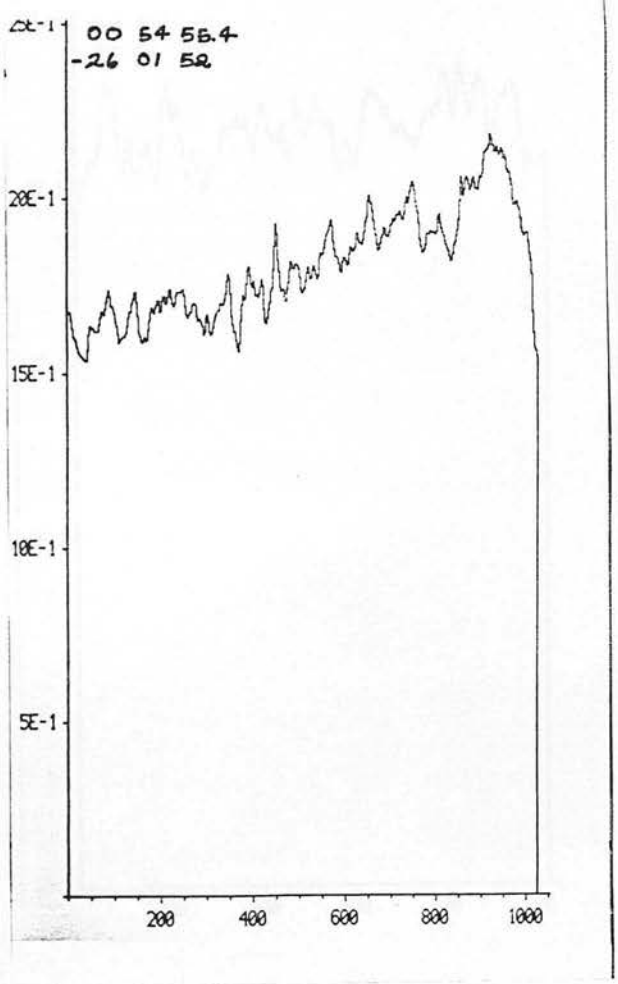
00 54 55.4
-26 01 52
20E-1
15E-1
10E-1
5E-1
200
400
600
800
1000

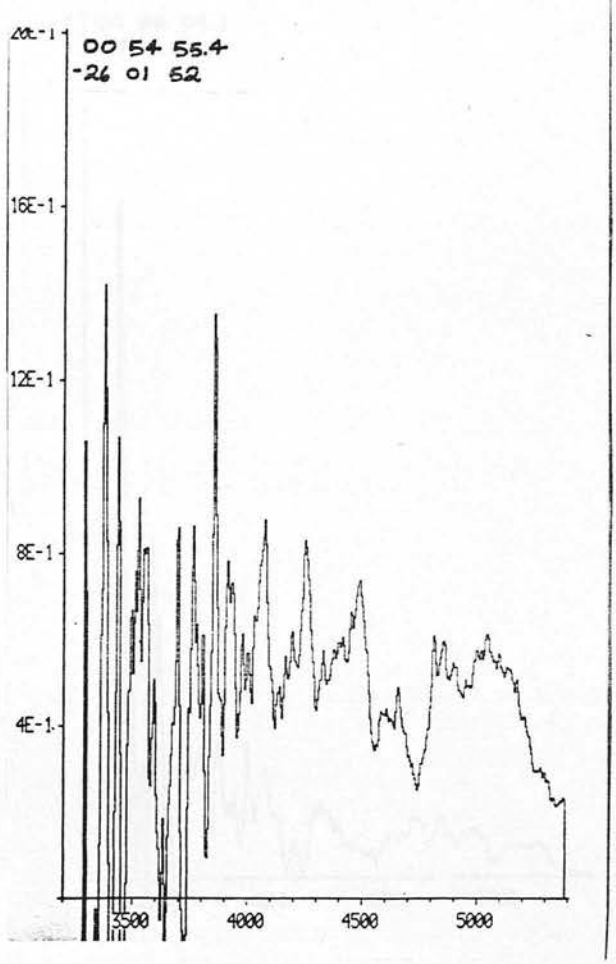
00 54 55.4
-26 01 52
16E-1
12E-1
8E-1
4E-1
3500
4000
4500
5000

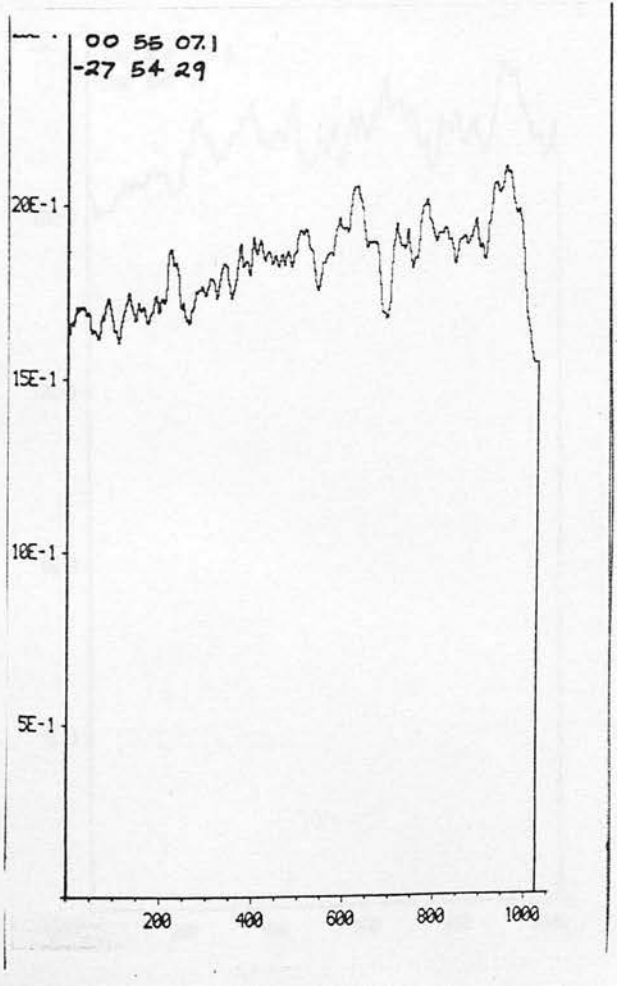
00 55 07.1
-27 54 29
20E-1
15E-1
10E-1
5E-1
200
400
600
800
1000

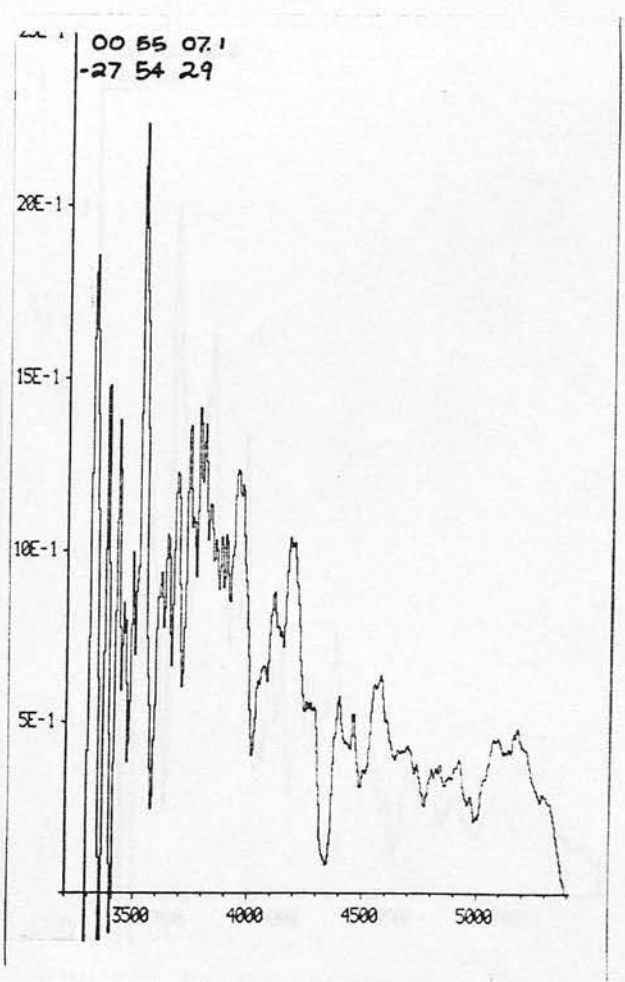
00 55 07.1
-27 54 29
20E-1
15E-1
10E-1
5E-1
3500
4000
4500
5000

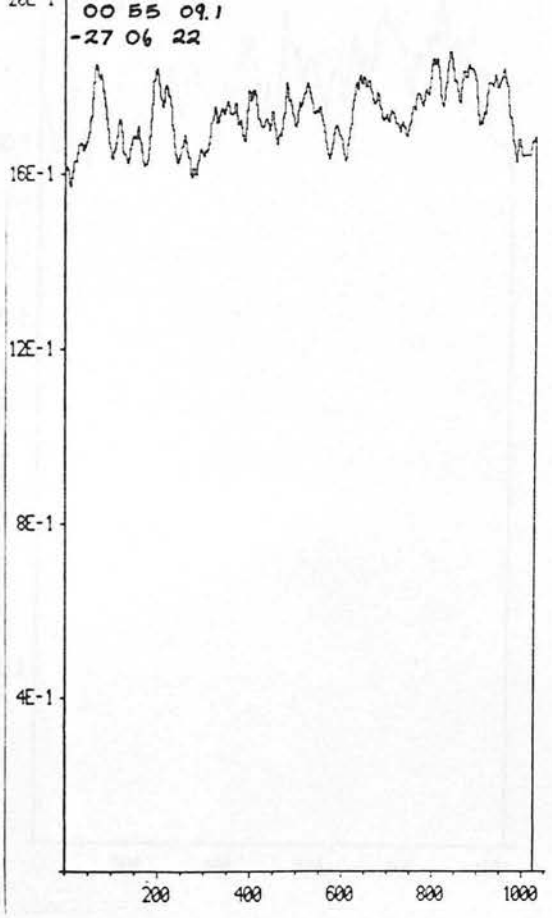
00 55 09.1
-27 06 22
16E-1
12E-1
8E-1
4E-1
200
400
600
800
1000

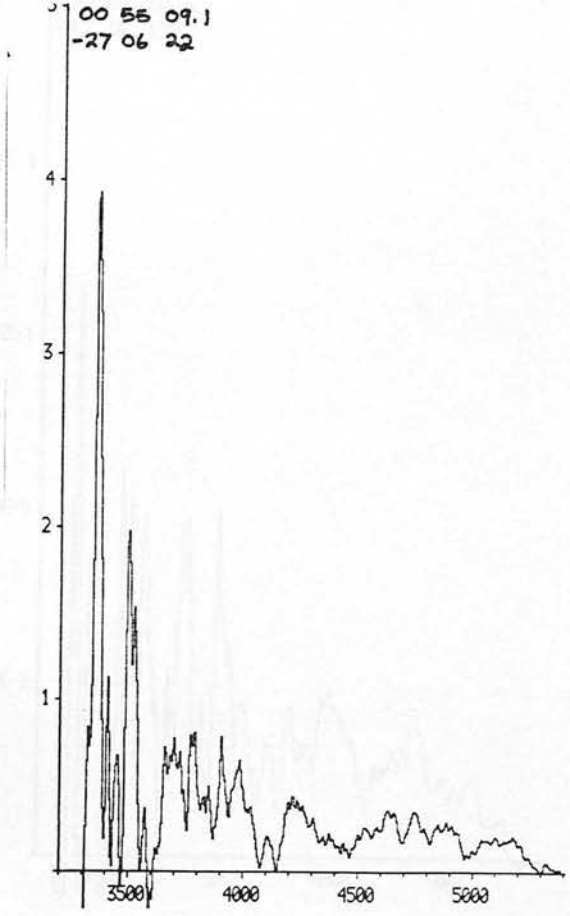
00 55 09.1
-27 06 22
4
3
2
1
3500
4000
4500
5000

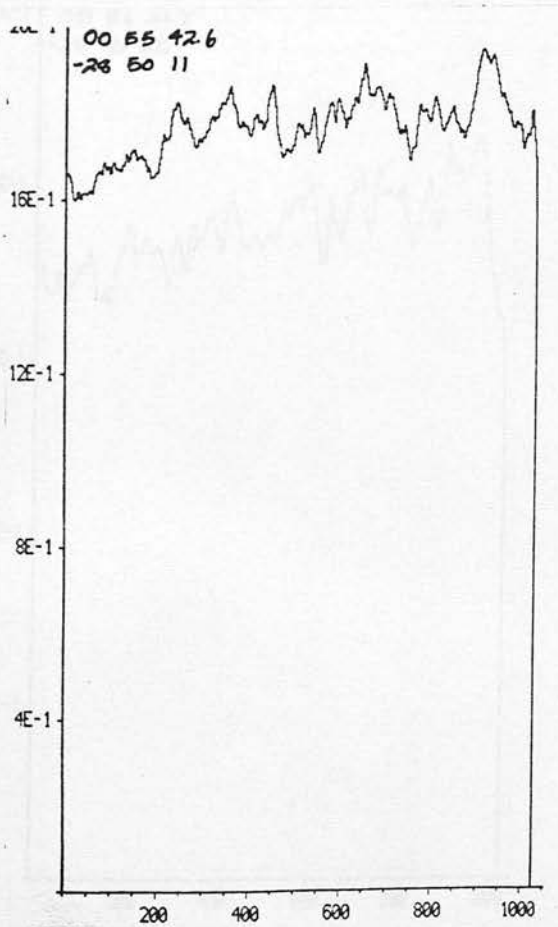
00 55 42.6
-28 50 11
16E-1
12E-1
8E-1
4E-1
200
400
600
800
1000

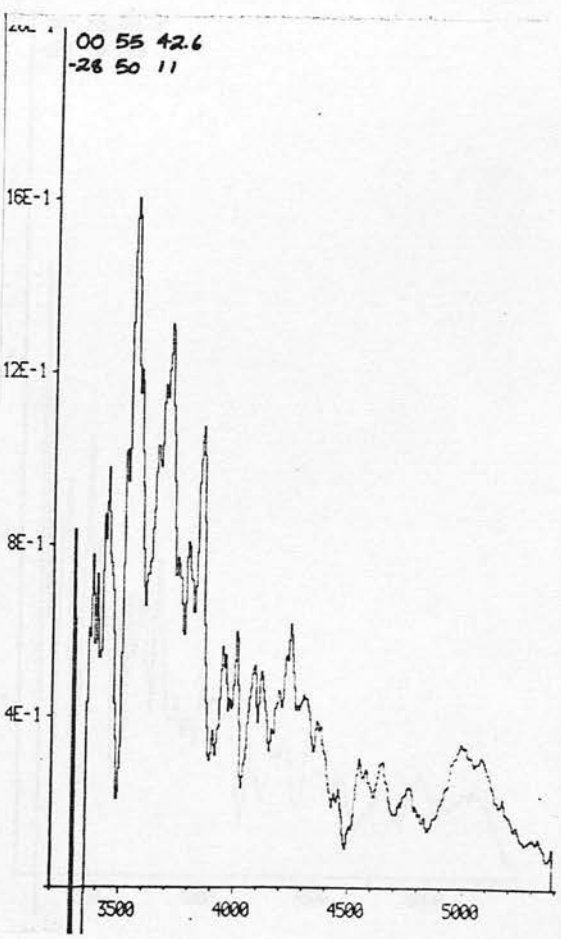
00 55 42.6
-28 50 11
16E-1
12E-1
8E-1
4E-1
3500
4000
4500
5000

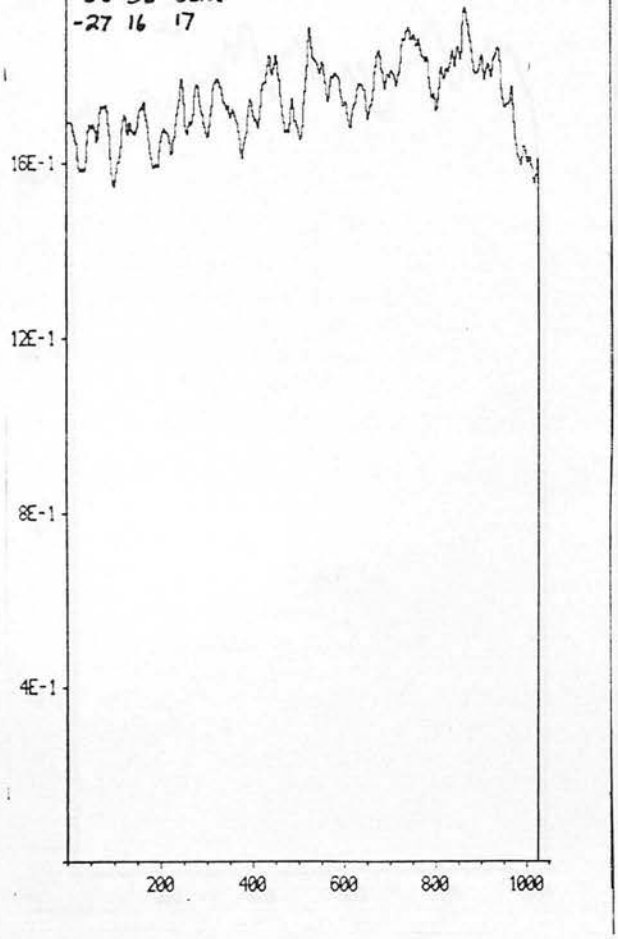
-27 16 17
16E-1
12E-1
8E-1
4E-1
200
400
600
800
1000

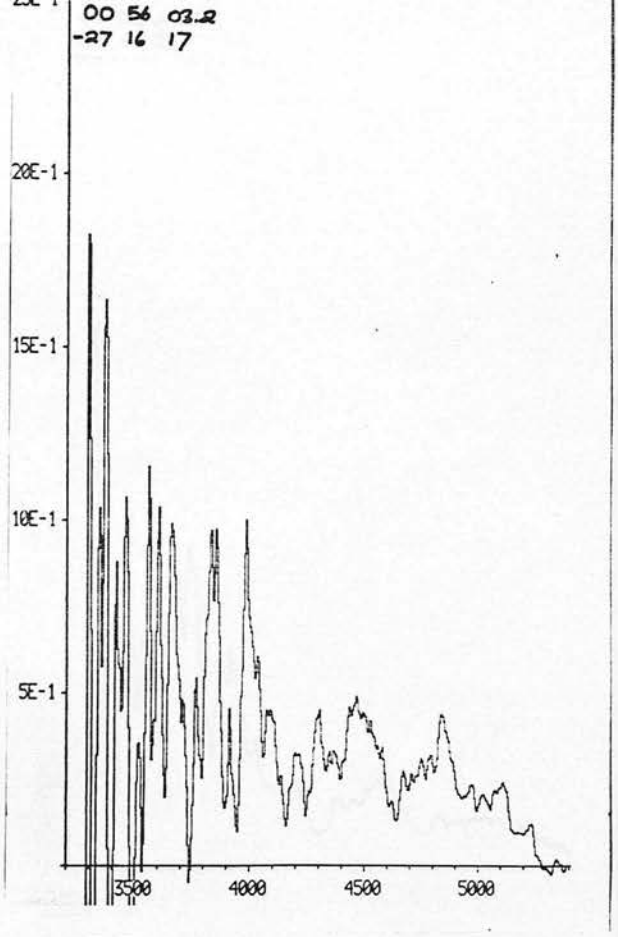
00 56 03.2
-27 16 17
20E-1
15E-1
10E-1
5E-1
3500
4000
4500
5000

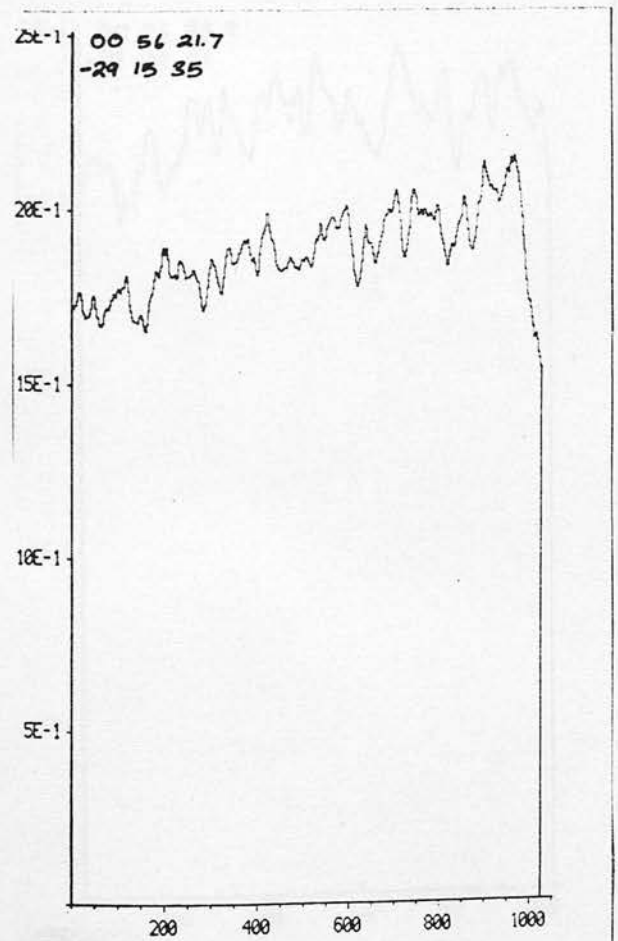
00 56 21.7
-29 15 35
20E-1
15E-1
10E-1
5E-1
200
400
600
800
1000

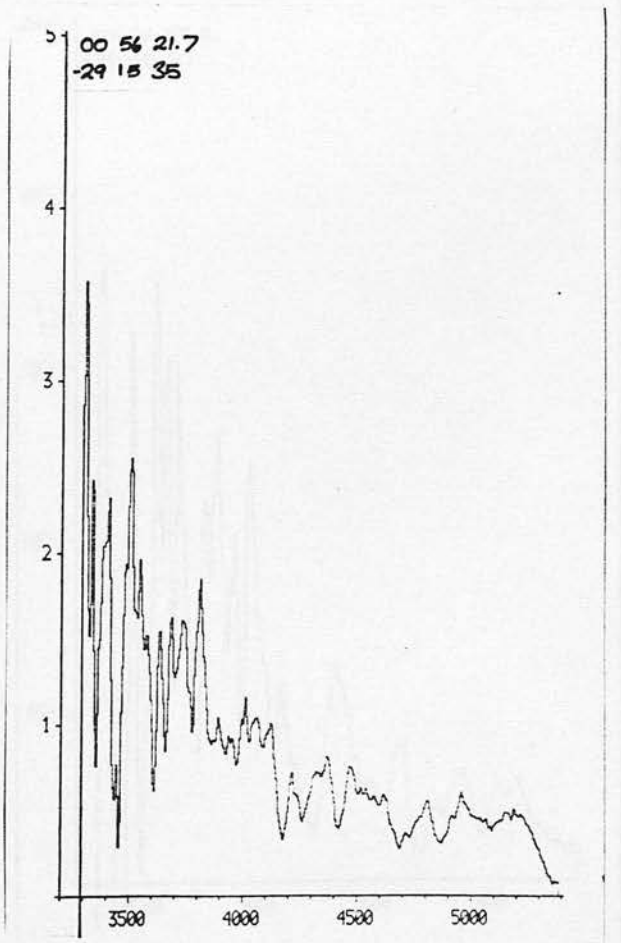
00 56 21.7
-29 15 35
4
3
2
1
3500
4000
4500
5000

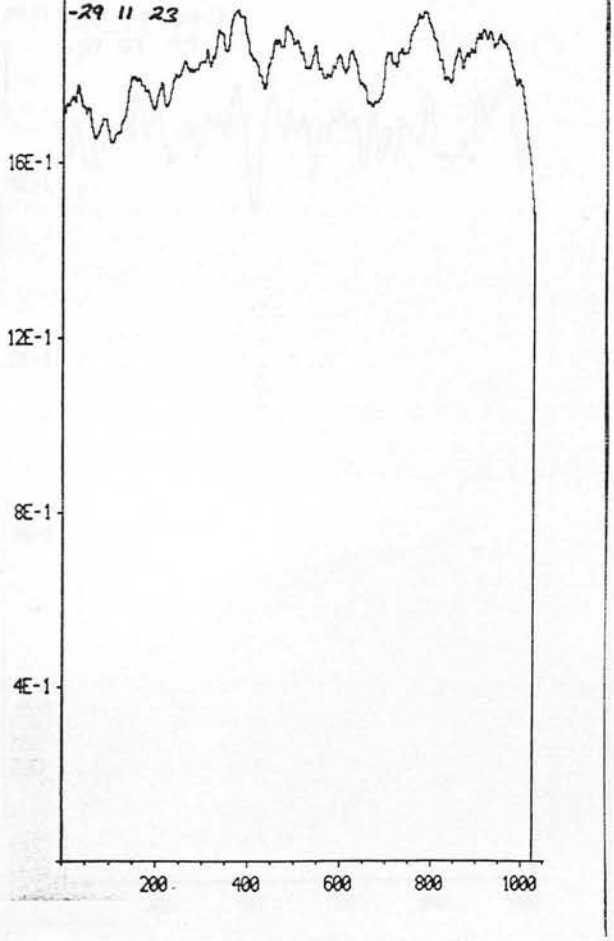
-29 11 23
16E-1
12E-1
8E-1
4E-1
200
400
600
800
1000

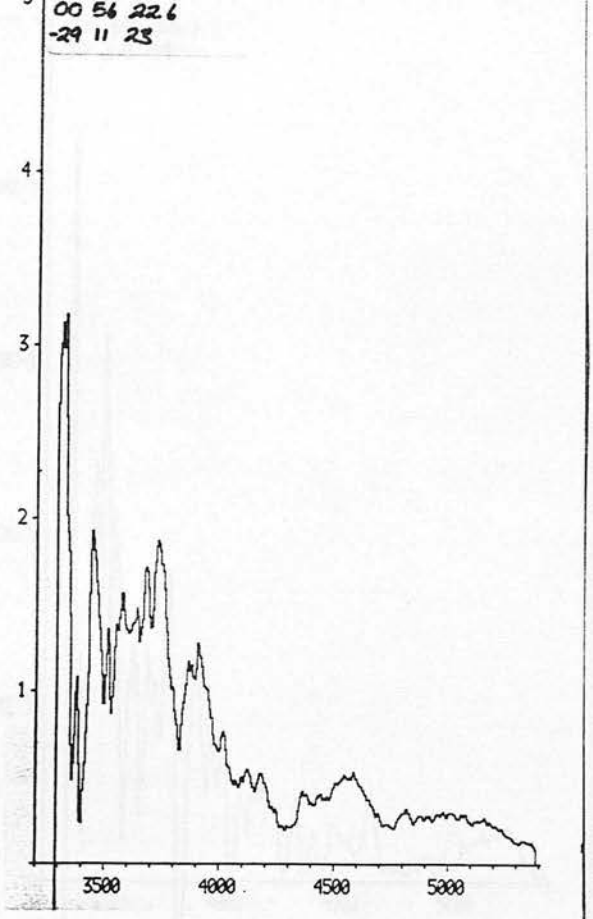
00 56 22.6
-29 11 23
4
3
2
1
3500
4000
4500
5000

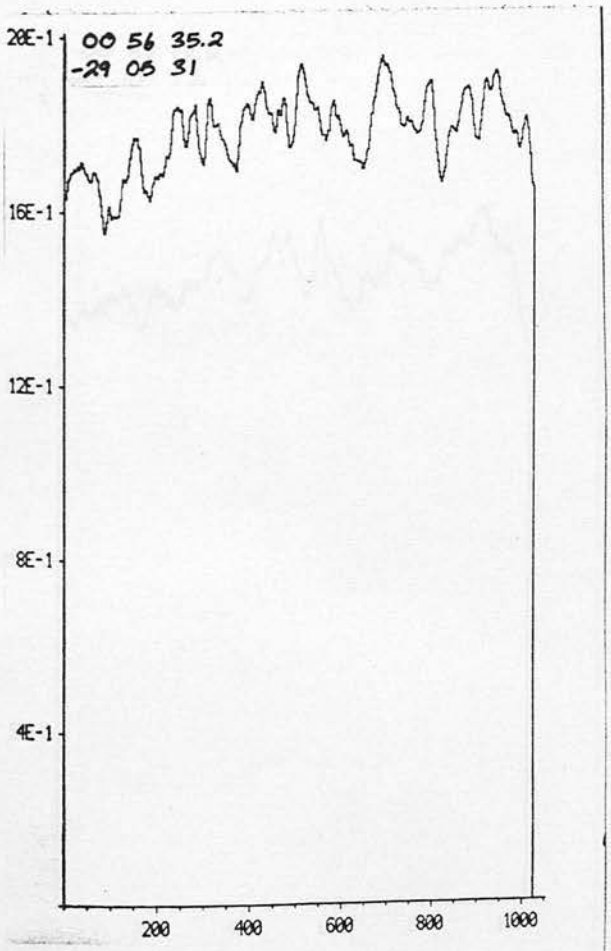
00 56 35.2
-29 05 31
20E-1
16E-1
12E-1
8E-1
4E-1
200
400
600
800
1000

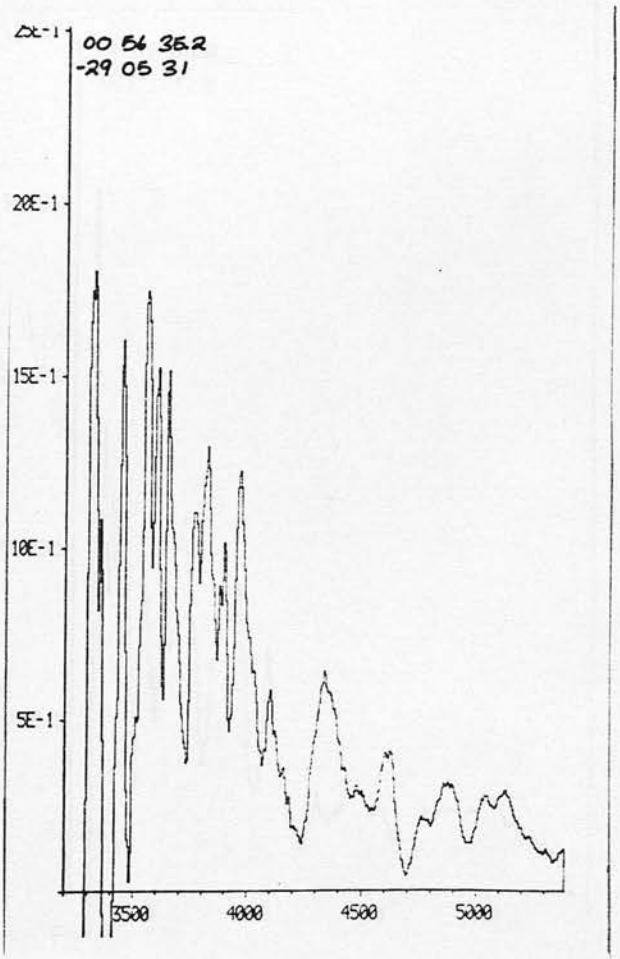
00 56 35.2
-29 05 31
20E-1
15E-1
10E-1
5E-1
3500
4000
4500
5000

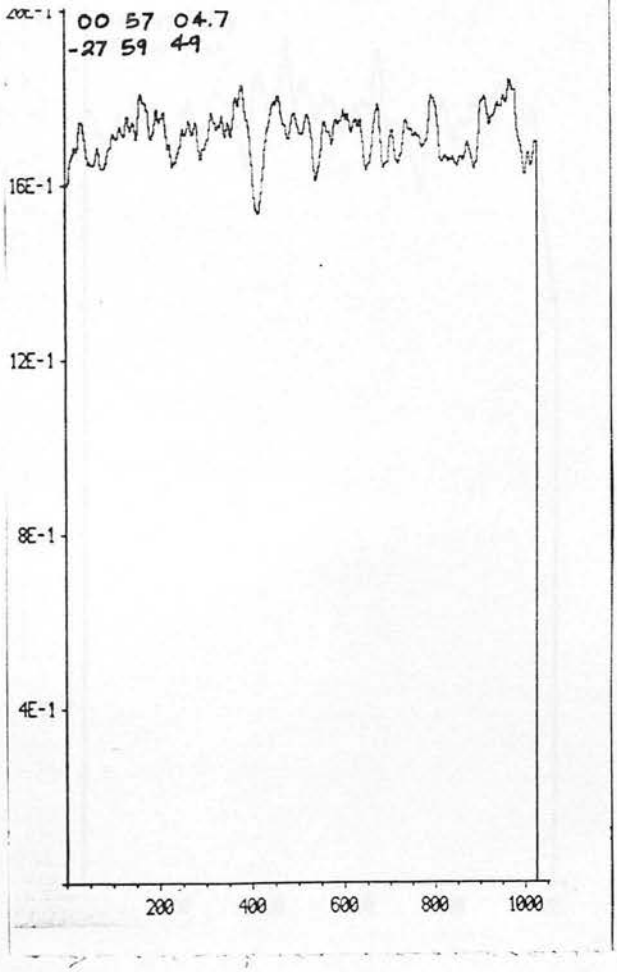
00 57 04.7
-27 59 49
16E-1
12E-1
8E-1
4E-1
200
400
600
800
1000

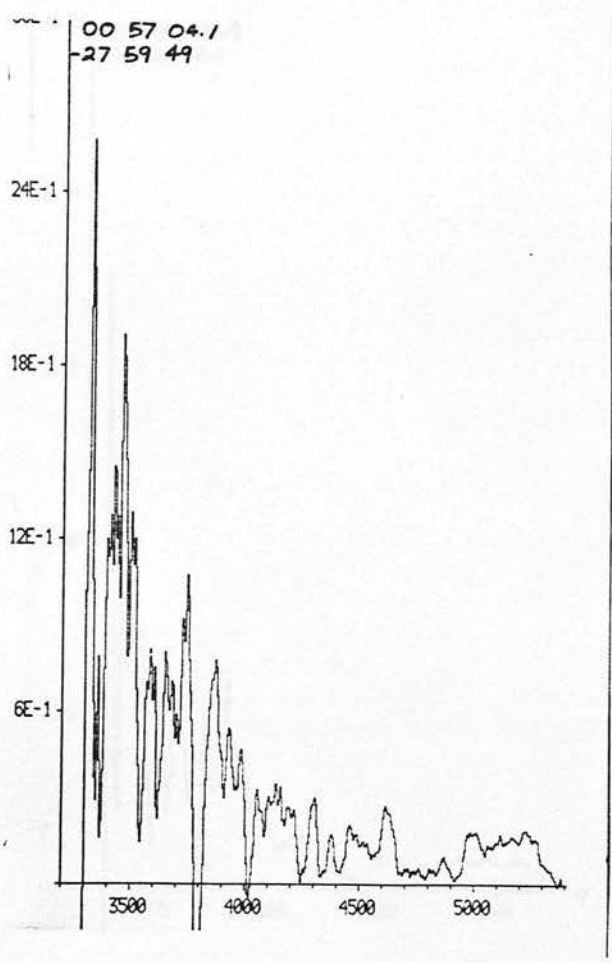
00 57 04.1
-27 59 49
24E-1
18E-1
12E-1
6E-1
3500
4000
4500
5000

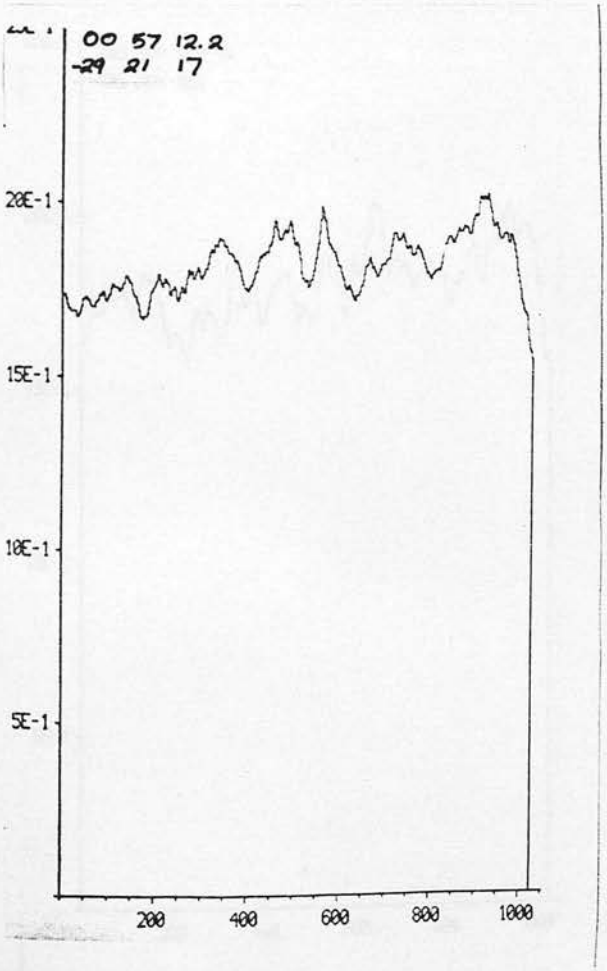
00 57 12.2
-29 21 17
20E-1
15E-1
10E-1
5E-1
200
400
600
800
1000

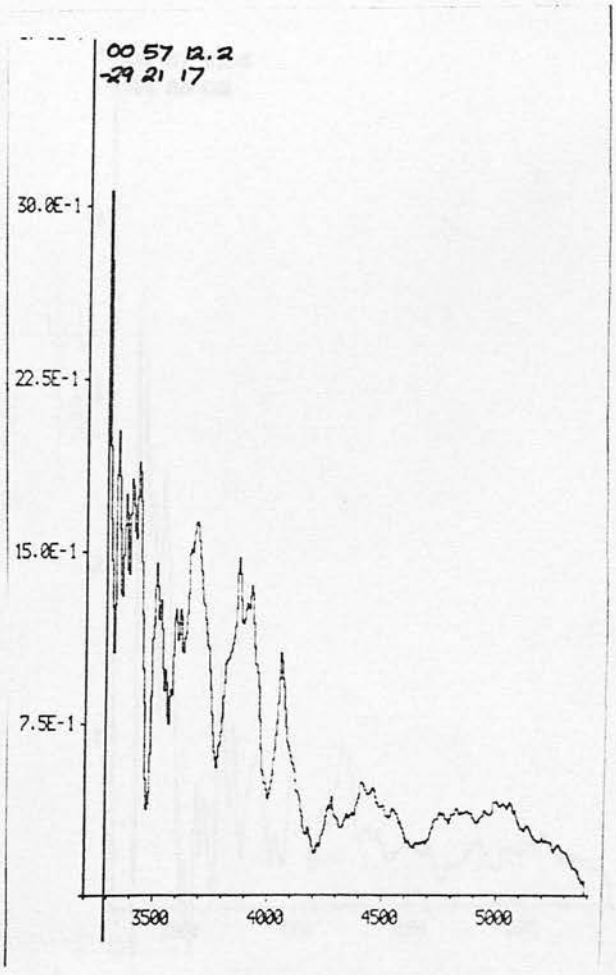
00 57 12.2
-29 21 17
30.0E-1
22.5E-1
15.0E-1
7.5E-1
3500
4000
4500
5000

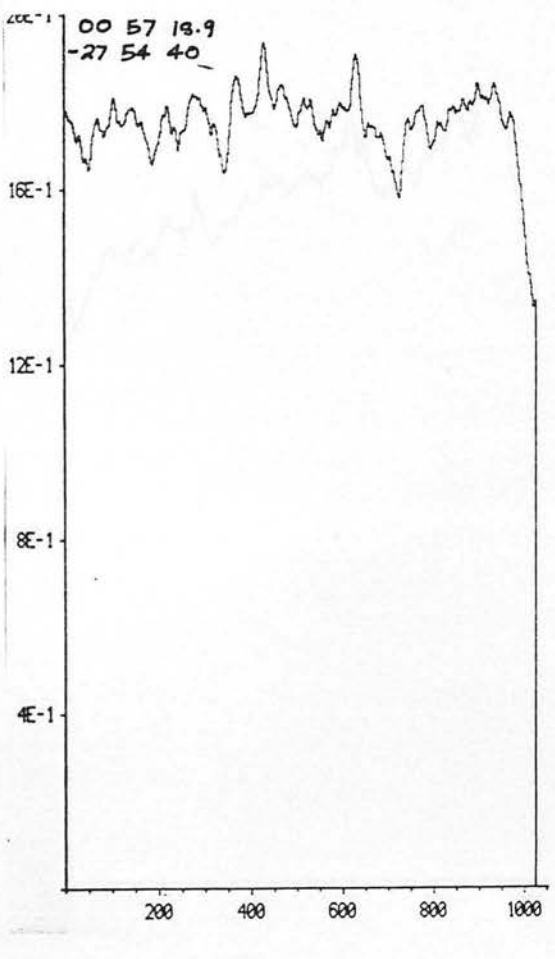
00 57 18.9
-27 54 40
16E-1
12E-1
8E-1
4E-1
200
400
600
800
1000

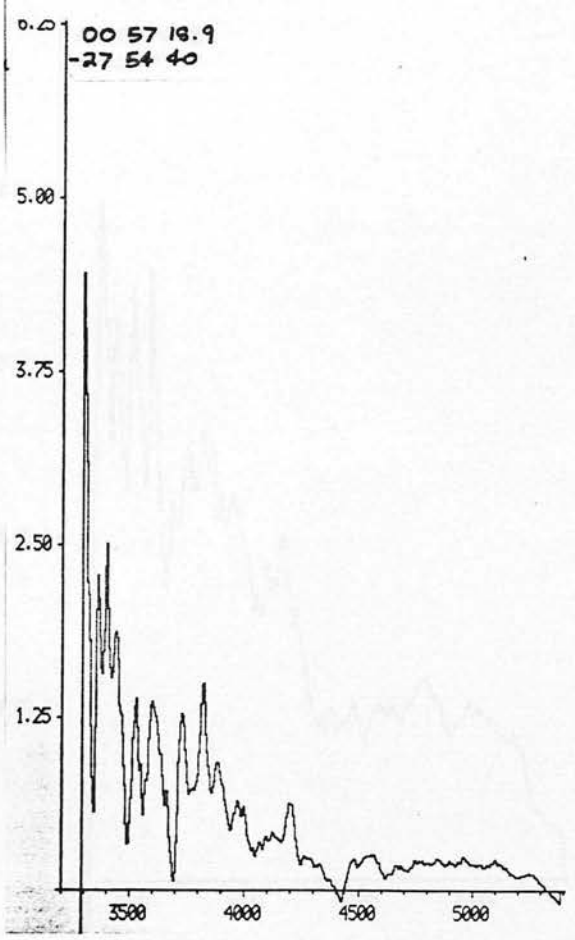
00 57 18.9
-27 54 40
5.00
3.75
2.50
1.25
3500
4000
4500
5000

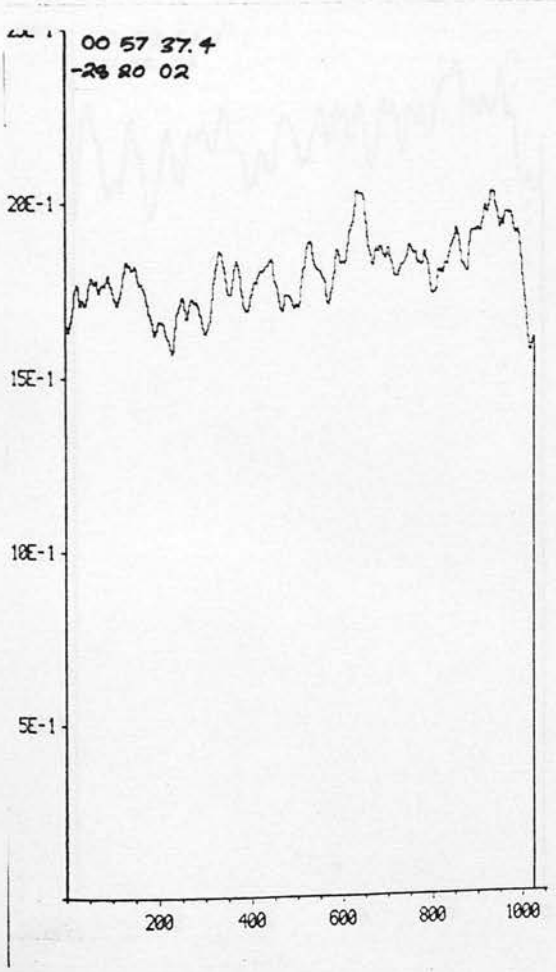
00 57 37.4
-26 20 02
20E-1
15E-1
10E-1
5E-1
200
400
600
800
1000

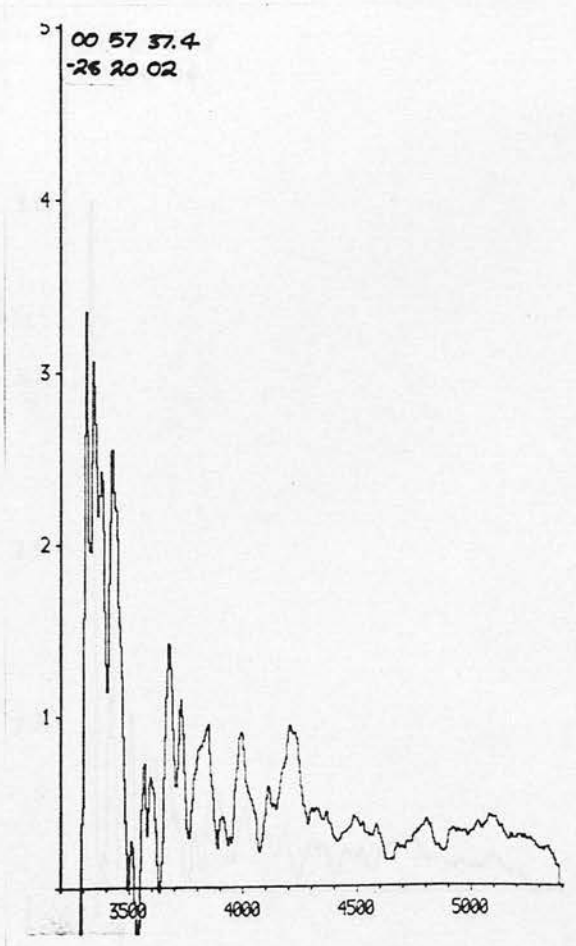
00 57 37.4
-26 20 02
4
3
2
1
3500
4000
4500
5000

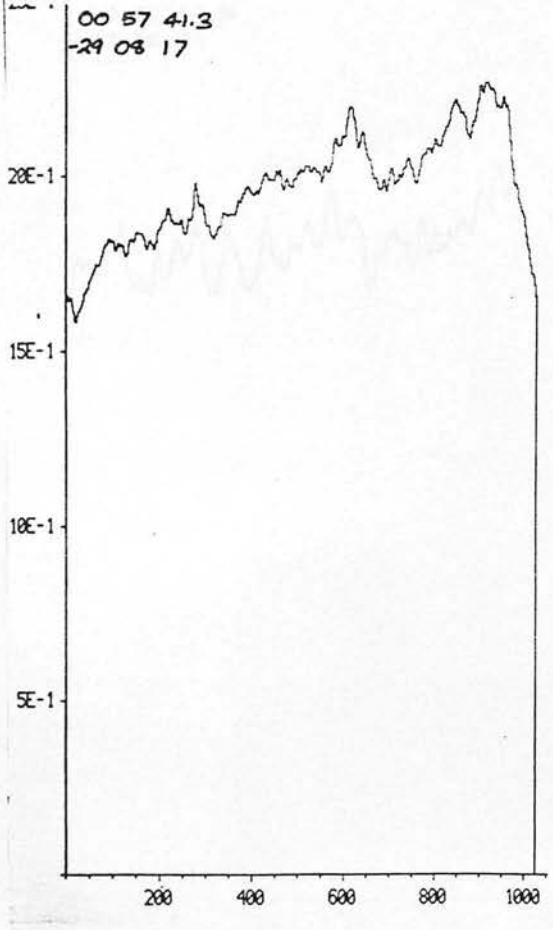
00 57 41.3
-29 08 17
20E-1
15E-1
10E-1
5E-1
200
400
600
800
1000

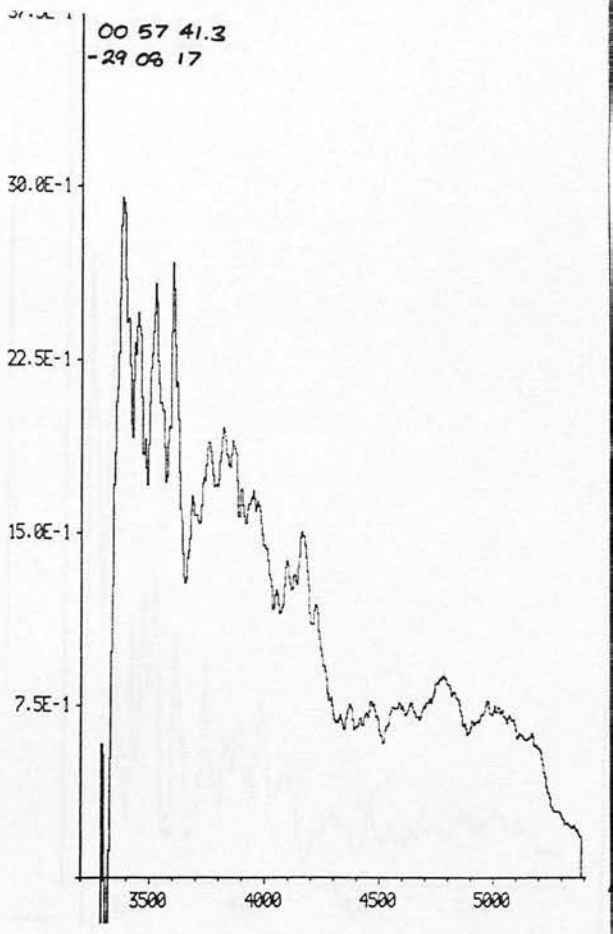
00 57 41.3
-29 08 17
30.0E-1
22.5E-1
15.0E-1
7.5E-1
3500
4000
4500
5000

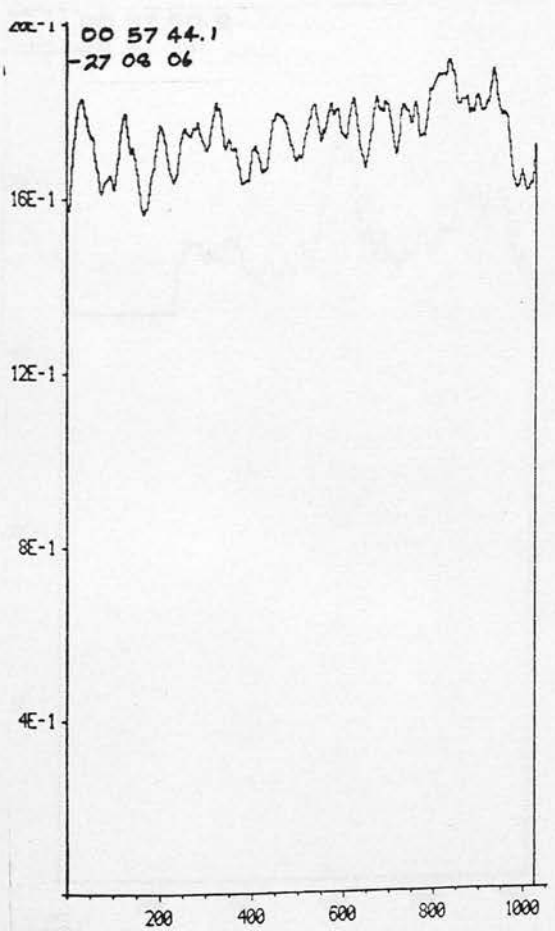
00 57 44.1
-27 08 06
16E-1
12E-1
8E-1
4E-1
200
400
600
800
1000

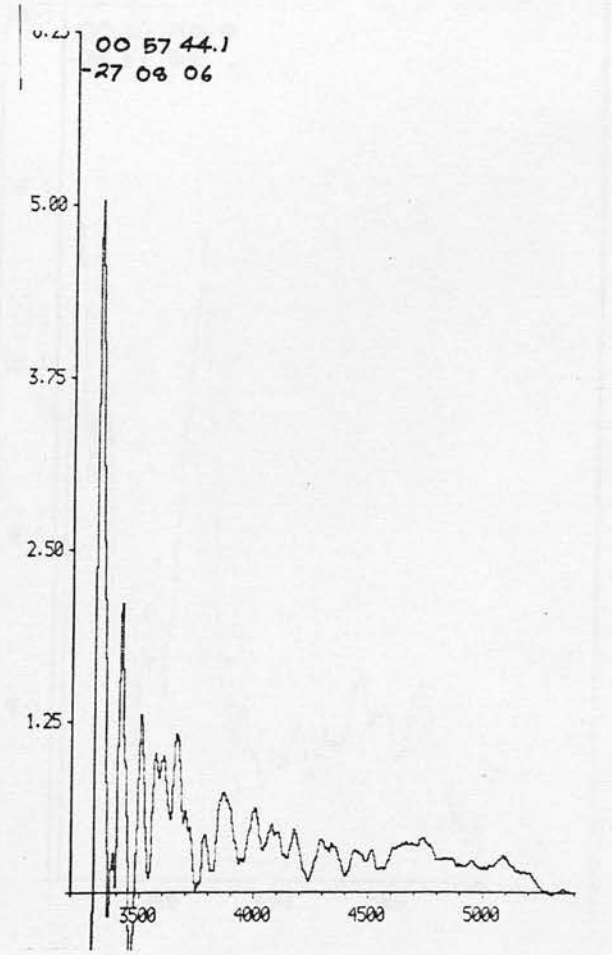
00 57 44.1
-27 08 06
5.00
3.75
2.50
1.25
3500
4000
4500
5000

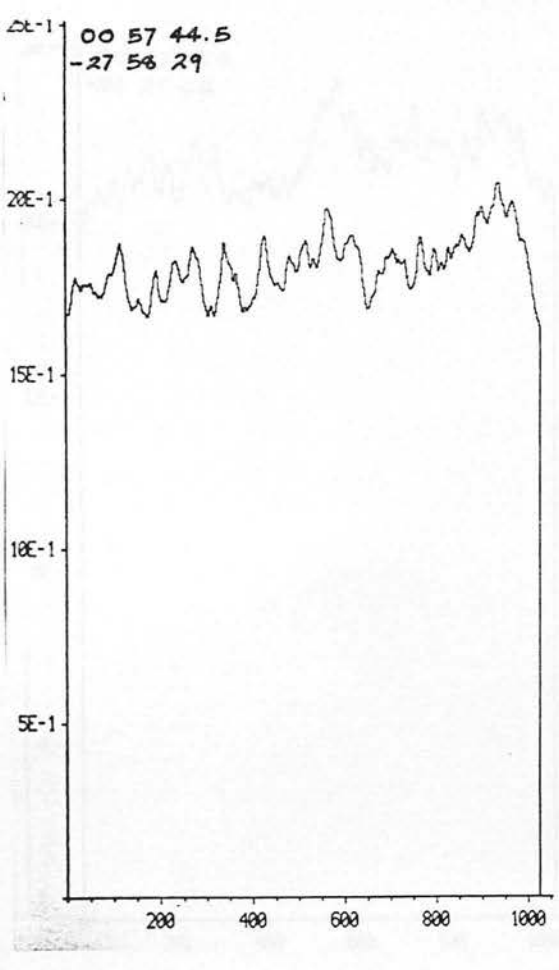
00 57 44.5
-27 58 29
2E-1
15E-1
1E-1
5E-1
200
400
600
800
1000

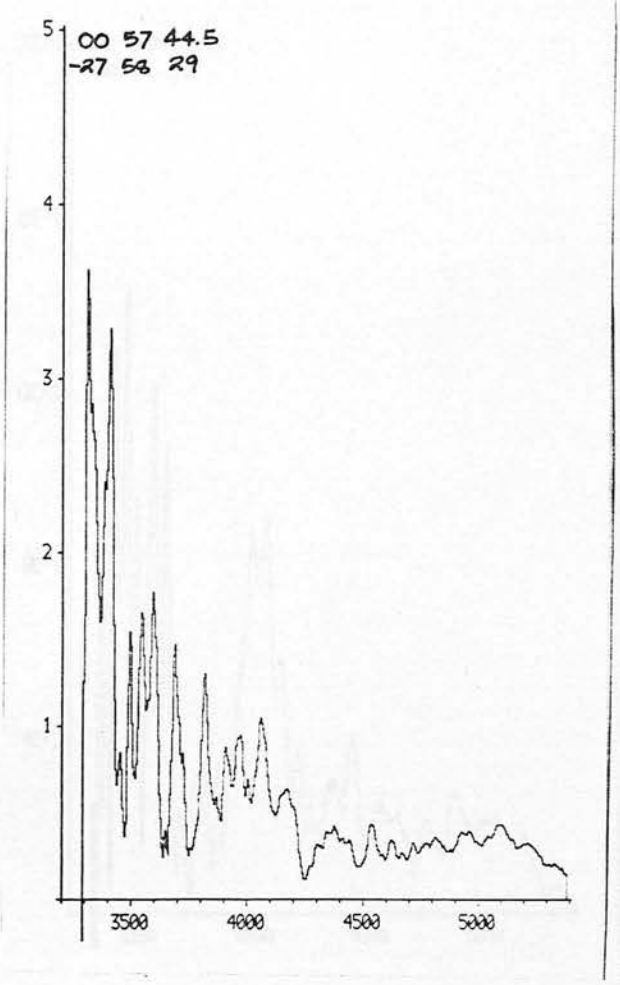
00 57 44.5
-27 58 29
5
4
3
2
1
3500
4000
4500
5000

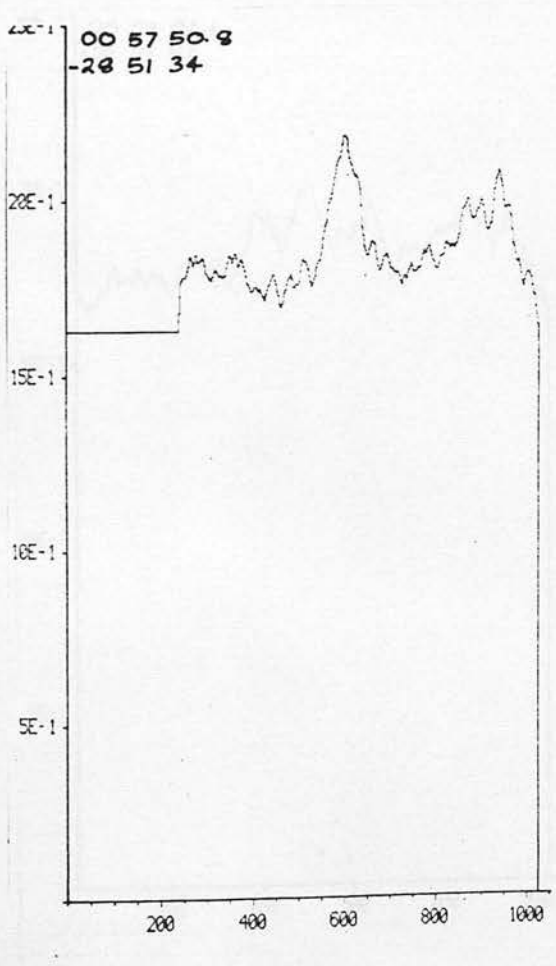
00 57 50.8
-28 51 34
2E-1
15E-1
1E-1
5E-1
200
400
600
800
1000

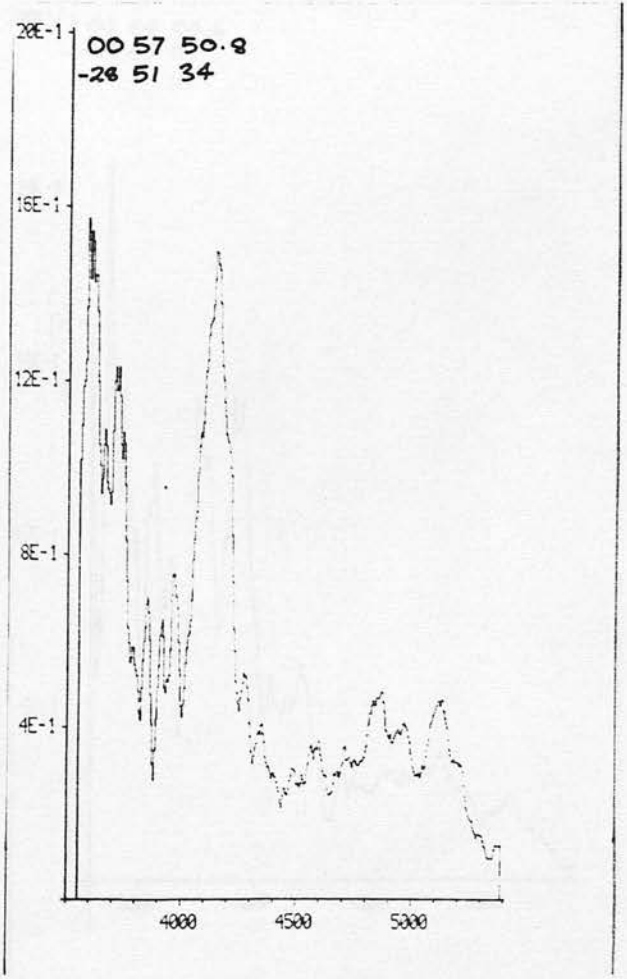
00 57 50.8
-28 51 34
2E-1
16E-1
12E-1
8E-1
4E-1
4000
4500
5000

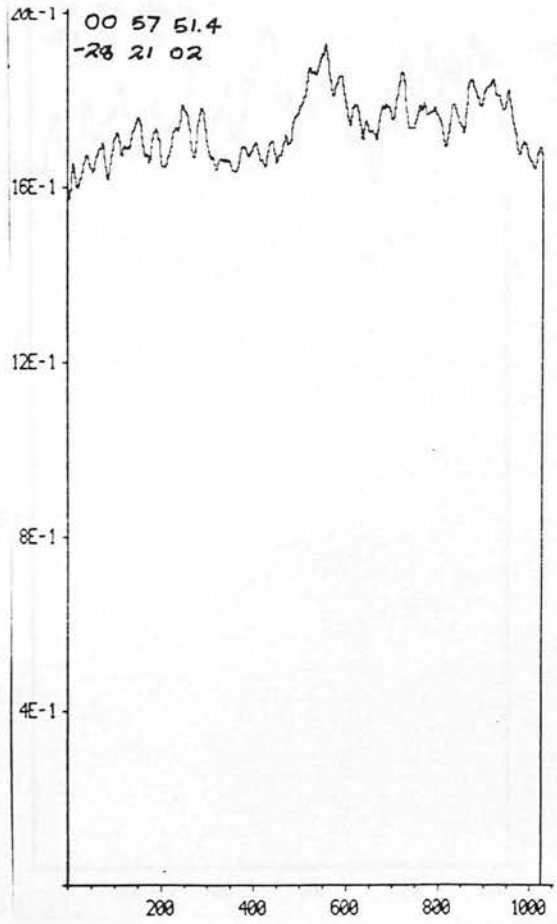
00 57 51.4
-28 21 02
20E-1
16E-1
12E-1
8E-1
4E-1
200
400
600
800
1000

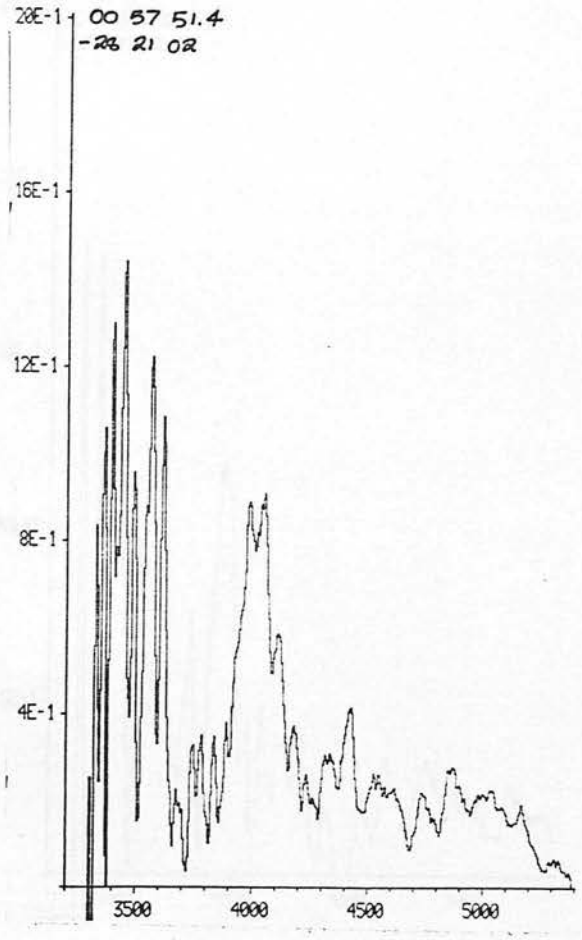
00 57 51.4
-28 21 02
20E-1
16E-1
12E-1
8E-1
4E-1
3500
4000
4500
5000

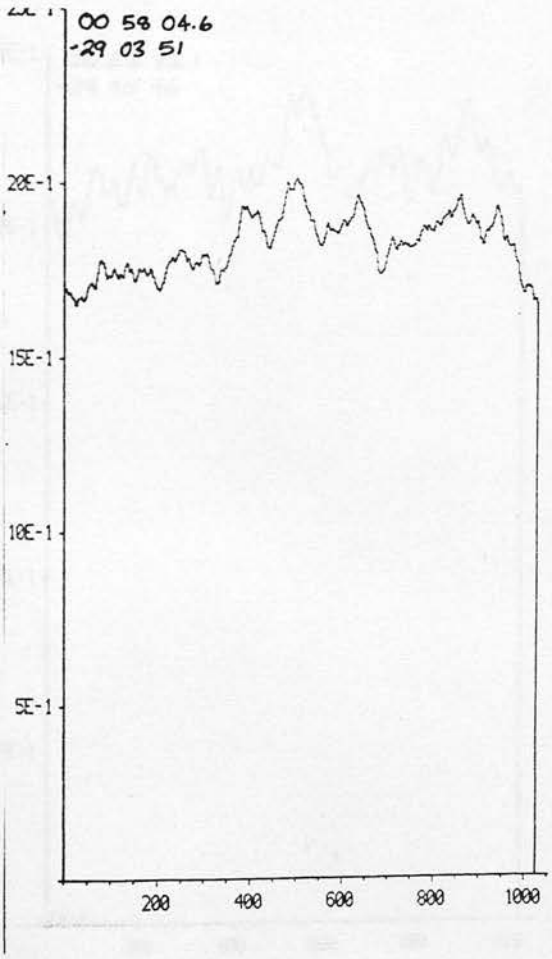
00 58 04.6
-29 03 51
20E-1
15E-1
10E-1
5E-1
200
400
600
800
1000

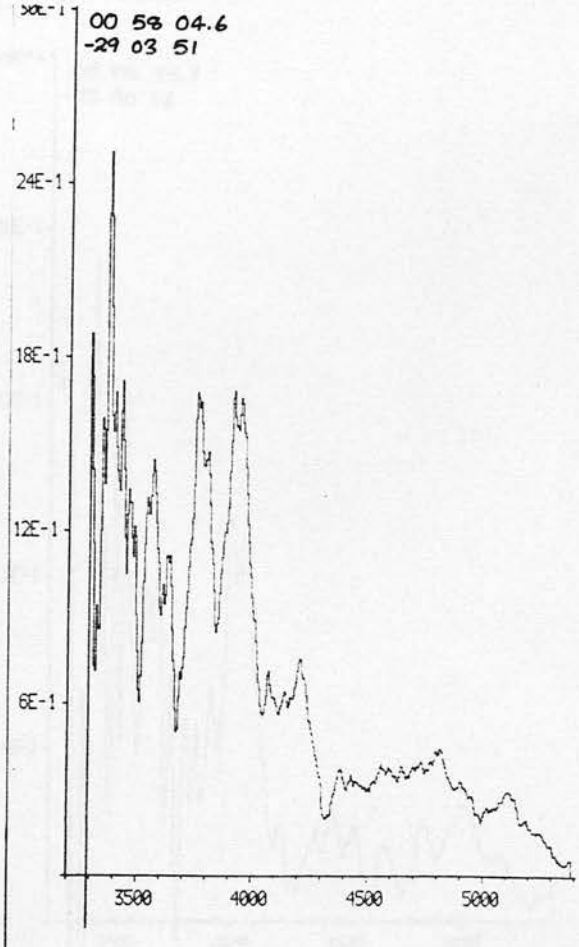
00 58 04.6
-29 03 51
24E-1
18E-1
12E-1
6E-1
3500
4000
4500
5000

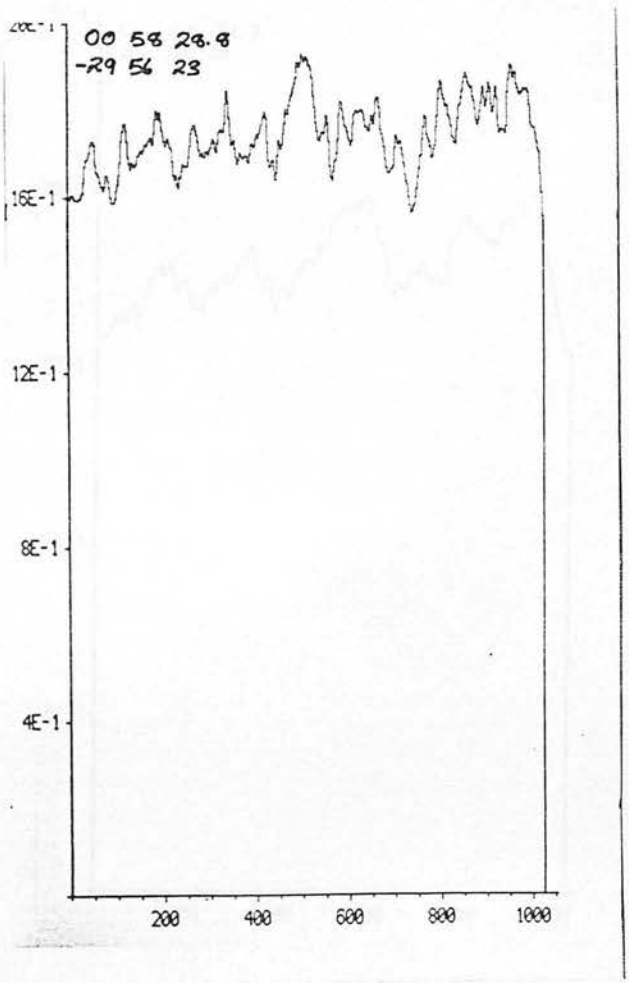
00 58 28.8
-29 56 23
16E-1
12E-1
8E-1
4E-1
200
400
600
800
1000

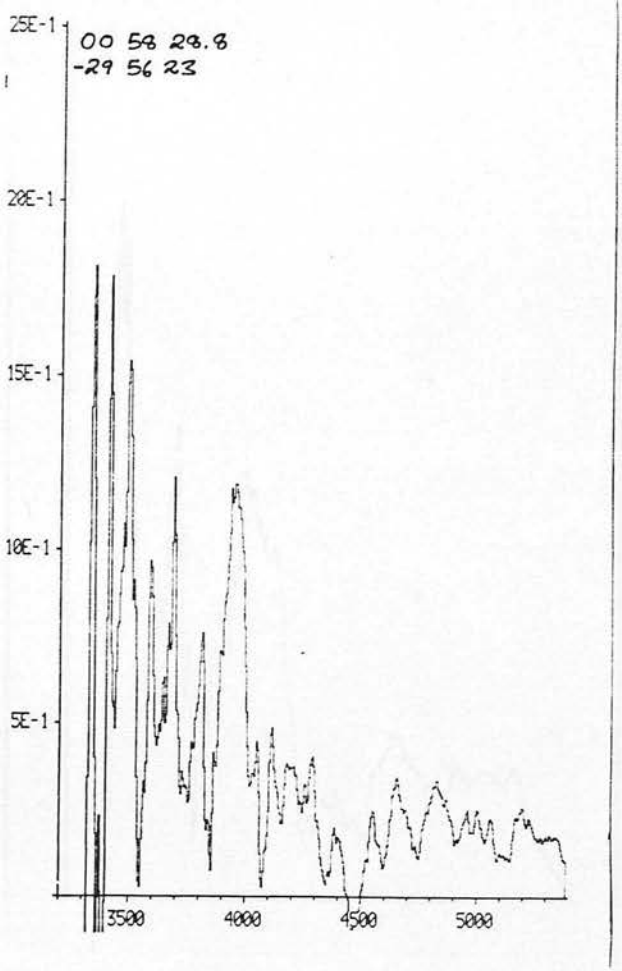
25E-1
00 58 28.8
-29 56 23
20E-1
15E-1
10E-1
5E-1
3500
4000
4500
5000

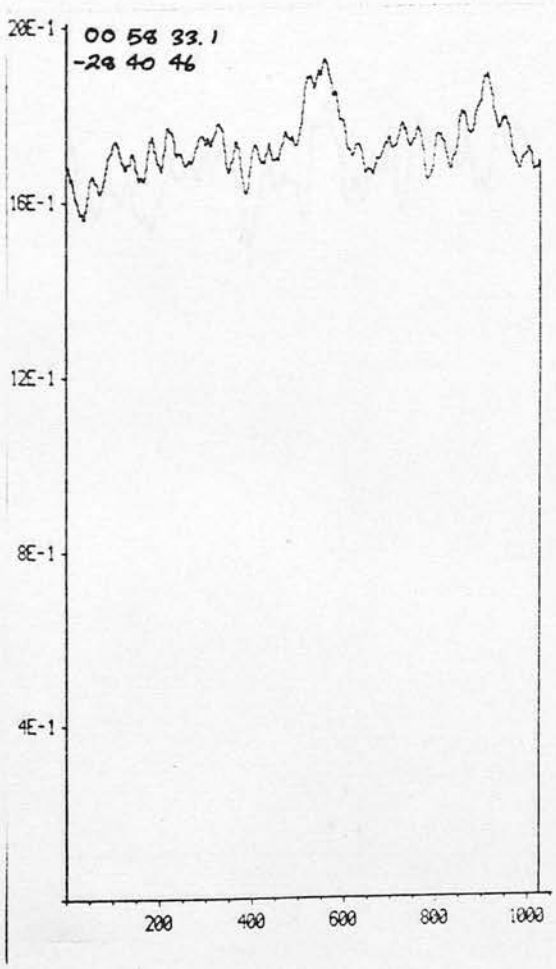
20E-1
00 58 33.1
-28 40 46
16E-1
12E-1
8E-1
4E-1
200
400
600
800
1000

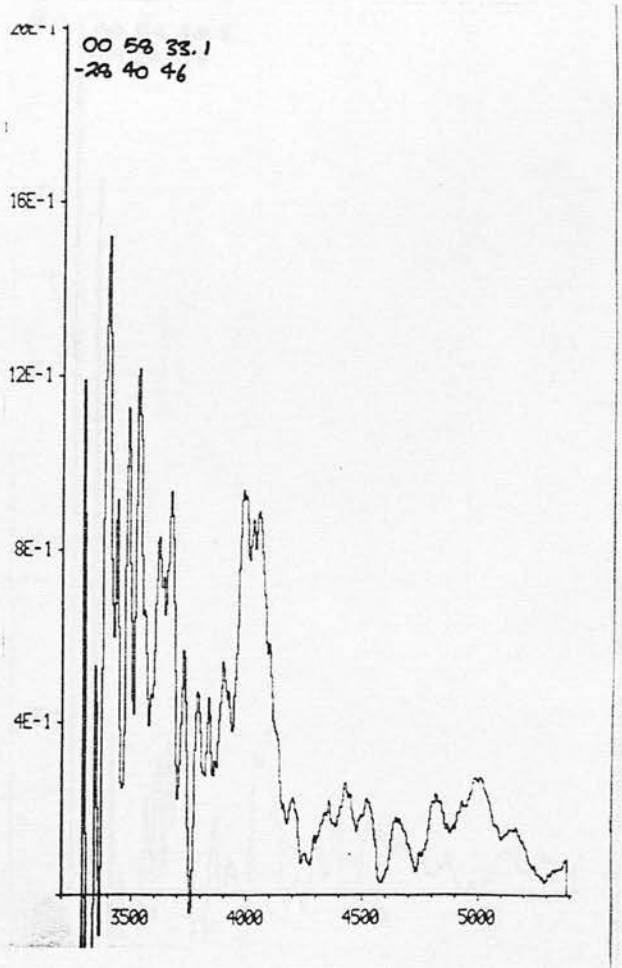
00 58 33.1
-28 40 46
16E-1
12E-1
8E-1
4E-1
3500
4000
4500
5000

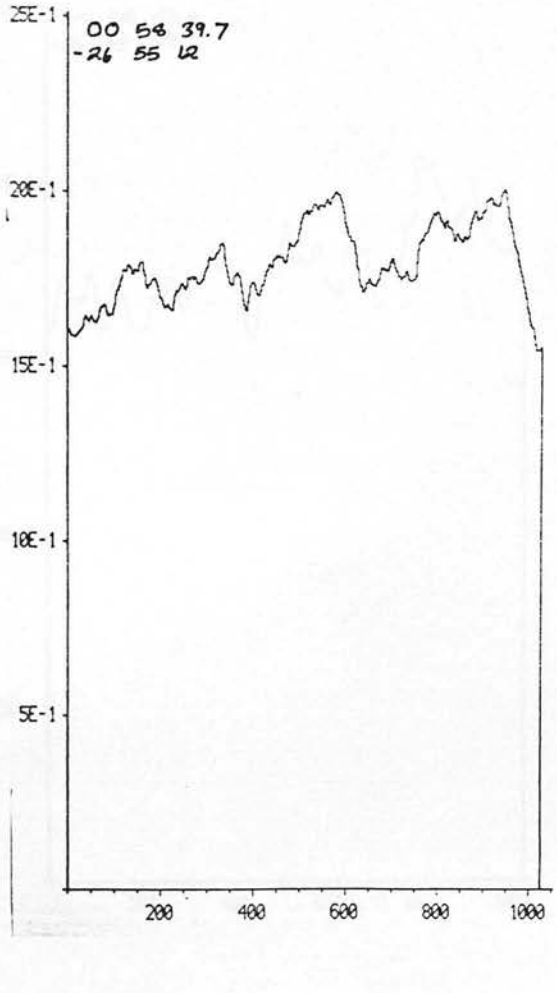
00 58 39.7
-26 55 42
25E-1
20E-1
15E-1
10E-1
5E-1
200
400
600
800
1000

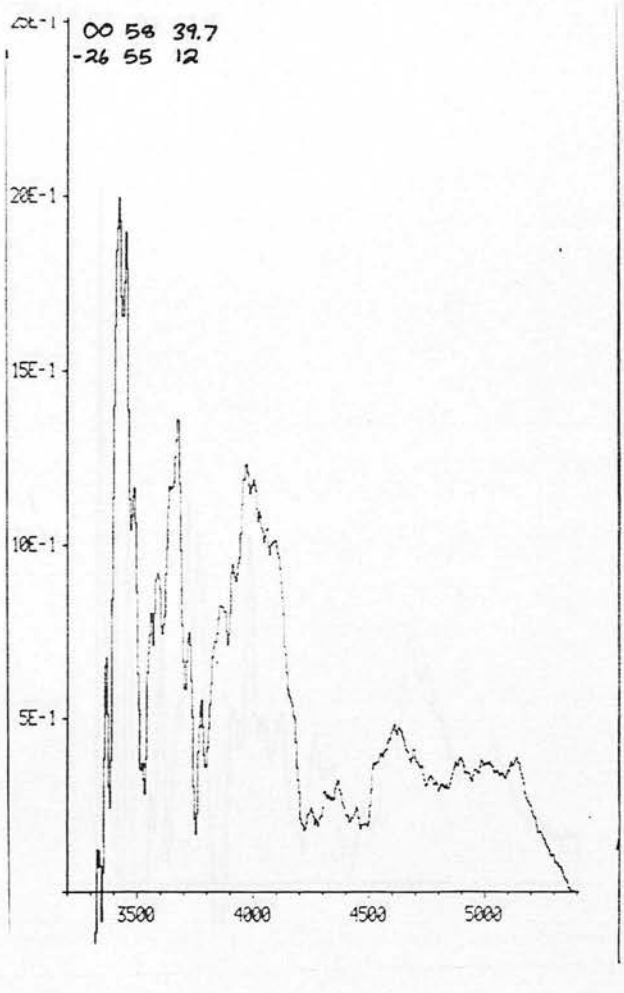
00 58 39.7
-26 55 12
20E-1
15E-1
10E-1
5E-1
3500
4000
4500
5000

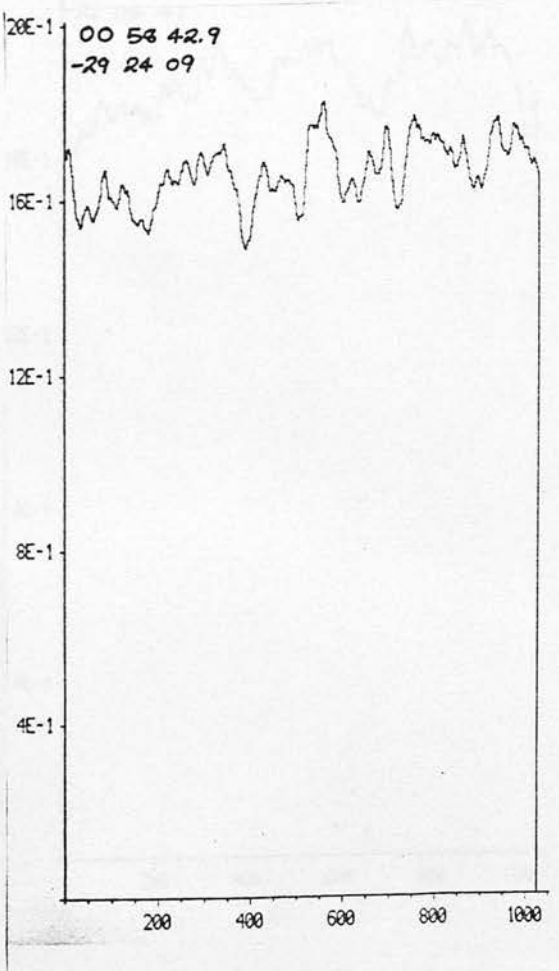
00 58 42.9
-29 24 09
20E-1
16E-1
12E-1
8E-1
4E-1
200
400
600
800
1000

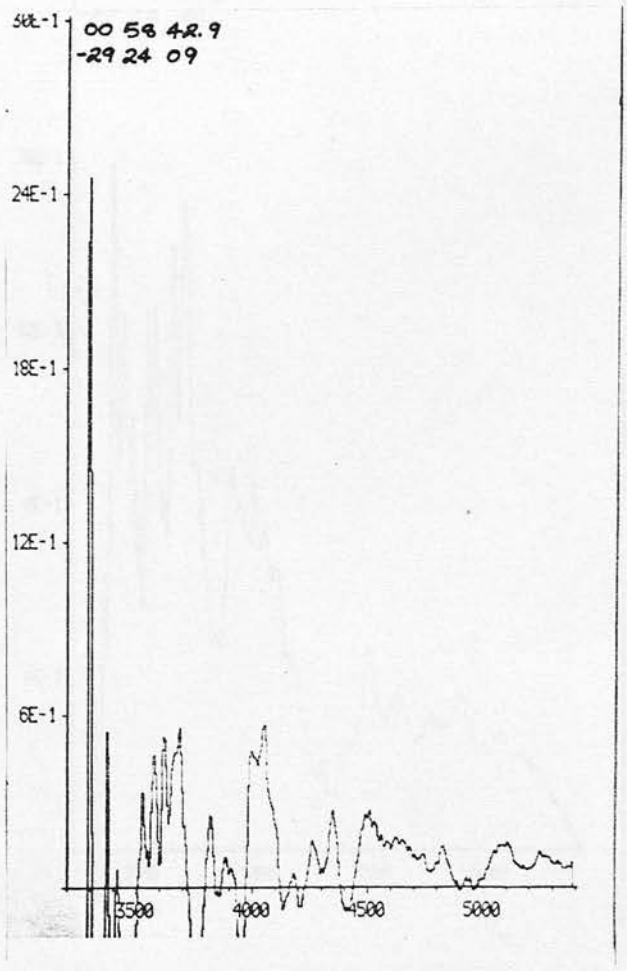
00 58 42.9
-29 24 09
24E-1
18E-1
12E-1
6E-1
3500
4000
4500
5000

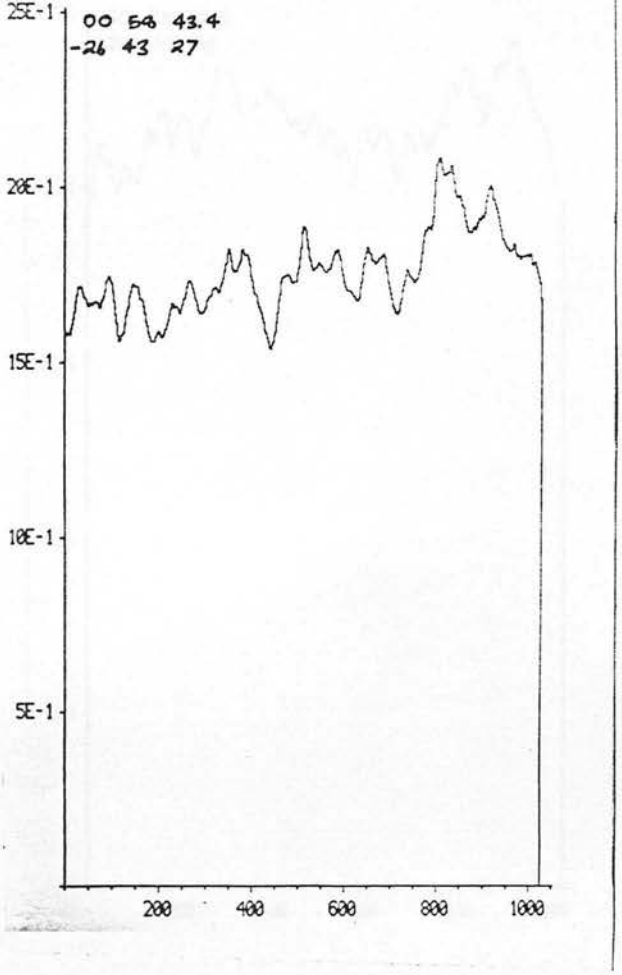
00 58 43.4
-26 43 27
25E-1
20E-1
15E-1
10E-1
5E-1
200
400
600
800
1000

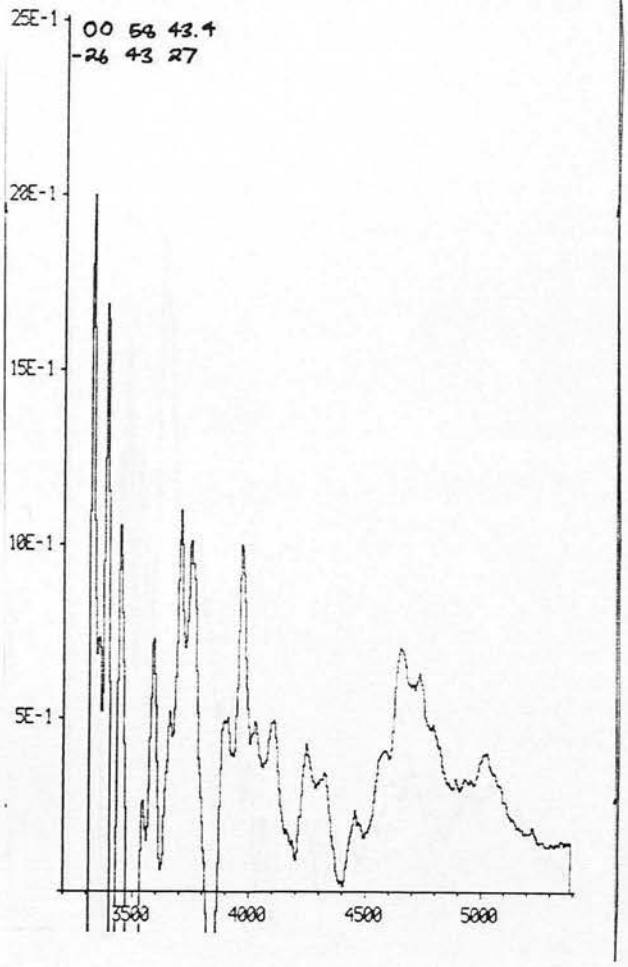
00 58 43.4
-26 43 27
25E-1
20E-1
15E-1
10E-1
5E-1
3500
4000
4500
5000

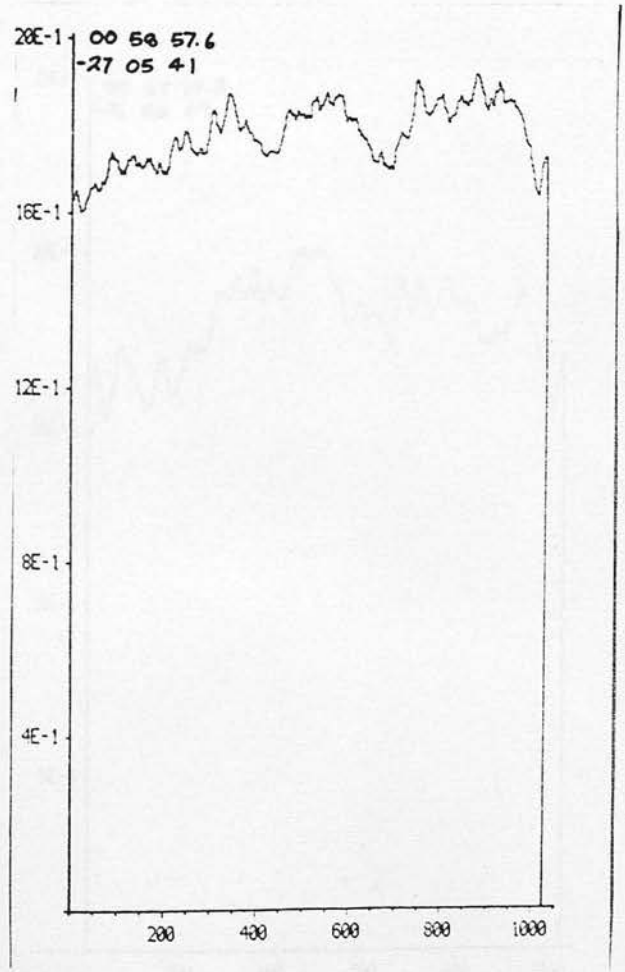
00 58 57.6
-27 05 41
20E-1
16E-1
12E-1
8E-1
4E-1
200
400
600
800
1000

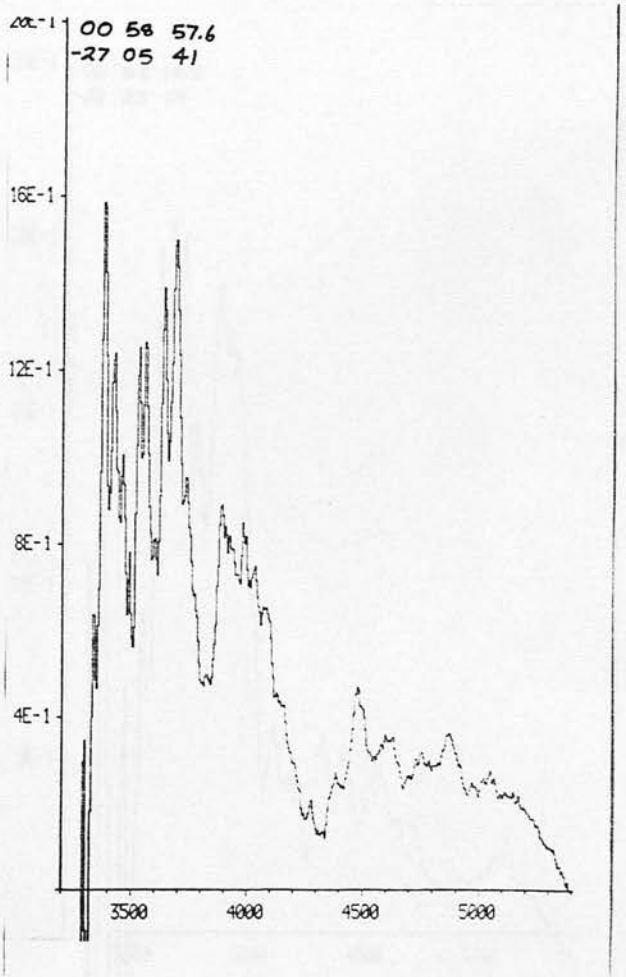
00 58 57.6
-27 05 41
16E-1
12E-1
8E-1
4E-1
3500
4000
4500
5000

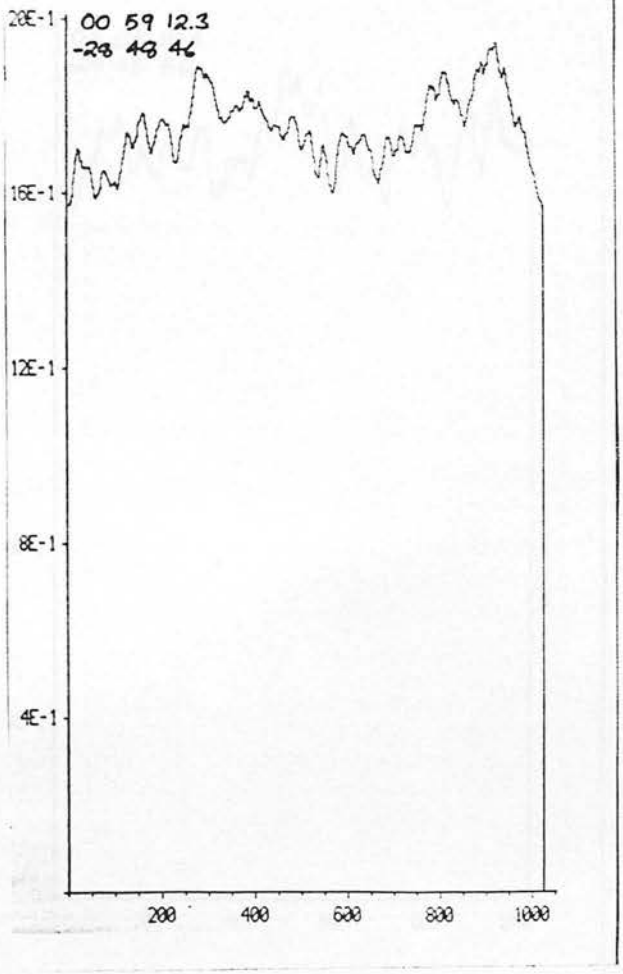
00 59 12.3
-28 48 46
2.0E-1
1.6E-1
1.2E-1
8E-1
4E-1
200
400
600
800
1000

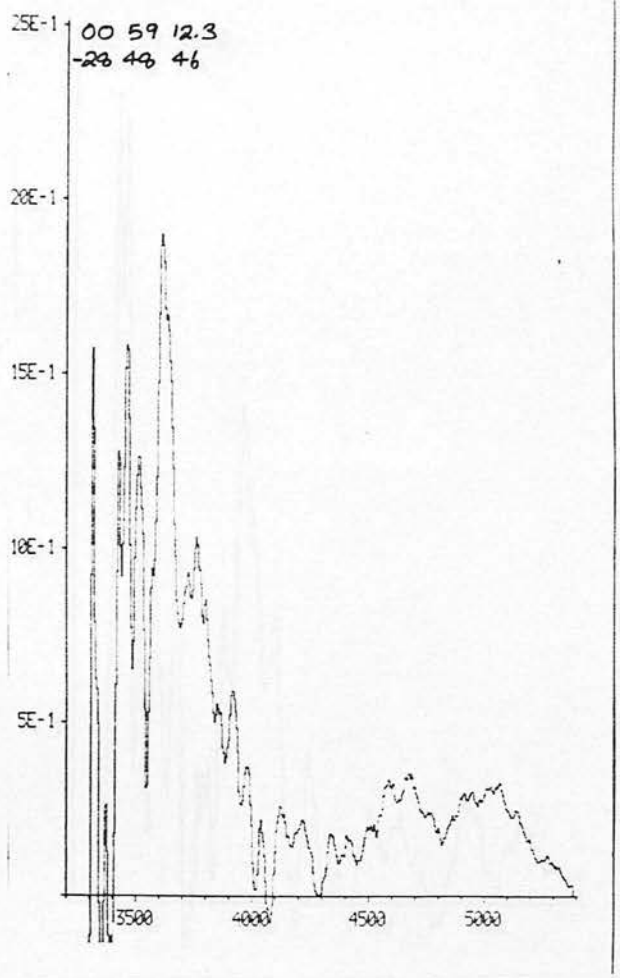
00 59 12.3
-28 48 46
2.5E-1
2.0E-1
1.5E-1
1.0E-1
5E-1
3500
4000
4500
5000

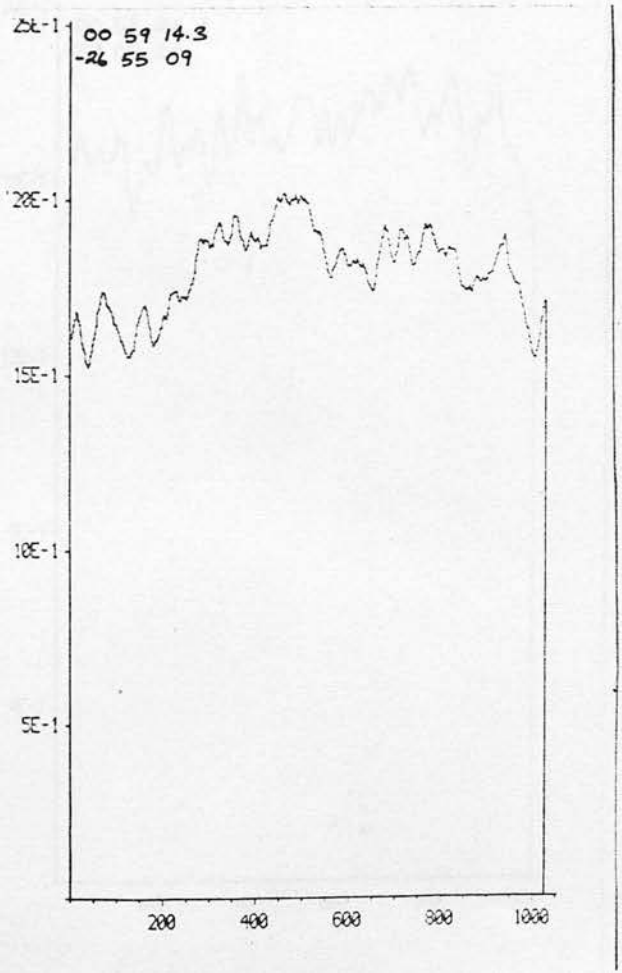
00 59 14.3
-26 55 09
2.0E-1
1.5E-1
1.0E-1
5E-1
200
400
600
800
1000

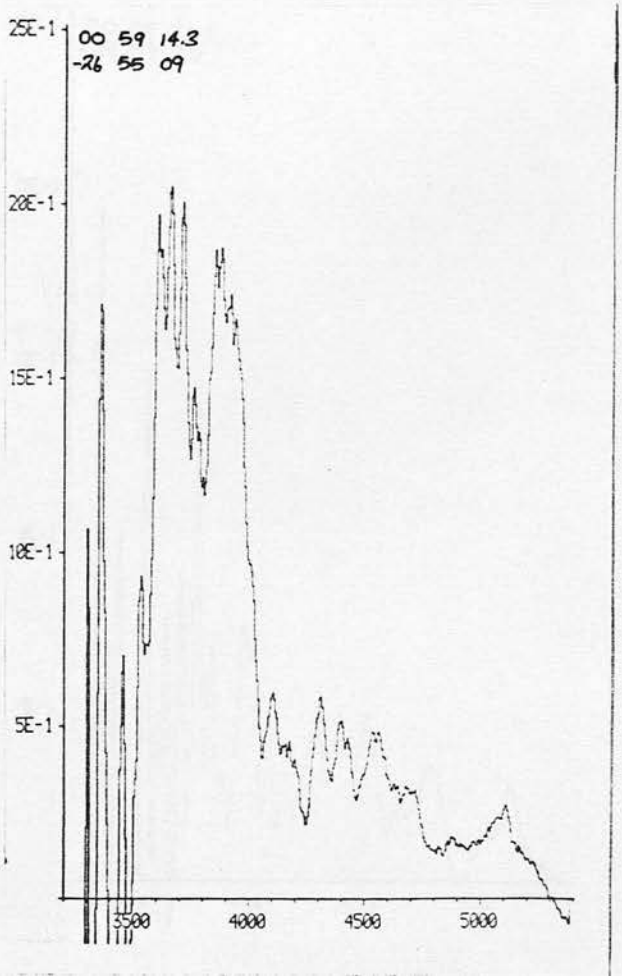
00 59 14.3
-26 55 09
2.5E-1
2.0E-1
1.5E-1
1.0E-1
5E-1
3500
4000
4500
5000

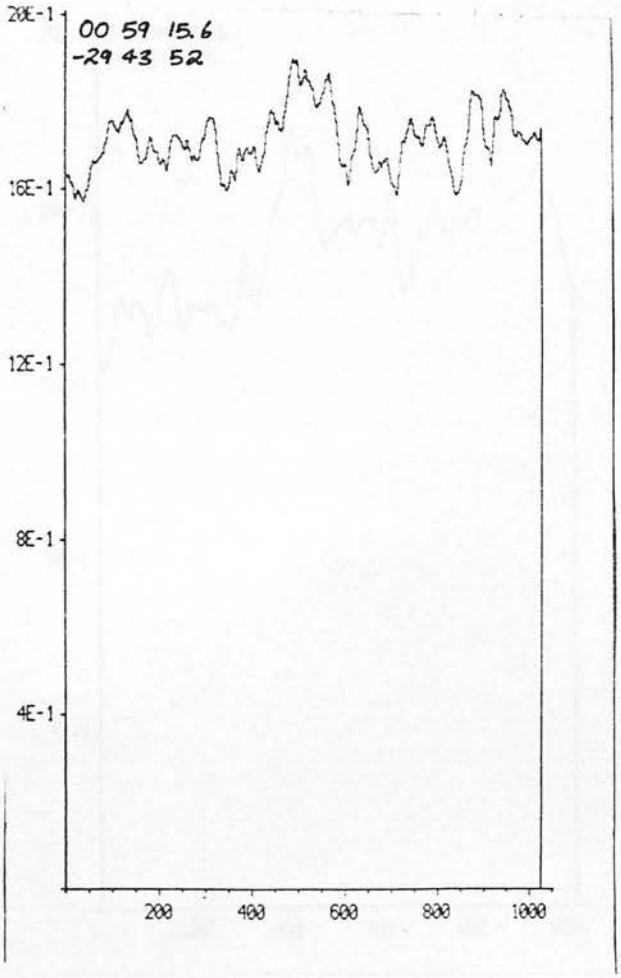
00 59 15.6
-29 43 52
20E-1
16E-1
12E-1
8E-1
4E-1
200
400
600
800
1000

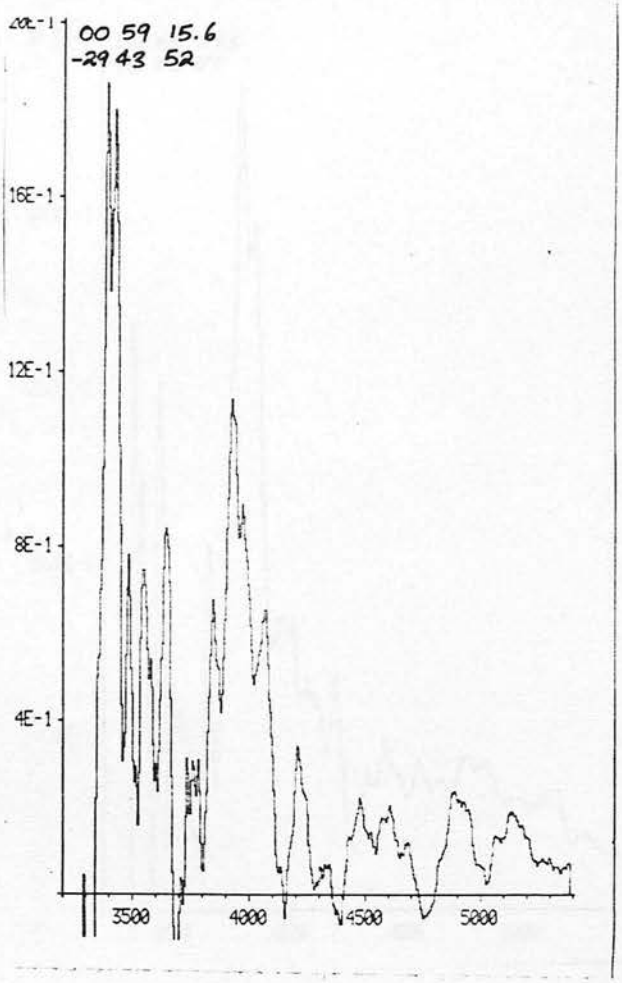
00 59 15.6
-29 43 52
16E-1
12E-1
8E-1
4E-1
3500
4000
4500
5000

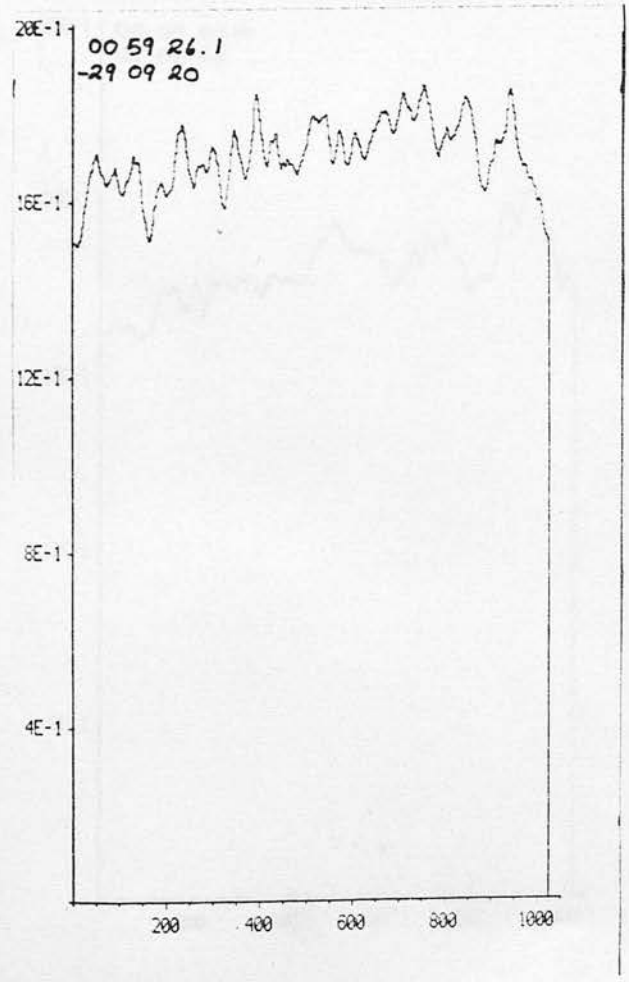
00 59 26.1
-29 09 20
20E-1
16E-1
12E-1
8E-1
4E-1
200
400
600
800
1000

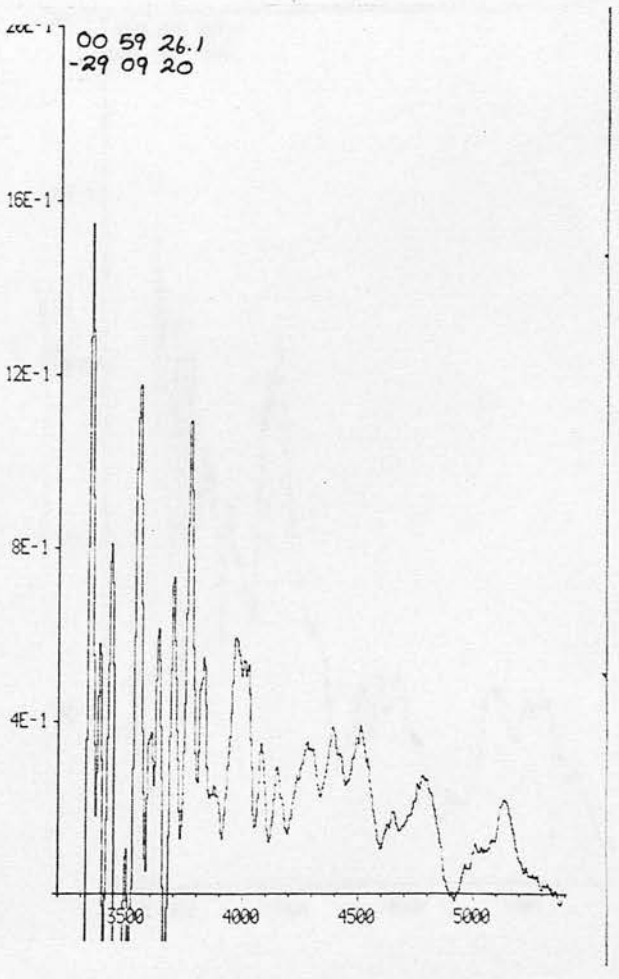
00 59 26.1
-29 09 20
16E-1
12E-1
8E-1
4E-1
3500
4000
4500
5000

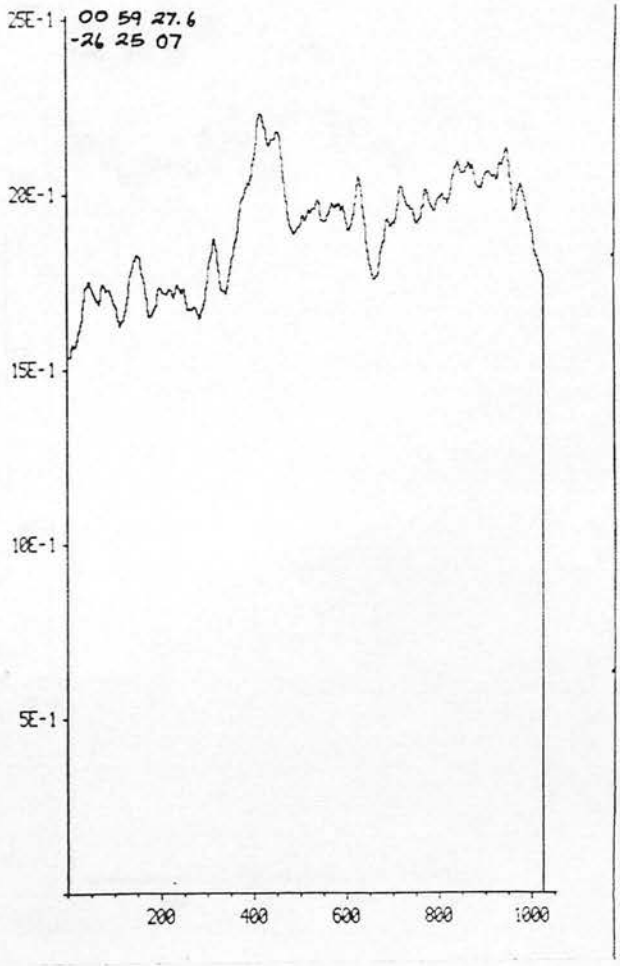
00 59 27.6
-26 25 07
25E-1
20E-1
15E-1
10E-1
5E-1
200
400
600
800
1000

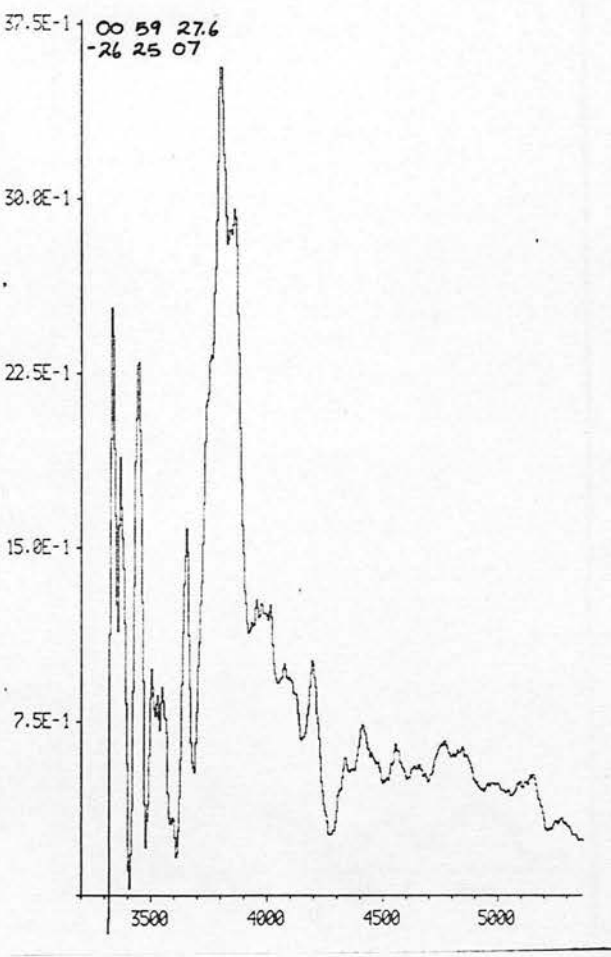
00 59 27.6
-26 25 07
37.5E-1
30.0E-1
22.5E-1
15.0E-1
7.5E-1
3500
4000
4500
5000

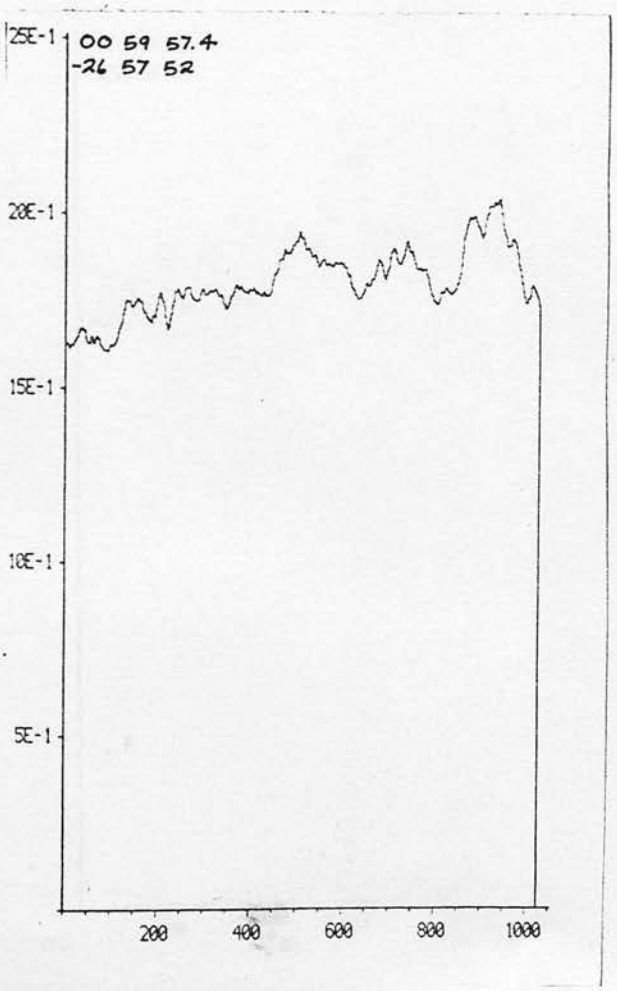
00 59 57.4
-26 57 52
25E-1
20E-1
15E-1
10E-1
5E-1
200
400
600
800
1000

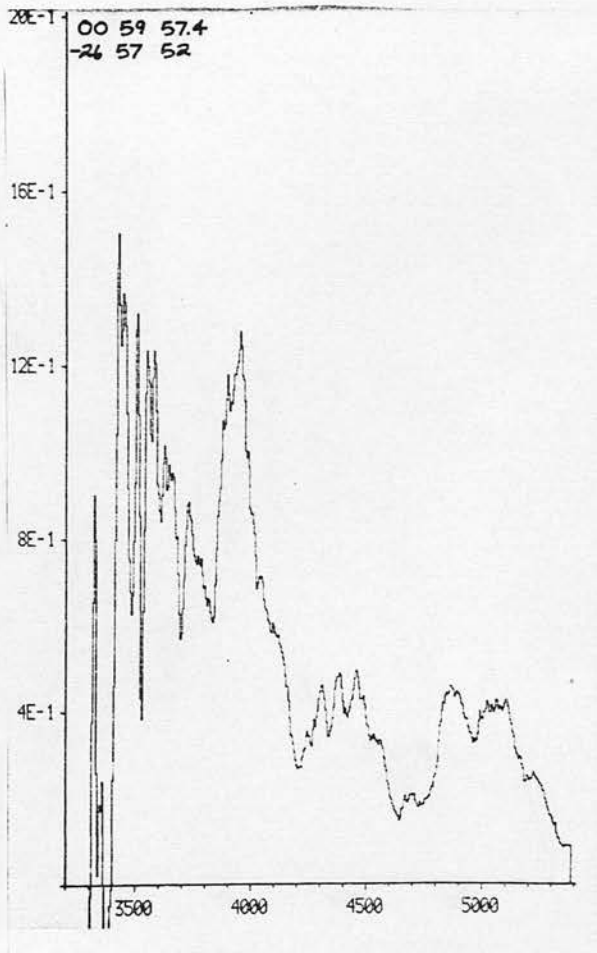
00 59 57.4
-26 57 52
20E-1
16E-1
12E-1
8E-1
4E-1
3500
4000
4500
5000

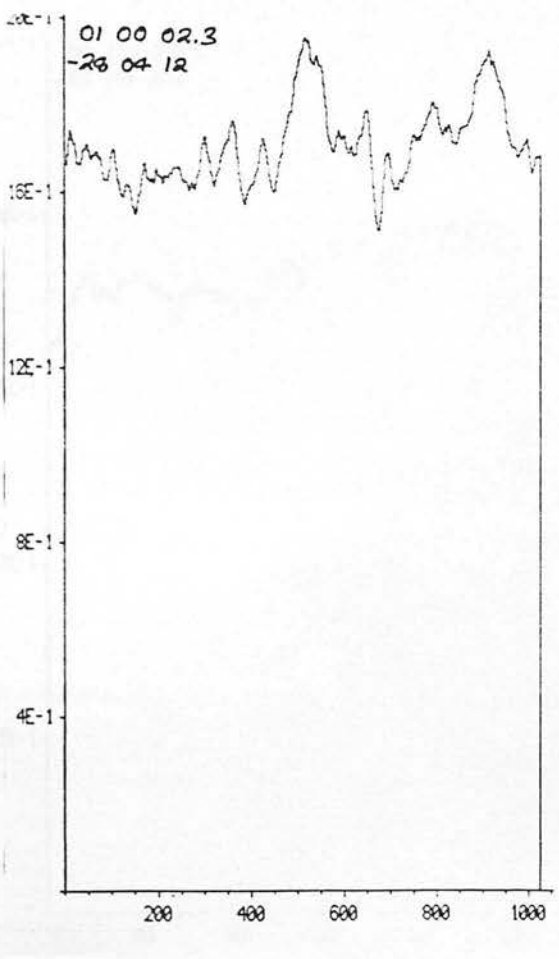
01 00 02.3
-28 04 12
16E-1
12E-1
8E-1
4E-1
200
400
600
800
1000

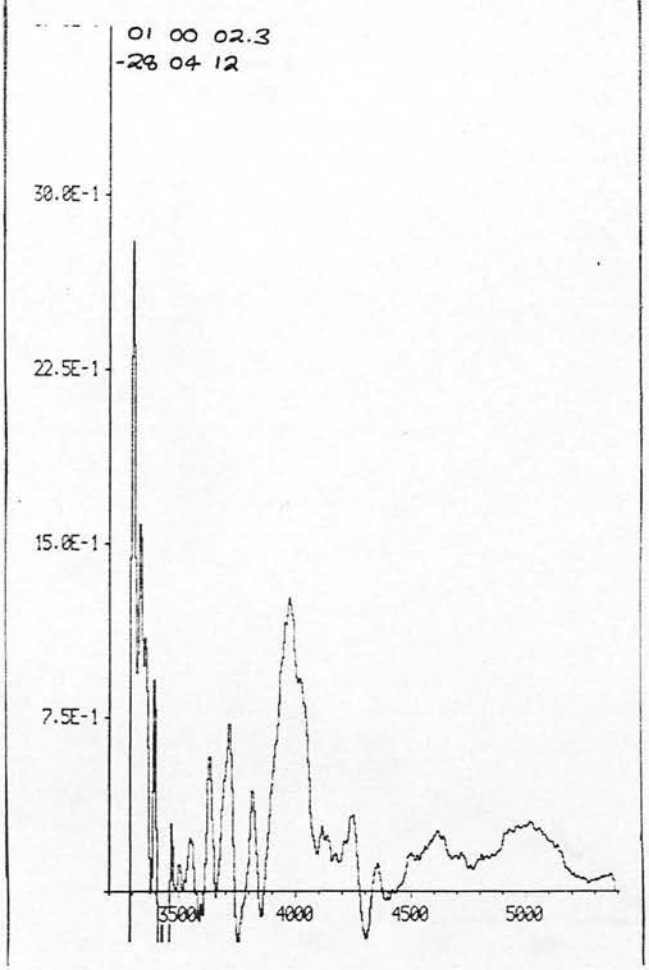
01 00 02.3
-28 04 12
30.0E-1
22.5E-1
15.0E-1
7.5E-1
3500
4000
4500
5000

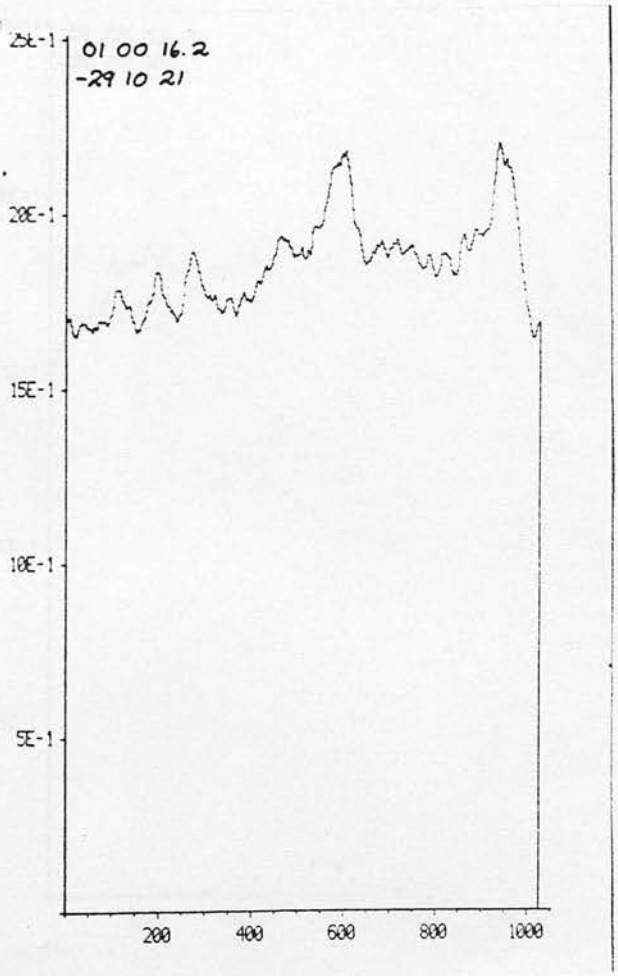
01 00 16.2
-29 10 21
20E-1
15E-1
10E-1
5E-1
200
400
600
800
1000

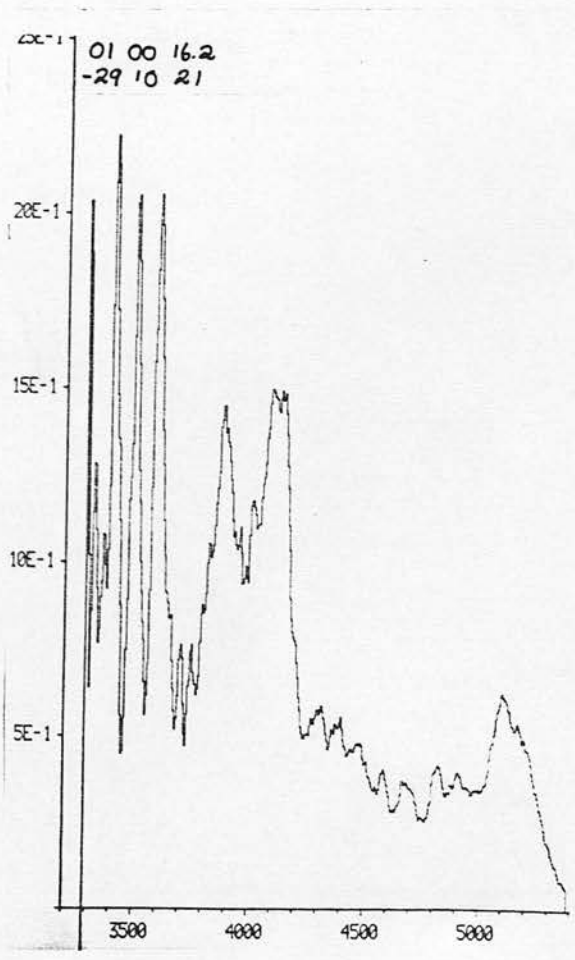
01 00 16.2
-29 10 21
20E-1
15E-1
10E-1
5E-1
3500
4000
4500
5000

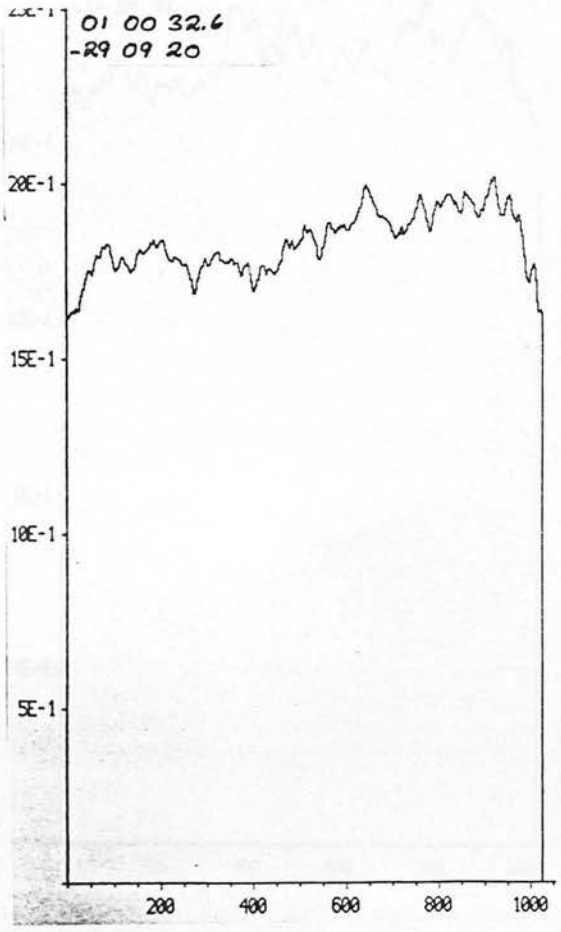
01 00 32.6
-29 09 20
20E-1
15E-1
10E-1
5E-1
200
400
600
800
1000

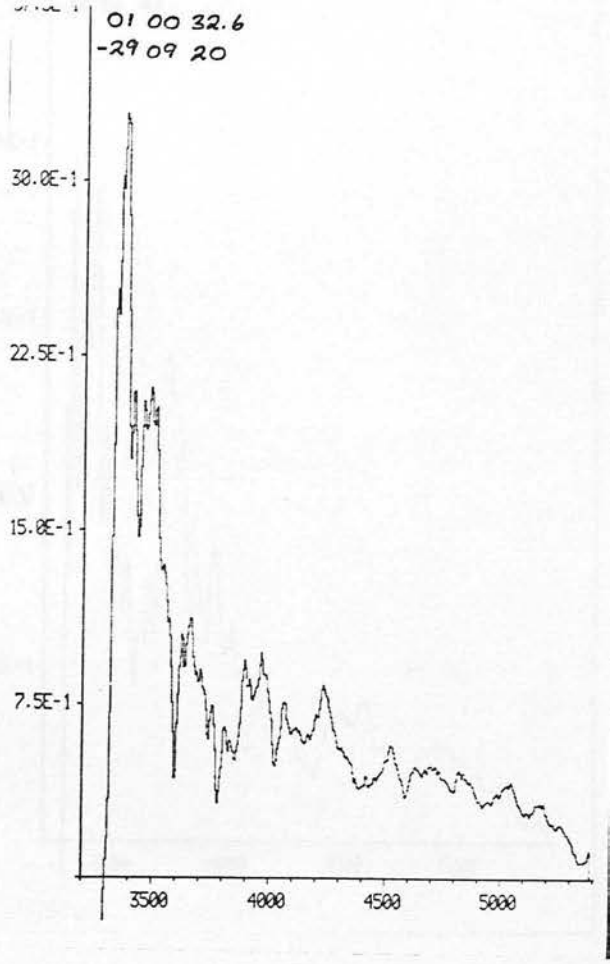
01 00 32.6
-29 09 20
30.0E-1
22.5E-1
15.0E-1
7.5E-1
3500
4000
4500
5000

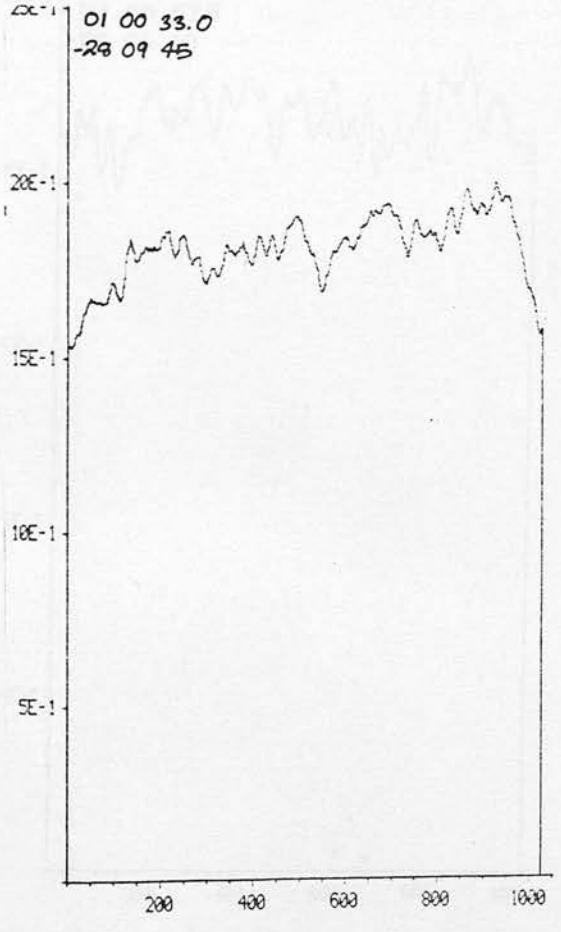
01 00 33.0
-28 09 45
20E-1
15E-1
10E-1
5E-1
200
400
600
800
1000

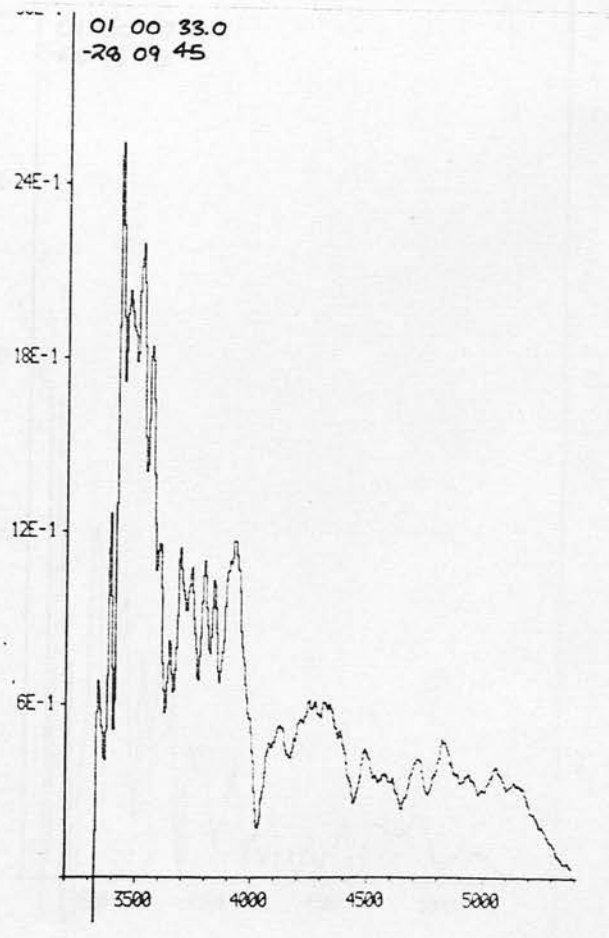
01 00 33.0
-28 09 45
24E-1
18E-1
12E-1
6E-1
3500
4000
4500
5000

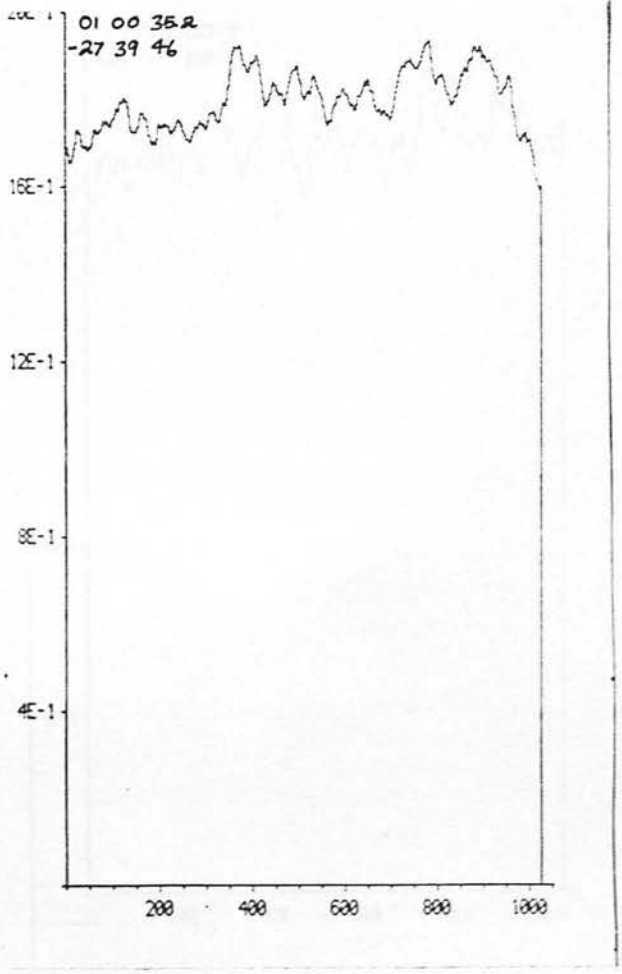
01 00 35.2
-27 39 46
16E-1
12E-1
8E-1
4E-1
200
400
600
800
1000

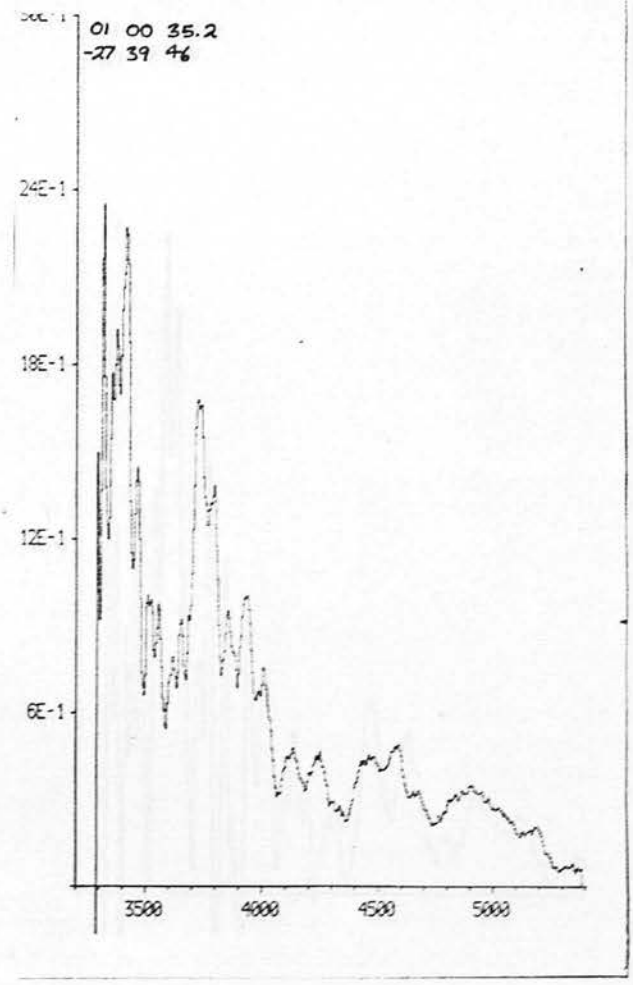
01 00 35.2
-27 39 46
24E-1
18E-1
12E-1
6E-1
3500
4000
4500
5000

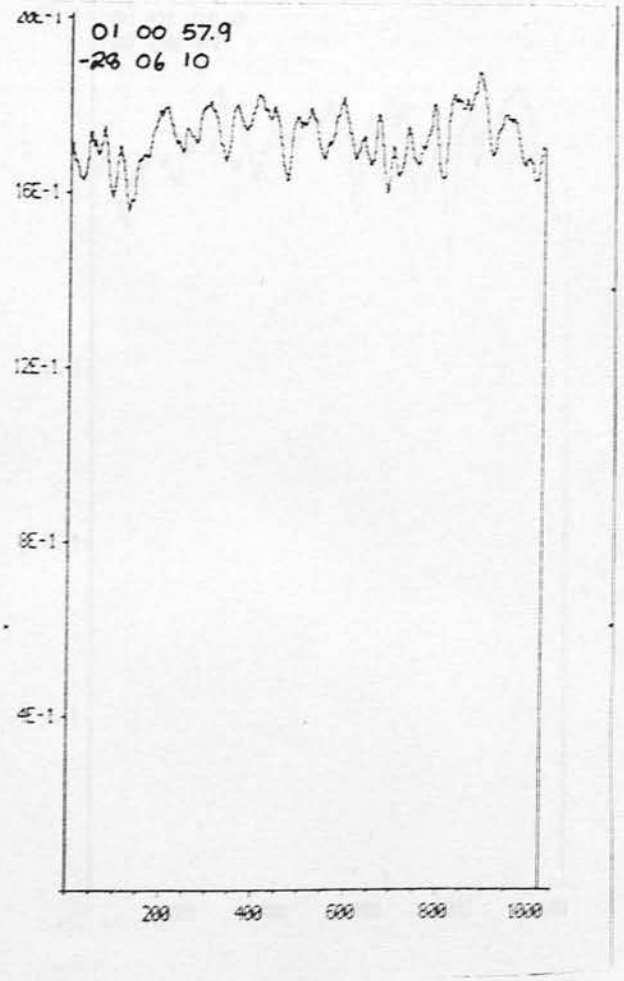
01 00 57.9
-28 06 10
16E-1
12E-1
8E-1
4E-1
200
400
600
800
1000

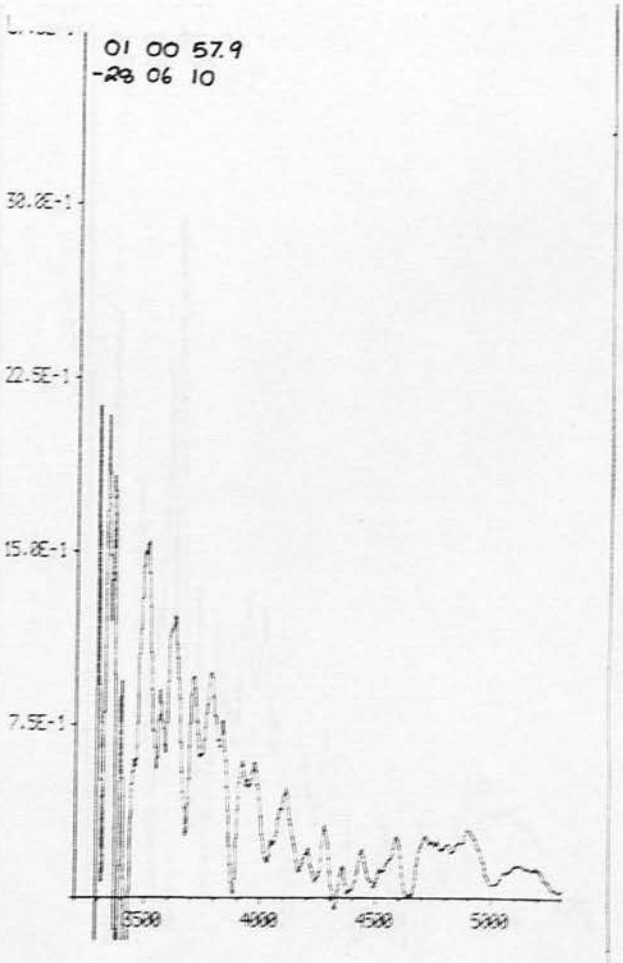
01 00 57.9
-28 06 10
30.0E-1
22.5E-1
15.0E-1
7.5E-1
3500
4000
4500
5000

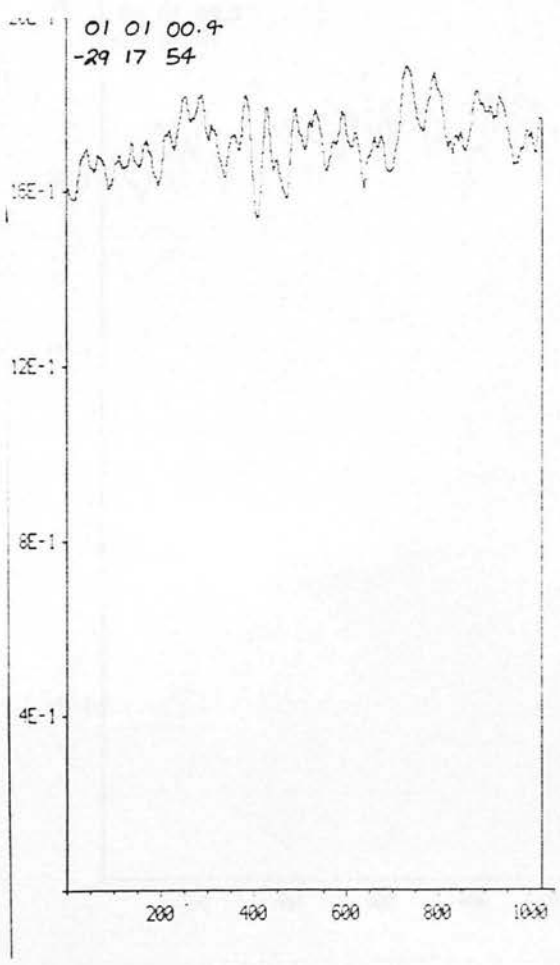
01 01 00.4
-29 17 54
16E-1
12E-1
8E-1
4E-1
200
400
600
800
1000

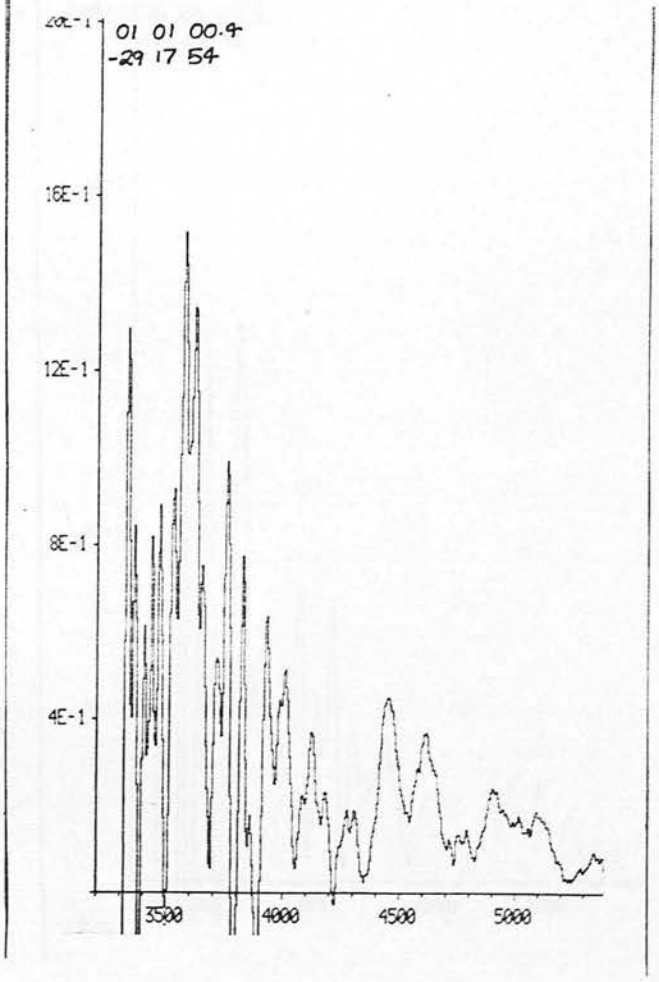
01 01 00.4
-29 17 54
16E-1
12E-1
8E-1
4E-1
3500
4000
4500
5000

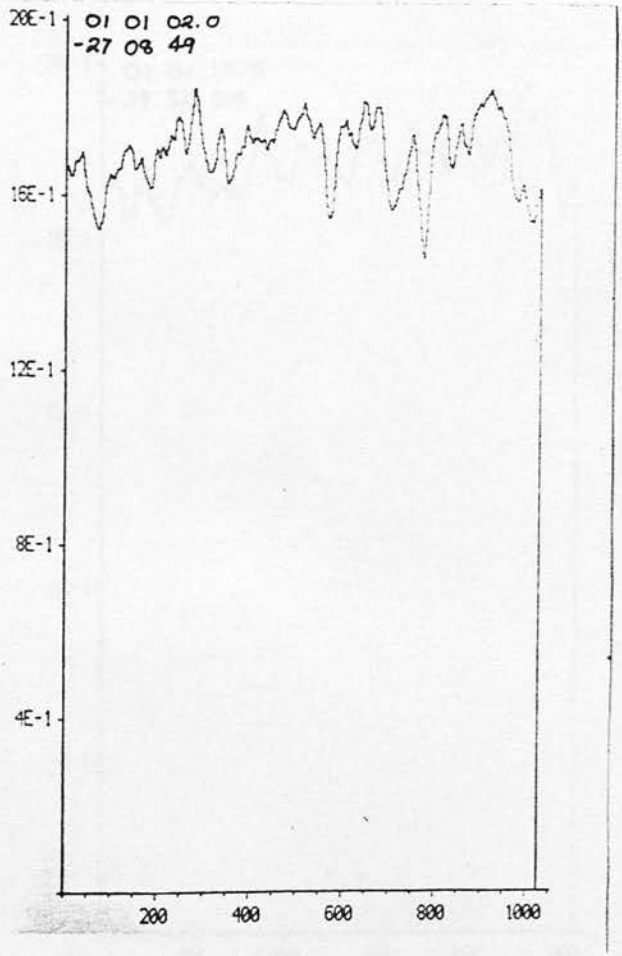
20E-1
01 01 02.0
-27 08 49
16E-1
12E-1
8E-1
4E-1
200
400
600
800
1000

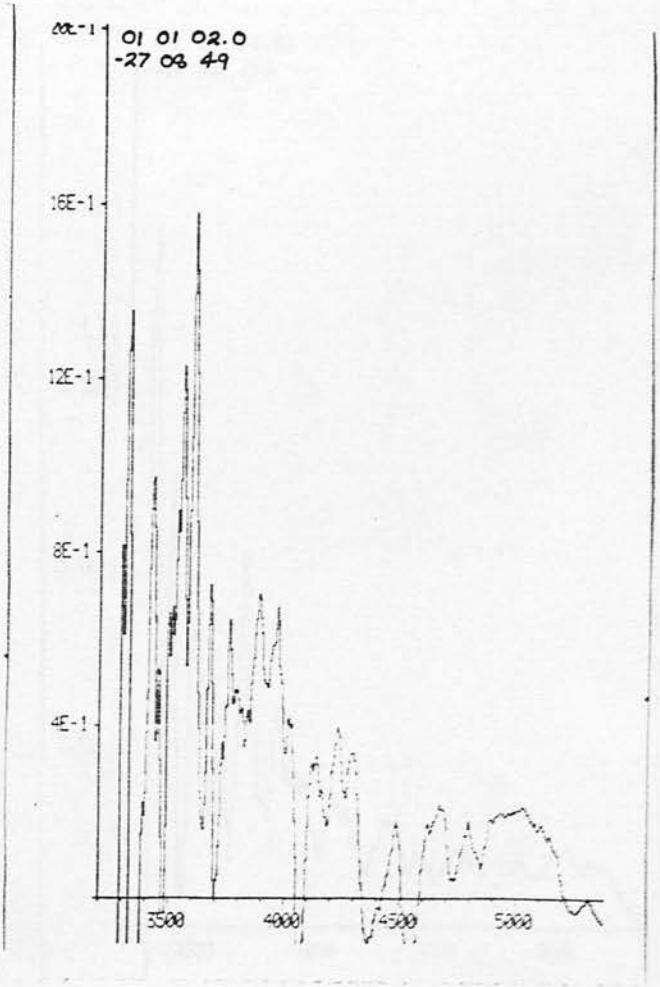
01 01 02.0
-27 08 49
16E-1
12E-1
8E-1
4E-1
3500
4000
4500
5000

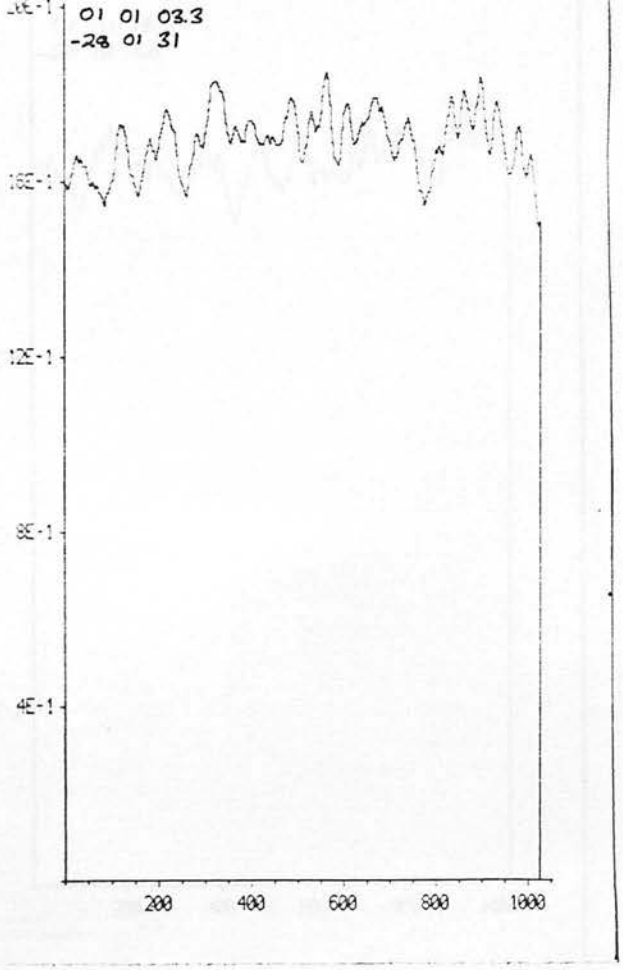
01 01 03.3
-28 01 31
16E-1
12E-1
8E-1
4E-1
200
400
600
800
1000

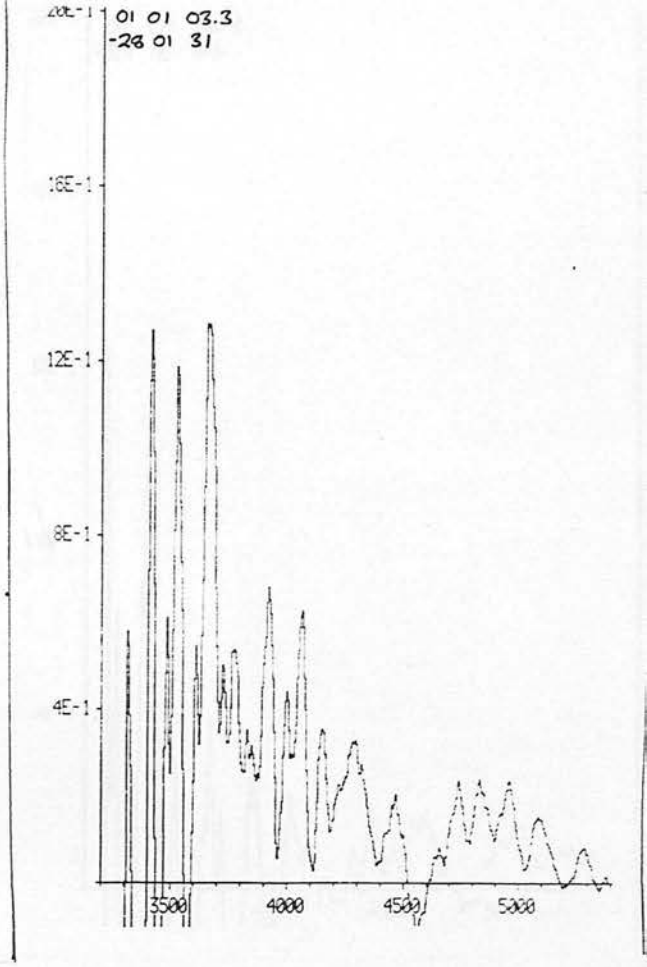
01 01 03.3
-28 01 31
16E-1
12E-1
8E-1
4E-1
3500
4000
4500
5000

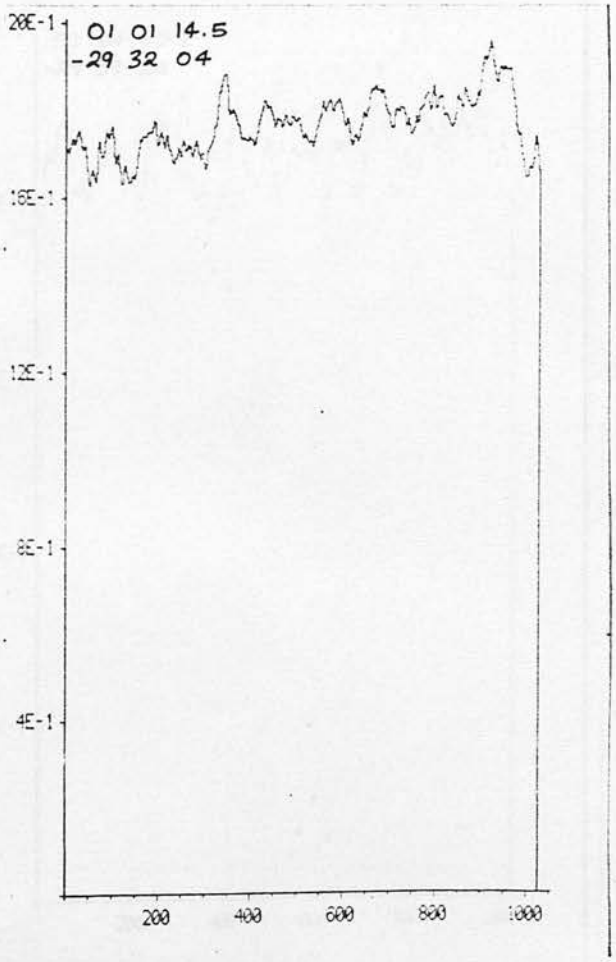
01 01 14.5
-29 32 04
20E-1
16E-1
12E-1
8E-1
4E-1
200
400
600
800
1000

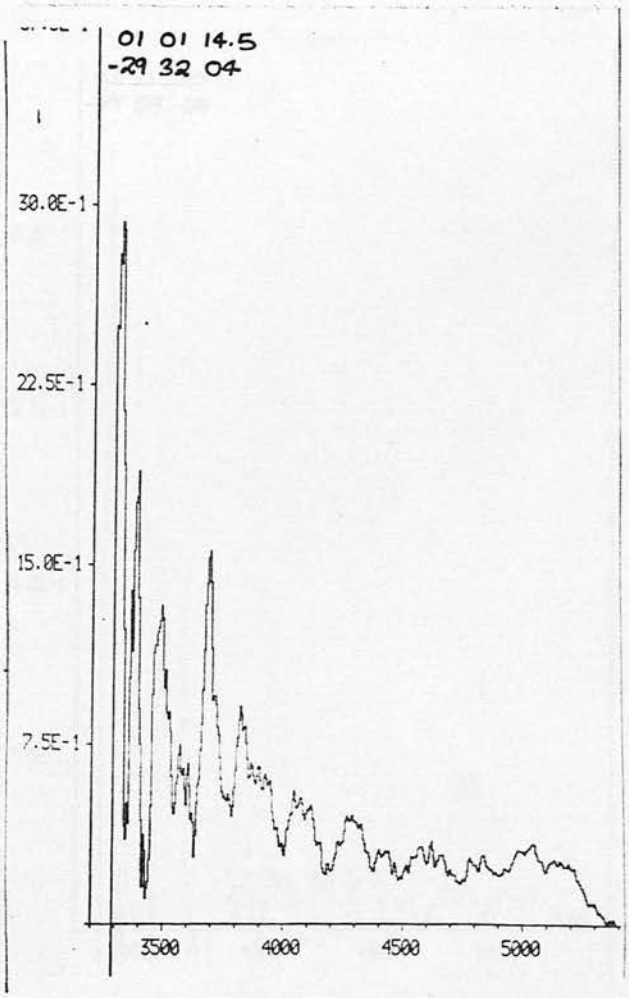
01 01 14.5
-29 32 04
30.0E-1
22.5E-1
15.0E-1
7.5E-1
3500
4000
4500
5000

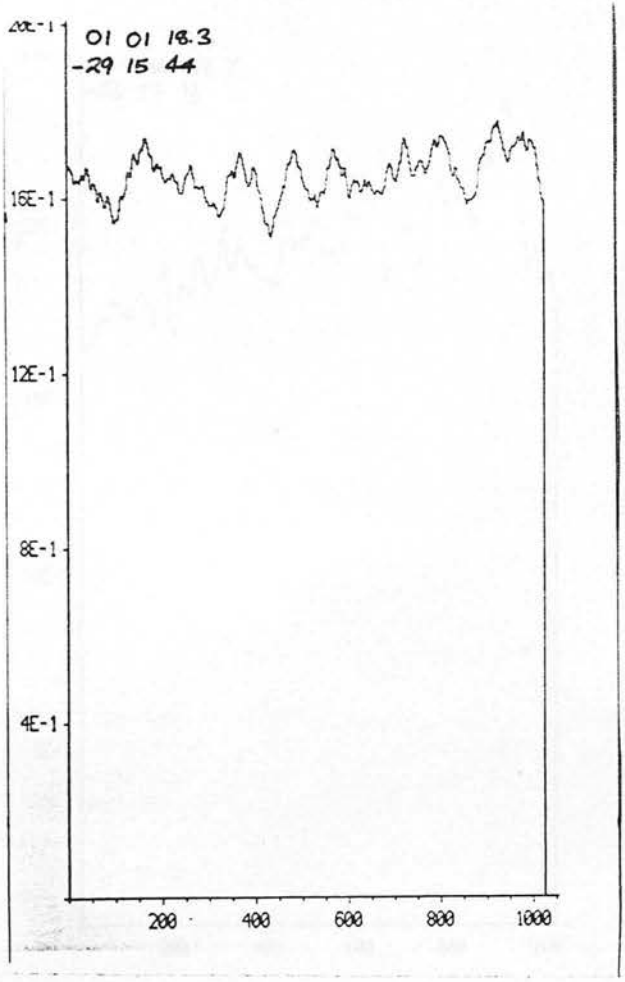
01 01 18.3
-29 15 44
16E-1
12E-1
8E-1
4E-1
200
400
600
800
1000

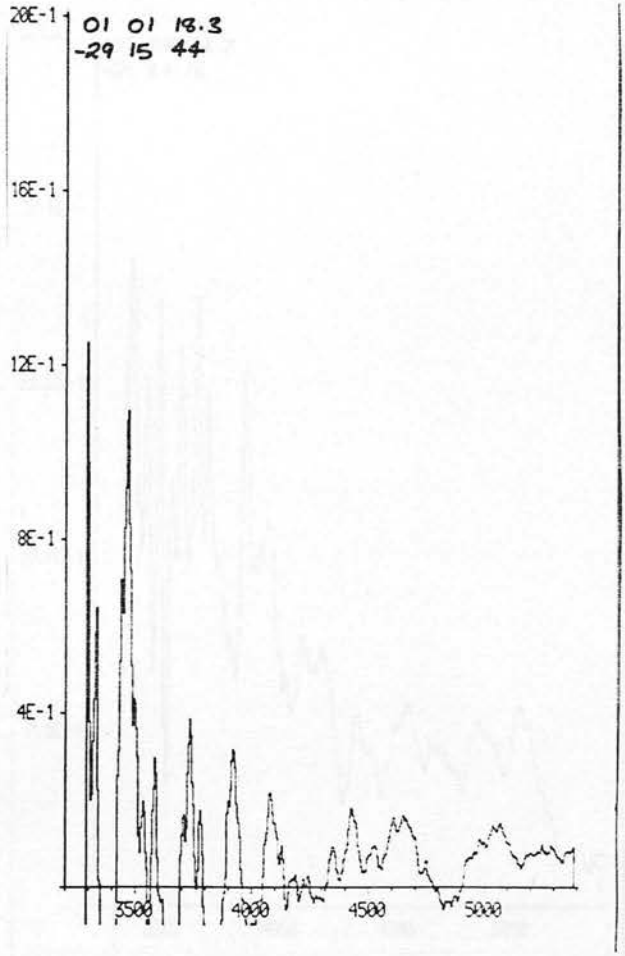
01 01 18.3
-29 15 44
16E-1
12E-1
8E-1
4E-1
3500
4000
4500
5000

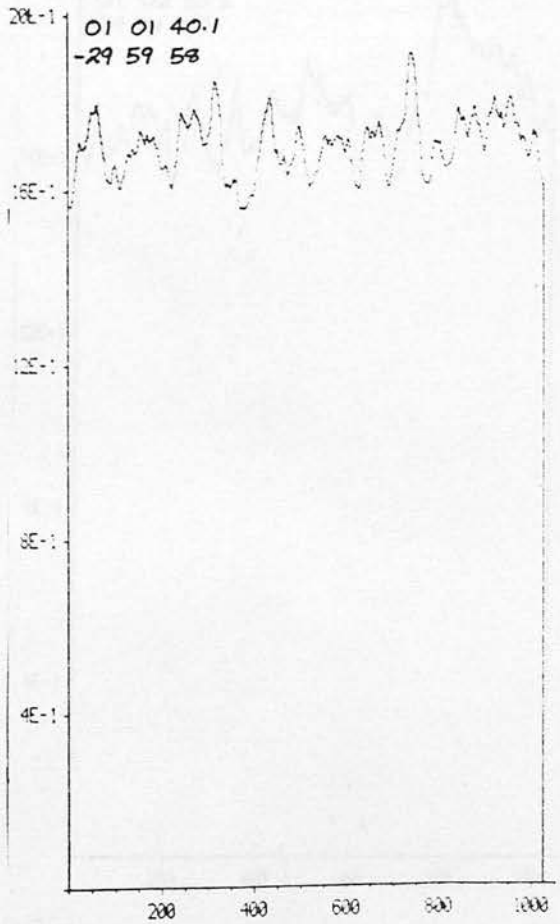
01 01 40.1
-29 59 58
8E-1
4E-1
200
400
600
800
1000

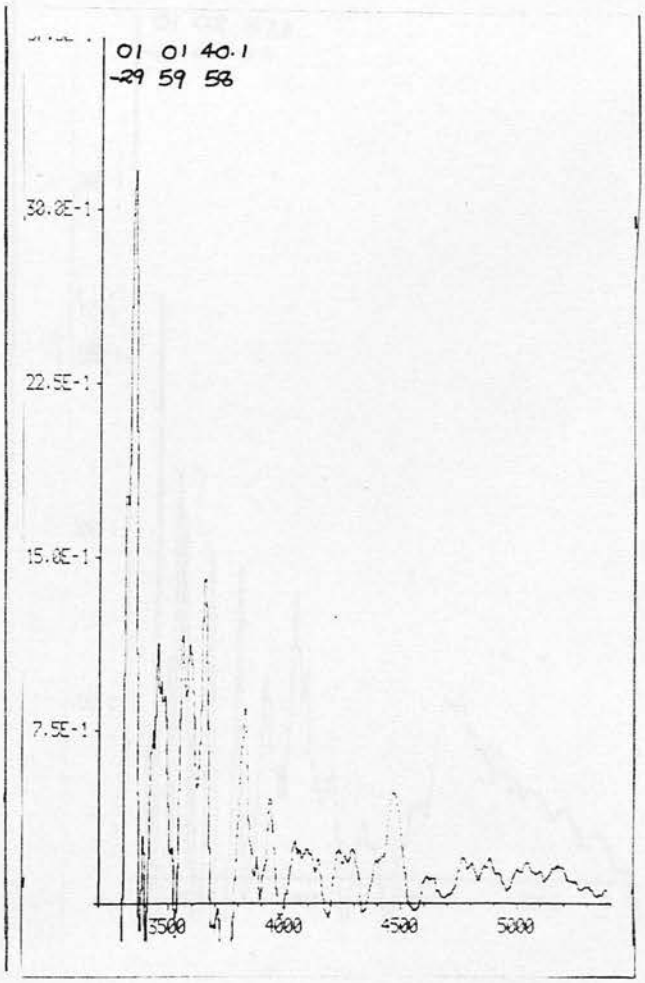
01 01 40.1
-29 59 58
22.5E-1
15.0E-1
7.5E-1
3500
4000
4500
5000

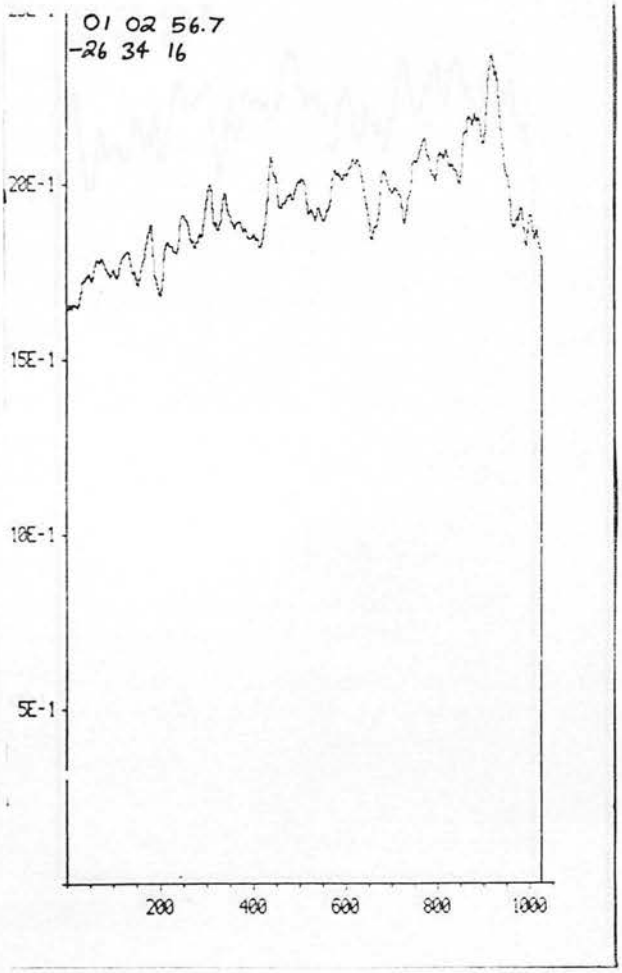
01 02 56.7
-26 34 16
20E-1
15E-1
10E-1
5E-1
200
400
600
800
1000

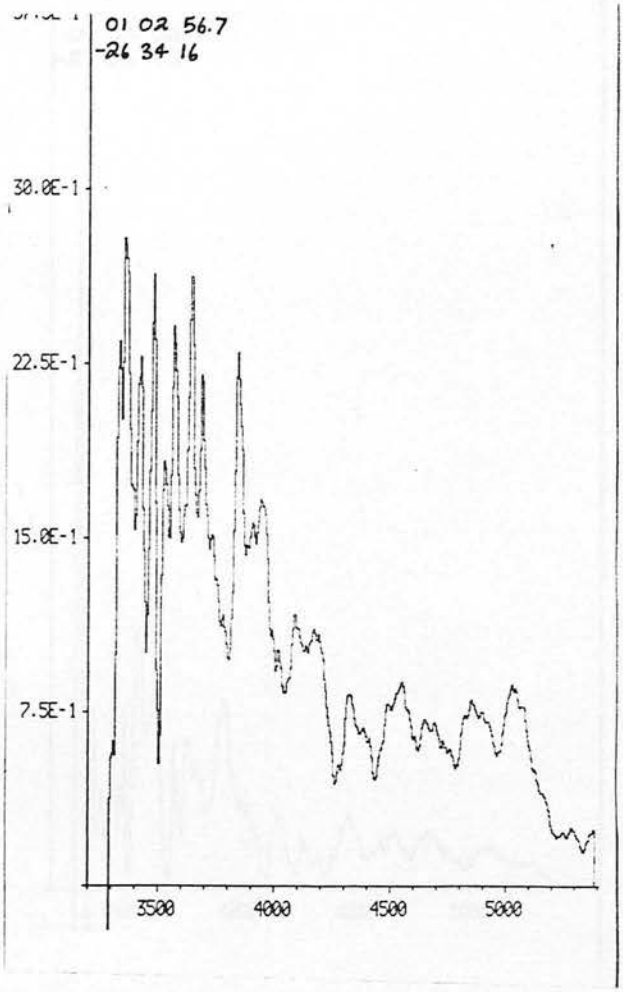
01 02 56.7
-26 34 16
30.0E-1
22.5E-1
15.0E-1
7.5E-1
3500
4000
4500
5000

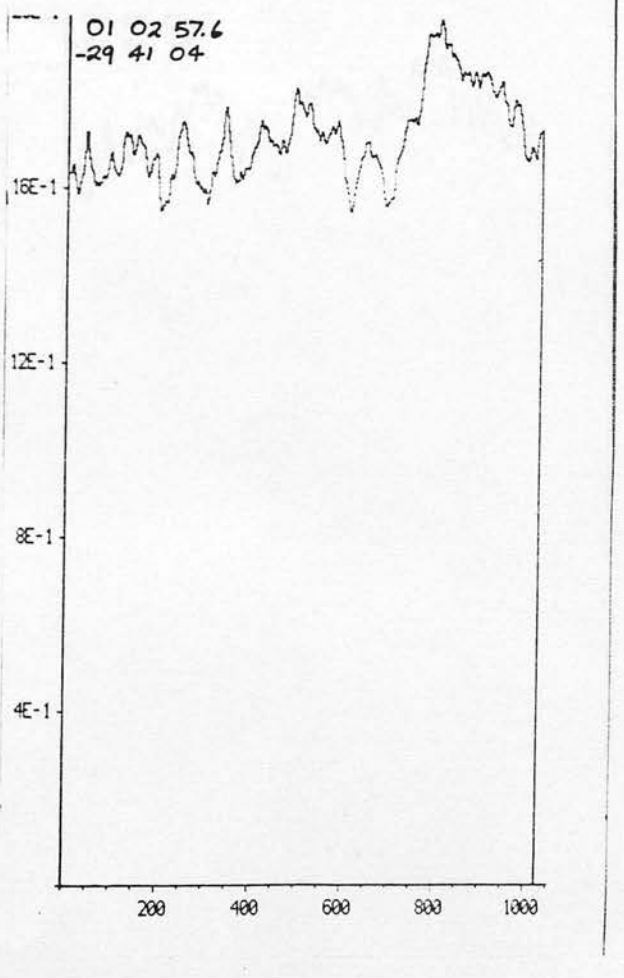
01 02 57.6
-29 41 04
16E-1
12E-1
8E-1
4E-1
200
400
600
800
1000

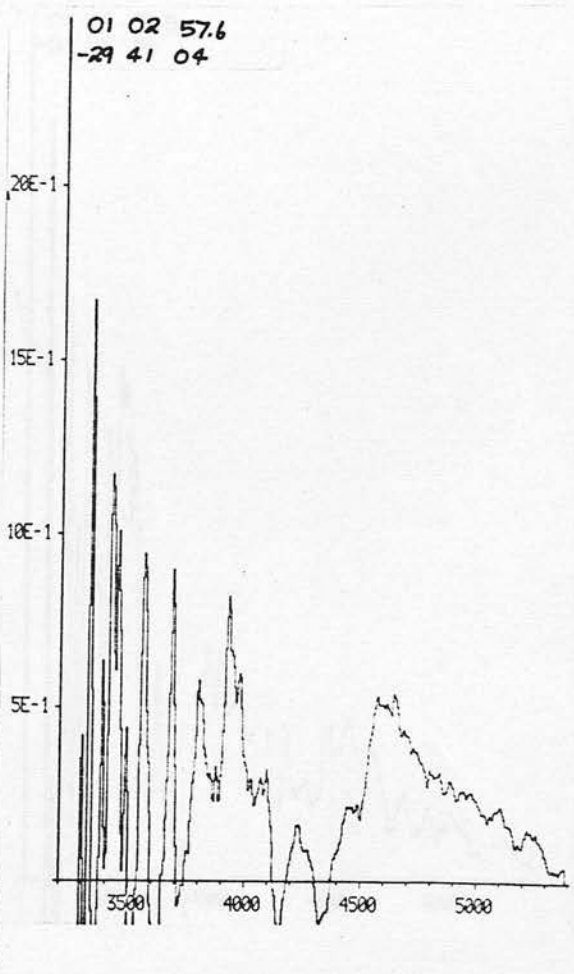
01 02 57.6
-29 41 04
20E-1
15E-1
10E-1
5E-1
3500
4000
4500
5000

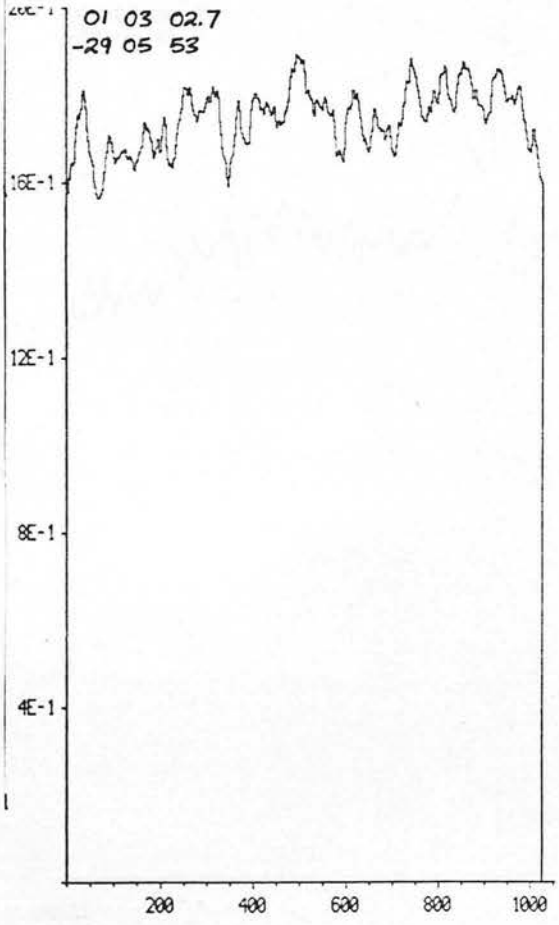
01 03 02.7
-29 05 53
16E-1
12E-1
8E-1
4E-1
200
400
600
800
1000

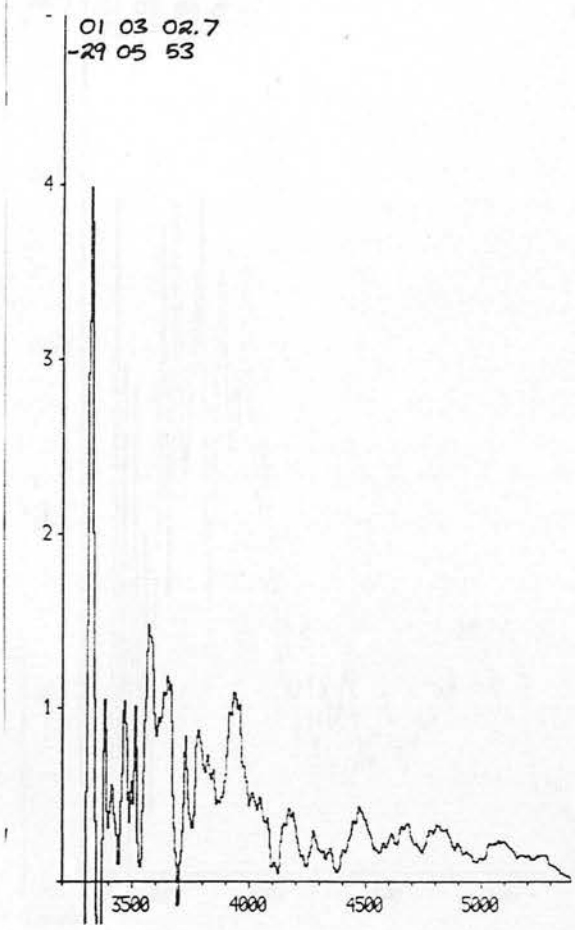
01 03 02.7
-29 05 53
4
3
2
1
3500
4000
4500
5000

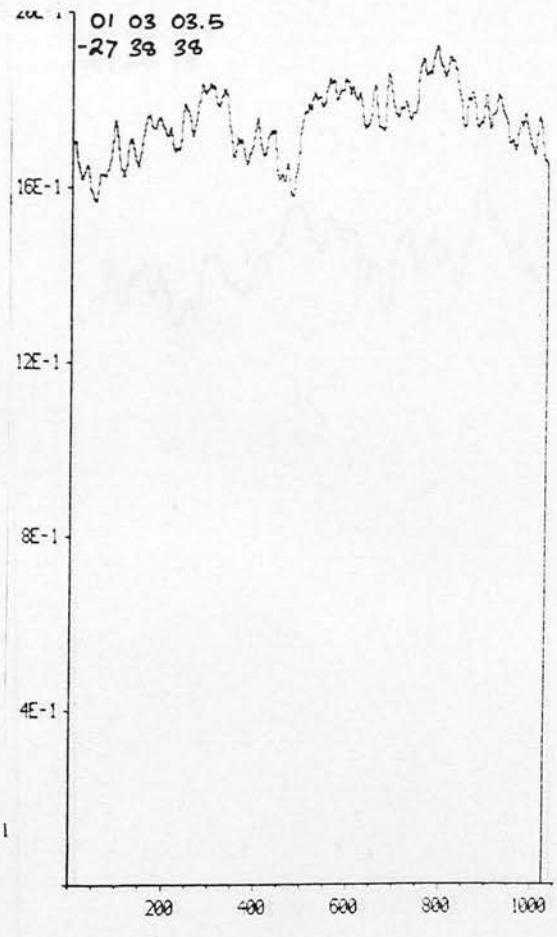
01 03 03.5
-27 38 38
16E-1
12E-1
8E-1
4E-1
200
400
600
800
1000

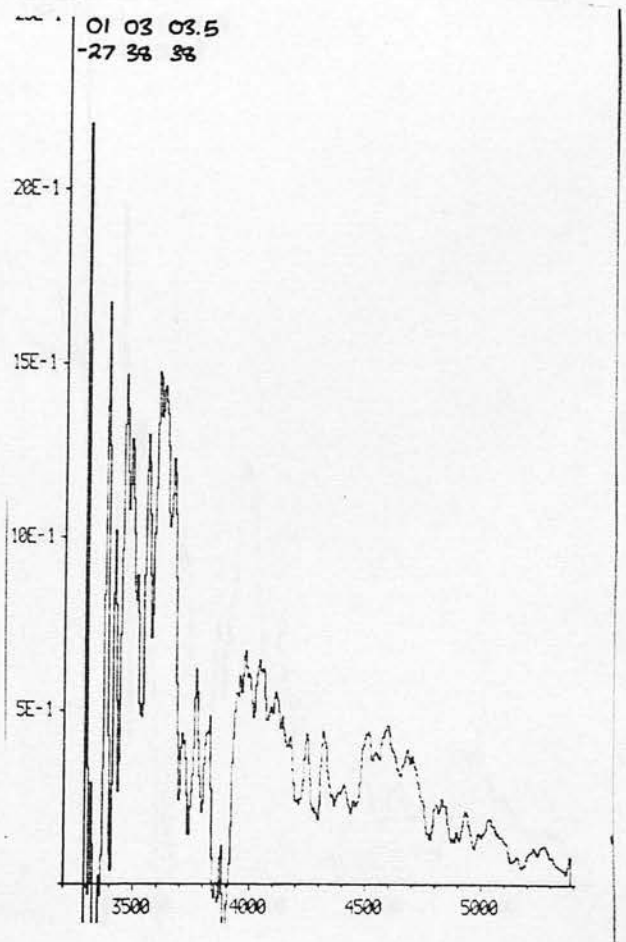
01 03 03.5
-27 38 38
20E-1
15E-1
10E-1
5E-1
3500
4000
4500
5000

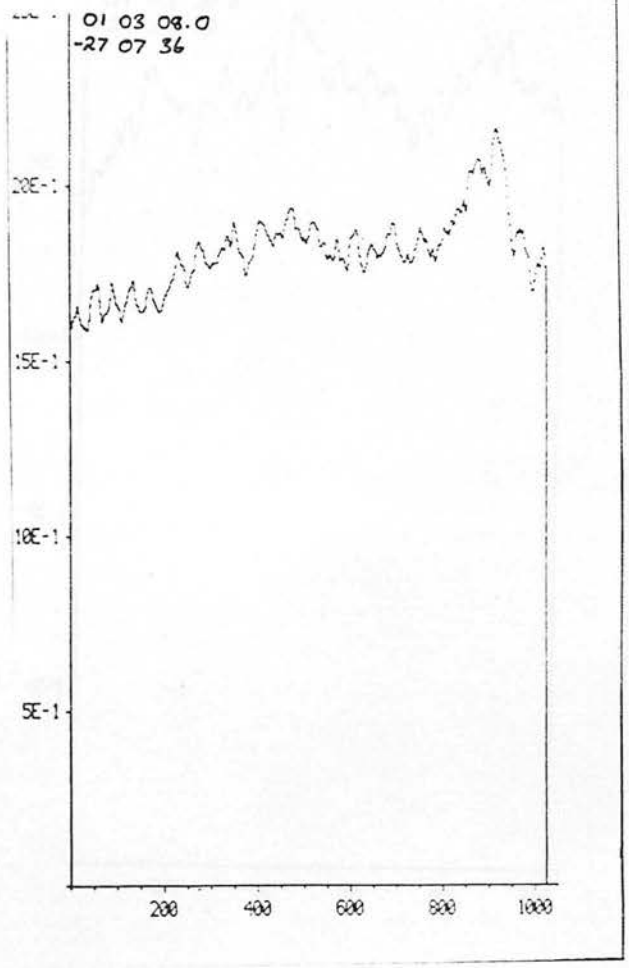
01 03 08.0
-27 07 36
20E-1
15E-1
10E-1
5E-1
200
400
600
800
1000

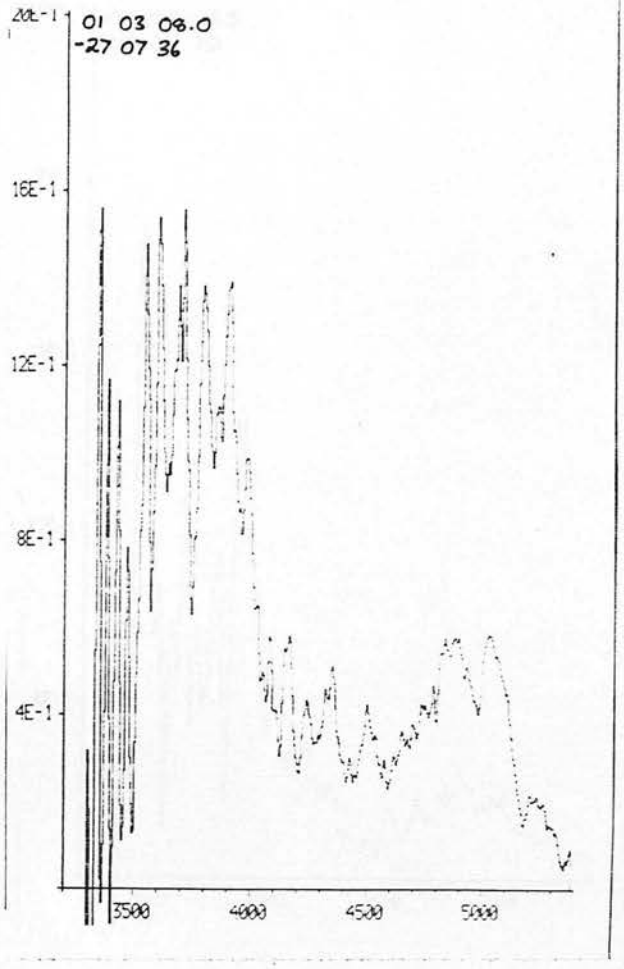
01 03 08.0
-27 07 36
20E-1
16E-1
12E-1
8E-1
4E-1
3500
4000
4500
5000

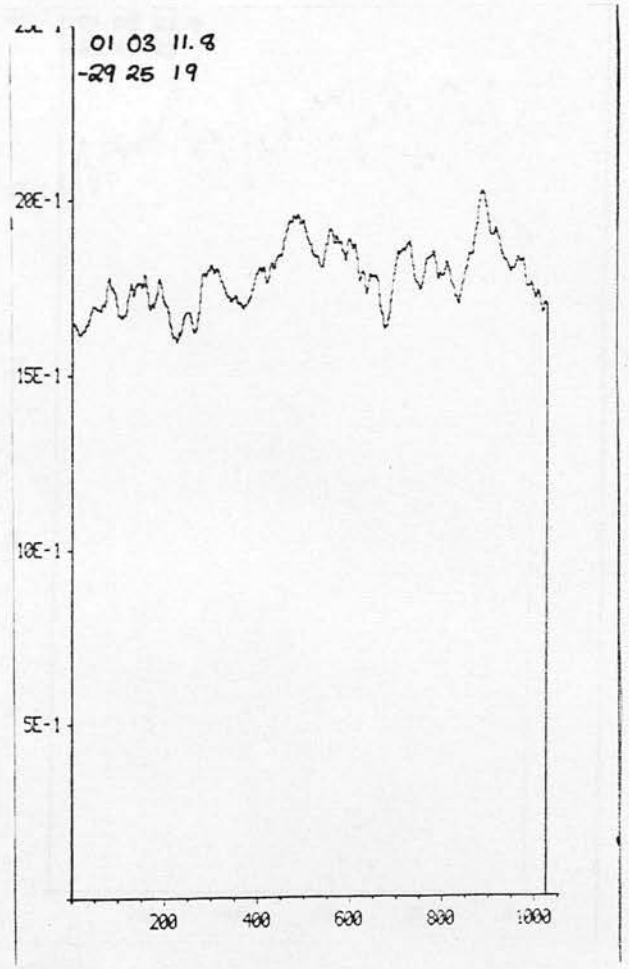
01 03 11.8
-29 25 19
20E-1
15E-1
10E-1
5E-1
200
400
600
800
1000

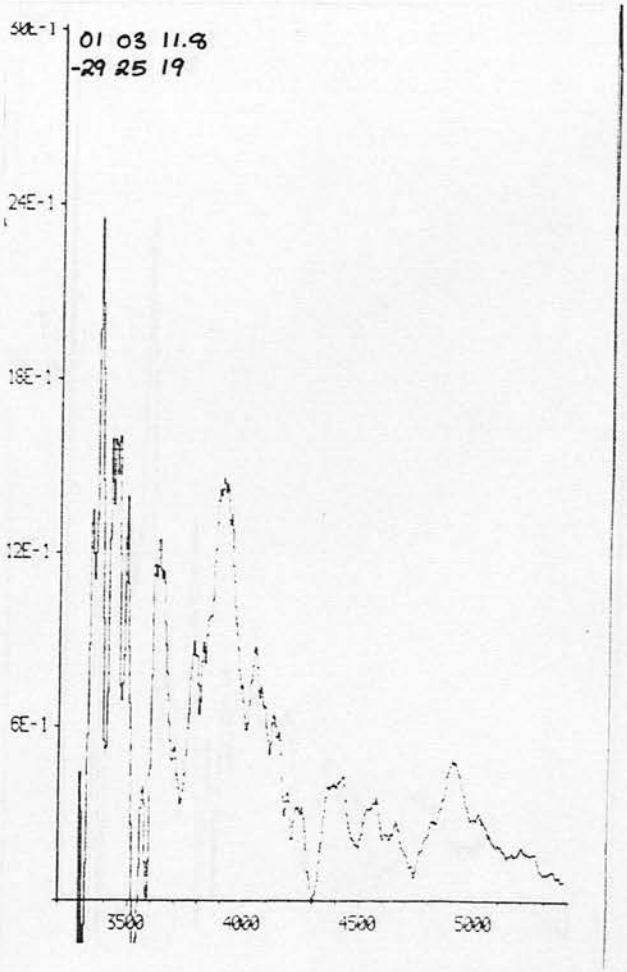
01 03 11.8
-29 25 19
30E-1
24E-1
18E-1
12E-1
6E-1
3500
4000
4500
5000

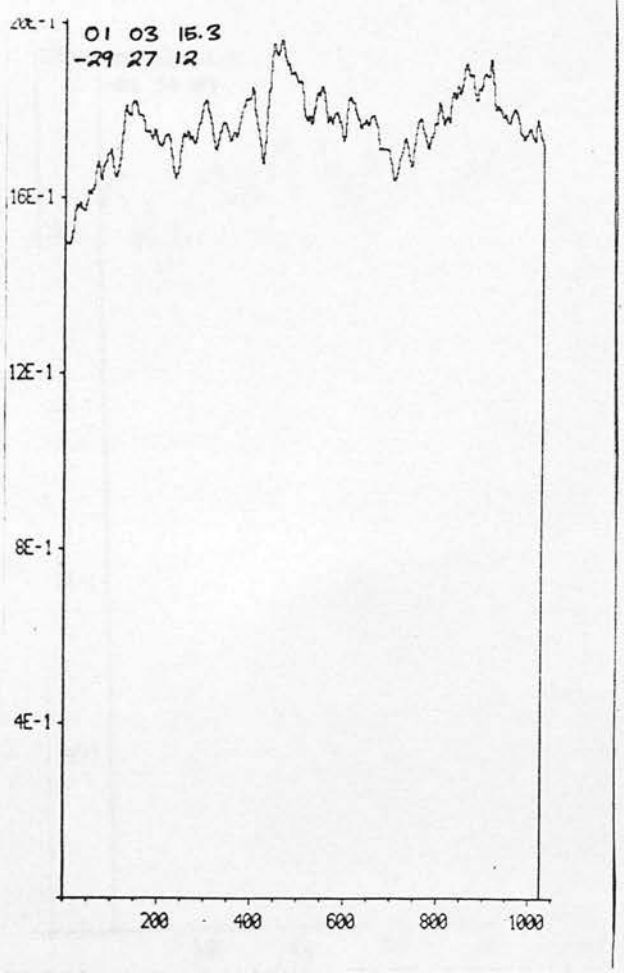
01 03 15.3
-29 27 12
16E-1
12E-1
8E-1
4E-1
200
400
600
800
1000

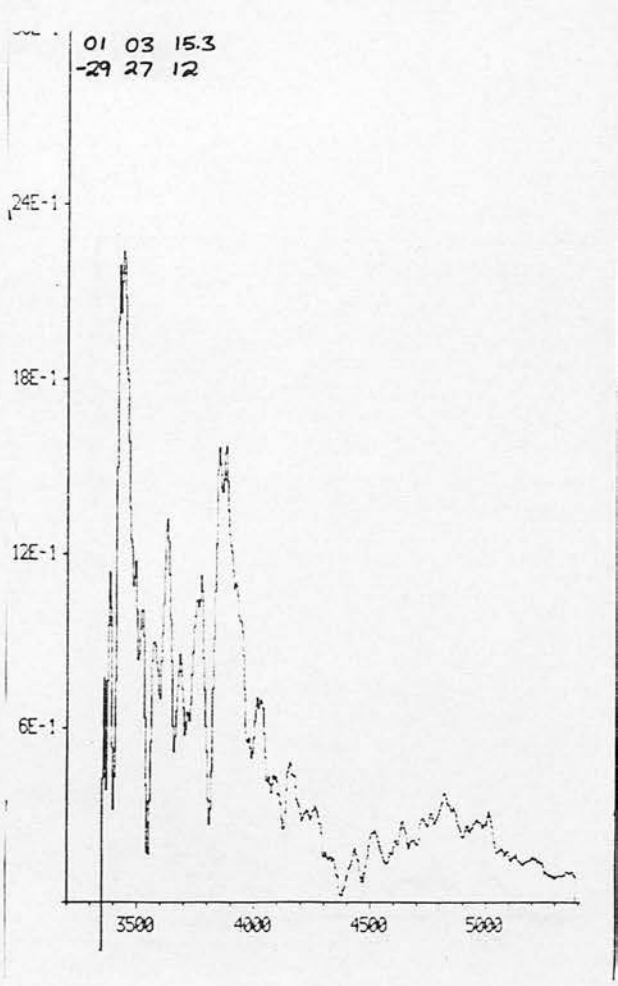
01 03 15.3
-29 27 12
24E-1
18E-1
12E-1
6E-1
3500
4000
4500
5000

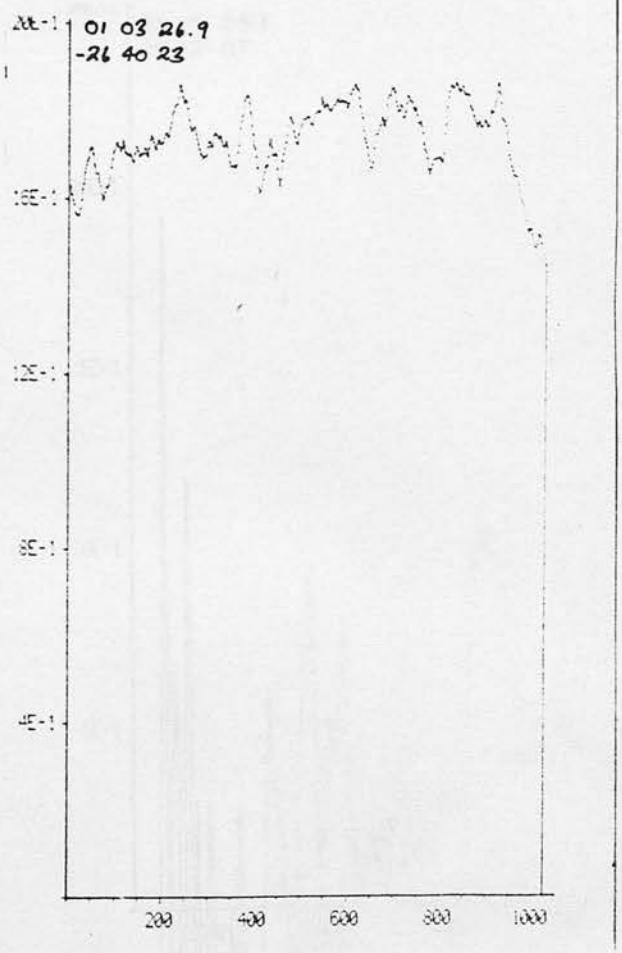
01 03 26.9
-26 40 23
16E-1
12E-1
8E-1
4E-1
200
400
600
800
1000

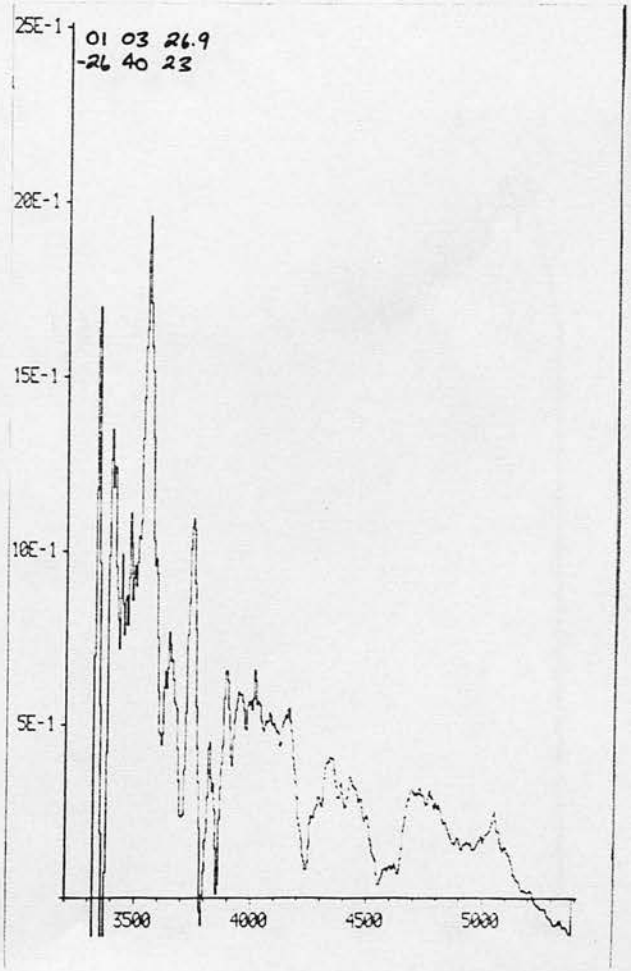
01 03 26.9
-26 40 23
25E-1
20E-1
15E-1
10E-1
5E-1
3500
4000
4500
5000

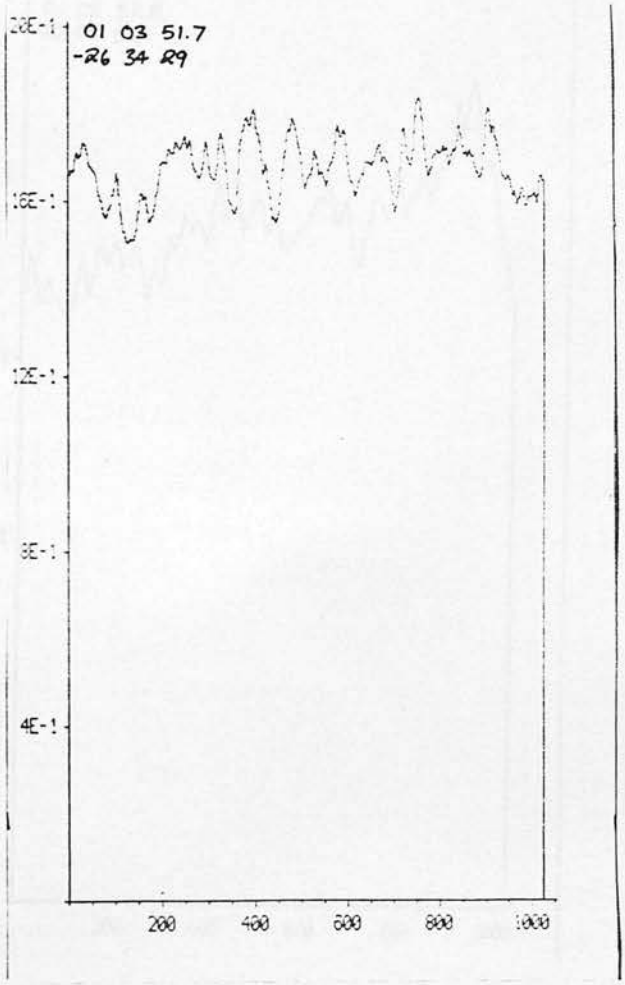
01 03 51.7
-26 34 29
2E-1
1E-1
8E-1
4E-1
200
400
600
800
1000

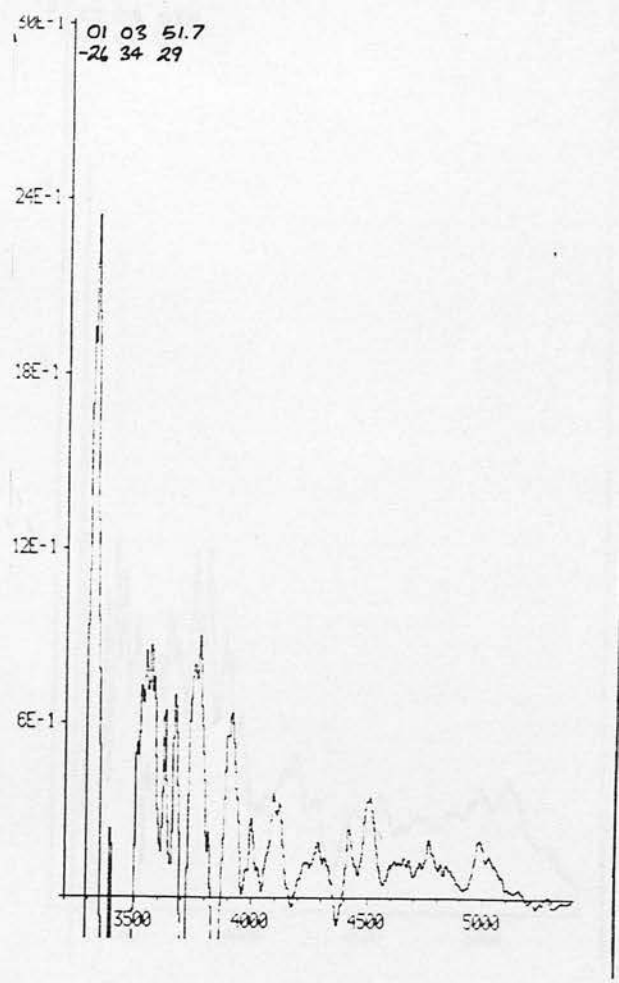
01 03 51.7
-26 34 29
3E-1
2E-1
1E-1
6E-1
3500
4000
4500
5000

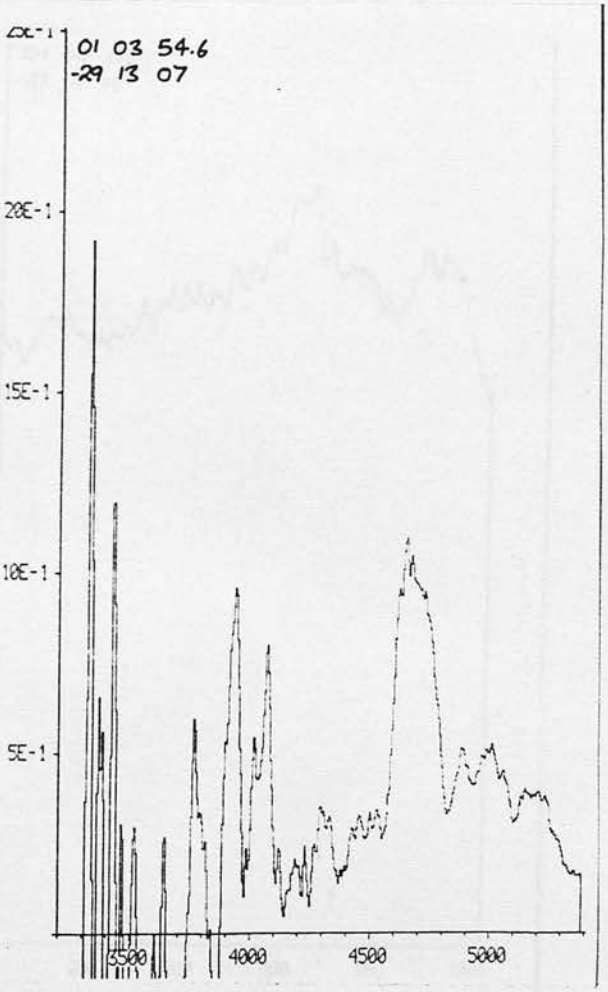
01 03 54.6
-29 13 07
2E-1
1E-1
5E-1
3500
4000
4500
5000

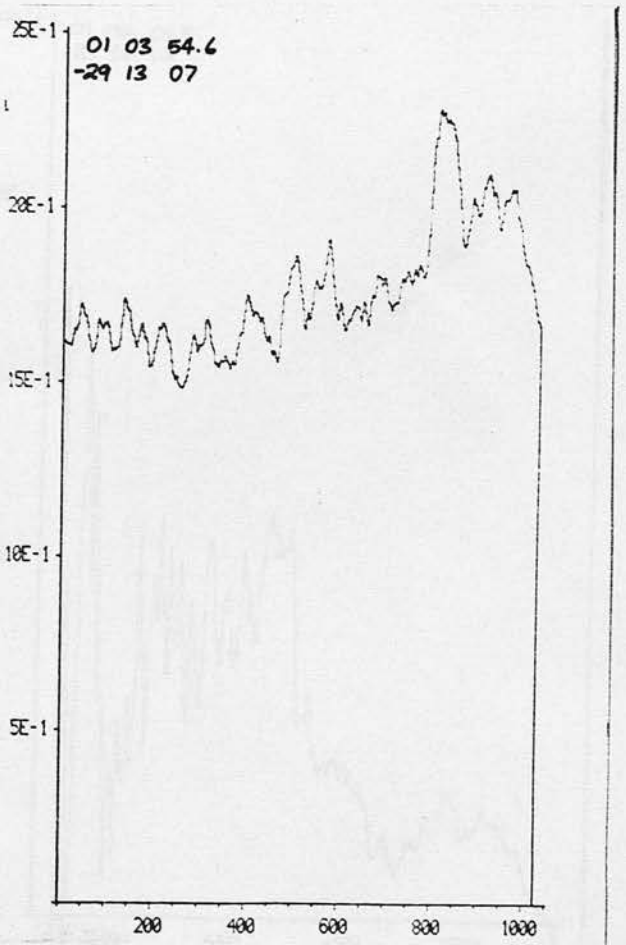
01 03 54.6
-29 13 07
2E-1
1E-1
5E-1
200
400
600
800
1000

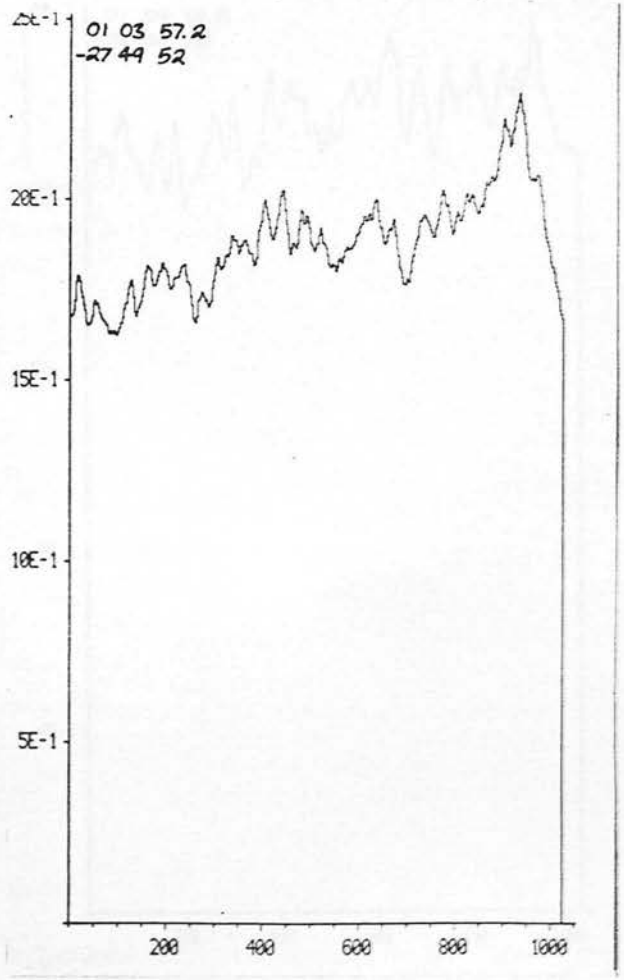
01 03 57.2
-27 49 52
20E-1
15E-1
10E-1
5E-1
200
400
600
800
1000


01 03 57.2
-27 49 52
4
3
2
1
3500
4000
4500
5000

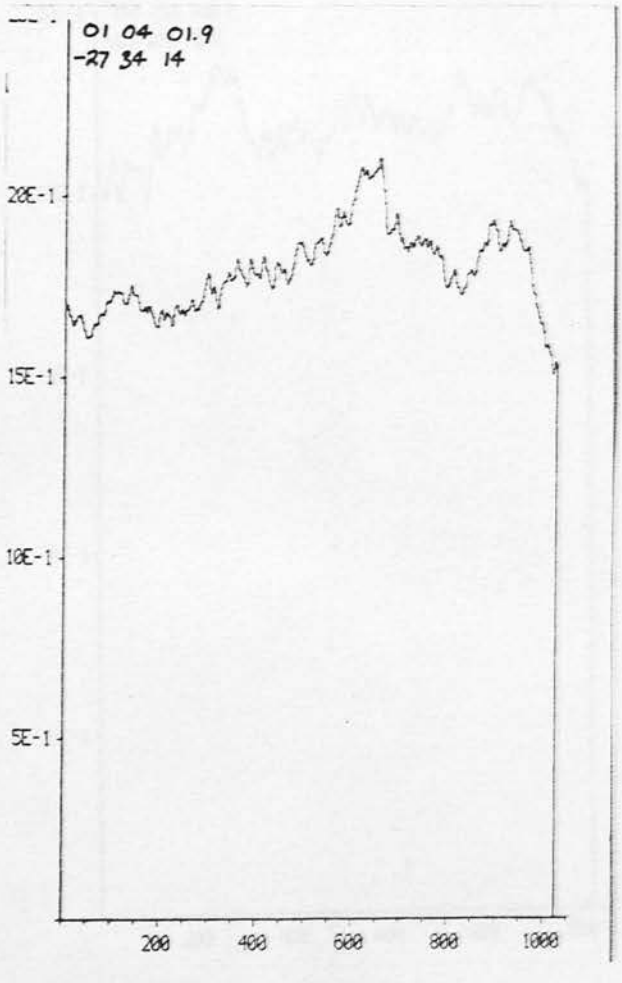
01 04 01.9
-27 34 14
20E-1
15E-1
10E-1
5E-1
200
400
600
800
1000

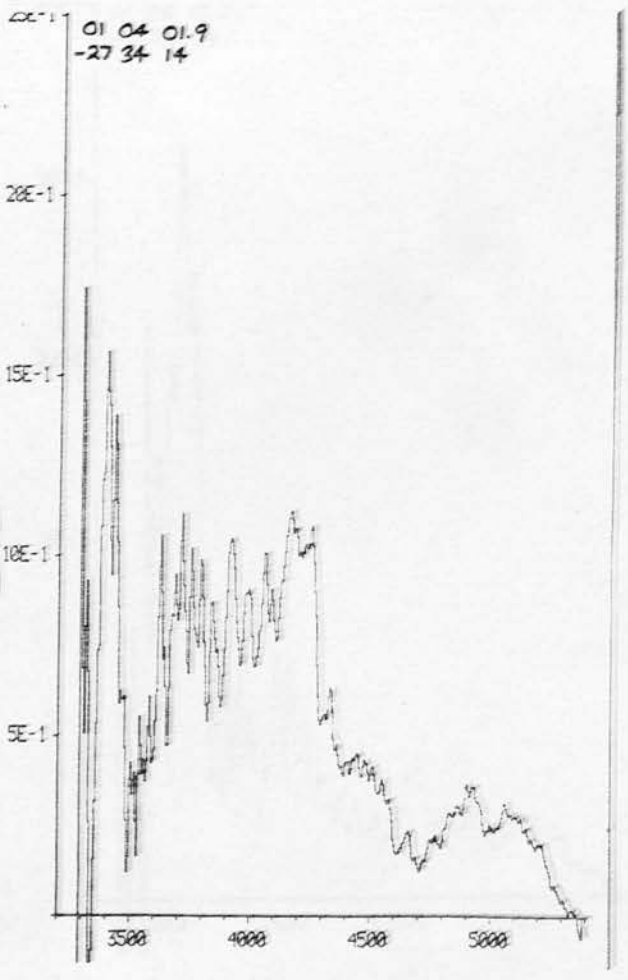
01 04 01.9
-27 34 14
20E-1
15E-1
10E-1
5E-1
3500
4000
4500
5000

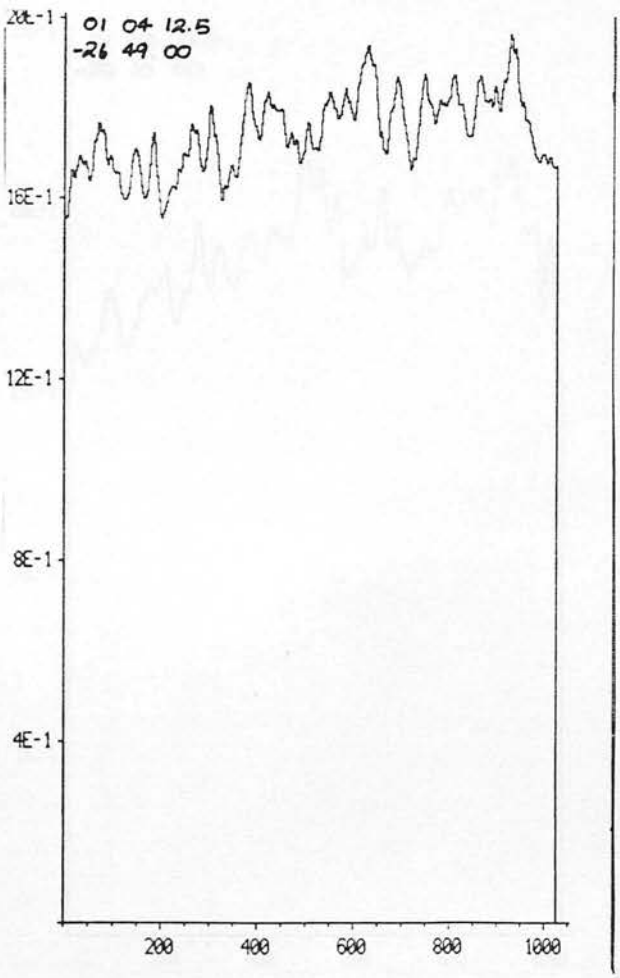
01 04 12.5
-26 49 00
16E-1
12E-1
8E-1
4E-1
200
400
600
800
1000

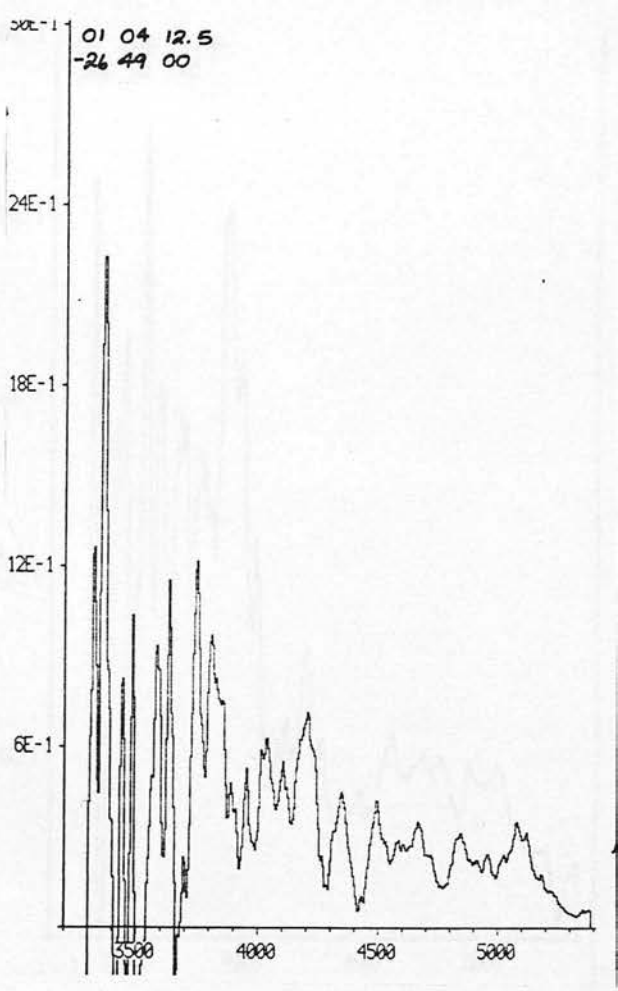
01 04 12.5
-26 49 00
24E-1
18E-1
12E-1
6E-1
3500
4000
4500
5000

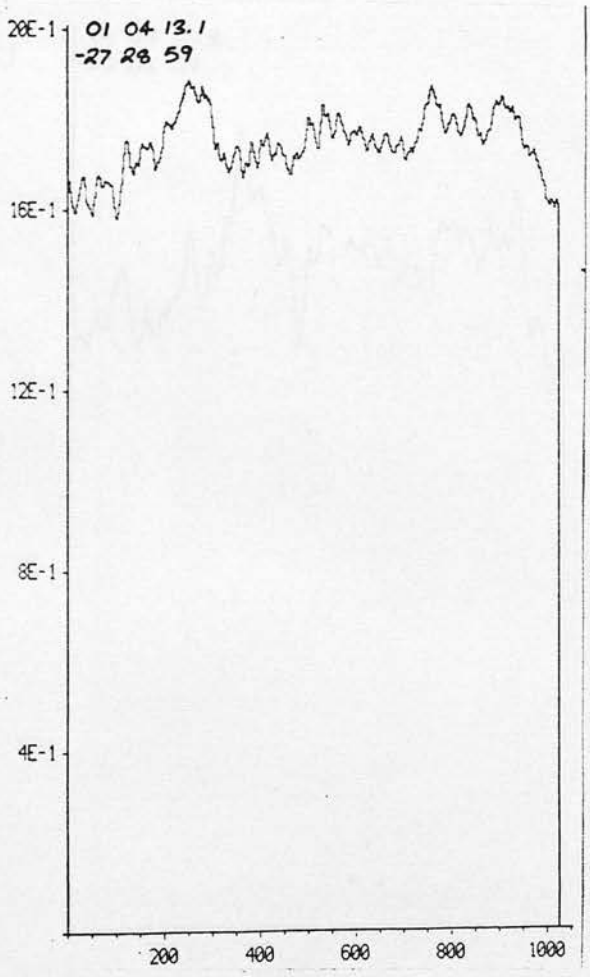
01 04 13.1
-27 28 59
16E-1
12E-1
8E-1
4E-1
200
400
600
800
1000

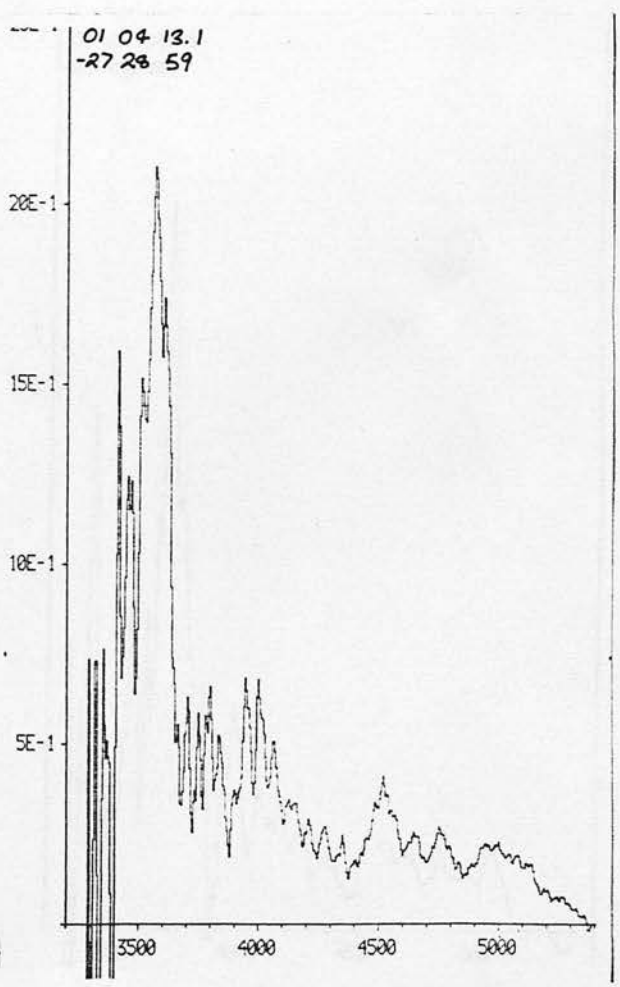
01 04 13.1
-27 28 59
20E-1
15E-1
10E-1
5E-1
3500
4000
4500
5000

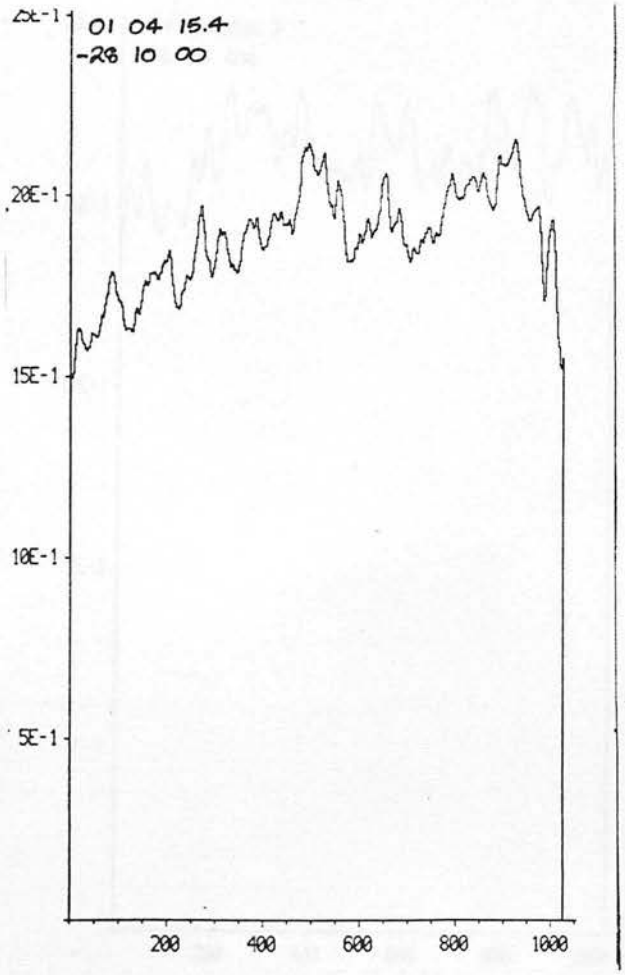
01 04 15.4
-28 10 00
25E-1
20E-1
15E-1
10E-1
5E-1
200
400
600
800
1000

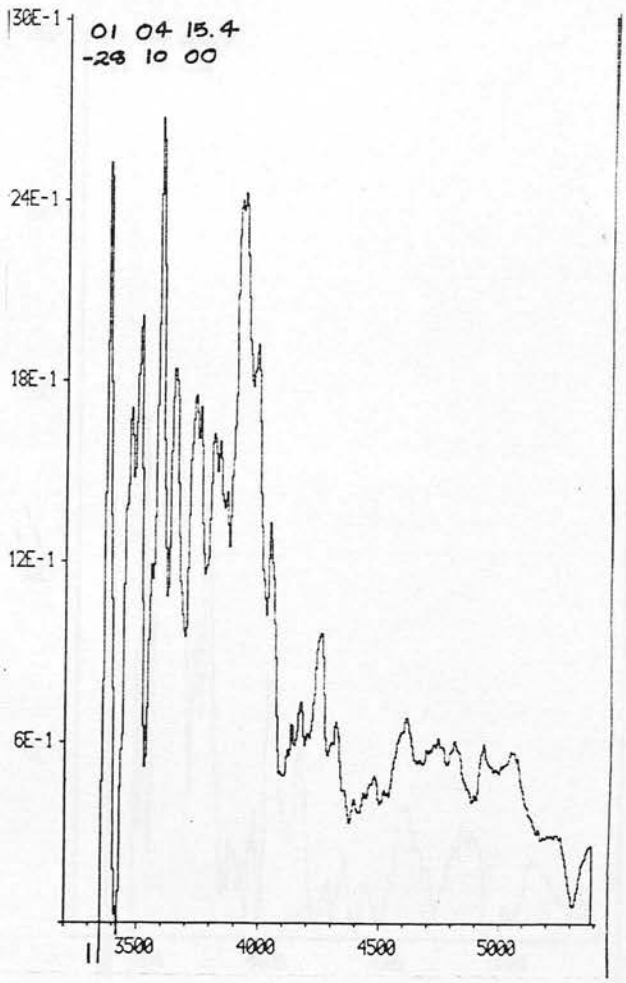
01 04 15.4
-28 10 00
30E-1
24E-1
18E-1
12E-1
6E-1
3500
4000
4500
5000

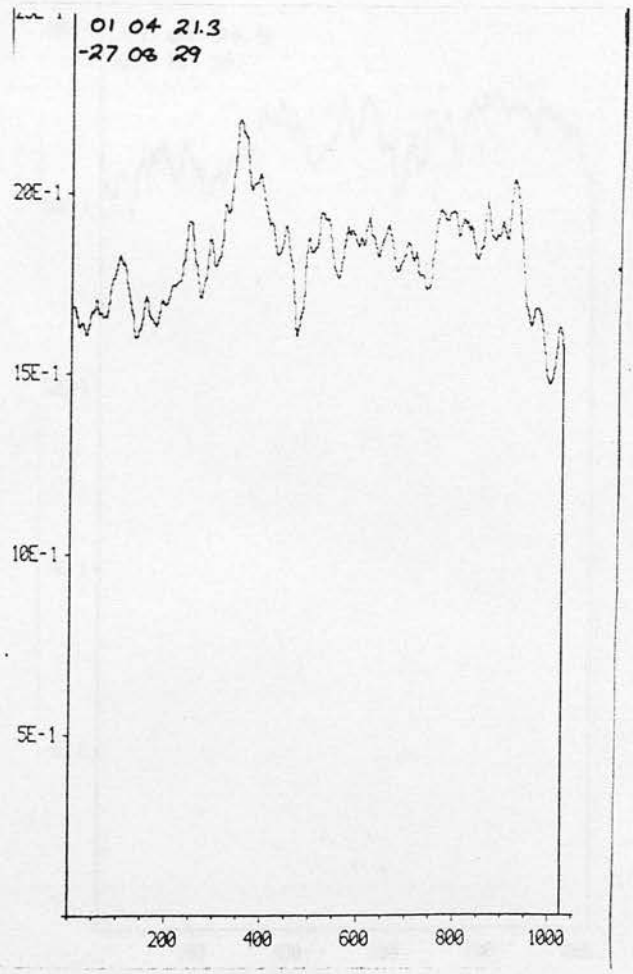
01 04 21.3
-27 08 29
20E-1
15E-1
10E-1
5E-1
200
400
600
800
1000

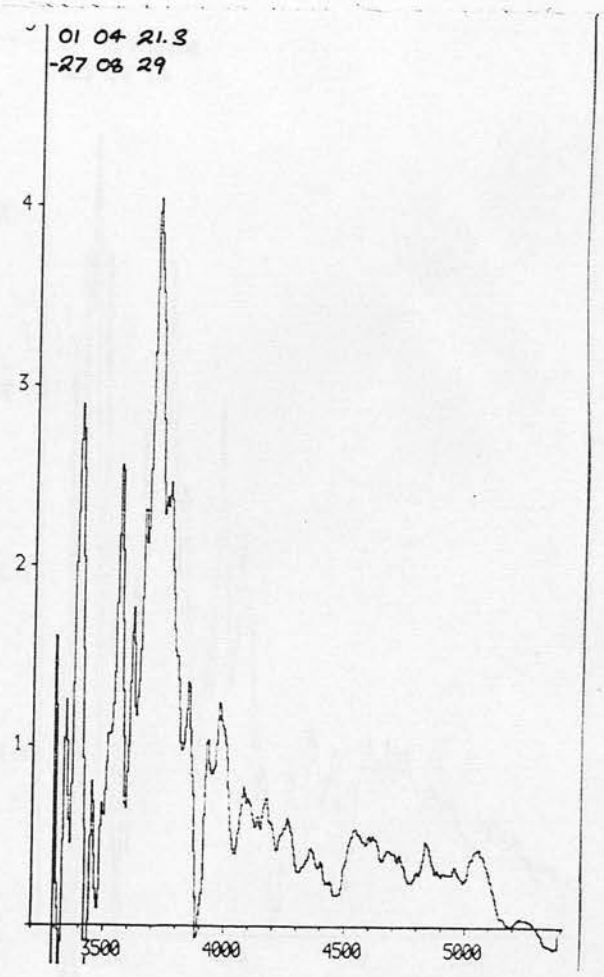
01 04 21.3
-27 08 29
4
3
2
1
3500
4000
4500
5000

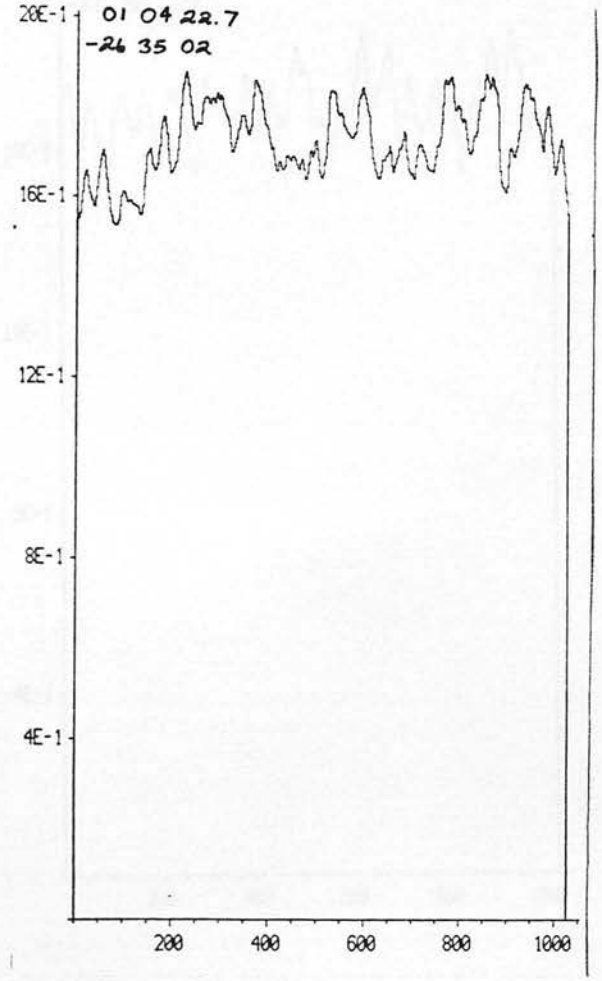
01 04 22.7
-26 35 02
20E-1
16E-1
12E-1
8E-1
4E-1
200
400
600
800
1000

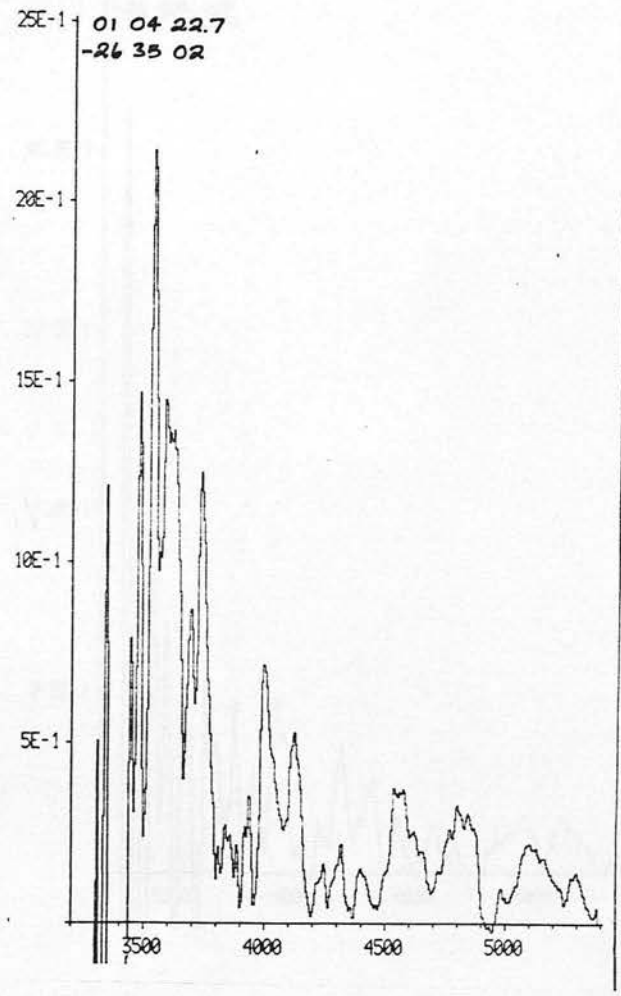
01 04 22.7
-26 35 02
25E-1
20E-1
15E-1
10E-1
5E-1
3500
4000
4500
5000

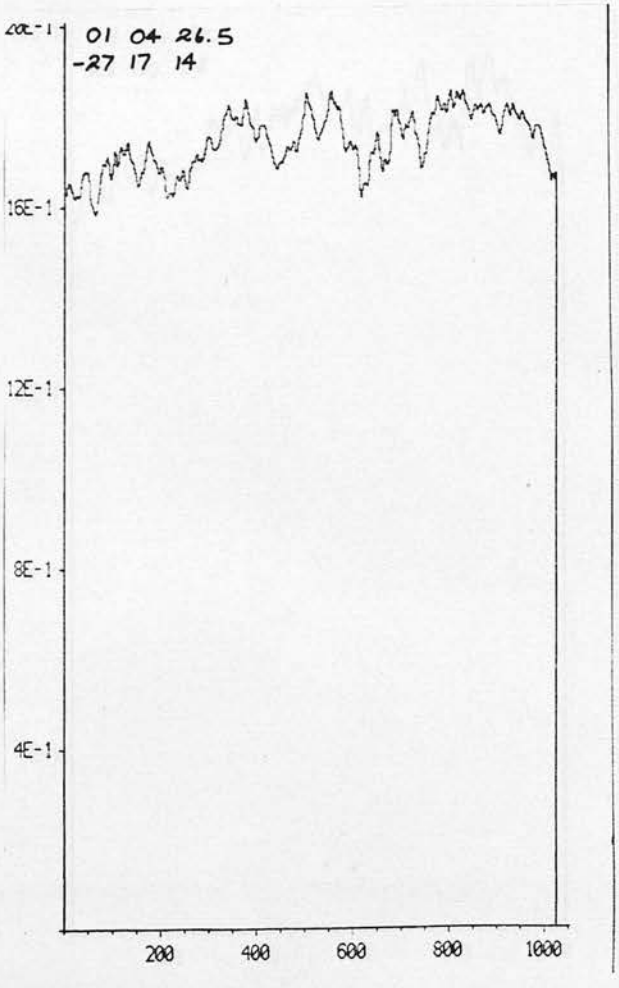
01 04 26.5
-27 17 14
16E-1
12E-1
8E-1
4E-1
200
400
600
800
1000

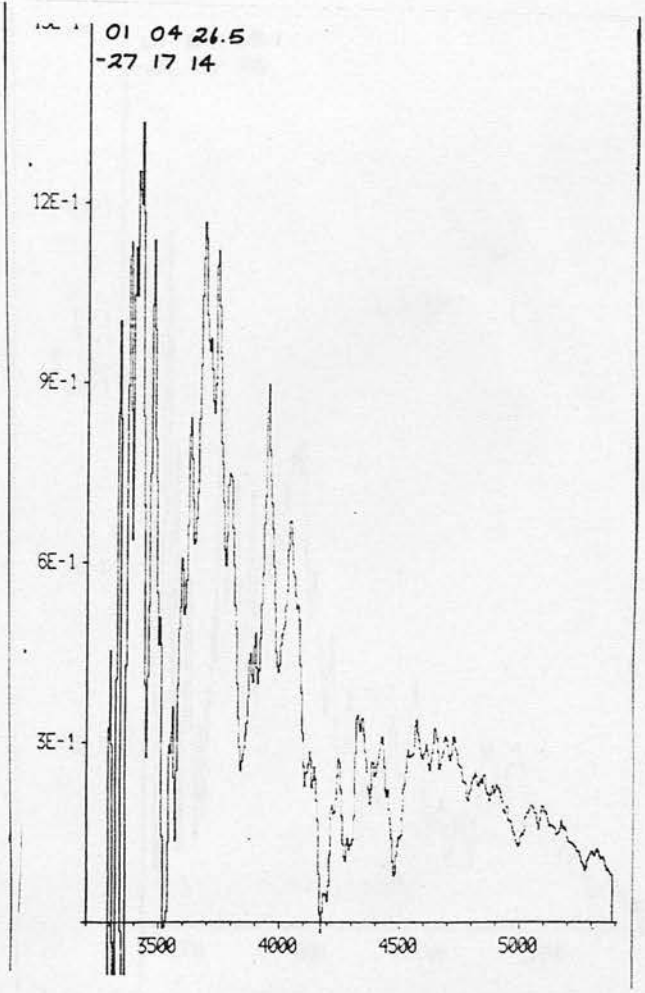
01 04 26.5
-27 17 14
12E-1
9E-1
6E-1
3E-1
3500
4000
4500
5000

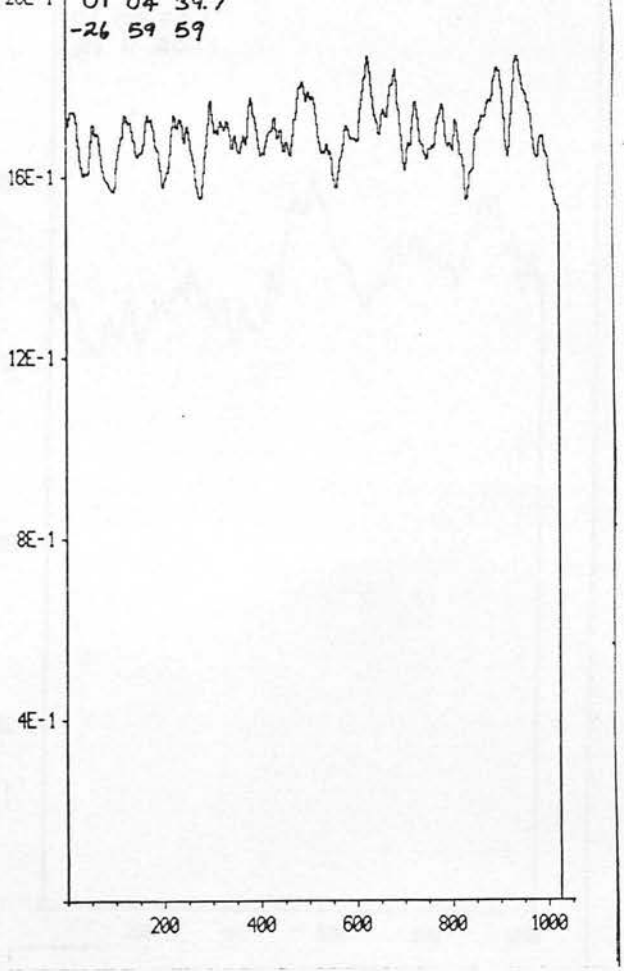
01 04 39.7
-26 59 59
16E-1
12E-1
8E-1
4E-1
200
400
600
800
1000

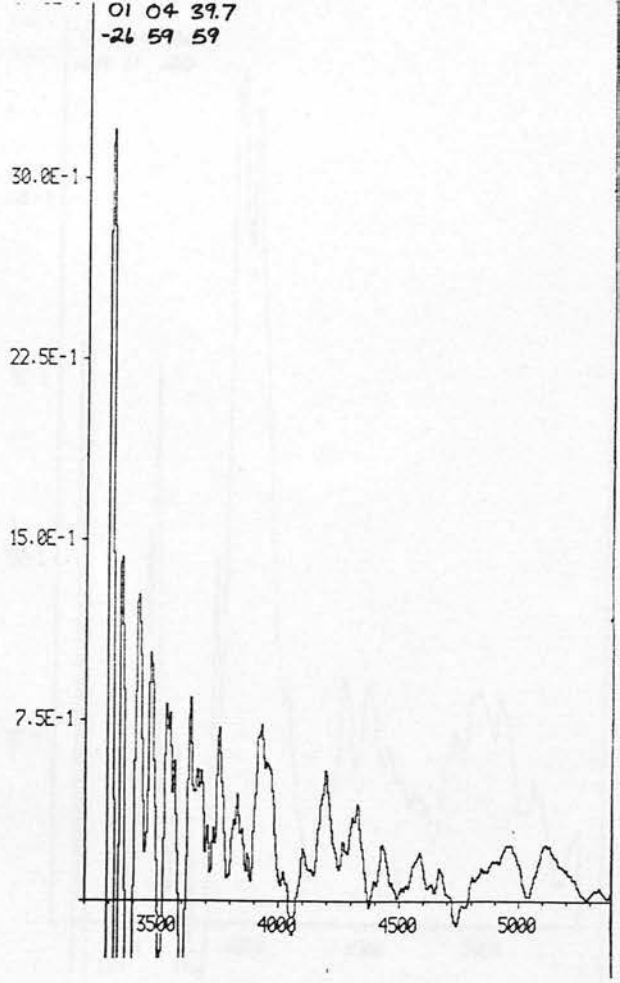
01 04 39.7
-26 59 59
30.0E-1
22.5E-1
15.0E-1
7.5E-1
3500
4000
4500
5000

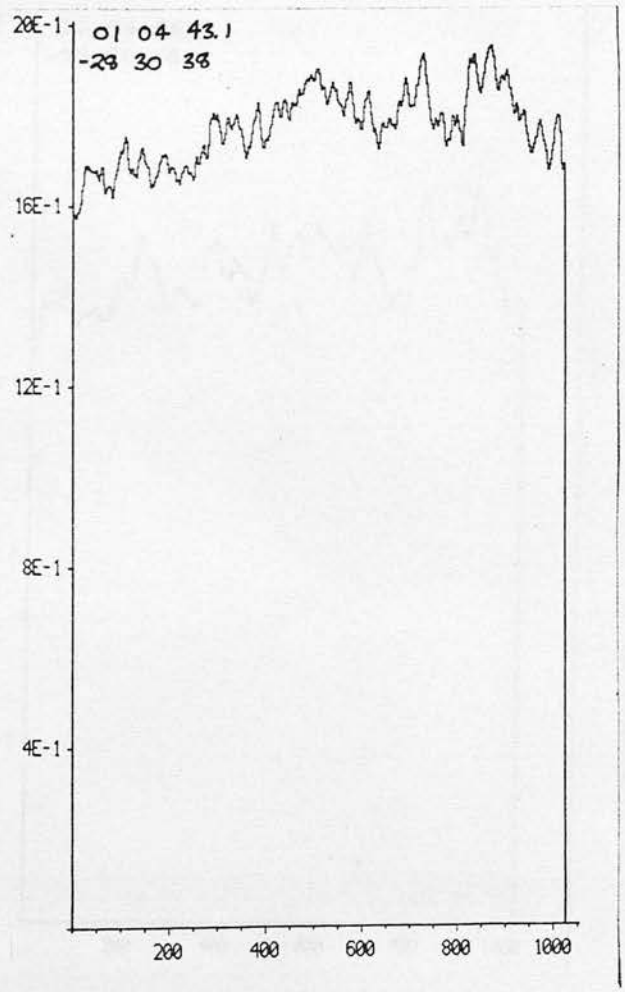
01 04 43.1
-28 30 38
20E-1
16E-1
12E-1
8E-1
4E-1
200
400
600
800
1000

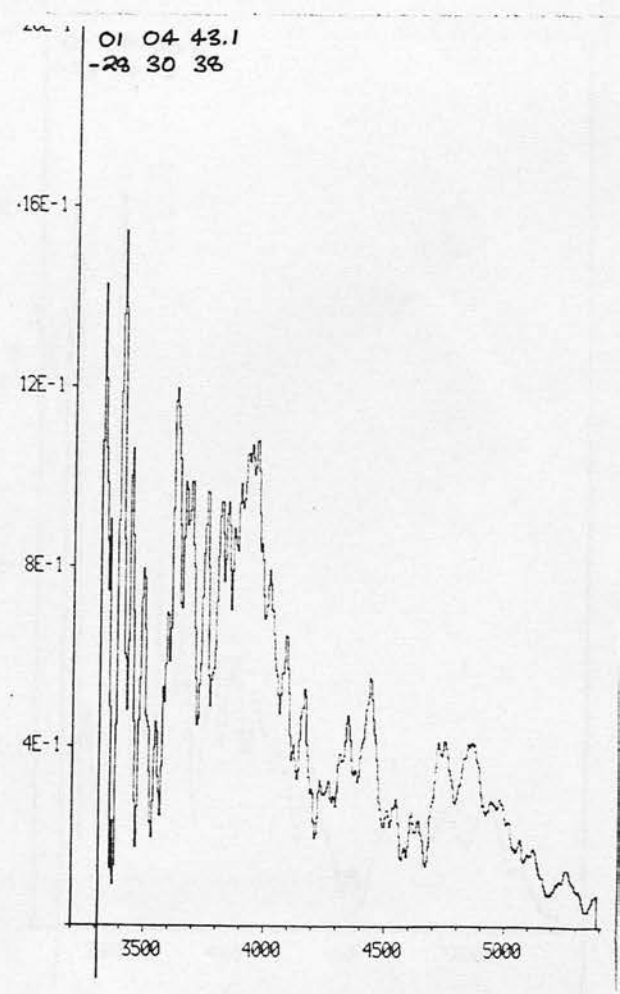
01 04 43.1
-28 30 38
16E-1
12E-1
8E-1
4E-1
3500
4000
4500
5000

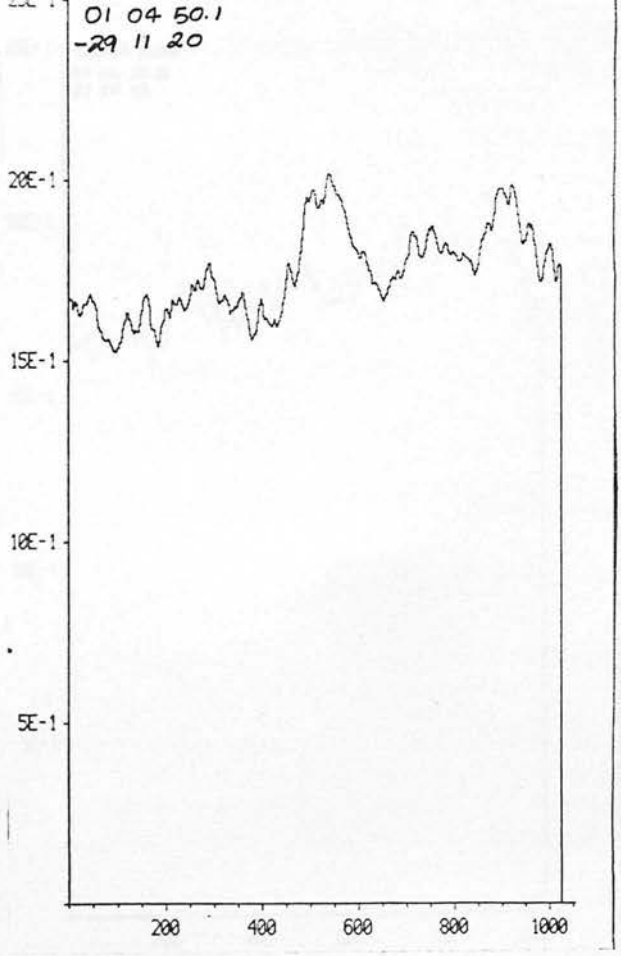
01 04 50.1
-29 11 20
20E-1
15E-1
10E-1
5E-1
200
400
600
800
1000

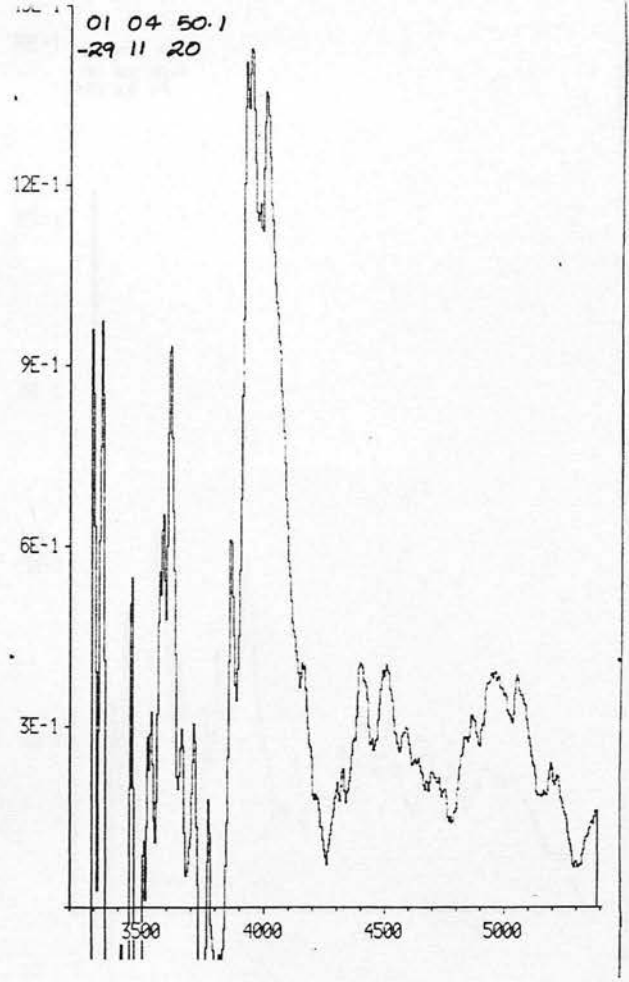
01 04 50.1
-29 11 20
12E-1
9E-1
6E-1
3E-1
3500
4000
4500
5000

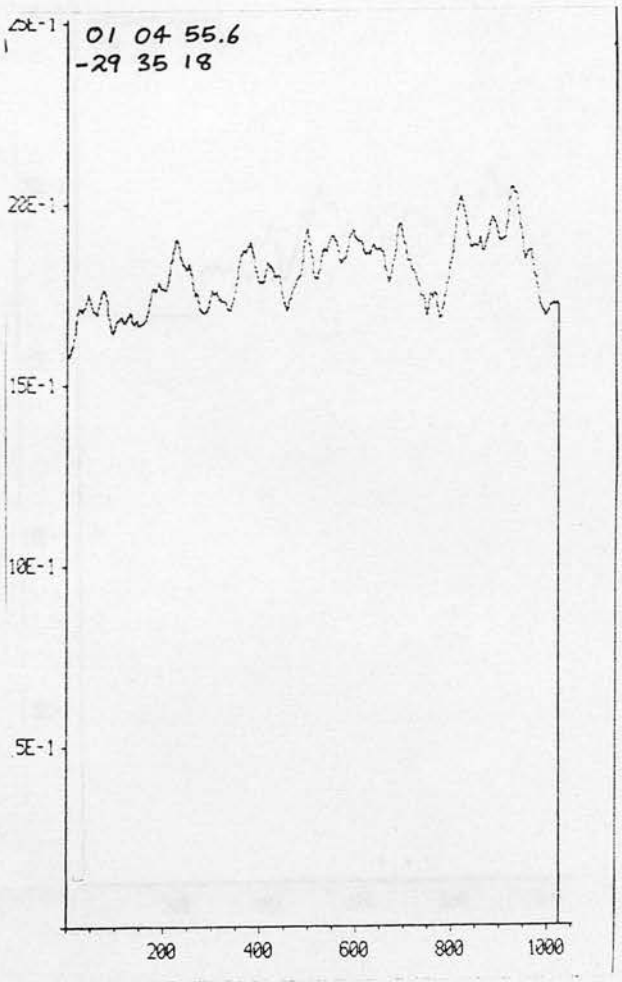
01 04 55.6
-29 35 18
20E-1
15E-1
10E-1
5E-1
200
400
600
800
1000

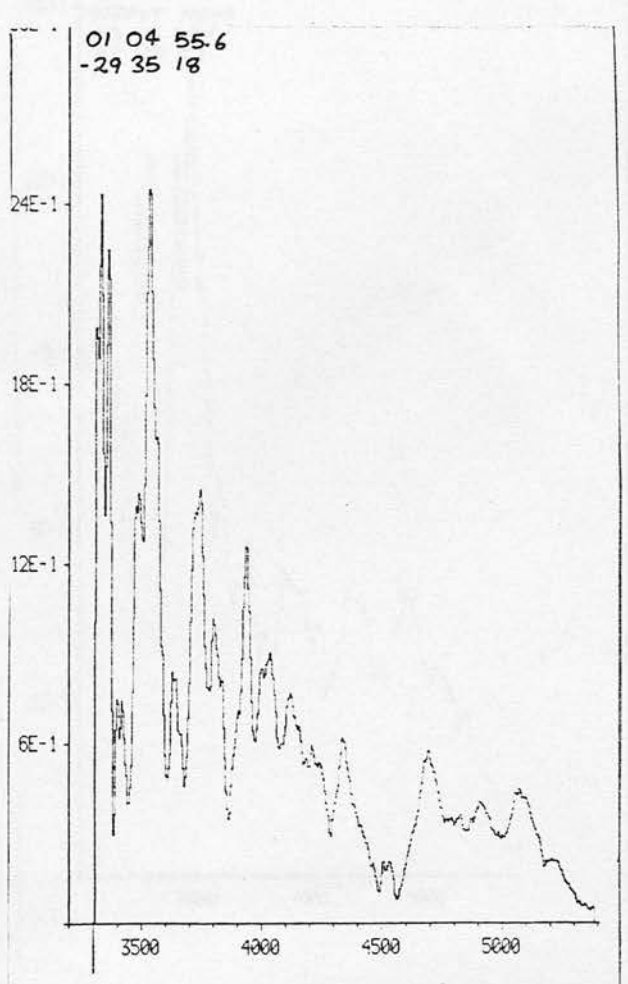
01 04 55.6
-29 35 18
24E-1
18E-1
12E-1
6E-1
3500
4000
4500
5000

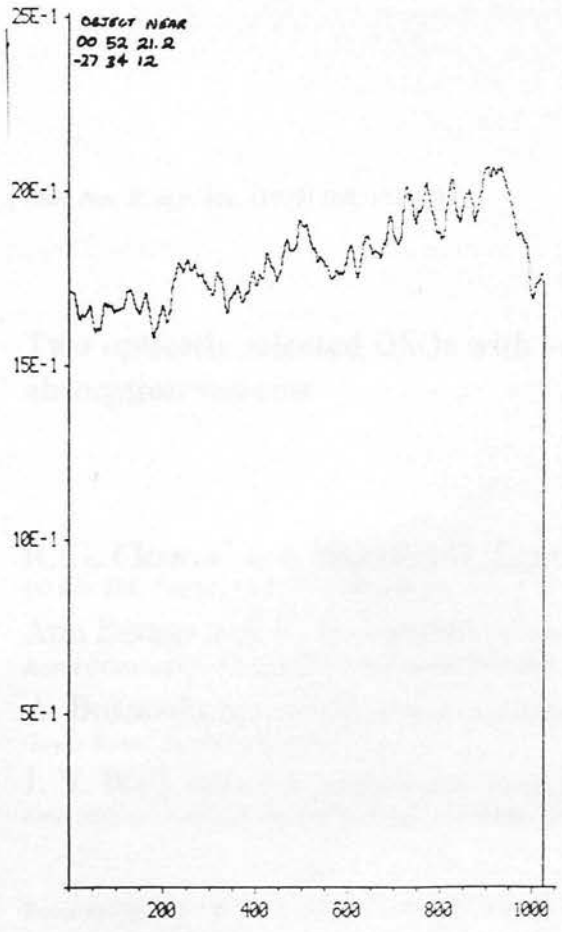
OBJECT NEAR
00 52 21.2
-27 34 12
25E-1
20E-1
15E-1
10E-1
5E-1
200
400
600
800
1000

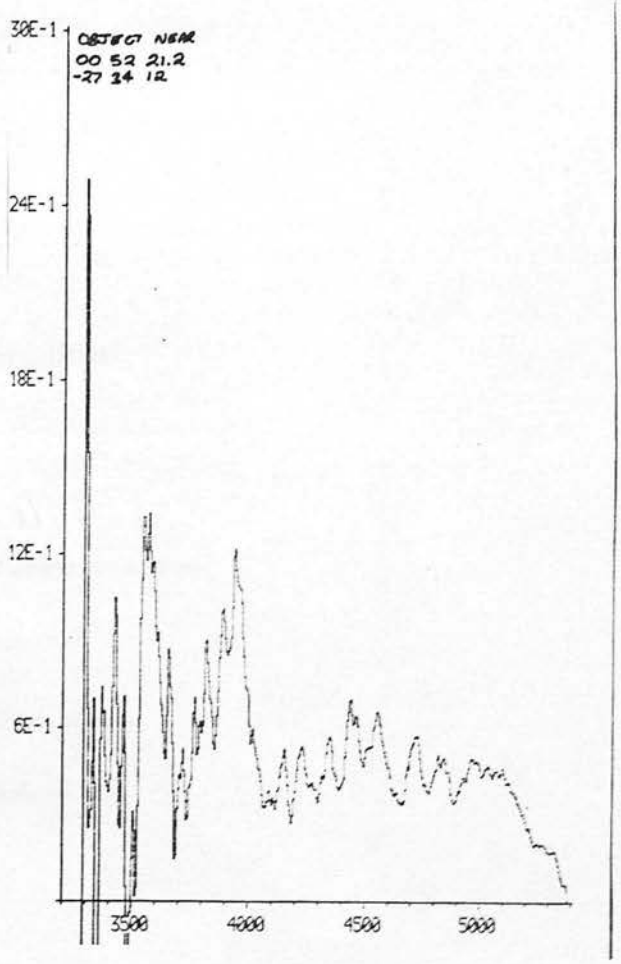
OBJECT NEAR
00 52 21.2
-27 34 12
30E-1
24E-1
18E-1
12E-1
6E-1
3500
4000
4500
5000

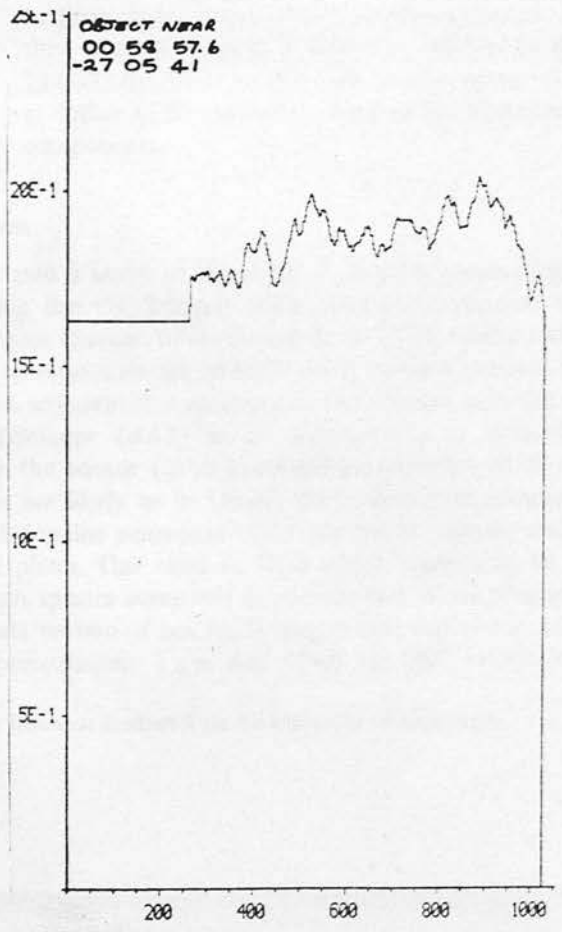
OBJECT NEAR
00 56 57.6
-27 05 41
25E-1
20E-1
15E-1
10E-1
5E-1
200
400
600
800
1000

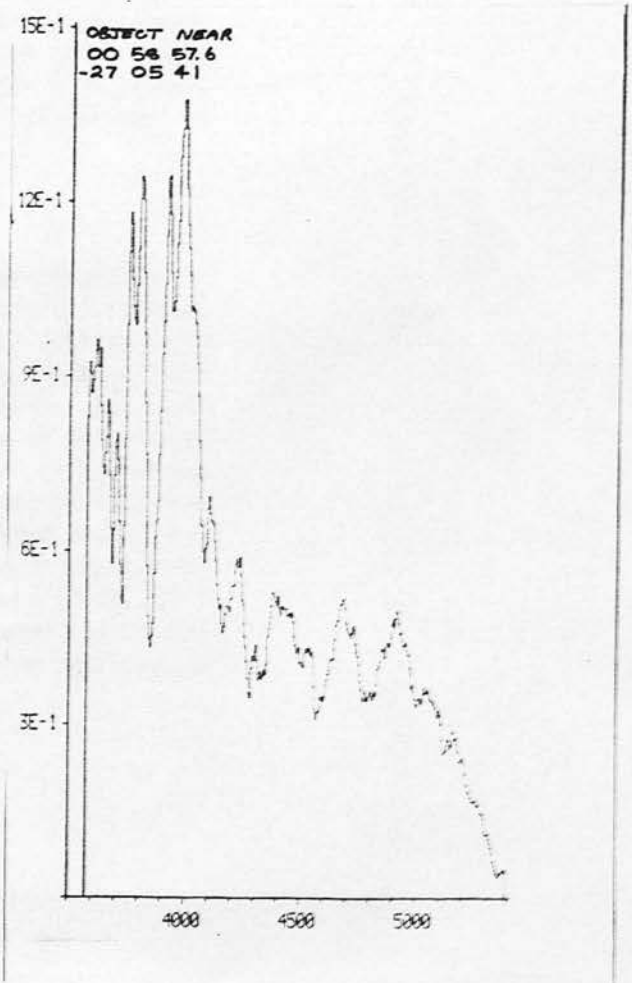
OBJECT NEAR
00 56 57.6
-27 05 41
15E-1
12E-1
9E-1
6E-1
3E-1
4000
4500
5000

Mon. Not. R. astr. Soc. (1979) **189**, 175–182

Two optically selected QSOs with very broad-lined absorption systems

R. G. Clowes* and Malcolm G. Smith *Anglo-Australian Observatory, PO Box 296, Epping, NSW 2121, Australia*

Ann Savage and R. D. Cannon *UK Schmidt Telescope Unit, Royal Observatory, Blackford Hill, Edinburgh EH9 3HJ*

A. Boksenberg *Department of Physics and Astronomy, University College, Gower Street, London WC1E 6BT*

J. V. Wall *Mullard Radio Astronomy Observatory, Cavendish Laboratory, University of Cambridge, Madingley Road, Cambridge CB3 0HA*

Received 1979 March 22; in original form 1979 January 8

Summary. We report the discovery and spectroscopic study of two QSOs with very broad absorption troughs. A low resolution spectrum of the brighter object shows several, apparently broad-lined, high-excitation absorption systems ranging in velocity, relative to the emission system, up to 22 000 km/s (0.07 c) and with widths up to ~ 11 000 km/s. When observed at higher (2 Å) resolution, some of the absorption is resolved into narrower components.

1 Introduction

We have initiated a study of a sample of about a thousand quasi-stellar objects expected from searching five UK Schmidt fields, with a combination of UV-excess and objective-prism techniques (Savage 1978; Savage *et al.* 1978; Smith 1975, 1978b). QSO candidates are assigned to various classes on the basis of the appearance of their objective-prism spectra and studies of representative members of these classes are being made with the 3.9-m Anglo-Australian Telescope (AAT) in an attempt (1) to delineate ranges of observational parameters in the sample, (2) to determine the reliability of the sample (i.e. what percentage of candidates are likely to be QSOs), (3) to determine completeness limits for continuum flux and emission-line equivalent width and (4) to calibrate redshifts derived directly from the Schmidt plates. One class of QSO which appears to be recognizable directly from objective-prism spectra comprises those with very broad absorption features (Smith 1979); the initial data on two of our fields suggest that sufficiently obvious members of the class constitute approximately 1 per cent of all our QSO candidates. Given the significance of

* SRC Visiting Research Student from the University of Edinburgh.

such objects to the question of the location of the absorbing material along the line of sight (see, e.g. Perry, Burbidge & Burbidge 1978), we propose to study some of these very rare objects in detail. Here we describe observations of two such candidates for which slit spectra have been obtained.

2 Discovery of the QSOs

The two objects, Q 2240.9 – 3702 and Q 2238.9 – 4115, were isolated by two of us (RGC and AS) from a UK Schmidt IIIaJ plate centred on RA $22^h\,32^m$, dec $-40°$ (ESO/SRC survey field #345) and exposed for 60 min through the 44 arcmin objective prism. Plate 1 includes finding charts (illustrations of the objective-prism discovery spectra), positions, estimated magnitudes and low-resolution slit spectra.

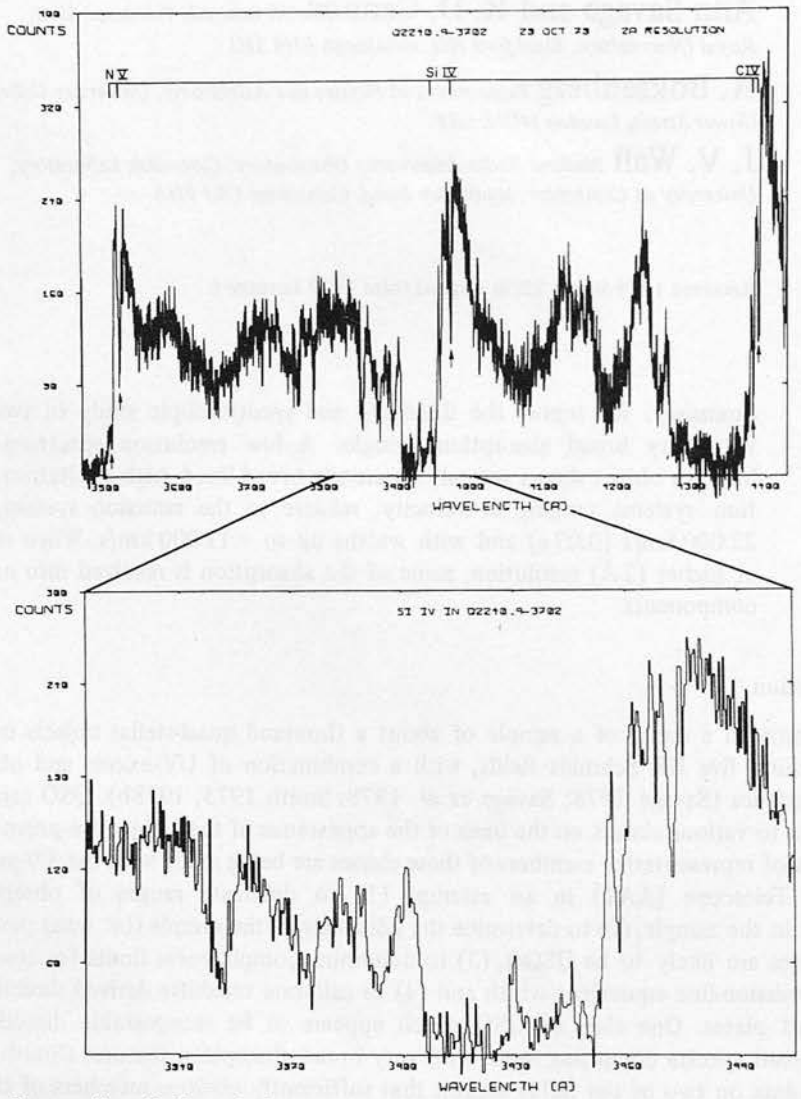

Figure 1. Intermediate (2 Å) resolution spectrum of Q 2240.9 – 3702. The ordinates in both plots have not been renormalized to a relative flux scale. (a) Illustration of the z_{abs} = 1.8316 sharp-lined absorption system. Lines identified in the system are marked with arrows. (b) Expanded section of the same spectrum to illustrate the structure in the main Si IV troughs.

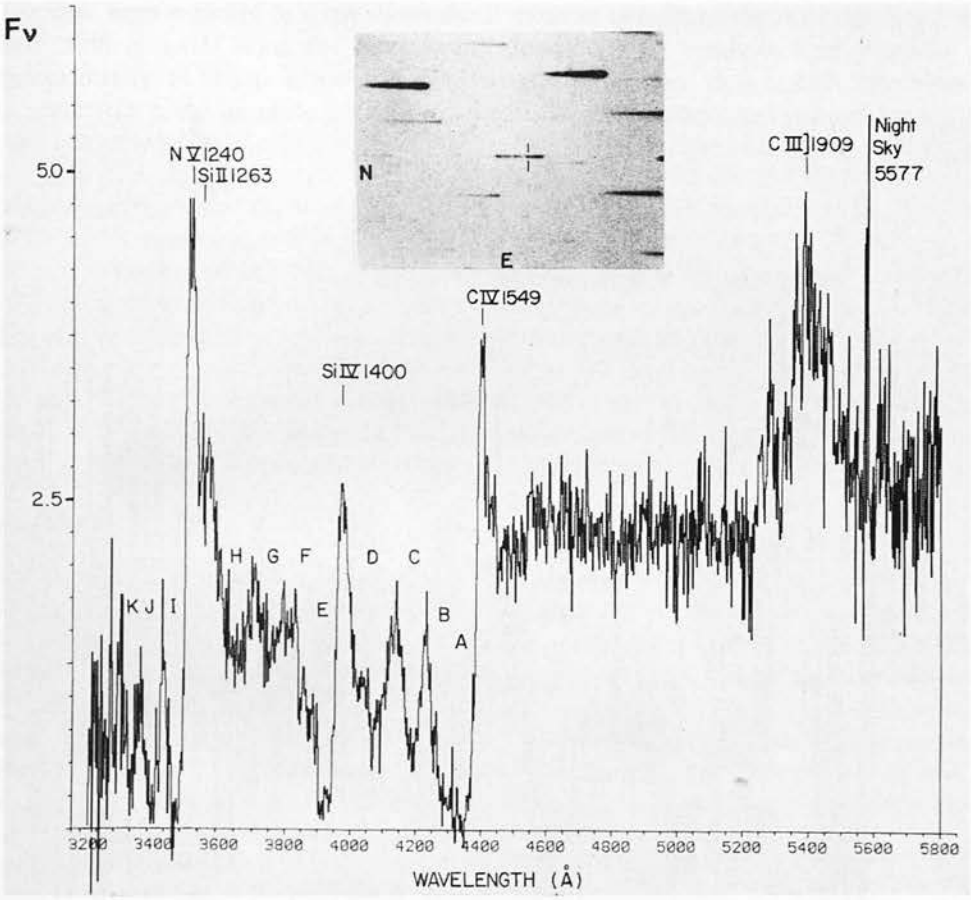

1a

Plate 1. Low resolution spectra of (a) Q2240.9–3702 and (b) Q2238.9–4115. F_ν, the flux per unit frequency interval, is in arbitrary units (because of cloud) and the calibration of both scales is suspect at wavelengths < 3600 Å. The main emission features and broad absorption troughs are marked. The finding charts are made from IIIaJ UK Schmidt objective-prism plates; the spectra are ~1 arcmin long, with wavelength increasing to the right. The position of C IV emission is marked in each case. Measured positions of the objects (epoch 1950.0) are (a) RA $22^h\ 40^m\ 55^s$, dec $-37°\ 02'\ 50''$; (b) RA $22^h\ 38^m\ 54^s$, dec $-41°\ 15'\ 04''$. Estimated magnitudes: Q2240.9–3702, 18; Q2238.9–4115, 19.5. These are based only on visual inspection of the plates and refer to the continua longward of the C IV emission line.

[*facing page* 176]

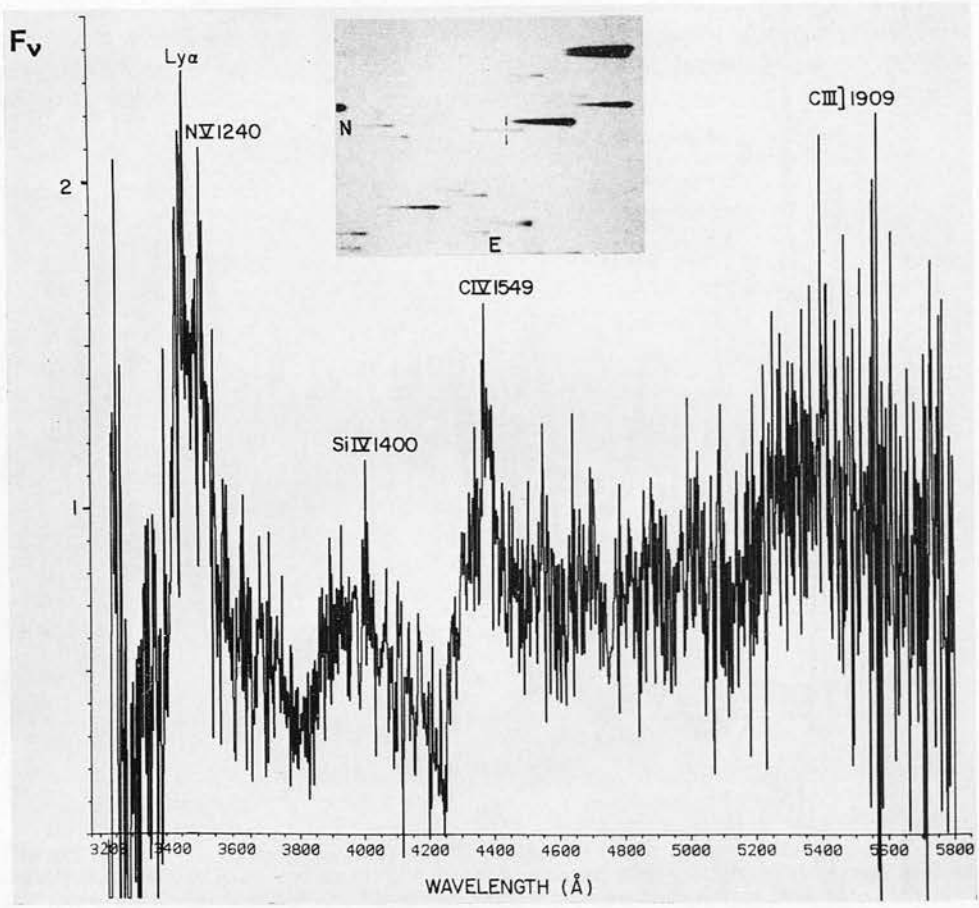
Fν
Lyα
NV1240
SiIV1400
CIV1549
CIII]1909
N
E
2
1
3200
3400
3600
3800
4000
4200
4400
4600
4800
5000
5200
5400
5600
5800
WAVELENGTH (Å)

1b

3 The slit spectra

Low-resolution spectra of both objects, Q 2240.9 – 3702 and Q 2238.9 – 4115, were taken on the night of 1978 September 29/30 using the AAT Image Photon Counting Spectrometer; total integration times of about 1 hr (through cloud) were used for each object. The data were recorded in a one-dimensional mode in two data windows (object and sky) over 2048 channels along the spectrograph dispersion; the windows were separated by approximately 15 arcsec. The object was observed for an equal time in each data window, so allowance could be made for asymmetries in the system response when subtracting the sky component. The positions of the object were exchanged from one window to the other at 1000 s intervals. The channel size along the dispersion was ~ 15 μm. For Q 2240.9 – 3702, the projected 2 arcsec slit width was ~ 4 channels, giving $\lesssim$ 8 Å resolution (FWHM). A slit width of 2.5 arcsec was used for Q 2238.9 – 4115. The standard star L 870 – 2 was observed through a neutral-density filter (of density 0.88) to provide an approximate relative flux calibration. Our wavelengths and relative flux calibrations are suspect below ~ 3600 Å. The cloudy weather precluded any attempt to measure absolute fluxes.

A spectrum at ~ 2 Å resolution was obtained of Q 2240.9 – 3702 on the night of 1978 October 20/21. We followed similar observing procedures to those described above, but used a slit width of 1.5 arcsec and a total integration time of just over 3 hr (with some interference, once again, from clouds). This spectrum is illustrated in Fig. 1.

4 Q 2240.9 – 3702

The emission-line redshift of $z_{em} = 1.82 \pm 0.02$ is poorly determined because of the complexity of the absorption features. We list the apparent centres of the emission lines in Table 1, but the emission-line redshift is based only on the C III] λ 1909 line, the most reliable indicator. The absorption clearly eats away the short wavelength sides of the C IV, Si IV and N V lines, while Ly-α fails to appear in emission above the level of the extrapolated continuum, being largely absorbed out by N V and Ly-α in the highest-redshift absorption-line systems [troughs I and J in Plate 1(a)]. Meaningful measures of emission-line equivalent widths were thus rendered impossible. Si II λ 1263 appears prominently in the redward wing of the N V emission feature.

Table 1. (a) Emission lines in Q 2240.9 – 3702. $z_{em} = 1.82 \pm 0.02$.*

Observed		Identification
λ_{air} (Å)	FWHM (Å)	
3518	—	N V λ 1240
3576	—	Si II λ 1263
3977	—	Si IV + O IV] λ 1400
4400	—	C IV λ 1549
5391	120:	C III] λ 1909

(b) Emission lines in Q 2238.9 – 4115. $z_{em} = 1.83 \pm 0.03$

3509	—	N V λ 1240
4380	40:	C IV λ 1549
5400	—	C III] λ 1909

* All redshifts in this paper are calculated from vacuum values of wavelength.

Even in the low resolution spectrum we find a series of at least eight wide absorption troughs between the C IV and N V emission features. These are labelled A to H in Plate 1; approximate wavelengths, widths and equivalent widths are listed in Table 2(a) along with identifications for these (and more troughs at wavelengths shortward of that of N V emission). Four absorption redshifts are identified from the low resolution spectrum at $z_{abs} \sim 1.62, 1.70, 1.76$ and 1.80.

Because of the uncertain continuum level and difficulties in defining the boundaries of the absorption troughs, equivalent widths and column densities can be determined only very approximately. The equivalent widths given in Table 2 are based on a continuum extrapolated from the region longward of the C IV emission line. Using the optically thin approximation (which is clearly a severe underestimate, at least for systems I and II), we obtain lower limits to the column densities as given in Table 3 (using atomic parameters taken from Morton & Smith (1973)).

Higher resolution (see Fig. 1) shows that most of the troughs possess considerable structure. Meaningful measures of equivalent widths in this extraordinary object are impossible on account of the uncertainty in the continuum level from which these sharper features absorb; there is also evidence for considerable blending of absorption features of all scales (narrow to trough-like). We can therefore make no further analysis of the physical conditions in the absorbing material beyond the crude estimates given above.

Sharper lines (of necessarily very uncertain equivalent width – see above) were found in the higher resolution spectrum at the following (air) wavelengths λλ 3507*, 3517*, 3603*,

Table 2. (a) Absorption troughs in Q 2240.9 – 3702.

Trough letter	λ_{air} (Å)	Observed EW (Å)	FWHM (Å)	System	Identification	z_{vac}
A	4340	60	67	I	C IV λ 1549	1.80
B	4280	59	74	II	C IV λ 1549	1.75
C	4189	44	92	III	C IV λ 1549	1.70
D#	4068	79	133	IV	C IV λ 1549	1.63
E	3925	50	53	I	Si IV λ 1400	1.80
F	3870	35	60	II	Si IV λ 1400	1.77
G	3768	33	—	III	Si IV λ 1400	1.69
H	3655	—	—	IV	Si IV λ 1400	1.61
I	3478	—	—	I	N V λ 1240	1.80
J	3405	—	—	I	Ly-α λ 1216	1.80
				II	N V λ 1240	1.75
K	3345	—	—	II	Ly-α λ 1216	1.75
				III	N V λ 1240	1.70

Adopted absorption redshifts z_{abs}: I 1.80; II 1.76; III 1.70; IV 1.62.

(b) Absorption troughs in Q 2238.9 – 4115

A	4181	123	150:	I	C IV λ 1549	1.70
B	3780	87	200:	I	Si IV λ 1400	1.70

Adopted absorption redshift, $z_{abs} = 1.70$ (may be complex of more systems).

#Trough D appears to consist of two features, similar to troughs A, B. These features in trough D do not individually match any structure in trough H. However, trough H may be confused by line emission. The higher resolution data indicate that trough F consists of several components. Thus the apparent systems I–IV are in fact only approximate simplifications of a very complex absorption structure.

Table 3. Relative velocities* and lower limits to column densities (cm^{-2}).

(a) Q 2240.9 – 3702

System	I	II	III	IV
$N(Si^{3+})$	1×10^{15}	9×10^{14}	9×10^{14}	–
$N(C^{3+})$	3×10^{15}	3×10^{15}	3×10^{15}	5×10^{15}
v_{rel}/c	0.01	0.02	0.04	0.07

(b) Q 2238.9 – 4115

$N(Si^{3+})$	2×10^{15}
$N(C^{3+})$	7×10^{15}
v_{rel}/c	0.06

* Derived from the relation $\frac{v_{rel}}{c} = \frac{(1+z_{em})^2 - (1+z_{abs})^2}{(1+z_{em})^2 + (1+z_{abs})^2}$.

3671, 3714, 3725, 3762*, 3851, 3874*, 3886, 3950, 3957*, 3962, 3967, 3971*, 4003*, 4129, 4154*, 4214, 4253*, 4258, 4331:*, 4383*, 4390*, 4404* Å (the asterisk denotes a resolved line). Some of the strongest lines in this list are identified by the following system:

Observed λ_{air} (Å)	Identification	z_{vac}
4390.0	C IV 1550.77	1.8316
4382.7	C IV 1548.20	1.8316
3971.4	Si IV 1402.77	1.8319
3517.5	N V 1242.80	1.8311
3507.0	N V 1238.82	1.8317

$z_{abs} = 1.8316$ (vacuum).

The line corresponding to Si IV λ 1393.76 expected near 3946 Å presumably forms a small part of the trough 'E'. Note that although $z_{abs} > z_{em}$ for this sharp-lined system, the uncertainties in z_{em} are too great to be sure whether or not there is an apparent blueshift with respect to the quasar.

It should be understood that no claim is made that the above list of sharper lines is in any way complete even down to quite large values of equivalent width because of the interference of the absorption troughs; to make further attempts to identify redshift systems, it is necessary to refer to the plots in Plate 1 and Fig. 1. The lines in the $z_{abs} = 1.8316$ system are resolved in the higher-resolution spectrum, with an estimated FWHM in the range 2–6 Å after deconvolution of the instrumental profile; the large uncertainty in the value of the FWHM is again associated with corresponding uncertainty in the continuum level from which the absorption occurs.

5 Q 2238.9 – 4115

Reference to Tables 1–3 provides the data derived from the spectrum for this object, shown in Plate 1(b). Similar caveats to those given in the previous section apply here, though with more force, as the object is substantially fainter and the signal-to-noise ratio in the spectrum is correspondingly poorer. Again the emission-line redshift, $z_{em} = 1.83 \pm 0.03$, is based only on the C III] λ 1909 line. However, the agreement with the C IV and N V emission lines

suggests that the emission lines may be less heavily eaten into by absorption than in Q 2240.9 – 3702.

At the low resolution and low signal-to-noise ratio of the plot in Plate 1(b), we can identify with certainty only the two very wide, asymmetric absorption troughs; they correspond to Si IV and C IV in a system with $z_{abs} \sim 1.70$, but involving some material travelling at a velocity $\sim 0.08\,c$ with respect to the emission-line frame of reference.

6 Discussion

The broad absorption lines in QSOs can conveniently be separated into two main astrophysical classes: (a) those objects with strongly damped Ly-α absorption, where the Doppler widths of the lines in the spectrum are relatively small, as in PHL 957 (Beaver *et al.* 1972), 1331 + 170 (Carswell *et al.* 1975) and PKS 0528 – 250 (Jauncey *et al.* 1978); the broad Ly-α troughs arise from high H I column densities and such spectra are not discussed further here: (b) objects with broad, often asymmetric lines, indicating large Doppler widths; those known at present involve several resonance lines with high degree of ionisation (e.g. C IV, N V). The prototype of this class is PHL 5200 (Lynds 1967; Burbidge 1969; Scargle, Caroff & Noerdlinger 1970), a photoelectric spectrum of which is illustrated by H. E. Smith (1978a). A similar object, RS23 (Burbidge 1970) was, for several years, the only other known member of this rare class of objects; like PHL 5200, it has fairly broad absorption in the blueward wings of the major emission features. On the basis of this sample of two objects, it was thought that such systems are likely to be produced by material ejected from the QSO, but that the ejection velocities would be unlikely to exceed the typical velocities found within the emission-line regions of QSOs.

The first object in this class discovered by means of slitless spectroscopy was Q 1246 – 057 (Osmer & Smith 1977). Boksenberg *et al.* (1978) have presented arguments to show that the material responsible for the (single) broad absorption system in Q 1246 – 057 was ejected from the QSO at a relative velocity of $\sim 0.05\,c$. Another quasar selected in this way, Q 0324 – 407 (Whelan, Smith & Carswell 1979), exhibits *two* apparently broad-lined systems in the one object. However, the line widths in that object (and other single-system objects like it) are not inconsistent with the velocity dispersions that one may expect from two intervening clusters of galaxies along the line of sight. The significance of objects such as Q 1246 – 057 and the even more extreme objects discussed here is that the lines are probably too wide to have been produced by any known intervening material, unless it was ejected from the QSO.

On the basis of existing observational data, all known sharp-lined systems could arise from material at cosmological distances from the QSO. One of the circumstantial arguments often used to support this concept is that no mechanism is known for containing the absorbing material within a velocity range of ~ 10–100 km/s while being ejected at velocities $\sim 10^4$ km/s or more. It is of interest, therefore, in the search for observational data on the degree of velocity containment possible in high velocity material that (1) Morton (1976) has found lines in ζ Pup with FWHM = 50 km/s, yet with a velocity of 2120 km/s less than that of the star, i.e. narrow lines *are* possible in high velocity mass flow, (2) Wright *et al.* (1979) have shown that the broad absorptions in PKS 1157 + 014 are due to the superposition of distinct components at different redshifts, (3) the absorbing material in Q 2240.9 – 3702 and Q 2238.9 – 4115 is probably being ejected from the QSOs at velocities up to $\sim 0.08\,c$ and (4) there is evidence that the absorption troughs in Q 2240.9 – 3702 could be breaking up into sharper components ejected from the QSO (whereas, for example, no such break-up was observed in the troughs of Q 1246 – 057). By producing a

reasonably large sample of broad-lined objects (a procedure most efficiently executed by using objective-prism Schmidt plates) we can now hope to gain greater insight into the properties, and particularly the possible evolution, of broad-lined systems.

Acknowledgment

RGC wishes to thank the SRC for a research studentship.

References

Beaver, E. A., Burbidge, E. M., McIlwain, C. E., Epps, H. W. & Strittmatter, P. A., 1972. *Astrophys. J.*, **178**, 95.
Boksenberg, A., Carswell, R. F., Smith, M. G. & Whelan, J. A. J., 1978. *Mon. Not. R. astr. Soc.*, **184**, 773.
Burbidge, E. M., 1969. *Astrophys. J.*, **155**, L43.
Burbidge, E. M., 1970. *Astrophys. J.*, **160**, L33.
Carswell, R. F., Hilliard, R. L., Strittmatter, P. A., Taylor, D. J. & Weymann, R. J., 1975. *Astrophys. J.*, **196**, 351.
Jauncey, D. L., Wright, A. E., Peterson, B. A. & Condon, J. J., 1978. *Astrophys. J.*, **221**, L109.
Lynds, C. R., 1967. *Astrophys. J.*, **147**, 396.
Morton, D. C., 1976. *Astrophys. J.*, **203**, 386.
Morton, D. C. & Smith, W. H., 1973. *Astrophys. J. Suppl.*, **26**, 333.
Osmer, P. S. & Smith, M. G., 1977. *Astrophys. J.*, **213**, 607.
Perry, J. J., Burbidge, E. M. & Burbidge, G. R., 1978. *Publs astr. Soc. Pacif.*, **90**, 337.
Savage, A., 1978. *PhD thesis*, University of Sussex.
Savage, A., Bolton, J. G., Tritton, K. P. & Peterson, B. A., 1978. *Mon. Not. R. astr. Soc.*, **183**, 473.
Scargle, J. D., Caroff, L. J. & Noerdlinger, P. D., 1970. *Astrophys. J.*, **161**, L115.
Smith, H. E., 1978a. *Mercury*, **7**, 27.
Smith, M. G., 1975. *Astrophys. J.*, **202**, 591.
Smith, M. G., 1978b. *Vistas Astr.*, **22**, 321.
Smith, M. G., 1979. *Proc. IAU Colloq. No. 47, Spectral Classification of the Future*, in press.
Whelan, J. A. J., Smith, M. G. & Carswell, R. F., 1979. *Mon. Not. R. astr. Soc.*, in press.
Wright, A. E., Morton, D. C., Peterson, B. A. & Jauncey, D. L., 1979. *Mon. Not. R. astr. Soc.*, in press.

Note added in proof

More quantitative evidence in support of some of our speculations has been obtained very recently (Weymann, R. J., Williams, R. E., Peterson, B. M. & Turnshek, D. A., 1979, *Preprints of the Steward Observatory*, No. 220). Based on a sample of 46 QSO's of intermediate redshift, they show that the majority of *sharp*-lined absorption systems in the redshift interval 3000 km/s $< c(z_{em} - z_{abs}) <$ 20 000 km/s are most likely to be identifiable with material ejected from the QSO. They also cite material in preparation at Steward Observatory (based on 'MCS' QSO's discovered by the Michigan group (MacAlpine *et al.*) using the Curtis Schmidt telescope and thin objective prism), which provides further evidence for multiple and detached absorption troughs; they interpret the debris from old PHL 5200-type systems as giving rise to the sharp-lined 'ejected' component observed in their survey of the 46 QSO's. The problem of accelerating material to near relativistic velocities while keeping the clouds coherent is not regarded by Weymann *et al.* as a serious difficulty; the coherence could arise, or the clouds could condense, long after the acceleration process. Indeed, Rees (1970, *Astrophys. J.*, **160**, L29) has already discussed such a process of condensation into filaments in some detail.

A related matter concerns the relatively high percentage of broad absorption-line systems

being found among the MCS QSO's (MacAlpine & Weymann, private communication). We have quoted a figure ~ 1 per cent for the very extreme objects discussed here because they can be recognized easily on the UK Schmidt plates. The superior seeing and larger dispersion available to the Curtis Schmidt should make detection of less extreme cases more reliable with that telescope. We have found suspected cases with less extreme absorption, but would need to check them with slit spectroscopy.